

251 p.

FACILITY FORM 802

N65-35286

(ACCESSION NUMBER)

(THRU)

251

1

(PAGES)

(CODE)

OR 51832

31

(NASA CR OR TMX OR AD NUMBER)

(CATEGORY)

GPO PRICE \$
CSFTI PRICE(S) \$

Hard copy (HC) \$6.00
Microfiche (MF) \$1.50

ff 653 July 65

VOYAGER DESIGN STUDIES

Volume Five: Lander Design
Part One

Prepared Under Contract Number
NASw 697 ■ Research and Advanced
Development Division ■ Avco Corpo-
ration ■ Wilmington, Massachusetts ■
National Aeronautics and Space Ad-
ministration ■ Avco/RAD ■ TR-63-34
■ 15 October 1963

VOYAGER DESIGN STUDIES

Volume V: Lander Design

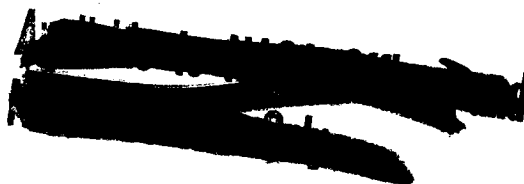
Part I

Avco RAD-TR-63-34

15 October 1963

Prepared under Contract No. NASw 697 by

RESEARCH AND ADVANCED DEVELOPMENT DIVISION
AVCO CORPORATION
Wilmington, Massachusetts
for
NATIONAL AERONAUTICS AND SPACE ADMINISTRATION



FOREWORD

The Voyager Design Study final report is divided into six volumes, for convenience in handling. A brief description of the contents of each volume is listed below.

Volume I -- Summary

A completely self-contained synopsis of the entire study.

Volume II -- Scientific Mission Analysis

Mission analysis, evolution of the Voyager program, and science payload.

Volume III -- Systems Analysis

Mission and system tradeoff studies; trajectory analysis; orbit and landing site selection; reliability; sterilization

Volume IV -- Orbiter-Bus System Design

Engineering and design details of the orbiter-bus

Volume V -- Lander System Design

Engineering and design details of the lander.

Volume VI -- Development Plan

Proposed development plan, schedules, costs, problem areas.

TABLE OF CONTENTS

1. MECHANICAL DESIGN.....	2
1.1 Systems Requirements	2
1.2 Reference Design--Mars Schilling Atmospheres.....	39
1.3 Design Concept for Mars Lander--Kaplan Atmospheres.....	49
2. DESCENT AND LANDING SYSTEMS	56
2.1 Parachute System.....	56
2.2 Landing System	82
3. AERODYNAMIC DESIGN--MARS	99
3.1 Vehicle Configuration	99
3.2 Vehicle Performance	106
3.3 Effects of Kaplan Atmosphere.....	109
4. HEAT SHIELD DESIGN--MARS.....	134
4.1 Thermal Analysis.....	134
4.2 Heat Shield Material for Mars	182
5. STRUCTURE DESIGN--MARS.....	202
5.1 General Approach	202
5.2 Analysis.....	207
5.3 Structural Consequences of Kaplan's Low-Pressure Atmosphere	219
6. POWER SUPPLY.....	221
6.1 Constraints	221
6.2 Power Supply Selection.....	221
6.3 System Description	231
7. COMMUNICATION SYSTEMS	240
7.1 System Requirements	240
7.2 Communication System Description.....	241
8. MECHANICAL DESIGN--VENUS.....	372

TABLE OF CONTENTS (Concl'd)

8.1 Capsule Entry from Orbit	372
8.2 Direct Entry Lander	384
9. DESCENT SYSTEM DESIGN--VENUS	388
9.1 System Requirements	388
9.2 Reference	388
9.3 Materials	388
10. AERODYNAMIC DESIGN--VENUS	392
10.1 Entry Concepts	392
10.2 Reference Designs	396
11. HEAT SHIELD DESIGN--VENUS	401
11.1 Thermal Analysis	401
11.2 Heat Shield Materials for Venus	434
12. STRUCTURE DESIGN--VENUS	447
12.1 General Approach	447
12.2 Analysis	451
13. POWER SUPPLY--VENUS	457
13.1 Capsule	457
13.2 Lander	458
14. COMMUNICATION SYSTEM--VENUS	463
14.1 Communication System Requirements	463
14.2 General System Description	463
14.3 Detailed System Description	464
14.4 Antenna Design	478
Appendixes	
A. Recommended Landing System for Voyager	489
B. Summary of Rocketdyne Studies on Lander Propulsion System	521
C. Simulation of Reentry Radiation Heat Transfer	565
D. High Altitude Breakdown	582

LIST OF TABLES

Table	1	Summary of Propulsion System Performance Parameters -- Mars Lander	15
	2	Parametric Weight Study, Voyager Mars Lander -- Self-Erecting Concept	29
	3	Allowable External Ambient Temperatures	35
	4	Physical Characteristics of Lander Navigation Equipment...	36
	5	Weight Summary, Mars Lander, Reference Design, Schilling Atmospheres, -- Self-Erecting Concept	46
	6	Weight Summary, Mars Lander, Reference Design, Kaplan Minimum Atmosphere -- Self-Erecting Concept	51
	7	Summary of Aerothermodynamic Tests	104
	8	Atmospheric Data used for Maps	107
	9	Mars JPL Atmosphere and Uncertainties	110
	10	Typical Physical Properties of Proposed Mars Heat	201
	11	Mars Lander Environmental Criteria	206
	12	Mars Lander (Direct and Relay) Major Subsystem Weight, Volume, and Power.	243
	13	Mars Lander (Direct and Relay) Data Handling Subsystems Weight, Volume, and Power	245
	14	Sampling Rates and Duty Cycles for Mars Lander Scientific and Engineering Measurements	246
	15	Mars Lander Engineering Data Channel Requirements	247
	16	Telecommunications Design Control Chart	252
	17	Mars Lander Altimeter Sensitivity Calculations.....	263
	18	Mars Lander Altimeter Design Parameters.....	264

LIST OF TABLES (Cont'd)

Table	19	Design Parameters for Transmitter Modulator -- Mars Lander Altimeter	266
	20	Mars Lander Altimeter (X-Band) Component Size, Weight, and Power	267
	21	Telecommunications Design Control Chart	270
	22	Telecommunications Design Control Chart	296
	23	Lander Altimeter Commanded Receiver Design Parameters	302
	24	Mars Lander Low-Capacity Command Receiver (S-Band) Size, Weight, and Power Requirement	302
	25	Telecommunications Design Control Chart	307
	26	Mars Lander Power Loading During Transmission	313
	27	Mars Lander Constant-Power Loading Between Transmission	313
	28	General Telecommunications Design Control Chart	317
	29	Telecommunications Design Control Chart	326
	30	Telecommunications Design Control Chart	335
	31	VHF Antenna Array on Mars Lander Vehicle	353
	32	Electrical Characteristics, Relay/ Command Link Antennas	364
	33	Altimeter Antenna Operating Characteristics	366
	34	Mars Lander Direct-Link Telemetry Antenna	371
	35	Weight Summary, Venus Atmospheric Probe, Reference Design	375
	36	Summary of System Performance Parameters, Venus Capsule	383

LIST OF TABLES (Cont'd)

Table 37	Weight Summary, Venus Lander, Reference Design 387
38	Venus Atmospheres 400
39	Typical Properties of Graphite -- and Carbon-Based Materials 445
40	Venus Capsule Power Consumption List 457
41	Power Consumption List 460
42	Venus Lander Subsystem Weights, Volumes, and Power Consumptions 465
43	Venus Capsule Subsystem Weights, Volumes, and Power Consumptions 466
44	Separation to Entry Telecommunications Design Control Chart 469
45	Atmospheric Data Mode, Telecommunications Design Control Chart 471
46	Transfer of Surface Data, Telecommunications Design Control Chart 473
47	Capsule Telecommunications Design Control Chart 475
48	Lander Antenna Characteristics 480
A1	Comparison of the Landing System for a 1635 Pounds Mars Lander Vehicle in the Schilling "Lower Limit" Atmosphere and the JPL "Minimum Density" Atmosphere 497
B1	Weight Summary 523
B2	Power Requirements 524
B3	Summary System Performance Parameter 531
B4	Predicted Component Failure Rates and System Reliability 532

LIST OF TABLES (Concl'd)

Table	B5	Thrust Chamber Design Parameters	534
	B6	Comparison of Candidate Propellant Tank Materials	539
	B7	Weight Summary	548
	B8	Power Requirements	549
	B9	Summary of System Performance Parameters	552
	B10	Predicted Component Failure Rates and System Reliability	553
	B11	Thrust Chamber Design Parameters	556
	C1	Preliminary Results	572
	C2	Linear Phenolic	573

LIST OF FIGURES

Figure 1	Landing Systems Chart	3
2	Crushup Pad Construction (Typical)	5
3	Relay Lander	7
4	Mars Parachute Sequence	10
5	Block Diagram of Mars Vehicle Descent System Sequence Controller	11
6	Comparison of Total Vehicle Weight and Weight of Heat Shield and Structure For V-1 and V-2 Vehicles	14
7	Design Layout of Mars Lander Integrated Propulsion System	16
8	Mars Lander Propulsion System Schematic	18
9	Mars Lander Total Heat Shield Material Weight (Excluding Substructure) versus Total Vehicle Weight at Entry (V-2 Shape, $M/C_D A = 0.6$, Schilling Minimum Atmosphere)	20
10	Mars Lander Total Heat Shield Material Weight (Excluding Substructure) versus Total Vehicle Weight at Entry (V-2 Shape, $M/C_D A = 0.6$, Schilling Maximum Atmosphere)	21
11	Mars Lander Total Heat Shield Material Weight (Excluding Substructure) versus Total Vehicle Weight at Entry (V-2 Shape, $M/C_D A = 0.9$, Schilling Minimum Atmosphere)	22
12	Mars Lander Total Heat Shield Material Weight (Excluding Substructure) versus Total Vehicle Weight at Entry (V-2 Shape, $M/C_D A = 0.9$, Schilling Maximum Atmosphere)	23
13	Mars Lander Total Heat Shield Material Weight (Excluding Substructure) versus Total Vehicle Weight at Entry (V-2 Shape, $M/C_D A = 1.5$, Schilling Minimum Atmosphere)	24

LIST OF FIGURES (Cont'd)

Figure 14	Mars Lander Total Heat Shield Material Weight (Excluding Substructure) versus Total Vehicle Weight at Entry (V-2 Shape, $M/C_D A = 1.5$, Schilling Maximum Atmosphere)	25
15	Mars Lander Total Heat Shield Material Weight (Excluding Substructure) versus Total Vehicle Weight at Entry (V-1 Shape, $M/C_D A = 0.9$, Schilling Minimum Atmosphere)	26
16	Mars Lander Total Heat Shield Material Weight (Excluding Substructure) versus Total Vehicle Weight at Entry (V-1 Shape, $M/C_D A = 0.9$, Schilling Maximum Atmosphere)	27
17	Mars Lander Parametric Weight Study	30
18	Transit Journey	33
19	Lander Journey (Spinning)	34
20	Lander Computer	38
21	Sterilized Sun Sensor	40
22	Lander Reference Design, Mars Schilling Atmosphere	41
23	Photograph of Lander "Acorn" Model	43
24	Mars Lander after Erection	44
25	Mars V-2 Entry Vehicle External Configuration	48
26	Weight versus Diameter for Mass Lander JPL Minimum Atmosphere Apollo Shape	52
27	Weight versus Diameter for Mass Lander JPL Minimum Atmosphere Aluminum Honeycomb Structure	53
28	Weight versus Diameter for Mars Lander JPL Minimum Atmosphere Aluminum Honeycomb Structure	54

LIST OF FIGURES (Cont'd)

Figure 29	Mars Lander -- Kaplan Atmosphere	55
30	Parachute Performance Envelope and Initiation Limits.....	58
31a	Temperature Characteristics of Organic Fibers for Parachute Fabrics	59
31b	Percent Strength Retained versus Exposure Time at Various Temperatures for MIL-T-5038 Type IV HT-1 Fabric	59
32	Typical Drogue Deployment Altitude versus Vehicle $M/C_D A$	62
33	Altitude versus Axial Deceleration for Lander Entry	63
34	Methods of Sensing for Drogue Chute Deployment	64
35	Effect of Velocity and Entry Angle Variation on Drogue Actuation	67
36	Effect of Atmospheric Model D/W for $M = 2.5$ versus Entry Angle	68
37	Altitude versus Mach Number for Typical Voyager Lander Drogue Flight	69
38	Drogue Deployment Altitude versus Entry Angle	72
39	Drogue Chute Area Tradeoff	74
40	Main Parachute Deployment Altitude versus Entry Angle	75
41	Drogue Flight Time to Main Chute Deployment versus Entry Angle	76
42	Main Chute Descent Time versus Main Chute Deployment Altitude	77
43	Total Flight Time from Entry to Impact versus Entry Angle	78

LIST OF FIGURES (Cont'd)

Figure 44	Altitude versus $M/C_D A$ for Mars Entry	80
45	Gain in Drogue Deployment Altitude with Variation in Entry Angle	81
46	Ratio of Parachute System Weight to Total Weight During Drogue Flight	83
47	Landing System Weight Fraction versus Impact Velocity	89
48	Landing System Weight Fraction versus Impact Velocity	90
49	Landing System Weight Fraction versus Impact Velocity	91
50	Landing System Weight Fraction versus Impact Velocity	92
51	Landing System Weight Fraction versus Impact Velocity	93
52	Landing System Weight Fraction versus Impact Velocity	94
53	Landing System Weight Factor versus Impact Velocity	95
54	Landing System Weight Factor versus Impact Velocity	96
55	Landing System Weight Factor versus Impact Velocity	97
56	Leg Length to Prevent Vehicle Toppling on a 30-degree Mars Slope versus Velocity Down the Slope	98
57	Mars V-2 Entry Vehicle Configuration	100
58	V-1 Vehicle Configuration	101
59	Drag Curve Comparison for V-1 and V-2 Shapes	102
60	Mars Lander Comparison Between V-1 and V-2 Vehicles Weight of Heat Shield, Bond, and Structure ($M/C_D A = 0.9$) ...	105
61	Results of Vehicle Dynamic Analyses	111
62	Results of Vehicle Dynamic Analyses	112
63	Results of Vehicle Dynamic Analyses	113

LIST OF FIGURES (Cont'd)

Figure 64	Results of Vehicle Dynamic Analyses	114
65	Results of Vehicle Dynamic Analyses	115
66	Results of Vehicle Dynamic Analyses	116
67	Total Angle of Attack Envelope versus Weight for V-2 Mars Entry	117
68	Total Angle of Attack Envelope versus Weight for V-2 Mars Entry	118
69	Total Angle of Attack Envelope versus Entry Angle of Attack for V-2 Mars Entry	119
70	Total Angle of Attack Envelope versus Entry Angle of Attack for V-2 Mars Entry	120
71	Total Angle of Attack Envelope versus Entry Angle for V-2 Mars Entry	121
72	Total Angle of Attack Envelope versus Entry Angle for V-2 Mars Entry	122
73	Total Angle of Attack Envelope versus Entry Velocity for V-2 Mars Entry	123
74	Total Angle of Attack Envelope versus Initial Roll Rate for V-2 Mars Entry	124
75	Total Angle of Attack Envelope versus Initial Pitch Rate for V-2 Mars Entry	125
76	Total Angle of Attack Envelope versus Initial Pitch Rate for V-2 Mars Entry	126
77	Total Angle of Attack Envelope versus Initial Pitch Rate for V-2 Mars Entry	127
78	Total Angle of Attack Envelope versus Entry Angle of Attack .	128
79	Effect of Model Atmosphere Change Altitude at $M = 2.5$ versus $M/C_D A$	129

LIST OF FIGURES (Cont'd)

Figure 80	Velocity versus Time for Mars Lander	130
81	Altitude versus Time for Mars Lander	131
82	Aerodynamic Deceleration versus Time for Mars Lander ..	132
83	Voyager Apollo-type Entry Vehicle (Mars Low-Density Atmosphere) Configuration	133
84	Velocity versus Stagnation Point Heat Transfer Rate.....	135
85	Stagnation Point Heating Rate Velocity Gradient Correction Factor (V-2 Configuration).....	137
86	Stagnation Convective and Radiative Heating Time Histories ($\gamma_E = -90$ degrees)	142
87	Stagnation Convective and Radiative Heating Time Histories ($\gamma_E = -20$ degrees)	143
88	Mars Entry Maximum Convective Stagnation Heating Rate ..	144
89	Mars Entry Integrated Convective Stagnation Heating	145
90	Mars Entry Maximum Radiative Stagnation Heating Rate....	146
91	Mars Entry Integrated Radiative Stagnation Heating.....	147
92	Mars Entry Ratio of Integrated Radiative Stagnation Heating to Convective Stagnation.....	148
93	Mars Entry Maximum Convective Stagnation Heating Rate	149
94	Mars Entry Maximum Convective Stagnation Heating Rate	150
95	Mars Entry Maximum Convective Stagnation Heating Rate	151
96	Mars Entry Maximum Radiative Stagnation Heating Rate ...	152
97	Mars Entry Maximum Radiative Stagnation Heating Rate ...	153

LIST OF FIGURES (Cont'd)

Figure 98	Mars Entry Maximum Radiative Stagnation Heating Rate	154
99	Mars Entry Integrated Convective Stagnation Heating Rate	155
100	Mars Entry Integrated Convective Stagnation Heating Rate	156
101	Mars Entry Integrated Convective Stagnation Heating Rate	157
102	Mars Entry Integrated Radiative Stagnation Heating	158
103	Mars Entry Integrated Radiative Stagnation Heating	159
104	Mars Entry Integrated Radiative Stagnation Heating	160
105	Mars Entry Ratio of Integrated Radiative Stagnation Heating to Convective Stagnation Heating	161
106	Mars Entry Ratio of Integrated Radiative Stagnation Heating to Convective Stagnation Heating	162
107	Mars Entry Ratio of Integrated Radiative Stagnation Heating to Convective Stagnation Heating	163
108	Possible Combinations of Integrated Stagnation Point Convective and Radiative Heating Rates for Mars Entry	166
109	Possible Combinations of Maximum Stagnation Point Convective and Radiative Heating Rates for Mars Entry	167
110	Material Selection Chart.....	168
111	Heat Shield Weight versus M/C_{DA} , Reference Vehicle	170
112	Total Integrated Heating versus M/C_{DA} for Stagnation Point of 2000-Pound Reference Vehicle	171
113	Maximum Radiative Heating Rate versus Entry Velocity, Entry Angle, and M/C_{DA} for 2000-Pound Reference Vehicle	172

LIST OF FIGURES (Cont'd)

Figure 114	Heat Shield Variation with Vehicle Size for Reference Vehicle	173
115	Heat Shield Weight versus M/C_{DA} Reference Vehicle	175
116	Heat Shield Weight versus M/C_{DA} Reference Vehicle	176
117	Heat Shield Weight versus Total Vehicle Weight	177
118	Heat Shield Weight versus Total Vehicle Weight--NERV Shape	178
119	Heat Shield Weight versus Total Vehicle Weight--NERV Shape	179
120	Heat Shield Weight versus Total Vehicle Weight--NERV Shape	180
121	Heat Shield Weight versus Total Vehicle Weight--Apollo Shape	181
122	Heat-Shield Performance Envelope for Reference Design	183
123	Heat-Shield Performance Envelope for Reference Design	186
124	Proposed Mars Heat Shield Material after Testing at Low Heat Fluxes in OVERS Arc	187
125	Dimensionless Enthalpy versus Heat Flux	188
126	Dimensionless Enthalpy versus Heat Flux	190
127	Proposed Mars Heat Shield After Testing in the 10-Megawatt Arc	191
128	Gas-Stabilized Arc for Radiation Studies	192
129	Test Samples After Exposure to Radiant Heating	193

LIST OF FIGURES (Cont'd)

Figure 130	TGA Curve for Avcoat 5026 Resin System Only	196
131	Vacuum System for Solar Simulator	197
132	Thermal Diffusivity versus Pressure for Proposed Mars Heat Shield Material.....	199
133	Structural Weight/Entry Weight Ratio versus $M/C_D A$	210
134	Structural Weight/Entry Weight Ratio versus $M/C_D A$	211
135	Structural Weight/Entry Weight Ratio versus $M/C_D A$	212
136	Weight of Six Petal Ribs versus Load on Six Petals	213
137	Weight of Internal Structure versus Entry Weight	214
138	Weight of Petal Structure versus Entry Vehicle Radius ...	215
139	Weight of Substructure versus Pressure	216
140	Weight of Substructure versus Pressure	216
141	Variation of Typical Unit Area Weight for Mars Entry	218
141a	Comparison of Some Lander Power Supply Sources	224
142	Incident Solar Intensity versus Time at 30°S Latitude on Mars	227
143	Isotope Availability Chart	229
144	Mars Lander Instrumentation Profile	232
145	Mars Lander Communication Profile	235
146	Load Profile for the Communication Phase	236
146a	Powerplant Weight versus Payout Time and RTG Size ...	238
147	Lander Communication System Block Diagram	249
148	Lander Data Multiplexer Simplified Block Diagram	250

LIST OF FIGURES (Cont'd)

Figure 149	Separation to Entry Critical Engineering Status Mode....	254
150	Chirp Error Reduction at Low Bit Rates	256
151	Entry and Descent Science Mode	259
152	Data Acquisition and Storage Entry and Descent Science Mode	261
153	Signal and Power Flow Diagram Mars Lander Tape Recorder 1	262
154	Lander Altimeter Block Diagram	265
155	Landings, Complete Engineering Status Mode	274
156	Main Science Mode.....	275
157	Multipath Interference Reduction	280
158	Chirp Receiver	280
159	Error Probability	287
160	Two-Signal Interference Vector Diagram.....	288
161	Instantaneous Angular Frequency	289
162	Transmitter Waveforms	292
163	Lander Transmitter Block Diagram	294
164	Transmitter Encoder Block Diagram	295
165	VHF Transmitter RF Circuits	301
166	Lander Command Receiver	303
167	Lander Command Receiver Decoder	304
168	Transmission System Block Diagram	306
169	Load Profile	312

LIST OF FIGURES (Cont'd)

Figure 170	Parabolic Antenna Weight	316
171	Theoretical Parabolic Antenna Gain	323
172	Worst Case Parabolic Antenna Gain	324
173	Command Demodulator and Detector	333
174	Command Decoder	344
175	Rect Function	346
176	VHF Relay Antenna	351
177	VHF Antenna Pattern	354
178	Typical VHF Antenna	356
179	Bandwidth versus Slot Length	357
180	Lander Relay/Command Antenna	358
181	Pictorial Assembly Relay/Command Antenna	359
182	E Plane Pattern, VHF Antenna	360
183	H Plane Pattern, VHF Antenna	361
184	E and H Plane Patterns, S-Band Antenna	362
185	Stress Time Characteristics of Glass	365
186	E and H Plane Patterns, Altimeter Antenna	367
187	Altimeter Antenna on Lander Vehicle	368
188	Cassegrain Antenna System	370
189	Orbital Injection Venus Lander Cross Section Showing Internal Details (W entry = 85 Pounds)	373
190	Voyager "Apollo Type" Entry Vehicle (Venus Entry from Orbit) Configuration	374

LIST OF FIGURES (Cont'd)

Figure 191	Descent Operational Sequence	376
191a	Mars Descent Sequence	379
192	Design Layout of Voyager Venus Lander Packaged Propulsion System	380
193	Voyager Venus Lander Propulsion Schematic	382
194	Direct-Entry Venus Lander Cross Section Showing Internal Packaging (W entry = 1100 Pounds)	385
195	Direct Entry Ballute System	389
196	Percent Strength Retained versus Time of Polyoxadiazole Fibers in Air and Nitrogen at 750°F	391
197	Venus Atmospheric Entry Altitude at $M = 2.5$ versus Vehicle $M/C_D A$	393
198	Venus Atmospheric Entry Altitude at $M = 2.5$ versus Entry Angle	394
199	Venus Lander Altitude at $M = 2.5$ versus Entry Angle ...	395
200	Venus Lander Orbital Entry	397
201	Voyager Apollo-Type Entry Vehicle (Venus Entry from Orbit) Configuration	398
202	Voyager V-2 Entry Vehicle (Venus Direct Entry) Configuration	399
203	Venus Entry Maximum Stagnation Convective Heating ...	402
204	Venus Entry Maximum Stagnation Convective Heating ...	403
205	Venus Entry Maximum Stagnation Convective Heating	404
206	Venus Entry Integrated Stagnation Convective Heating ...	405
207	Venus Entry Integrated Stagnation Convective Heating ...	406

LIST OF FIGURES (Cont'd)

Figure 208	Venus Entry Integrated Stagnation Convective Heating ...	407
209	Venus Entry Maximum Stagnation Radiative Heating	408
210	Venus Entry Maximum Stagnation Radiative Heating	409
211	Venus Entry Maximum Stagnation Radiative Heating	410
212	Venus Entry Integrated Stagnation Radiative Heating	411
213	Venus Entry Integrated Stagnation Radiative Heating	412
214	Venus Entry Integrated Stagnation Radiative Heating	413
215	Venus Entry Ratio of Integrated Stagnation Radiative Heating to Integrated Stagnation Convective Heating	414
216	Venus Entry Ratio of Integrated Stagnation Radiative Heating to Integrated Stagnation Convective Heating	415
217	Venus Entry Ratio of Integrated Stagnation Radiative Heating to Integrated Stagnation Convective Heating	416
218	Venus Lander Altitude at Maximum Stagnation Heating versus Entry Angle	417
219	Venus Lander Altitude at 10 Percent Maximum Stagnation Heating	418
220	Venus Orbital Entry Radiative and Convective Heating Pulses	419
221	Venus Orbital Entry Stagnation Convective Peak Rate and Total Integrated Input	420
222	Venus Orbital Entry Stagnation Radiative Peak Rate and Total Integrated Input	421
223	Venus Orbital Entry Ratio of Integrated Radiative Heating to Integrated Convective Heating	422
224	Venus Entry Radiative and Convective Heating Pulses ...	423

LIST OF FIGURES (Cont'd)

Figure 225	Venus Entry Stagnation Convective Peak Rate and Total Integrated Input	424
226	Venus Entry Stagnative Radiative Peak Rate and Total Integrated Input	425
227	Venus Entry Ratio of Integrated Radiative Heating to Integrated Convective Heating	426
228	Venus Lander Heat Shield Weights, Kaplan Standard-Temperature Atmosphere	429
229	Venus Lander Heat Shield Weights, Kaplan Standard-Temperature Atmosphere	430
230	Venus Lander Heat Shield Weights, Kaplan Standard-Temperature Atmosphere	431
231	Venus Lander Heat Shield Weights, Stagnation Point	432
232	Venus Lander Heat Shield Weights, Kaplan Standard-Temperature Atmosphere	435
233	Venus Lander Heat Shield Weights, Kaplan Standard-Temperature Atmosphere	436
234	Venus Lander Heat Shield Weights, Kaplan Standard-Temperature Atmosphere	437
235	Venus Lander Heat Shield Weight, Apollo Shape Stagnation Region	438
236	Oblique Tape-Wound Refrasil (OTWR) after Testing in 10-Megawatt Arc	441
237	Graphite-Based Materials After Testing in 10-Megawatt Arc	442
238	Avco RAD Solar Furnace	444
239	Venus Entry Maximum Dynamic Pressure	449
240	Venus Entry Maximum Axial Load Factor	450

LIST OF FIGURES (Cont'd)

Figure 241	Venus Orbital Entry Maximum Dynamic Pressure.....	453
242	Variation of V-1 Shape Entry Vehicle Structural Weight, for Aluminum Sandwich Construction	454
243	Variation of V-2 Shape Entry Vehicle Structural Weight, for Aluminum Sandwich Construction	455
244	Variation of V-2 Shape Entry Vehicle Structural Weight, for Stainless Steel Construction	456
245	Output of a Windmill	459
246	Venus Lander Load Profile	461
247	Venus Lander Communication System Block Diagram...	467
248	Venus Atmospheric Capsule Communication System Block Diagram	477
249	VHF Antenna Installation	479
250	E Plane Pattern	482
251	H Plane Pattern	483

LIST OF FIGURES (Cont'd)

Figure A1	Block Diagram of Mars Vehicle Descent System Sequence Controller	493
A2	Mars Lander Descent and Touchdown Sequence	494
A3	Block Diagram of Venus Vehicle Descent System Sequence Controller	500
A4	Venus Lander Descent System Sequence	501
A5	Vertical Descent Rate versus Altitude for the Venus Vehicle with Ballute Decelerator - Kaplan "Maximum Temperature" Atmosphere	503
A6	Vertical Descent Rate versus Altitude for the Venus Vehicle with Ballute Decelerator - Kaplan "Standard" Atmosphere	504
A7	Program Schedule	518
B1	Propulsion System Layout	522
B2	Propulsion System Schematic	526
B3	Mars Lander Propulsion System Weight versus Mixture Ratio	528
B4	Mars Lander Propulsion System Weight versus Chamber Pressure	529
B5	Mars Lander Propulsion System Weight versus Expansion Area Ratio	530
B6	Thrust Chamber Assembly	535
B7	Pressurant Tank	537
B8	Propellant Tanks	540
B9	Pressure Regulator	542
B10	Check Valve	544

LIST OF FIGURES (Cont'd)

Figure B11	Propulsion System Layout	547
B12	Propulsion System Schematic	551
B13	Thrust Chamber Assembly	555
B14	Pressurant Tank	559
B15	Propellant Tanks	561
B16	Pressure Regulator	562
B17	Check Valve	564
C1	Schematic View of the Reentry Radiation Heat-Transfer Simulator	566
C2	View of the First Arc Facility	568
C3	Schematic Diagram of the Second Arc Facility	569
C4	View of the Second Arc Facility	570
C5	Arc in Operation	574
C6	Radiation Spectra of High-Powered Arc at 1.5 ATM and 3.78 ATM	575
C7	Broadening of the H_{β} Line	576
C8	View of Samples After Test	577
C9	Heat Ablation of Linen Phenolic as a Function of Pressure	578
C10	Comparison Between Blackbody and High-Temperature Gas-Radiation Densities at Operating Conditions	579
D1	Cruciform Antenna With Low Temperature Window	584
D2	Power/Altitude Breakdown Curves, Air, N_2 , and A, at 900 mc	585

LIST OF FIGURES (Concl'd)

Figure D3	Power/Altitude Breakdown Curves, Argon 450 and 900 mc	586
D4	Power/Altitude Breakdown Curves, Argon 450 mc	588
D5	Power/Altitude Breakdown Curves, Argon at 900 mc with 1/8-Inch Limonite over Antenna Windows	589

SUMMARY

This report presents the results of a 6-month conceptual design study conducted by Avco Research and Advanced Development Division for the National Aeronautics and Space Administration. The objectives of the study were the synthesis of a conceptual design of an unmanned spacecraft to perform scientific orbiter-lander missions to Mars and Venus during planetary opportunities from 1969 to 1975, and the formulation of a plan delineating the development program leading to first launch during the Mars 1969 opportunity.

The basic approach makes use of a 6000- to 7000-pound orbiter-lander; tradeoff studies were conducted to determine the payload and mission capabilities with smaller and larger spacecraft. The orbiter-lander was selected as yielding the maximum in scientific value short of manned exploration. The lander separates from the orbiter-bus and descends to the planet surface by parachute, where it makes atmospheric and surface measurements and conducts a variety of scientific experiments. The information obtained is relayed to Earth via the orbiter-bus which meanwhile is placed in a planetocentric orbit. The orbiter-bus collects scientific data in transit and maps the planet while in orbit. The lifetime of both orbiter-bus and lander is 6 months for the Mars missions. For Venus, the orbiter life is also 6 months, but the lander life is only 10 to 20 hours because of the hostile environment. A small capsule was designed for Venus, in addition to the lander, to conduct atmospheric measurements after entering from orbit; the capsule does not survive landing. Landers and capsules would be sterilized to avoid contamination of the planets, but the orbiter-bus would be placed on a trajectory which would ensure that it would remain above the sensible atmosphere for at least 50 years; thus, no sterilization would be required. The development plan shows that to obtain the scientific value desired, two spacecraft should be scheduled for each launch opportunity and hardware development should begin in 1964 to meet the 1969 launch date for Mars.

1. MECHANICAL DESIGN

1.1 System Requirements

1. Landing system. Several landing concepts were investigated, characterized as toppled, toppled with reerection, and erect. Figure 1 is a chart showing the various schemes. The concepts discussed herein are numbered in the order in which they appear in figure 1.

a. Landing systems designed to stay erect. Concepts 1, 2, and 3 are different variations of a landing lander which remains upright during touchdown. The principle expressed in these designs is that of using outriggers to stabilize the lander. In concept 1, the heat shield spherical cap is retained; this cap helps to distribute uneven loads due to rough terrain. The impact attenuation system could consist of buckling struts, frangible tubes, fluid shock absorbers, crushable honeycomb, or even a cylindrical airbag.

When the heat shield is discarded, then concept 2 (which involves a large, segmented, toroidal gas-filled bag), illustrates one way in which uneven terrain loads can be distributed.

Concept 3 shows shaped plastic foam used as the energy absorber. The shaping is done so that, for most impact conditions, the loads will be directed into the same load-carrying members in the payload as are used during launch and entry. Additional protection, perhaps in the form of a higher density, stiffer material such as balsa wood, is provided over the bottom of the payload to cushion localized shocks due to rough terrain or rocks.

Dynamic analysis of landing systems designed to maintain the lander in an upright altitude were performed by Avco and Northrup, Ventura Division. The details of the analysis are given in the Descent and Landing Systems section. As a result of these studies, it was concluded that the possibility of tumbling was quite high due to winds and terrain uncertainties even for very large outriggers.

b. Reerectable landers. Concepts 4, 5, and 6 illustrate landers which will reerect if they topple during impact. Since practically complete surface protection is required, the impact attenuation system requires more weight. Extra weight is also required in these concepts for load carrying structure needed and for the reerecting system. The complications in these systems arise after the touchdown phase is completed. The landers must erect themselves; concepts 4 and 6 erect externally while the nested spheres use internal erection, stabilize their position, and then deploy instruments. These latter operations are particularly difficult in the sphere concept, where stabilization and deployment must take place by breaking through the outer covering.

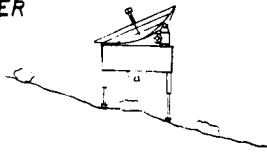




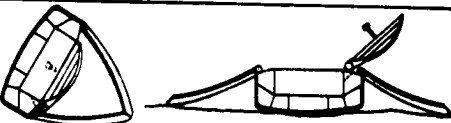



E R E C T	SOFT LANDER 	1
	AIR BAG 	2
	OUTRIGGER 	3
R E E R E C T	CLAM SHELL 	4
	SPHERE IN SPHERE 	5
	TULIP BUD 	6
S T A Y T O P P E D	TURTLE SHELL 	7
	TETRAHEDRON 	8
	POTTED SPHERE 	9

Figure 1 LANDING SYSTEMS CHART

c. Landers without erection. The next three concepts, 7, 8, 9, illustrate landers which are allowed to topple and stay toppled. Orbiter relay communications are implicit in these concepts. For most conceivable terrain models, the turtle-shell (No. 7), can end up on only two different ways; the tetrahedron (No. 8) in four; and the potted sphere, of course, can end up in any orientation. Obviously, there are other, similar designs involving partially constrained orientation of the capsule, such as a cube, cylinder, or cone. The preferred orientation of most of these concepts simplifies the design of the instrument deployment systems. Once again, the requirement of overall protection will be required.

Concept 10 is a redundant lander which, if it remains upright, can communicate directly to Earth and, if it topples, can relay to the orbiter.

This concept can be incorporated into configuration No. 6 with the additional feature that an internally packaged high-gain Earth antenna is not subject to ground-impact loads. This combination has been chosen as the reference design, and is discussed in the sections that follow. The reerection capability is considered to be of prime importance due to both the relatively small amount of Martian topographical information directly measureable from Earth and the widely varying surface features proposed by different authorities.

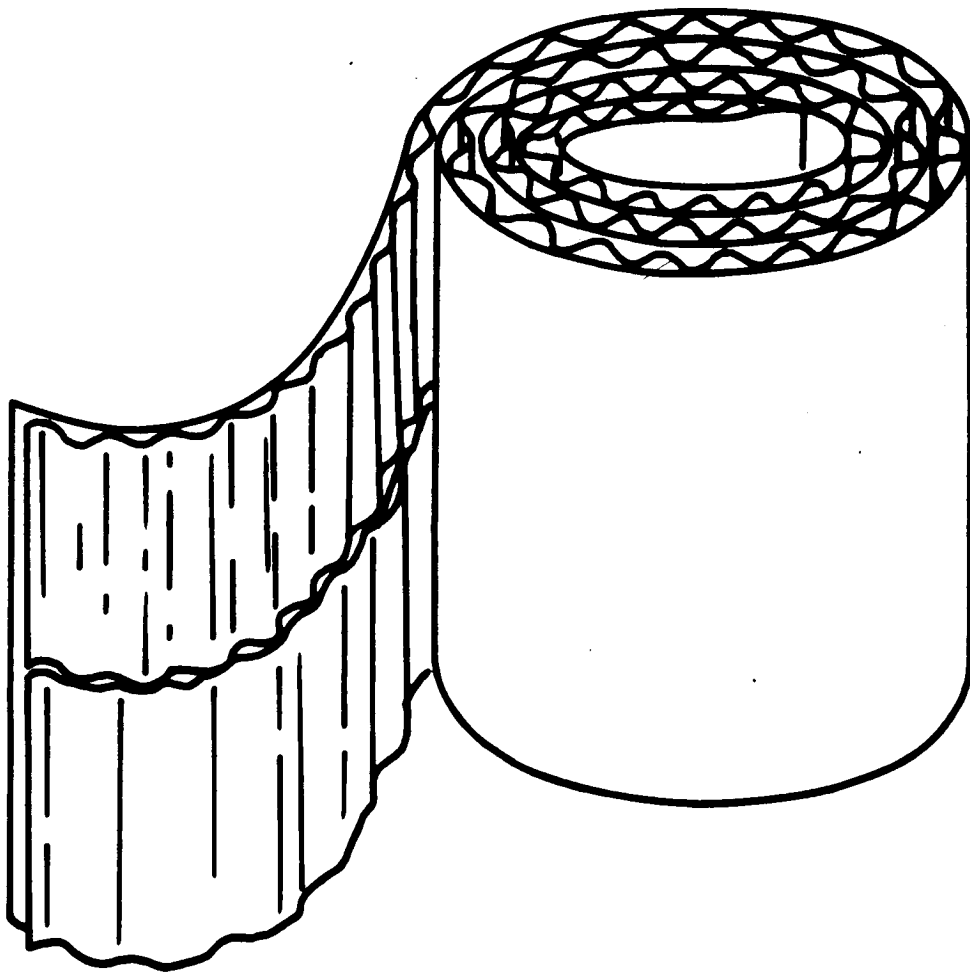
As a means of dissipating the impact energy, crushable materials appear to be very attractive. Aluminum spiral grid pads have been chosen. Two material thicknesses have been incorporated into the pad. The initial low-density grid is used if the full bottom area of the lander contacts the planetary surface. If the terrain is such that one pad contacts first, the low-density material crushes up quickly and the high-density spiral grid then carries the load. The crushing stress has been taken as a function of the number of pads in contact in such a manner as to present an almost constant g load to the payload, regardless of the number of pads in contact.

Figure 2 illustrates a typical pad. Details of the structural features of the pad are given in the Structure Design section.

2. Communication mode. Three basic communications modes were evaluated as to their effect on lander design. They are:

- 1) Direct Earth link
- 2) Relay to Earth via orbiting vehicle
- 3) Primary direct Earth link, with a backup relay-to-orbiter capability

a. Direct Earth link. Parametric tradeoffs on antenna size, bit rate, lifetime, lander configuration and power supply, led to the selection of



CRUSH UP PAD CONSTRUCTION (TYPICAL)

63-10294

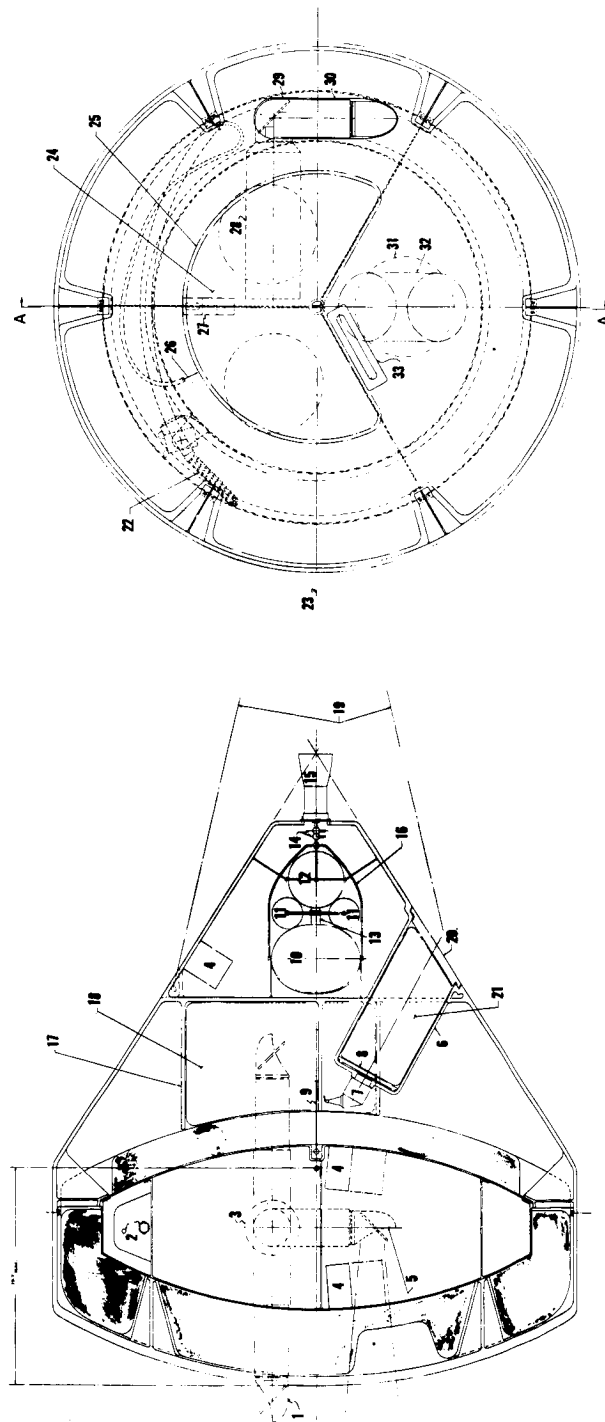
Figure 2 CRUSHUP PAD CONSTRUCTION (TYPICAL)

a 5-foot diameter high-gain antenna for the direct Earth communication link. The need for the direct link stems from the life time and information levels desirable from the lander. To accommodate the high-gain antenna, lander erection and elevation and azimuth control of the antenna are required. The antenna azimuth and elevation drives are contained in a single post, located on the outside diameter of the payload structure. The antenna elevation hinge point is positioned on the outer diameter of the antenna dish, allowing the dish to be folded over and above the payload structure. This linkage arrangement was chosen both for its mechanical simplicity and its ability to accommodate large angular deviations between the local horizontal and the payload package orientation. Earth tracking for elevation angles near the planetary horizontal is also enhanced. The erection, linkage, and space problems associated with a payload package central post-mounted antenna are thus circumvented. Antenna stowage after handing (within the erection petal envelope) may be effected, if required by long inactive periods in the mission profile, minimizing environmental performance degradation. A design using electrical multi-circuit slip rings in the post, for azimuth and elevation angular variations, is a likely configuration.

The requirement for a preferred orientation of the lander (to provide a basis for antenna orientation) has been met through the use of a self-erecting design. This configuration allows considerable simplification in design of the other deployable internal systems. An onboard system, with local vertical and sun sensors, must be accomplished in order to provide information for location of the lander impact site on the planetary surface and for Earth antenna aiming. In addition to the high-gain antenna, a hemi-omni-antenna is provided for low bit rate backup.

b. Relay to Earth through orbiter vehicle. In this concept, engineering and scientific data must be transmitted from the lander to the orbiter and thence relayed to DSIF. A simple, rugged landed package design having the ability to communicate from any attitude has been chosen. Final orientation of the package is determined by its geometry, with two preferred surfaces. The use of a local vertical sensor determines which of a system of hemispherical omnidirectional antennas are used to relay data to the orbiter. Considerable care must be given to the packaging of deployable science systems, as they must remain internal to the package until the vehicle comes to rest, and then access must be provided to the planetary environment. The weight of the communications system required for this design is less than, but of the same order of magnitude as, the Earth direct-link communications system. This is because many of the same functions must be performed and antenna redundancy must be provided. (See figure 3.)

c. Direct Earth link, with backup relay capability. A third possible communication mode consists of a combination of those two previously discussed. A study showed that adding the relay capability to the Earth-link



1. DEPLOYED POSITION OF T.V. PERISCOPE
IF LANDER RESTS ON ITS TOP SIDE.
2. SOIL SAMPLER
3. T.V. CAMERA
4. OMNI ANTENNA
5. T.V. PERISCOPE IN FLIGHT POSITION
& POSITIONED TO TAKE DESCENT PICTURES
6. CANISTER FOR DROGUE CHUTE
(BUILT INTO ENTRY HEAT SHIELD)
7. GAS GEN.
8. SABOT
9. MAIN CHUTE ATTACHMENT LINE
(SINGLE CONCEPT SHOWN)
10. OXIDIZER
11. PRESSURANT
12. FUEL
13. PRESSURE REGULATOR
14. VALVES
15. THRUST CHAMBER
16. LIQUID PROPELLANT MOTOR
17. CANISTER FOR MAIN CHUTE
(CLOTH BAG SECURED TO CANISTER)
18. MAIN CHUTE IN CLOTH BAG
19. DROGUE CHUTE ATTACHMENT LINES (2)
WITH DROGUE CHUTE DEPLOYED
20. DROGUE CHUTE COVER
21. DROGUE CHUTE IN CLOTH BAG

22. VOL. 300 IN³ WT. 15#
SOIL SAMPLER DRILL FOR BIO-PACK
(SEE LA 5325 SHEET 4 FOR CONCEPTS)
23. PITCH AXIS
24. MAIN PARACHUTE
25. CANISTER FOR MAIN PARACHUTE
26. SUCTION HOSE FROM DRILL
TO BIO PACK
27. OMNI ANTENNA
28. T.V. CAMERA (FIXED)
29. T.V. PERISCOPE (DEPLOYABLE)
30. OPENING IN TOP & BOTTOM FOR
DEPLOYING T.V. PERISCOPE
31. RELIEF POCKETS IN BASE CRUSH-UP
32. DROGUE CHUTE
33. OMNI ANTENNA

Figure 3 RELAY LANDER

system (as discussed previously) is desirable. A single omnidirectional antenna is gimballed from the top end of one of the erection petals and weighted so that its radiative pattern is always perpendicular to the planetary horizontal. The petals are designed with a reinforced fiberglass top half, so that transmission to the orbiter is not seriously impaired with the petals closed, and may also be effected with the petals opened. The increase in mission confidence due to the redundancy of communications channels is enhanced, and the rather small percentage in weight increase over the lone direct-link communications system appears to be well worthwhile.

3. Descent system.

a. Heat shield retention or jettisoning. From a design standpoint, once the external entry vehicle shape has been chosen and the final trajectory data determined, one of the main design problems is to determine when and how to discard the vehicle heat shield, and, if it is necessary.

Retention of the heat shield and structure during the main parachute descent phase, however, was determined to be unacceptable, for the following reasons:

- 1) Thermal energy stored in the heat shield, is transferred to the scientific payload.
- 2) A higher parachute system weight and a decreased payload results.
- 3) Deployment of atmospheric sampling devices and other instruments is more difficult.
- 4) The parachute actuation system is more difficult.
- 5) Communications with both Earth and the orbiter vehicle must be made in the presence of the reentry vehicle heat shield and structure.

Jettisoning the heat shield allows the ground impact load path to be unloaded during planetary atmospheric entry, without requiring deployment of the impact attenuation system just prior to landing.

Scientific instrument deployment, without the heat shield, of such items as the descent television camera, atmospheric samplers, etc. is also made considerably easier.

b. Drogue and main parachute deployment. State of the art drogue parachute designs are available, capable of deployment at Mach numbers up to 2.5. The sensing system for this design has been predicated on the use of state of the art components. The parachute system is similar to Earth designs with few exceptions. It consists of a drogue parachute for stabilizing

and retarding the capsule, and main chute for descent with rapid retardation capability in case of entry angle trajectories approaching 90 degrees with a minimum loss of altitude. Dynamic pressures of 250 lb/ft² maximum and 80 lb/ft² maximum are well within the state of the art for drogue and main parachutes respectively. A detailed description of the parachute system is given in section 2, Descent and Landing.

The main parachute was sized to provide the desired descent time, and resulted in a maximum impact velocity of 40 ft/sec. This impact velocity resulted from a compromise between parachute and crushup weight and descent time. The main parachute will be deployed at Mach 0.8, or less. (All specific sizes and numerical examples in the following sequence are based on the 1410-pound entry weight reference design).

4. Descent sequence (see figures 4 and 5).

a. Preentry phase. Prior to separation from the spacecraft, the drogue actuation system is updated with the estimated entry angle. This information is used to preset the drogue deployment accelerometer. At entry, the angle of attack of the vehicle is likely to be close to 90 degrees with a spin rate of 20 rpm. The effects of the vehicle dynamic motions will therefore play an important role in the design of the parachute actuation system.

b. Hypersonic entry phase. Aerodynamic forces, caused by the planet's atmosphere acting on the reentry vehicle, cause the vehicle to assume a forward attitude. An increase in deceleration during entry causes a switch to close at a preset g level, arming the sequence controller of the parachute system. A sensing system capable of measuring the angle of attack may be required.

c. Drogue ejection by mortar at preset g level. A decrease in deceleration, after peak entry heating, causes a switch to close at a preset g level, energizing the drogue mortar and initiating drogue deployment as the first event in the landing sequence. The drogue chute is packaged in the bore of a small cylinder internally suspended from the flat rear face of the reentry vehicle.

Mortar operation results as the initiation cartridge pressurizes the volume between the bottom of the small cylinder and a piston-seal sabot which pushes out the drogue chute in its cloth packing bag. A thermal protection cover is required above the drogue chute package and within the cylinder. This cover is fastened in such a manner that it is flush with the flat back surface of the reentry vehicle. The compartment and retainer channels are so designed that no sharp edges are presented to the drogue chute harness. Two harness legs are required, and should be attached to the outer cylindrical wall of the reentry vehicle at diametrically opposite points. As with the drogue

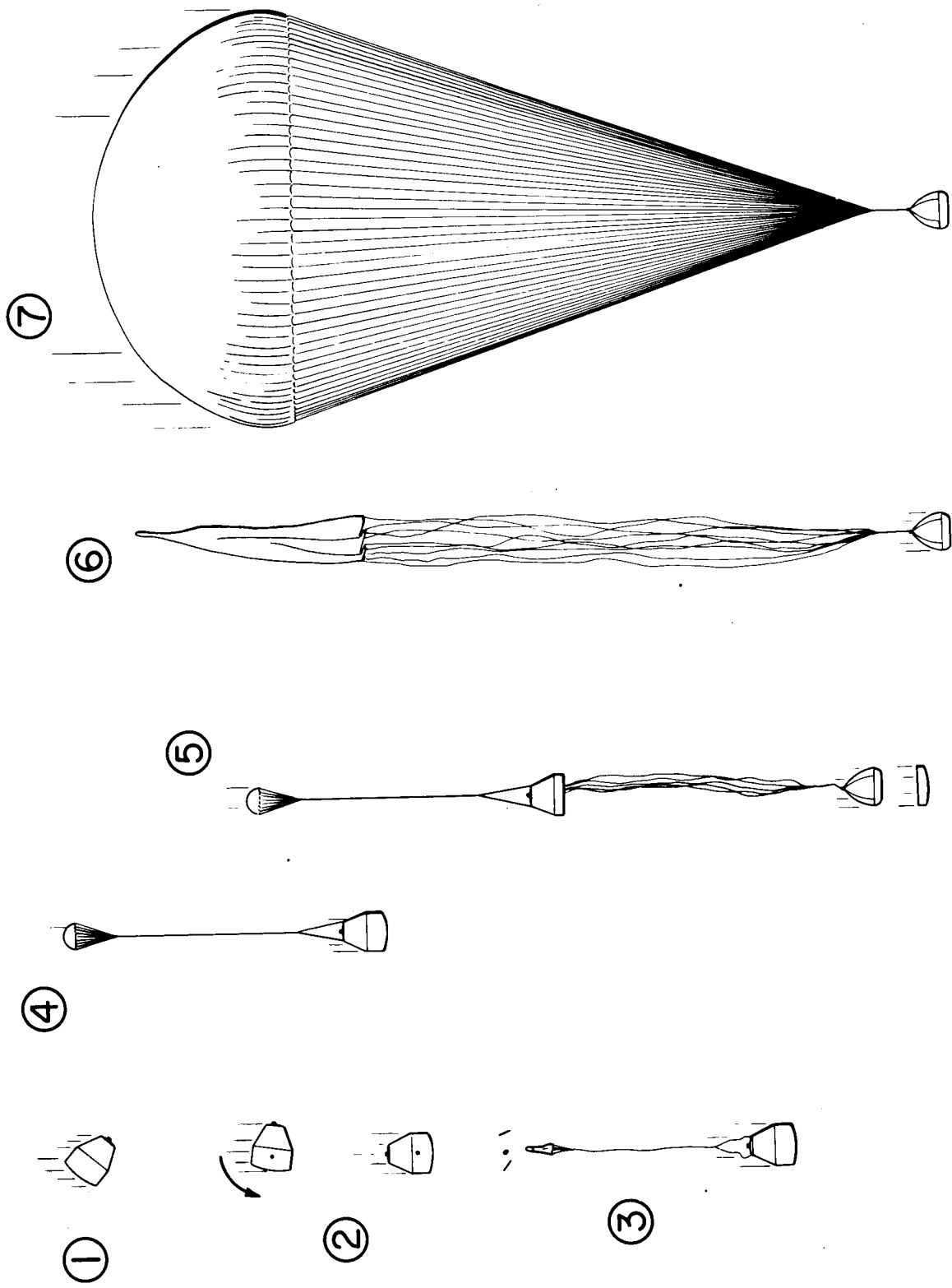
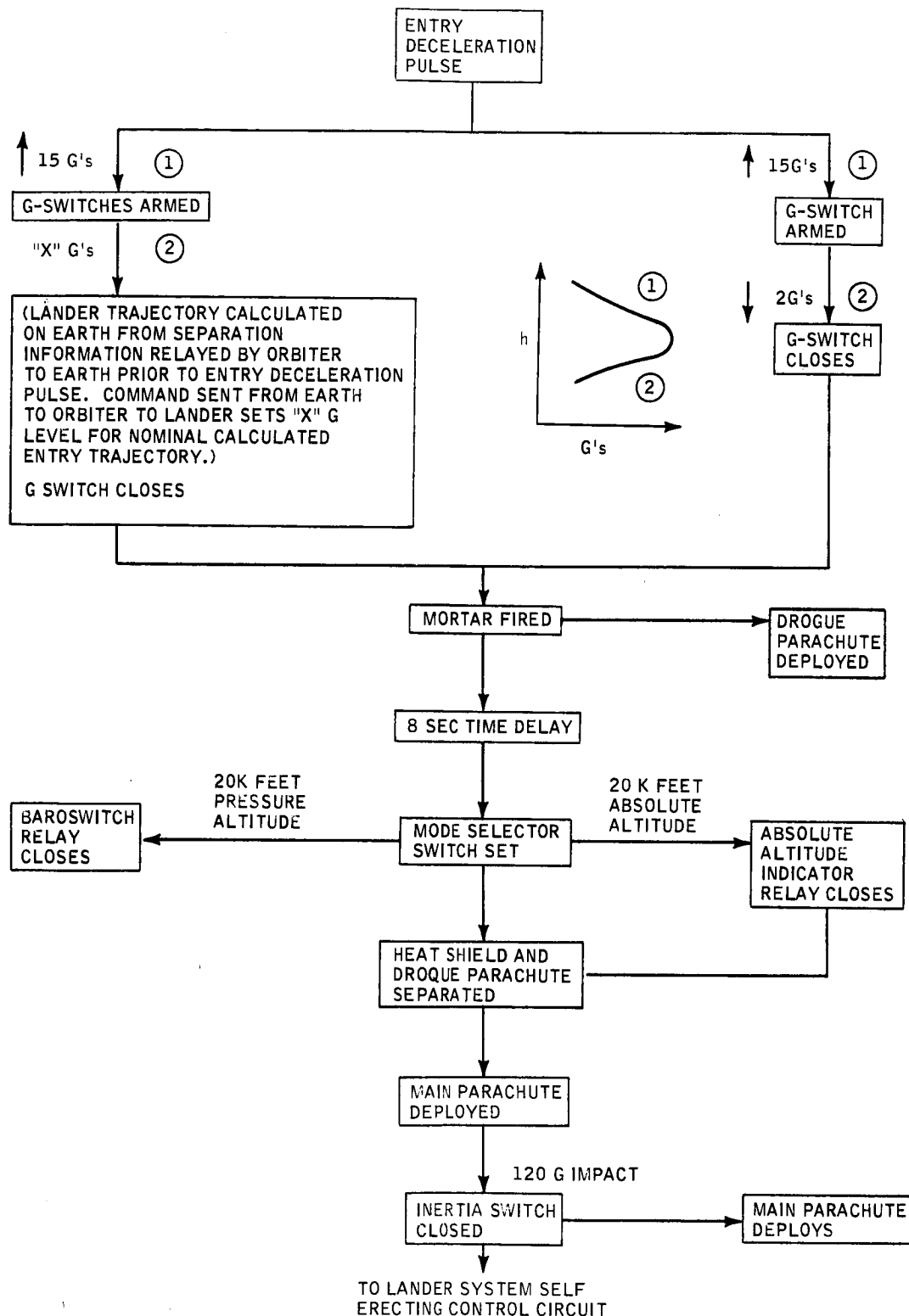


Figure 4 MARS PARACHUTE SEQUENCE



63-10291

Figure 5 BLOCK DIAGRAM OF MARS VEHICLE DESCENT SYSTEM SEQUENCE CONTROLLER

chute, thermal protective covers are supplied to provide a flush surface over each channel from the outer attachment points to the mortar cylinder. As the harness becomes taut, the insulated harness covers are deployed. For the reference design, the ejection force that is felt by the cylinder is in the order of 400 pounds. The drogue chute harness legs come together at a point about 8.5 feet behind the vehicle. A riser about 30 feet long then connects to the drogue chute in its cloth packing bag. An inertia weight in the back end of the bag causes the bag to strip itself off the drogue chute. The drogue chute suspension lines form a confluence point at the connection with the single riser and are about 11.0 feet in slant length.

An 11-foot inflated diameter-hemisflo drogue is currently being considered for this application. A 20,000-pound opening load (maximum) should be anticipated at either reentry vehicle attach point, at an angle of from 0 to 135 degrees to the flat rear face of the reentry vehicle. A maximum deployment Mach number of 2.5 has been suggested, due to air flow considerations. Drogue chute weight is about 27.0 pounds including riser, bag, and gas generator. A 10-inch diameter by 16-inch high cylinder (internal size) is required for packaging.

d. Heat shield and structure jettison. Upon a signal from the initial logic package, a linear shaped charge cuts the entry vehicle circumferentially. The drogue removes the aft portion of the heat shield and the forward portion falls free. The main chute deploys from a bag suspended from the aft portion of the heat shield.

At a preset time after the drogue chute has been deployed, the landing sequence altimeter (or baroswitch) electrically initiates a linear shaped charge which causes the rear portion of the heat shield and structure to become disconnected from the forward portion. The drogue chute force then retards the afterbody and in so doing unfolds from its cloth pack, a 2-foot central riser followed by the main parachute canopy. The cloth pack is secured to the canister built into the side of the afterbody.

At this point, the drogue chute and afterbody of the lander have separated from the main parachute.

e. Final descent phase. For the 960.7¹-pound lander weight considered, and for a 40 ft/sec final descent rate, with an atmospheric density of 1.44×10^{-4} slug/ft³ and using a C_D of 0.75, a 75.0 diameter (unloaded) chute with a loaded diameter of 50.0 feet has been selected.² This chute weighs 65.0 pounds including cloth bag, attachment lines, single central riser and shroud lines. Angularity of the load and attachment line considerations are the same as previously mentioned for the drogue chute.

¹960.7 + 65 = 1025.7 pound recovery weight

²Recovery weight = residual weight landed plus main parachute weight.

f. Touchdown. A final impact sensing g switch has been included in the parachute electronic logic package. This device initiates a squib which releases the main parachute from the lander at the top of the petals. If no crosswinds exist at final impact, an extremely remote possibility, the basic instability of the unloaded main parachute will prevent the parachute canopy from dropping over the lander. The release of the main chute is concurrent with the initiation of deployment of the individual erection petals.

A tradeoff study has been made to determine the optimum drogue area to weight landed ratio for the worst entry conditions, in order to ensure certain minimum descent times and main chute deployment altitudes. This problem is discussed in the Descent and Landing Systems section.

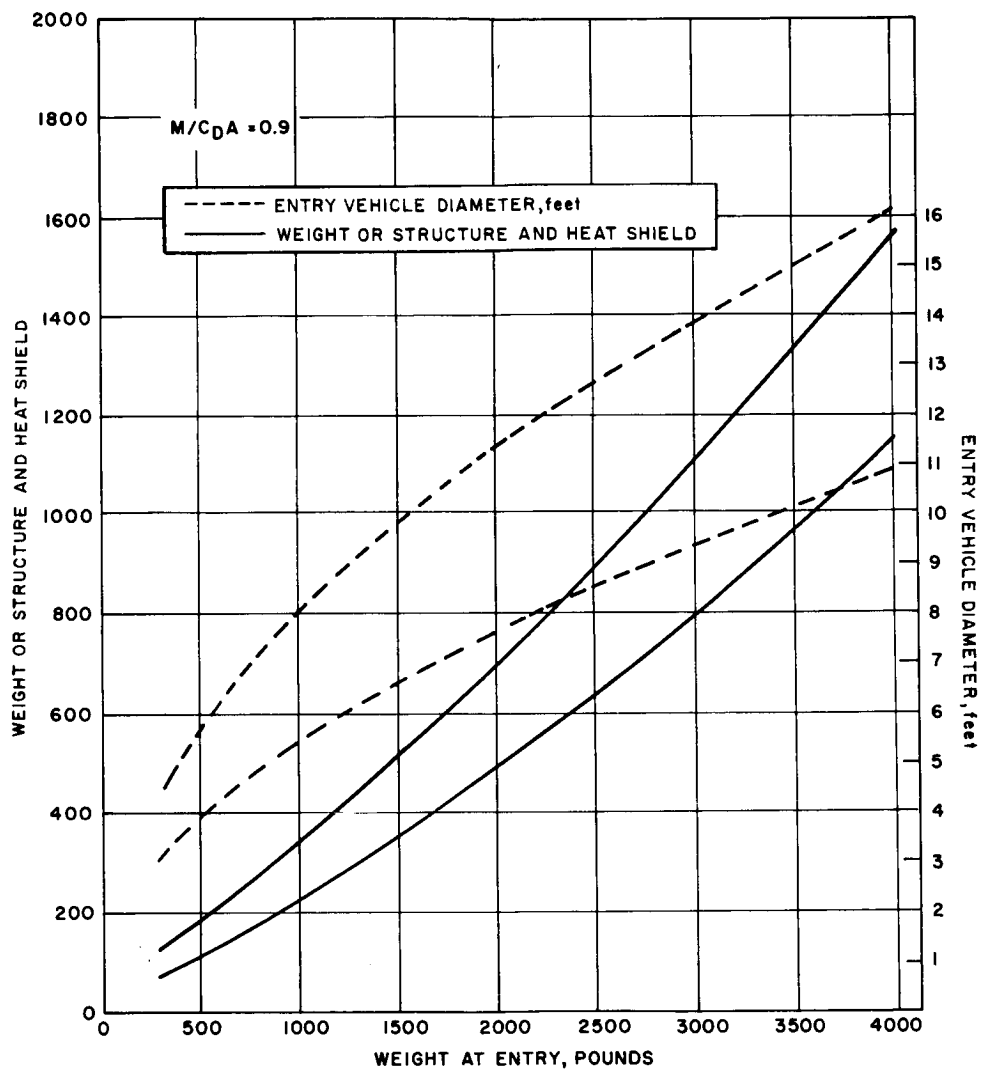
5. Packaging concepts. For the range of M/C_{DA} values considered, 0.6 to 1.5 slug/ft², the V-1 and V-2 shapes have sufficient internal volume for packaging of the required payloads. (The Apollo type shape, at values of M/C_{DA} of 0.2 to 0.3, is also of sufficient size, but as 0.6 is approached, its requirement for a relatively far forward c. g. location for dynamic stability begins to require extremely high packaging densities). The V-1 and V-2 shapes are described in the Aerodynamics Design section.

The choice between the V-1 and V-2 vehicles was based on the difference in landed weight for a given entry vehicle total weight. A comparison of entry vehicle weights between the two shapes, for a specific set of entry conditions, is shown in figure 6. A difference arose due to the larger diameter required to maintain the same M/C_{DA} for the V-1 vehicle, as compared to the V-2 vehicle.

The self-erecting configuration, which must be packaged internal to the entry vehicle, has its largest diameter at its most forward end, which conforms to the internal shape of the V-2. With the V-2 shape, the payload, in a short cylindrical package, has its axial inertial loads carried by compression members to the spherical front cap of the entry vehicle. Lateral inertial loads are carried by radial members to the external cylinder of the entry vehicle. Proper positioning of the lander on the booster allows the same load paths to be used to carry the launch loads.

For thermal control on the planetary surface, a minimum surface area scientific package is desirable. The c. g. of the landed package should also be as close to the ground as possible, and the package should have a broad base to prevent wind tipping, span local surface depressions, and so forth. The large diameter concept, as previously outlined for the V-2, is a practical means for achieving these results.

6. Propulsion system. A velocity increment is necessary to alter the lander trajectory from that of the orbiter to a planetary impact course. This is provided by a propulsion system attached to the rear of the entry vehicle.



63-10290

Figure 6 COMPARISON OF TOTAL VEHICLE WEIGHT AND WEIGHT OF HEAT SHIELD AND STRUCTURE FOR V-1 AND V-2 VEHICLES

The lander propulsion system was designed by the Rocketdyne Division of NAA, and a summary of their results is given in appendix B. The major elements of the system are summarized here for an entry vehicle weight of 1670 pounds. The reference system, with 1410-pound entry weight as shown in tables 2 and 5 is scaled from this system.

The Mars lander propulsion system shown in figure 7 is a pressure-fed, storable, hypergolic bipropellant propulsion system with a total delivered impulse of 5150 lb-sec, for the 1670-pound case. The system propellants are mixed oxides of nitrogen (MON) composed of 85 percent nitrogen tetroxide and 15 percent nitric oxide, and an eutectic blended fuel (EMHF) compound of 88 percent monomethylhydrazine and 12 percent hydrazine. An all-welded configuration will be used to prevent leakage. The system is prepackaged with propellants and the fill and vent connections will be welded after filling. This system is capable of being sterilized in the prepackaged condition at a temperature of 295°F for periods of 24 hours or more. A summary of propulsion system performance parameters is shown in table 1.

TABLE 1
SUMMARY OF PROPULSION SYSTEM PERFORMANCE
PARAMETERS -- MARS LANDER

Thrust, pounds	40
Chamber pressure (psia)	100
Mixture ratio	2.15
Characteristic velocity C^* (fps)	5284
Thrust coefficient (C_f)	1.904
Specific Impulse (seconds)	312.7
C^* Efficiency	0.94
C_f Efficiency	0.98
Throat area (in ²)	0.210
Expansion area ratio	40
Fuel Flowrate (lb/sec)	0.0406
Oxidizer Flowrate (lb/sec)	0.0873

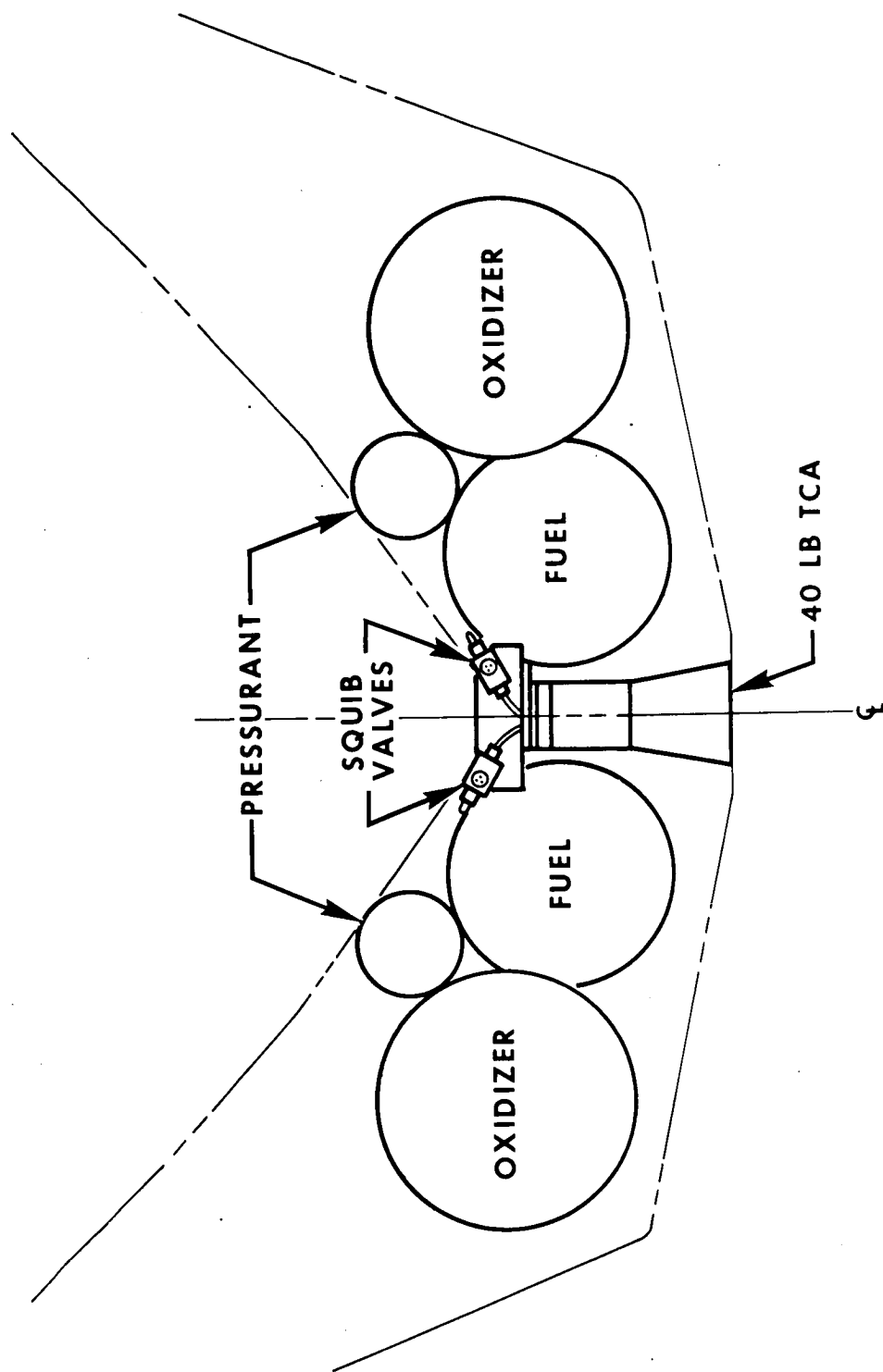


Figure 7 DESIGN LAYOUT OF MARS LANDER INTEGRATED PROPULSION SYSTEM

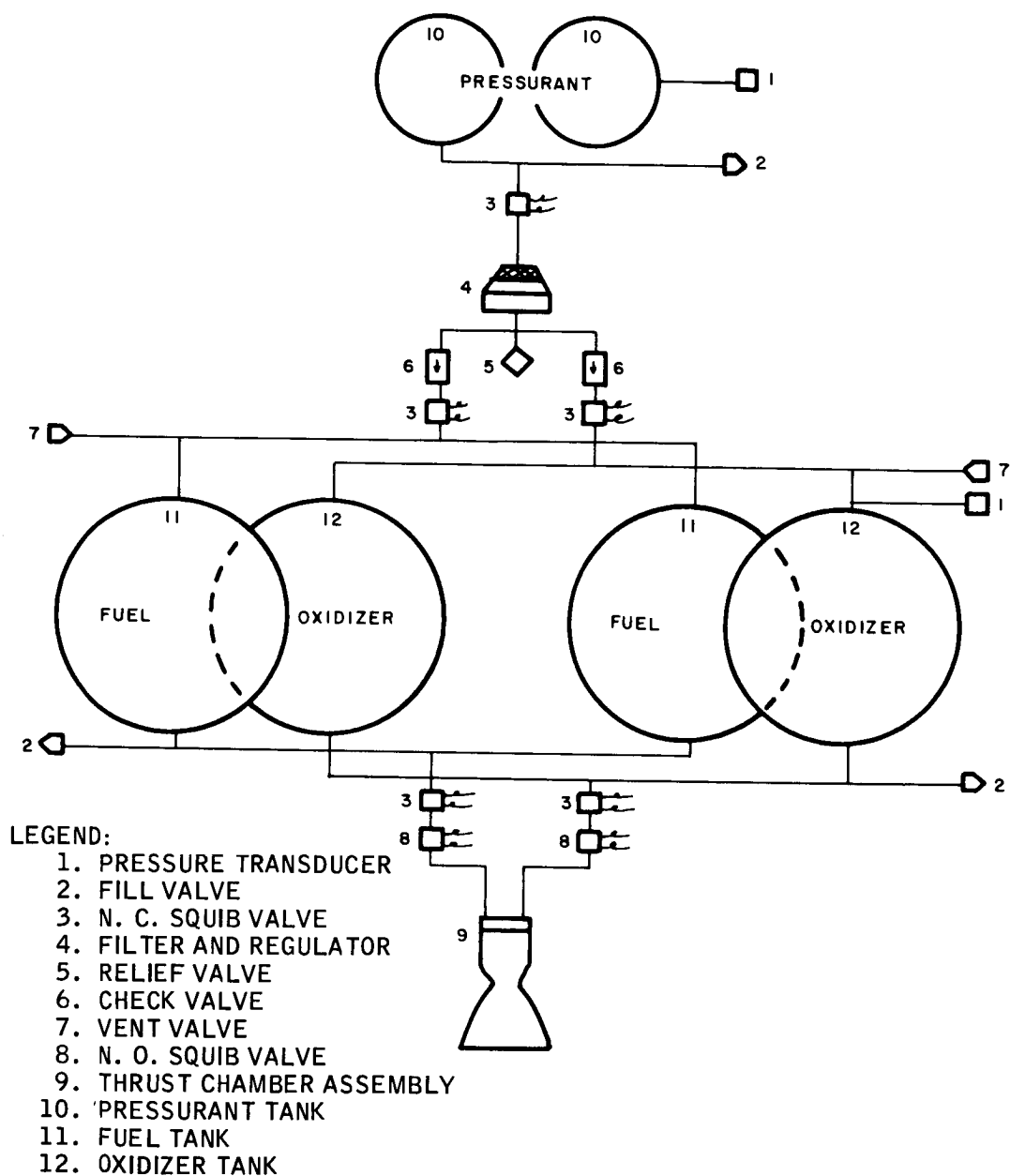
The main thrust chamber is rigidly mounted, ablatively cooled, and is controlled for the one period of operation by normally closed and normally open squib valves in series. The chamber is designed to produce 40 pounds of thrust at a chamber pressure of 100 psia. Propellant tank pressure will be regulated to 140 psia. Thrust vector alignment tolerances are 0.01 inch for lateral displacement, and 0.26 degree angular misalignment. The effect of these inaccuracies upon the velocity vector is reduced to an acceptable value by spinning the lander at 10 rpm. Initial separation velocity is given by a spring. Spinup is accomplished by a pair of solid propellant rockets attached to the exterior of the lander sterile container.

The propellant is contained in two equal-volume oxidizer tanks and two equal-volume fuel tanks. The tanks are packaged as near to each other as possible in a dynamically balanced arrangement within the space allowed. The lander spin rate is utilized as a means of propellant orientation to give a dependable means of propellant expulsion. Tank outlets are positioned to allow maximum propellant utilization (see figure 7). The propellant tanks are filled with the required amount of propellant before sterilization. During sterilization at 295 °F, the oxidizer will generate a high vapor pressure. The generated pressure is a function of ullage volume; in this case being designed for a pressure of 1150 psia for a 10 percent ullage volume. A stainless steel which is compatible with the oxidizer at the elevated temperature was chosen for tank material. The steel has such a high strength that manufacturing capability is the governing factor in determining minimum wall thickness. Vapor pressure of the fuel is 53 psia at 275 °F, which is below the tank design pressure of 140 psia. Aluminum was chosen for the fuel tank material, wall thickness governed again by manufacturing capability rather than stress requirements. Normally closed squib valves are used above the tanks rather than check valves because of the absence of diaphragms or bladders in the propellant tanks. The valves ensure propellant isolation until system activation. Check valves will then provide isolation of the propellants from one another.

Pressurization is provided by stored helium contained in two equal-volume spheres manifolded together. The two-tank configuration was chosen from packaging and dynamic balance considerations. Pressurant is isolated from the pressure regulator by a normally closed squib valve until the system is activated.

7. Separation system. In the separation sequence, the following events occur:

a. The sterilization can and micrometeorite shield, with lander internally packaged, is mechanically detached from the orbiter-bus, which has been previously put into the proper attitude with respect to the flight path. A small velocity component relative to the space craft is provided by a spring device.



63-8447

Figure 8 MARS LANDER PROPULSION SYSTEM SCHEMATIC

b. As separation begins, the sterilization can and lander is spun about the lander's roll axis (which lies along the separation velocity vector) by small solid-fuel spin rockets attached to the outside of the sterilization can. A rotational speed of 10 to 20 rpm is reached at spin-rocket burnout.

c. A linear shaped charge is fired after a preset interval, which cuts the sterilization can axially into two half cylinders and releases the lander. Due to the rotation of the system, the two halves fly away in opposite directions.

d. Following a delay which will provide a sufficient distance between the lander and the space craft to avoid significant plume effects, the lander propulsion system is activated.

Upon reaching the required velocity increment, as measured by integrating accelerometers, thrust is terminated. The dry system is then carried along with the entry vehicle for the remainder of the mission.

During the thrusting period, the outer shell of the entry vehicle provides the reactive load path. At the low thrust level used, there are no particular attachment problems. Hypergolic propellants are used, obviating the necessity of a separate system for ignition initiation.

8. Heat shield and structure. In the design study, two external aerodynamic configurations were investigated, namely the V-1 and V-2 shapes. Digital computer results of the planetary atmospheric entry heating programs have been presented elsewhere, which show the heat shielding requirements. The parameters investigated include entry angle and velocity, atmospheric composition, and characteristic vehicle size and ballistic parameter, $M/C_D A$. A series of plots of total heat shield weight versus entry vehicle weight has been made for the following cases:

<u>Vehicle Shape</u>	<u>V-1</u>	<u>V-2</u>
$M/C_D A$ (slug/ft ²)	0.9	0.6, 0.9, 1.5
Weight (pounds)	500 to 4000	500 to 4000
Entry angle (degrees)	-20, -45, -90	-20, -45, -90
Entry velocity (ft/sec)	20,000, 24,000, 29,000	20,000, 24,000, 29,000
Model atmosphere	Schilling Max, Min.	Schilling Max, Min.

The results are shown in figures 9 to 16.

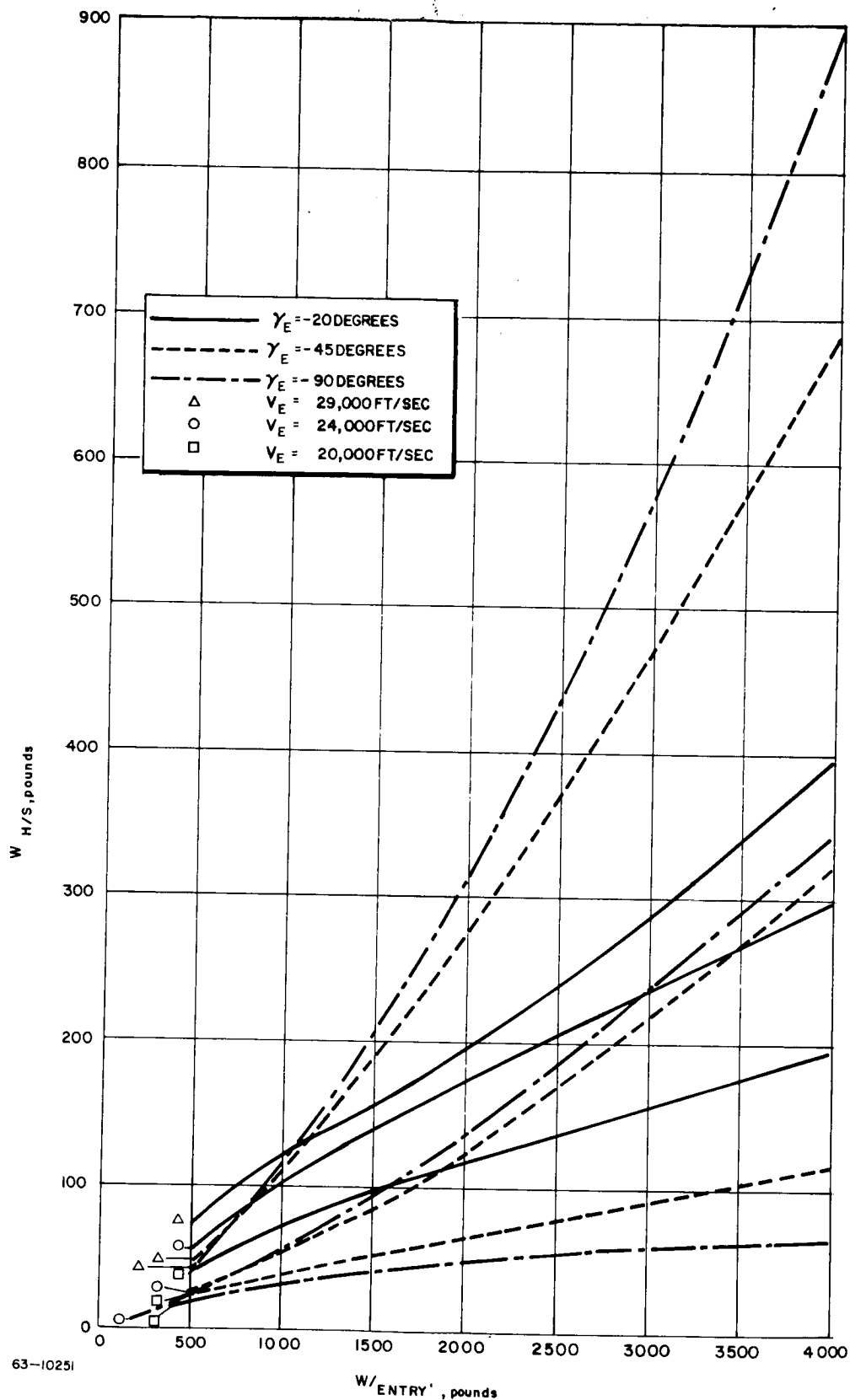
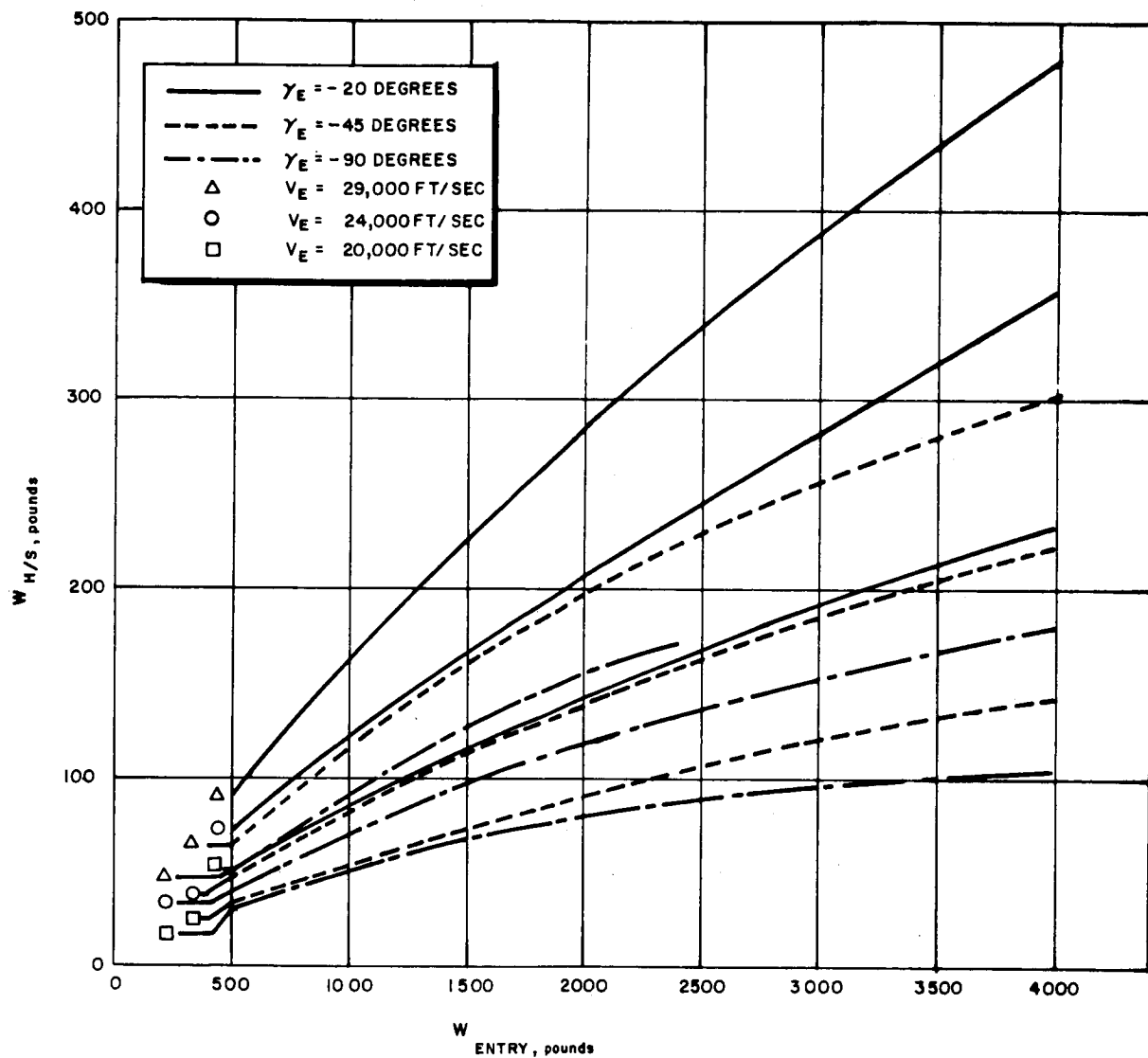


Figure 9 MARS LANDER TOTAL HEAT SHIELD MATERIAL WEIGHT (EXCLUDING SUBSTRUCTURE) VERSUS TOTAL VEHICLE WEIGHT AT ENTRY (V-2 SHAPE, $M/C_D A = 0.6$, SCHILLING MINIMUM ATMOSPHERE)



63-10252

Figure 10 MARS LANDER TOTAL HEAT SHIELD MATERIAL WEIGHT (EXCLUDING SUBSTRUCTURE) VERSUS TOTAL VEHICLE WEIGHT AT ENTRY (V-2 SHAPE, $M/C_D A = 0.6$, SCHILLING MAXIMUM ATMOSPHERE)

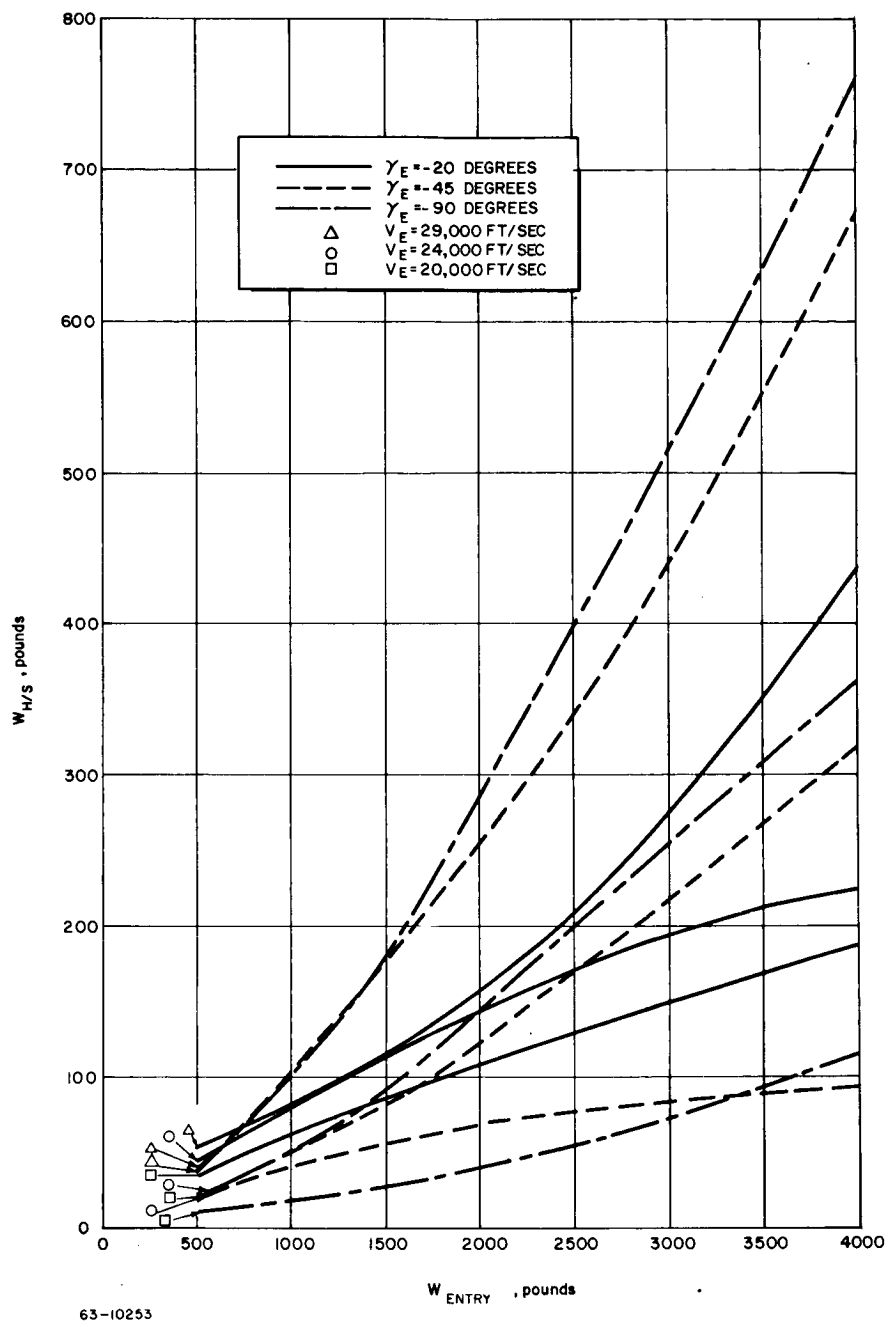
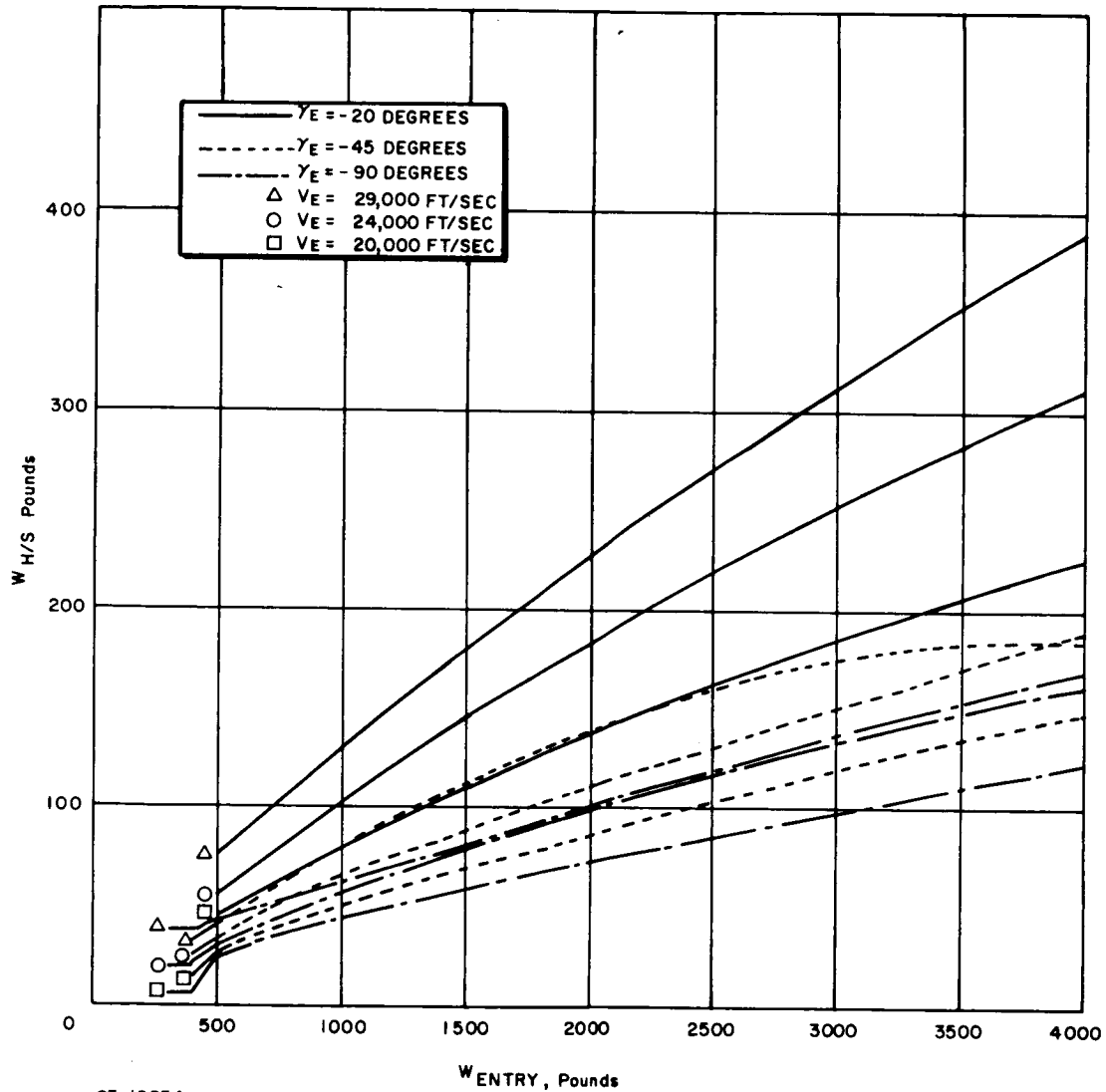
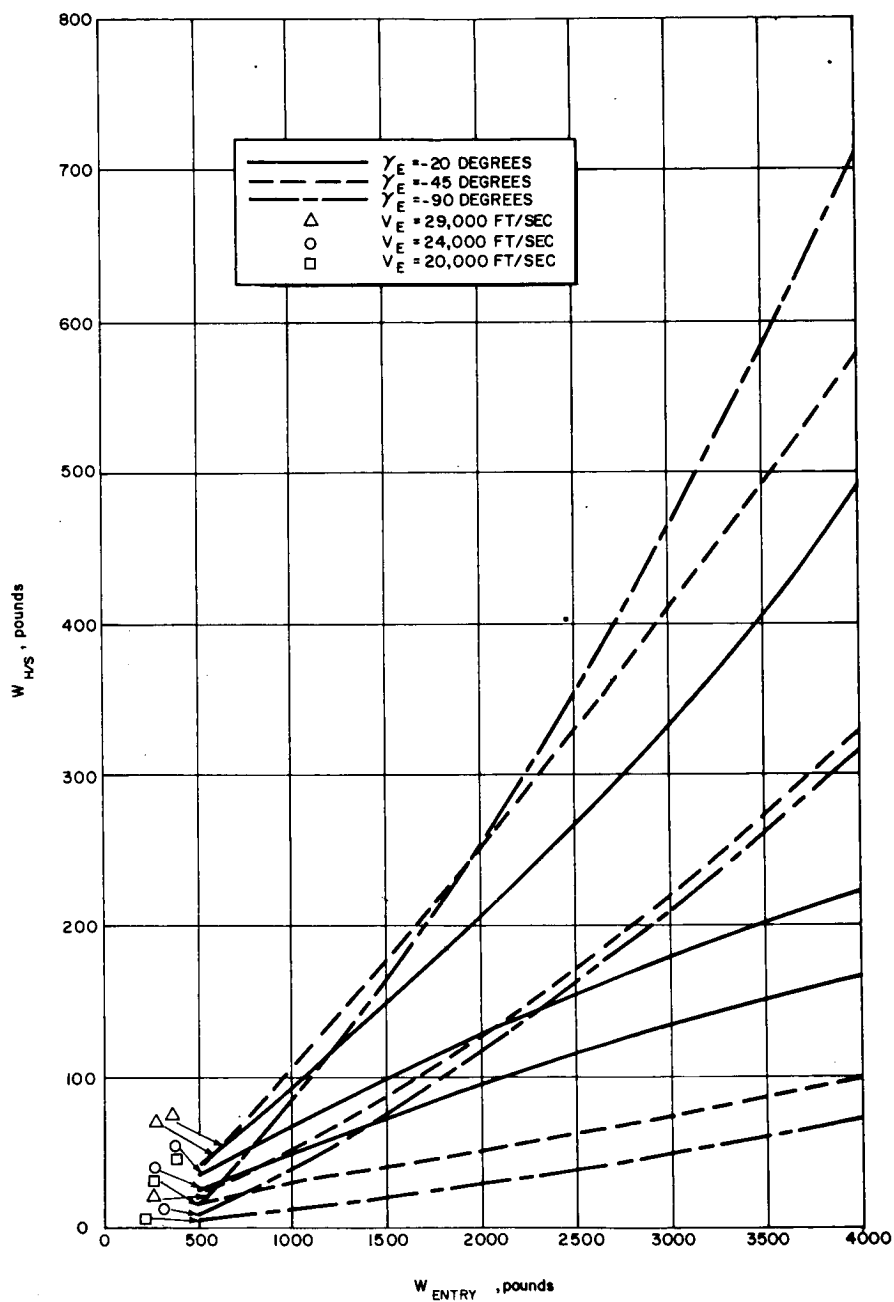


Figure 11 MARS LANDER TOTAL HEAT SHIELD, MATERIAL WEIGHT (EXCLUDING SUBSTRUCTURE) VERSUS TOTAL WEIGHT AT ENTRY
(V-2 SHAPE, $M/C_D A = 0.9$ SCHILLING MINIMUM ATMOSPHERE)



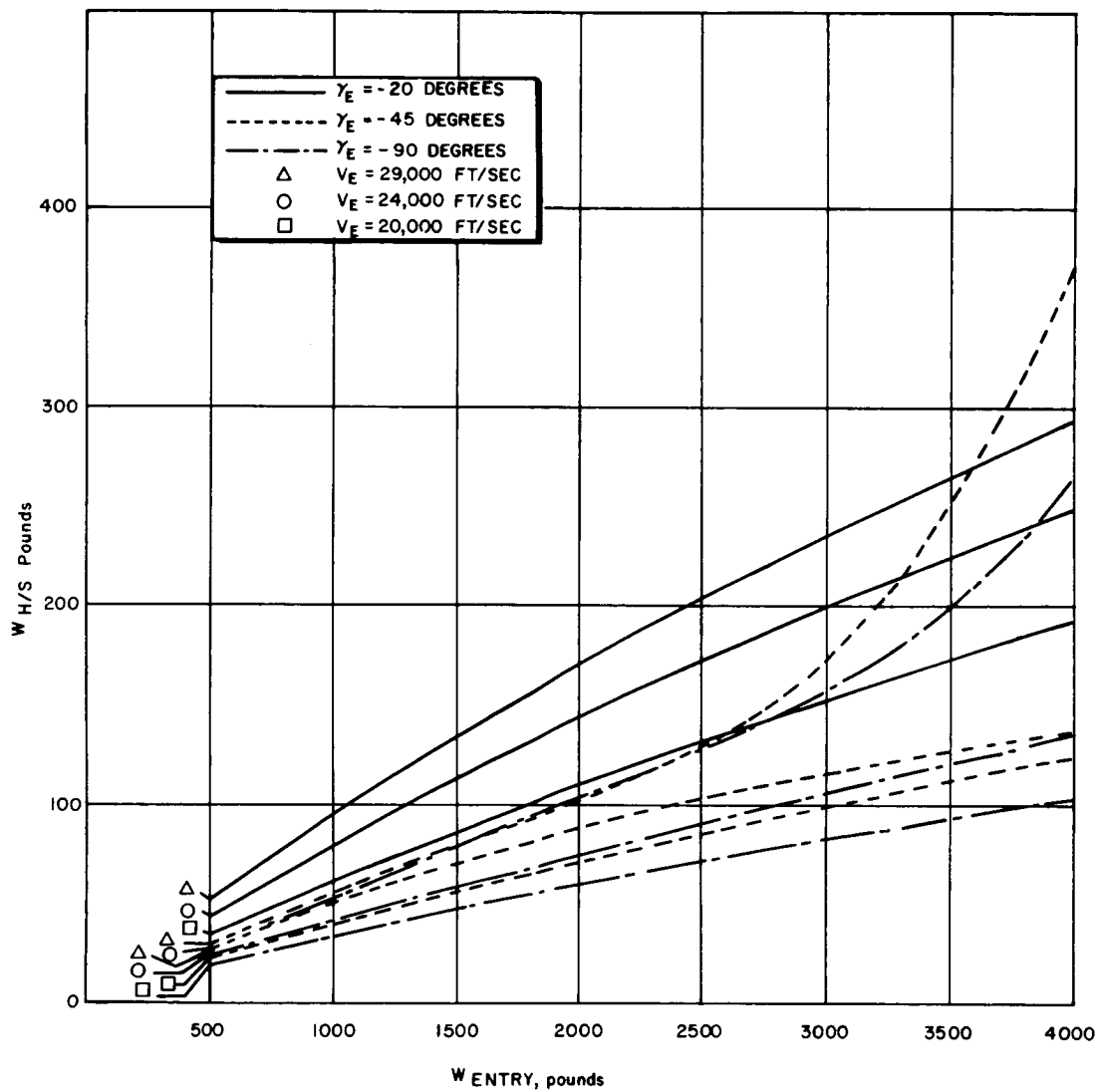
63-10254

Figure 12 MARS LANDER TOTAL HEAT SHIELD MATERIAL WEIGHT (EXCLUDING SUBSTRUCTURE) VERSUS TOTAL VEHICLE WEIGHT AT ENTRY (V-2 SHAPE, $M/C_D A = 0.9$, SCHILLING MAXIMUM ATMOSPHERE)



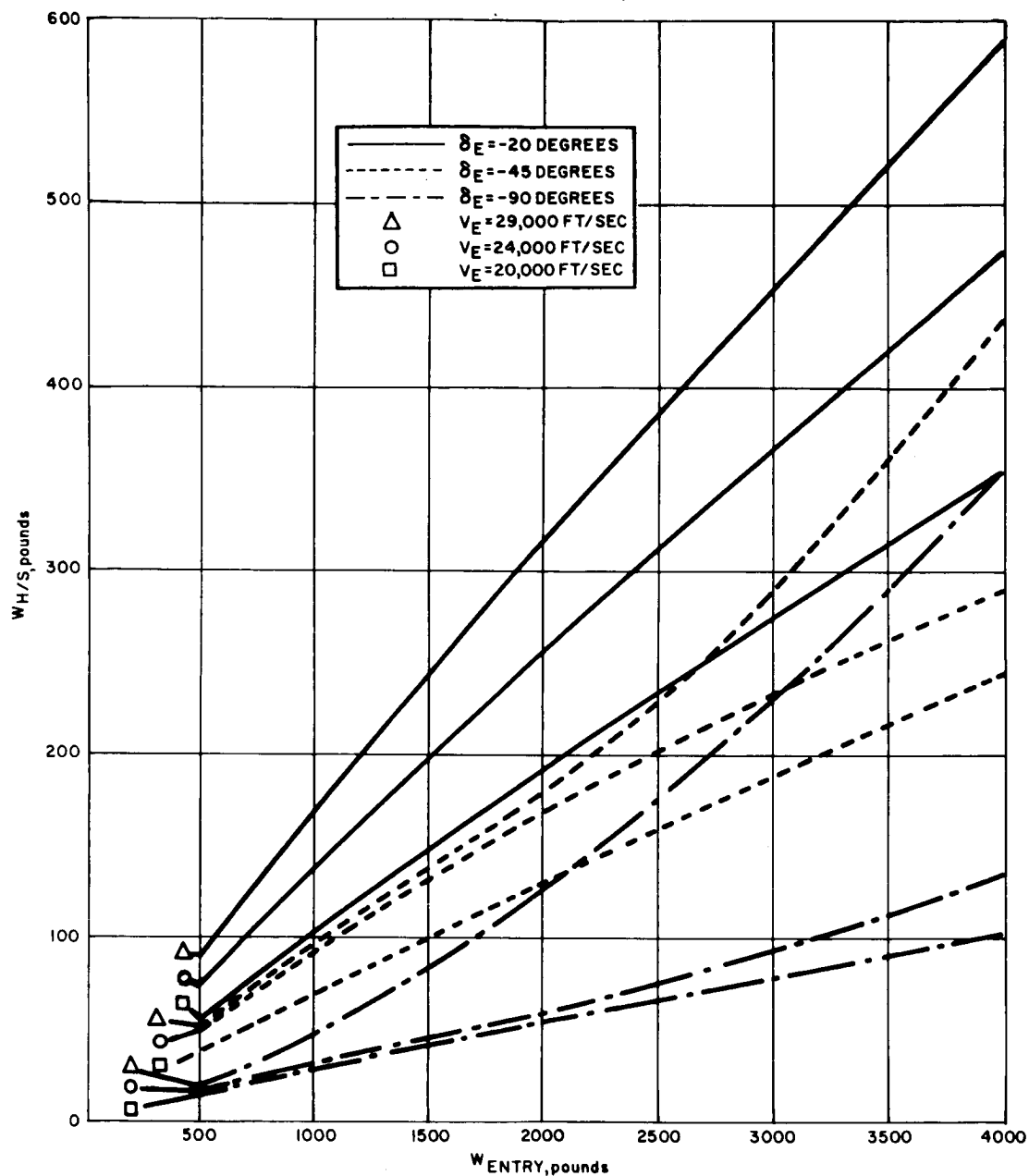
63-10255

Figure 13 MARS LANDER TOTAL HEAT SHIELD, MATERIAL WEIGHT (EXCLUDING SUBSTRUCTURE) VERSUS TOTAL WEIGHT AT ENTRY
(V-2 SHAPE, $M/C_D A = 0.5$, SCHILLING MINIMUM ATMOSPHERE)



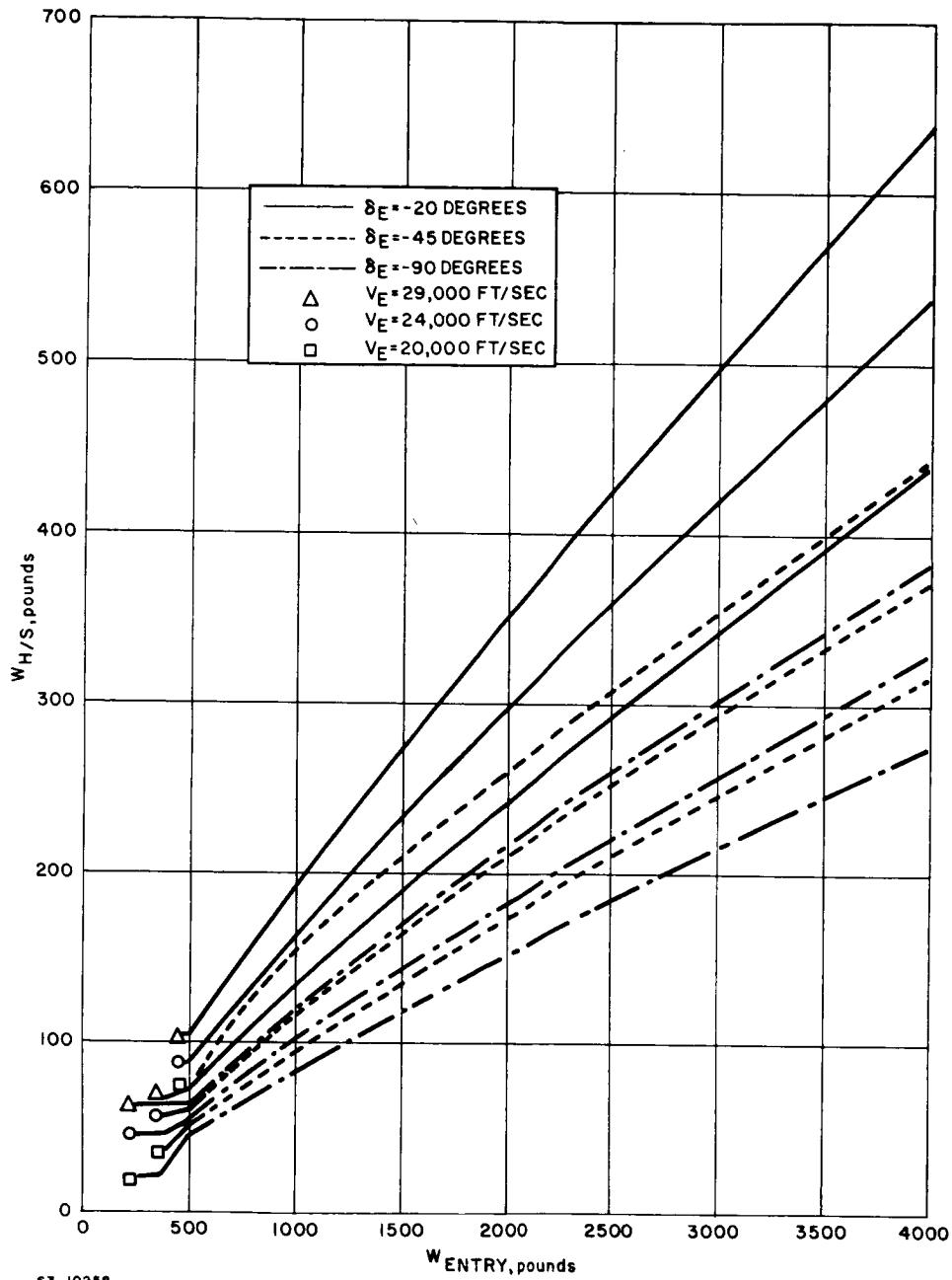
63-10256

Figure 14 MARS LANDER TOTAL HEAT SHIELD MATERIAL WEIGHT (EXCLUDING SUBSTRUCTURE) VERSUS TOTAL VEHICLE WEIGHT AT ENTRY (V-2 SHAPE, $M/C_D A = 1.5$, SCHILLING MAXIMUM ATMOSPHERE)



63-10257

Figure 15 MARS LANDER TOTAL HEAT SHIELD MATERIAL WEIGHT (EXCLUDING SUBSTRUCTURE) VERSUS TOTAL VEHICLE WEIGHT AT ENTRY (V-1 SHAPE, $M/C_{DA} = 0.9$, SCHILLING MAXIMUM ATMOSPHERE)



An investigation of both aluminum and stainless steel honeycomb substructures was made for each of the cases considered in the previously mentioned heat shield study. Except for only a few of the largest vehicles, of 12-foot diameter or greater, aluminum honeycomb was found to offer a weight saving. For the cases when stainless steel was lighter, only a small weight saving was noted, and it was felt that for consistency the aluminum construction would be used as a reference.

9. Parametric vehicle study -- reference design. A reference design was chosen which is the V-2 self-erecting design with direct Earth communication, and relay capability. A reference performance of $M/C_D A = 0.9$ slug/ft.² was selected, based on residual weight studies.

For various entry vehicle weights, the residual weights or payload capacities were determined. Table 2 shows the resultant weight breakdowns. The following assumptions were made:

a. Heat shield material was chosen to be Avcoat 5026. Total heat shield weight was based on the highest individual heat shield component weights for either Schilling minimum or maximum atmospheres, the most conservative case.

b. Entry vehicle structure was assumed to be aluminum honeycomb and was sized for the highest entry loadings and inertial loading, at an entry angle of -90 degrees.

c. Drogue parachutes for each vehicle were assumed to be of HT-1 construction, deployed at Mach 2.5, and of such an area as to provide for sufficient vehicle deceleration so that the main parachutes could be deployed at 15,000 feet at a Mach number of 0.8 or less. Main parachutes, also of HT-1 material, were designed to provide a sea-level vertical descent velocity of 40 ft/sec.

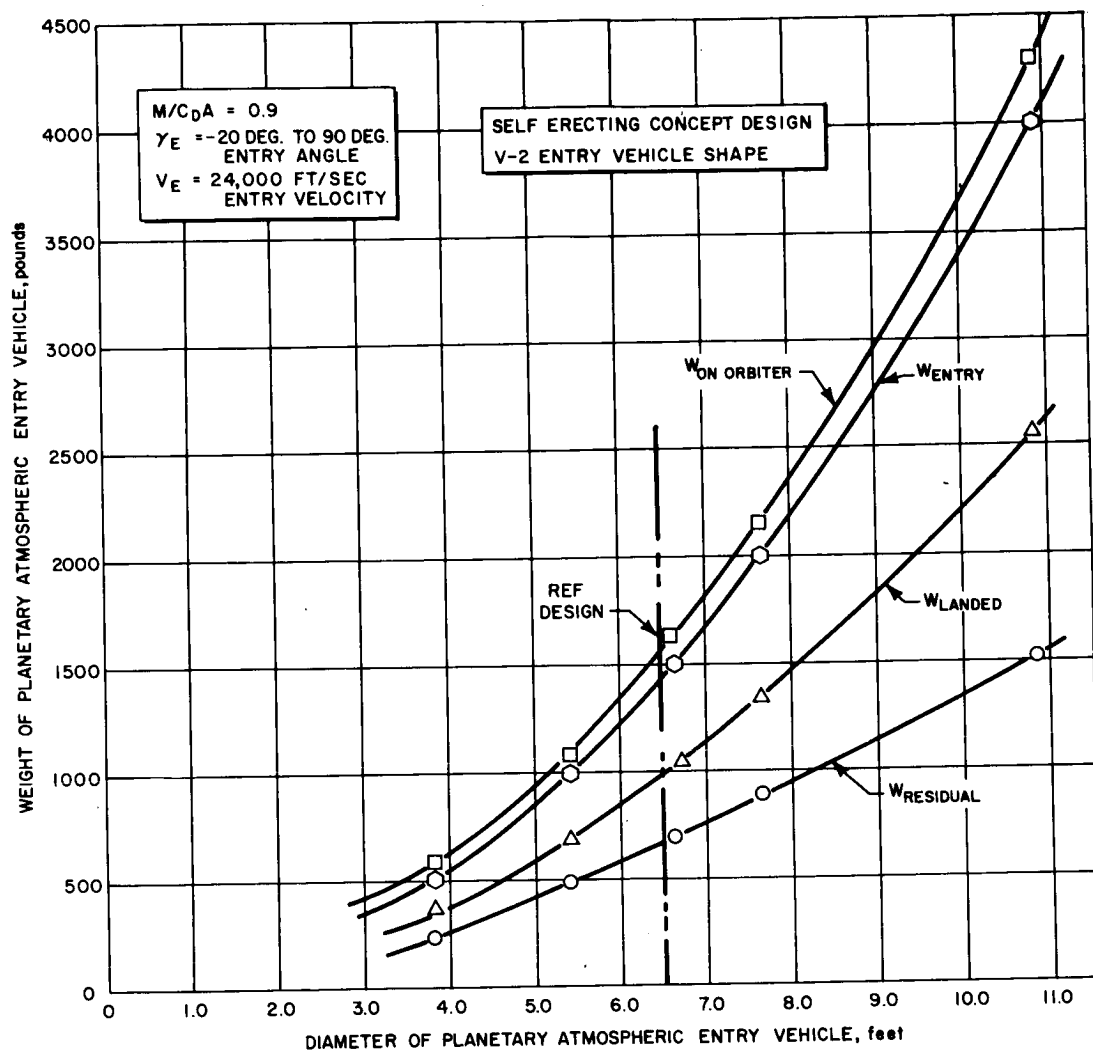
d. Entry angle was assumed to be in the range from -20 to -90 degrees and entry velocity was chosen as 24,000 ft/sec. Figure 17 shows curves of weight on orbiter, weight at entry, landed weight, and residual weight, plotted versus the diameter of the planetary atmospheric entry vehicle. For a residual weight of 658.4 pounds, corresponding also to an entry weight of 1410 pounds, a 6.45-foot diameter vehicle is indicated as the reference design point. This residual weight corresponds to a certain specific scientific payload, with the necessary communications equipment and power supply. The actual physical weight breakdown, other than the residual weight, is also shown in table 2, as a separate column. The ballistic parameter, $M/C_D A$, was chosen as 0.9 slug/ft.² as a practical maximum value for which internal packaging would be consistent with c.g. requirements for aerodynamic stability, while also providing sufficient aerodynamic retardation to preclude excessive heat shield, structure, and parachute system weights. (See figure 17.)

TABLE 2
PARAMETRIC WEIGHT STUDY
VOYAGER MARS LANDER--SELF-ERECTING CONCEPT

	500	1000	1500	2000	4000	Reference Design ¹
Nominal Entry Weight	3,834	5,423	6,641	7,669	10,845	1410.7
Entry Vehicle Diameter (feet)						
Weight on Orbiter (pounds)	540.6	1078.63	1613.45	2149.49	4296.37	1517.95
Less Weight of Sterilization Can	34.00	66.00	94.00	123.00	240.00	89.0
Less Spin Rocket Weight	1.0	1.43	2.65	4.09	11.57	2.35
Less Main Fuel Weight	5.6	11.2	16.8	22.4	44.8	15.9
Subtotal = Weight at Entry	500	1000	1500	2000	4000	1410.7
Less Weight of Heat Shield ²	58.26	116.53	174.79	233.0	466.1	163.0
Less Heat Shield Bond Weight	17.40	34.79	52.19	69.58	139.17	49.0
Less Heat Shield Structure Weight ²	39,000	87,500	145,000	210,000	558,000	135.0
Less Main Rocket (dry weight)	9.02	10.28	11.16	11.86	13.85	11.0
Subtotal = Weight Descending (includes drogue chute)	376.32	750.90	1116.86	1475.56	2822.88	1052.7
Less Drogue Chute Weight	9.06	18.20	29.0	41.0	93.60	27.9
Subtotal = Weight Descending (includes main chute)	367.27	732.70	1087.86	1434.56	2729.28	1025.7
Less Main Chute Weight	23.3	46.5	69.0	91.0	173.1	65.0
Subtotal = Weight Landed	343.97	686.2	1018.86	1343.56	2556.18	960.7
Less Miscellaneous - Weight Landed	17.20	34.31	50.94	67.17	127.81	48.0
Less Internal Structure ($\gamma_E = -90$ degrees)	30.4	76.5	143.1	218.2	570.1	130.0
Less Weight of Petal Actuators	21.2	33.4	46.1	58.6	104.2	44.0
Less Navigational Equipment Weight	13.0	13.0	13.0	13.0	13.0	13.0
Less Weight of Parachute Logic	6.0	6.0	6.0	6.0	6.0	6.0
Less Weight of Crushup Pads	5.2	10.29	15.29	20.16	38.34	14.3
Less Weight of Self-erecting Petals	12.5	33.0	51.0	77.0	179.0	47.0
Subtotal = Residual Weight	238.47	479.70	693.43	883.43	1517.73	658.4
Reference Data: M/CDA - 0.9						
Planetary Atmospheric Entry Velocity - 24,000 ft/sec						
Planetary Atmospheric Entry Angle - 20 degrees to -90 degrees						
Planetary Atmospheric Model ² - Schilling Min. and Max.						
Planetary Atmospheric Entry Vehicle - V-2 Shape						

¹Residual Weight equals Residual Weight required for Reference Design Scientific Payload.

²Most conservative assumptions were used.



63-10259

Figure 17 MARS LANDER PARAMETRIC WEIGHT STUDY

10. Sterilization. A rigid requirement has been established that the lander must not carry any Earth-originated organisms to the target planet. In order to maintain the sterile levels required, care must be given during all phases of the mission. The present design has been predicated on a heat soaking sterilization procedure for all components for which this is feasible, followed by sterile assembly techniques for those presterilized nonheatable components.

As a result of the sterilization requirement, the propulsion system tankage has been sized to allow for the pressure increases during heating. In order to avoid subjecting the RTG to the heat sterilization, provision has been made to allow the aseptic assembly of the RTG (radioactive power generation unit) at the last possible instance before the heat shield and entry vehicle are sealed and assembled into the sterilization can. This can be done by inserting it between the erection petals into its position atop the main internal structure.

An umbilical connection for both internal pressure and electrical connections between the lander and the sterile can are required. A pressure differential valve will also be attached to the can, allowing internal pressure during space flight to remain at a few pounds per square inch absolute. This will allow convection to distribute the internal heat load more evenly throughout the capsule. Another purpose of the umbilical will be to monitor internal temperatures, both during sterilization and during the actual mission profile.

11. Thermal control. During transit from Earth to Mars, the lander is located in the shade of the solar panels of the orbiter-bus. This condition causes the lander internal temperature to be determined by the energy balance between surface radiation to the space environment and heat inputs from internal heat generators and spacecraft conduction and radiation paths. The use of an RTG packaged internally to the lander capsule has been the basis of this particular thermal design concept. During interplanetary transit, the vehicle must radiate excess heat from the sterilization can and, after landing on the planetary surface, heat must be retained to maintain the instrument box at a warm enough temperature.

The internally packaged RTG has a 110-watt power output, with an 8 percent power generation efficiency, giving a total heat load of 4700 Btu. During space flight, this must be distributed throughout the package, and then radiated by the 180 ft² external area of the sterilization can. Assuming a view factor of 1.0, the thermal control system utilizes an internal can and lander pressure of about 1.0 psi to allow forced convection within the lander. Two small fans, on the lander, absorb part of the excess RTG electrical power in circulating the internal air. There is a direct radiation path from the RTG, placed on top of the instrument box, to the petals and thence to the lander entry vehicle outer shell. The lower part of the petals in the vicinity of the RTG are made of aluminum. Based on combined radiation and conduction effects, no catastrophic failure occurs in case either the fans malfunction or the can/capsule sustains a loss of internal pressure.

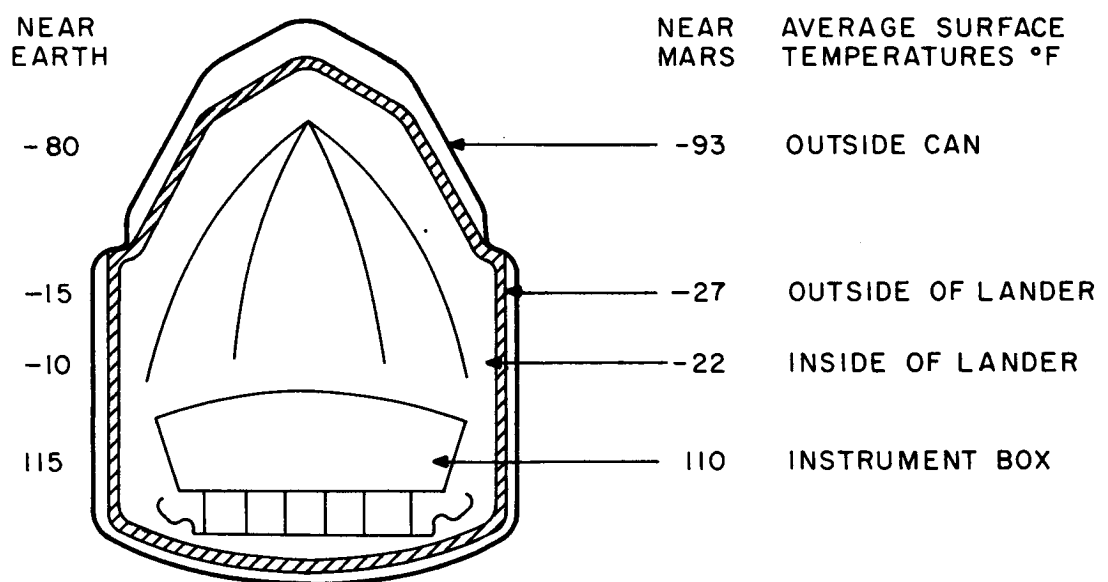
The aft section of the lander is enclosed on the orbiter-bus by the lander support structure. The propellants stored within the lander will be protected by this shielding. Heated by the circulating internal convection currents they are kept at a temperature within the design limits of 0 to 100 °F. The anticipated interplanetary average surface temperatures are shown on figure 18 for on-orbiter, near-Earth, and near-Mars conditions. After separation, the sterilization can is shed and the spinning lander continues on an impact course towards Mars. Figure 19 shows the expected temperature levels, with sun input perpendicular to the spin axis of the vehicle. A coating with an α/ϵ of 0.25 will be used for the exterior surface of the lander.

During planetary atmospheric entry, the heat shielding analysis has been predicated on an entry vehicle external surface temperature of 100 °F. However, figure 19 shows that lower initial values are anticipated, adding a degree of conservatism to the heat shielding analysis. During entry, the externally generated heat pulse causes an attendant rise in the temperature at the back face of the heat shield material. This can be accommodated by the heat sink capacity of the internally packaged equipment. The fan-induced internal convection currents will preclude extreme temperature gradients.

For planetary operation, the internal characteristics of the RTG (low-efficiency or high-heat-load per unit of electricity produced) are a benefit in the cold environment. After surface impact, the lander operational sequence will be designed to minimize the detrimental effects of the extreme cold. As the erection petals open, the used crushup on the instrument box is raised above the ground level, avoiding direct contact and the resultant heat conduction path. The storage batteries will be well insulated and provided with internal electric heaters to maintain a minimum electrolyte temperature of 50 °F. (During interplanetary transit, the temperature will be maintained by the internal heat convection). The RTG will be mechanically mounted to the top of the instrument box to allow maximum heat conduction to the instrument box top cover. The location of instruments within the box will be such that equipment with low allowable upper temperature limits is located furthest from the RTG. Each electronic component will be normally operated in a skin temperature range from -20 to +150 °F, and will be capable of sustaining, without permanent damage, the sterilization soak at 295 °F. It is expected that these temperatures will not jeopardize either performance or reliability. Earth testing of the system will establish thermal paths and allow a design to be realized where the extremely low planetary environmental temperatures will not be easily communicated to the internal components.

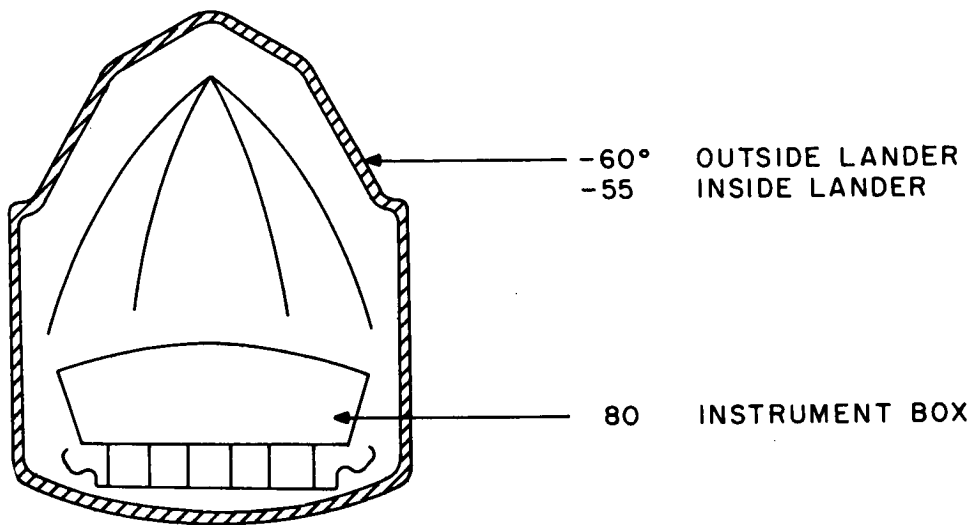
To ensure the adequacy of the thermal control system, two on-the-planet-surface conditions were investigated. These were:

a. No wind, average heat transfer coefficient from the 55.0 ft² surface area of the instrument box of 1.0 Btu/hr-ft²-°F. (For the Schilling atmospheric



63-8624

Figure 18 TRANSIT JOURNEY



63-8463

Figure 19 LANDER JOURNEY (SPINNING)

conditions set forth as a guideline for Mars studies, the average ambient temperature is -10°F).

b. Wind velocity of 5 mph, heat transfer coefficient of $3.0 \text{ Btu/hr-ft}^2\text{-}^{\circ}\text{F}$ for the 30 ft^2 area of the box top surface and upper cylinder portion, and $1.0 \text{ Btu/hr-ft}^2\text{-}^{\circ}\text{F}$ for the shielded lower cylinder portion and the bottom box surface.

For these cases, the entire instrument box outer surface was first allowed to be as low as -10°F and then as high as $+130^{\circ}\text{F}$. The resultant allowable external ambient temperature for all four cases are shown in table 3 for the internal RTG-generated heat load of 4700 Btu.

TABLE 3
ALLOWABLE EXTERNAL AMBIENT TEMPERATURES

Instrument Box Surface Temperature (degrees)	Wind Velocity (mph)	Allowable External Ambient Temperature to Maintain Instrument Box at specified temperature ($^{\circ}\text{F}$)
-10	0	-95
-10	5	-53
+130	0	+45
+130	5	+87

12. Lander navigation system. The lander vehicle will be spin-stabilized and will not require a stabilization and control system. Furthermore, the separation technique and the use of a fixed thrust engine on the lander has eliminated the need for inflight guidance so that the only guidance equipment required on the lander will be an accelerometer or timer for thrust cutoff, and navigation equipment to determine the lander location after its touchdown on Mars.

The navigation system consists of a computer and Sun sensor. The weight, volume, and power requirements of these components are shown in table 4.

TABLE 4
PHYSICAL CHARACTERISTICS OF LANDER
NAVIGATION EQUIPMENT

	Weight (pounds)	Volume (in ³)	Power Required (watts)
Sun Tracker	3	64	6
Computer and Power Supply	28	1,000	30
Precision Frequency Reference	<u>0.7</u>	<u>20</u>	<u>6</u>
Totals	31.7	1,084	42

a. System operations. The function of the lander system is to determine its position on Mars after impact. Following impact, the vehicle will right itself to a nominally level orientation. At this time, the solar panels, antennas, and Sun sensor are deployed. The Sun sensor will then be put in a self-leveling mode to obtain local level. The level reference is obtained from miniature bubble level sensors mounted on each gimbal. Once the level reference has been established, the sensor will be put in the track mode. In this mode, the Sun sensor output will be used to drive the gimbals to obtain a null. The two gimbal angle measurements monitored by the computer provide the necessary information to determine position since time and Mars ephemeris (stored in computer) are known. The computations required are given in ref. 1.

b. System description.

1) Computer. The lander computer is a fixed-stored program, fractional, binary fixed-point digital computer. It has 2,048 twenty-four-bit words of which 256 twenty-four-bit words are alterable (scratch pad memory), and 1,792 twenty-four-bit words are unalterable (cold storage memory). By using a 12-bit instruction word, it is possible to store 3,584 instructions in cold storage, and use scratch pad for constants and intermediate storage. There is no distinction in storage format between data and instructions. The memory capacity may be increased in convenient multiples of 256 words by adding memory elements and electronics. This addition in no way alters the basic machine organization.

The lander memory is designed for minimum power and weight. It contains a wired core portion used for program data storage, and a read-restore core portion for scratch pad. Memory access is serial-parallel; for example, to obtain a 24-bit operand, four sequential 6-bit parallel fetches are performed.

a) Arithmetic operations. Arithmetic is performed bit serial. Addition is performed in normal binary fashion, using a full adder and the carry flip-flop (KFF). Subtraction is performed by one's complementing the output of the MR, which holds the subtrahend, forcing an initial carry in KFF, and adding. Multiplication and division are performed bit by bit by subroutine.

The operand from memory is fetched by 6-bit characters in parallel. The MR is bit-shifted right, and the sum formed. The bit sum is bit-shifted into the high order bit of the accumulator, so the sum (difference) logical product replaces the old contents of the accumulator.

b) Input/output. There are provisions for addressing 16 inputs and 16 outputs.

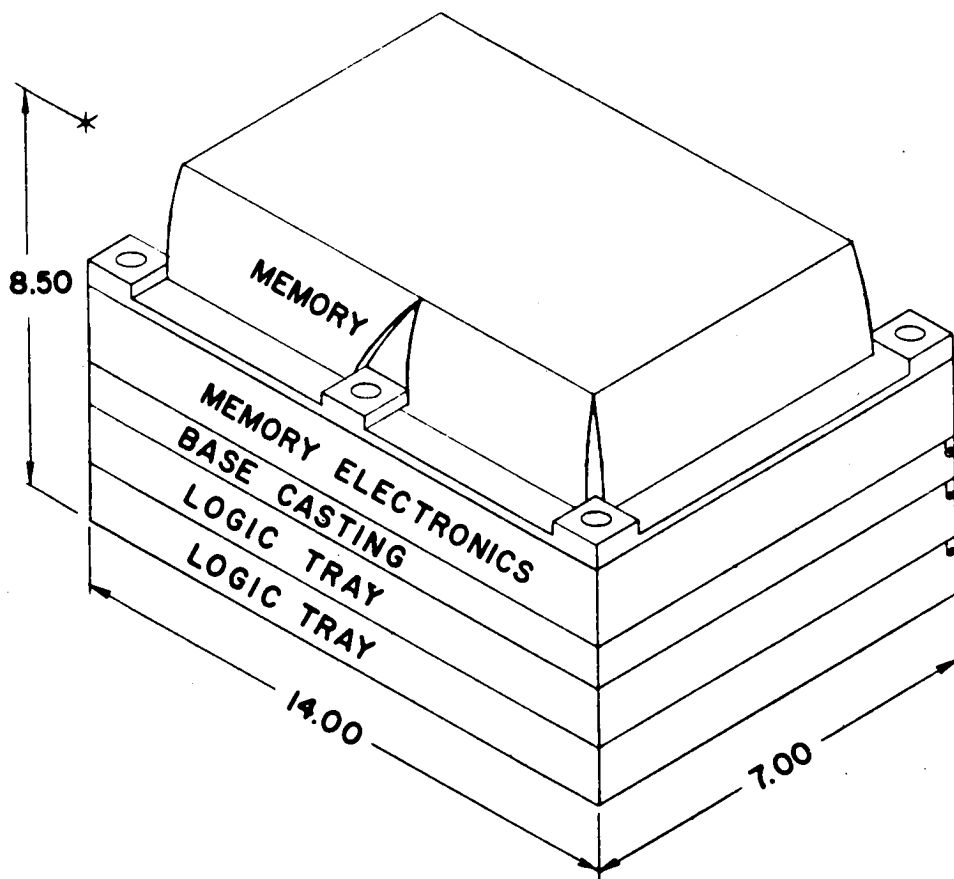
1 Inputs. The lander computer has three 3-bit counters using a Gray code. These precount or accumulate the incremental inputs from the 400 pps precision time input and the optisyns. They are transferred to the AR upon command. Discrete inputs are transferred to the sign flip-flop (SFF) under command. If parallel inputs are required, they will be transferred to the AR under command.

2 Outputs. A 1-bit telemetry register is provided. The high order bit of the AR is transferred to the telemetry bit, and by command, an "existence" bit is set/reset to gate the telemetry output to the external system. Discrete outputs are set/reset by the SFF under command. If parallel outputs are required, they will be loaded from the AR under command.

c) Packaging. In any system that must withstand severe environmental conditions, the accuracy and reliability of the equipment is only as good as its packaging. Chief aims are to achieve minimum size and weight, maximum reliability, accessibility, ease of manufacture and ease of repair without sacrificing the capability of withstanding extreme environmental conditions.

The basic chassis of the lander computer, as shown in figure 20, is a magnesium casting. It houses the memory electronics and miscellaneous components and assemblies not mounted in the circuit board trays. The trays are mounted to the chassis with integral hinges and are through-bolted for strength when closed. They consist of a magnesium frame in which are mounted circuit boards, connector strips, and cabling. The circuit boards consist of multilayer printed circuit boards on which integrated networks and connector strips are mounted. This allows maximum circuitry while maintaining minimum size and weight.

2) Lander power supply. The lander power supply furnishes all regulated voltages and power necessary to independently operate the computer. In addition, it supplies a precision square wave generator circuit which is used



63-9309

Figure 20 LANDER COMPUTER

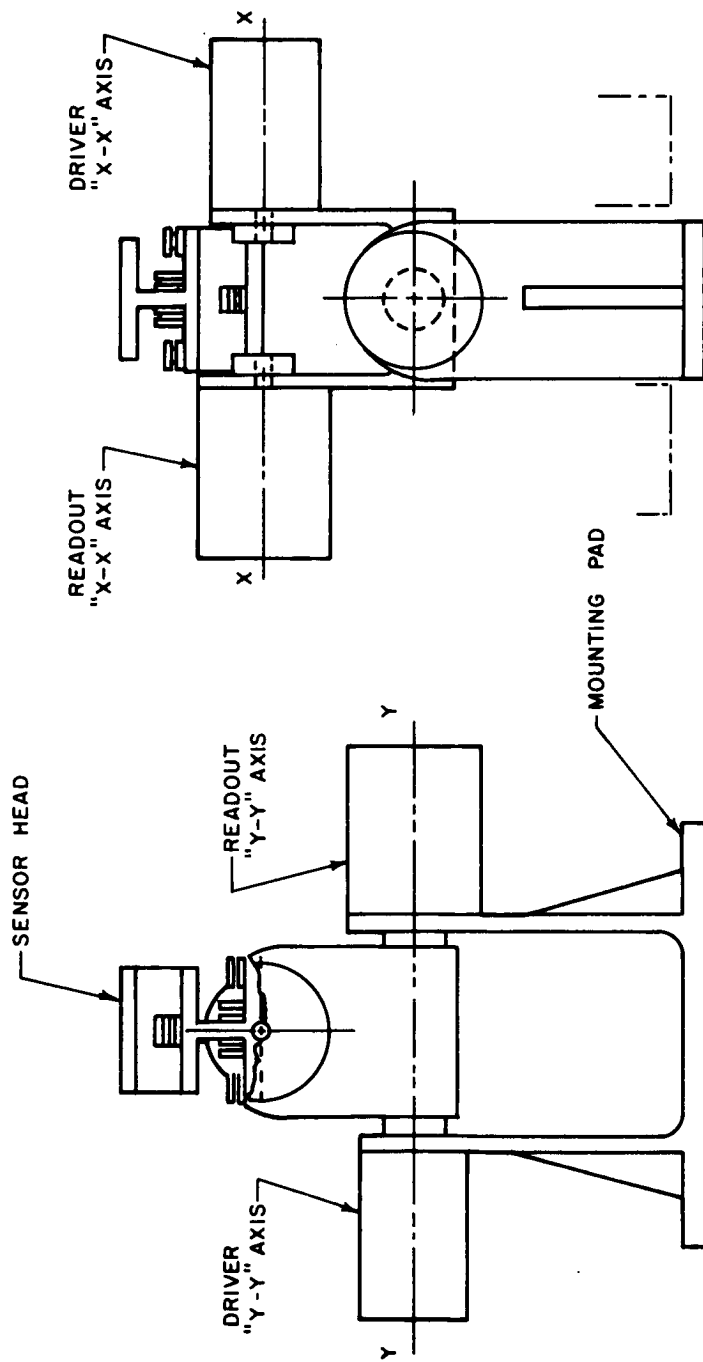
in conjunction with the computer. In operation, the lander power supply is identical to the orbiter power supply. The major difference is the power furnished to the load.

3) Precision frequency and timing reference. The precision frequency and timing reference for the lander system will include a temperature-controlled crystal oscillator and countdown circuitry required to provide computer timing signals.

4) Sterilized sun sensor (SSS). The sterilized Sun sensor is a gimbaled detector package with binary outputs accurate to ± 1 arc minute over ± 90 degrees in each of two orthogonal axes of rotation. The detector package, shown in figure 21 consists of four detectors and a shadow plate in each axis. The detectors are connected in a bridge and fed into a low impedance load so as to behave like current sources. In this mode, output current is proportional to detector area covered by sunlight and the level of incident flux density. The geometry is established to result in a linear output signal over ± 1.0 degree with the signal beyond ± 1.0 degree being non-linear but maintaining polarity out to greater than ± 90 degrees. The detector bridge output is fed into an amplifier, then to a dc motor which drives the gimbal until the bridge output is zero. Gimbal readout is by optisyn, a high reliability, precision, pulse output device. Pulses are counted as the gimbal rotates from a known reference position. The counting circuitry consists of integrated circuits, each circuit performing the same function as a multicomponent network, but with the same weight, volume, and reliability as a single transistor.

1.2 Reference Design -- MARS Schilling Atmospheres

1. Communication system. As outlined in section 1.1, a natural evolution of design selection was followed, wherein certain attractive design features were incorporated into the final concept. Perhaps the most evident of these is the use of a direct Earth communication system, shown in figure 22. The high gain antenna with its pointing capabilities dominates the cross-sectional view. The large overall dish diameter provides a large bit rate transmission with low power levels. Although the antenna is carefully adjusted and calibrated on Earth, it must endure severe loadings during planetary atmospheric entry and planetary surface impact which could distort it. With these requirements in mind, provision has been made to enclose this vital piece of equipment within a protective structure and to minimize the loads to which it must necessarily be subjected. The antenna driver amplifier is cradled on top of the rigid main equipment box, and attached to the antenna dish. This is done to allow the high g inertial loads to be transmitted to a stiff member, rather than distorting the lightweight antenna. The mounting of these pieces of equipment to the antenna allows the design to dispense with long microwave guides or plumbing and eliminates the use of radio-frequency rotary joints, which would be needed otherwise to allow azimuth and elevation attitude adjustments.



63-9310

Figure 21 STERILIZED SUN SENSOR



Operation of the main Earth communication system is dependent on proper petal deployment. However, a backup system has been incorporated, if either the terrain characteristics are more difficult than supposed, or if the petals do not perform as anticipated. A gimballed omnidirectional antenna with orbiter relay link capability is attached internally to one of the petals. The transmitter and driver are placed on the side of the inner gimbal opposite to the hemispherical omnidirectional transmitting surface, causing the central axis of the transmitting surface to always be normal to the local planetary horizontal. The fiberglass construction of the upper part of the petals allows a minimum of signal attenuation. Whether the petals are open or closed and even during normal operations, communications may be carried on with the orbiter.

2. Erection systems. The "acorn" external shape of the landed package can be seen in figure 23, which is a photograph of a lander model, dynamically scaled to allow a rough evaluation of lander capabilities. Figure 24 shows the extended acorn petals in the open position. For the model, mechanical spring actuators, pneumatically damped, with simultaneous action were used. The actual vehicle would use small electric motors with gear reduction driving double extension ball-screw actuators. The linkage investigated provided maximum mechanical advantage just at the beginning of petal actuation, at which time the vehicle ground attitude would most likely require it. Each actuator and petal system is powerful enough to turn the vehicle by itself, and it is anticipated that the vehicle, upon petal actuation, will roll itself to such a position that two of the petals will be utilized. A natural vehicle righting moment has been provided by the external shape of the "acorn" and the center of gravity location. Once in a final ground attitude, this moment in conjunction with the petal forces will turn the lander into its preferred orientation for Earth communication. A motor current sensing device or a local vertical sensor in conjunction with a logic package would enable differential petal action to achieve a horizontal attitude for the instrument package while still allowing one or more of the surfacesample collectors to perform. Lifting of the entire science package off of the base crushup pads allows a minimum of interior heat to be conducted to the planetary surface during the night portion of the mission. This thermal control function is a by-product or secondary consideration, but demonstrates the interdependence of the various systems. Equipment protection during inactive portions of the mission is also of interest. Equipment not in use would require less thermal control, and possibly one or more of the petals could be closed, maintaining the vehicle attitude.

3. Packaging. The acorn lander shape requires an entry vehicle configuration with sufficient internal volume to allow packaging of the lander. As previously mentioned, the V-2 shape was chosen. When packaged, the lander is captured between a set of compression struts from the front cap and a series of brackets attached to the cylindrical outer shell of the entry vehicle. The shaped charge, which cuts the entry vehicle at main parachute deployment, is located between the front cap and the retention brackets on the outer shell. The aluminum honeycomb crushup pads, under the lander, have a fiberglass bottom

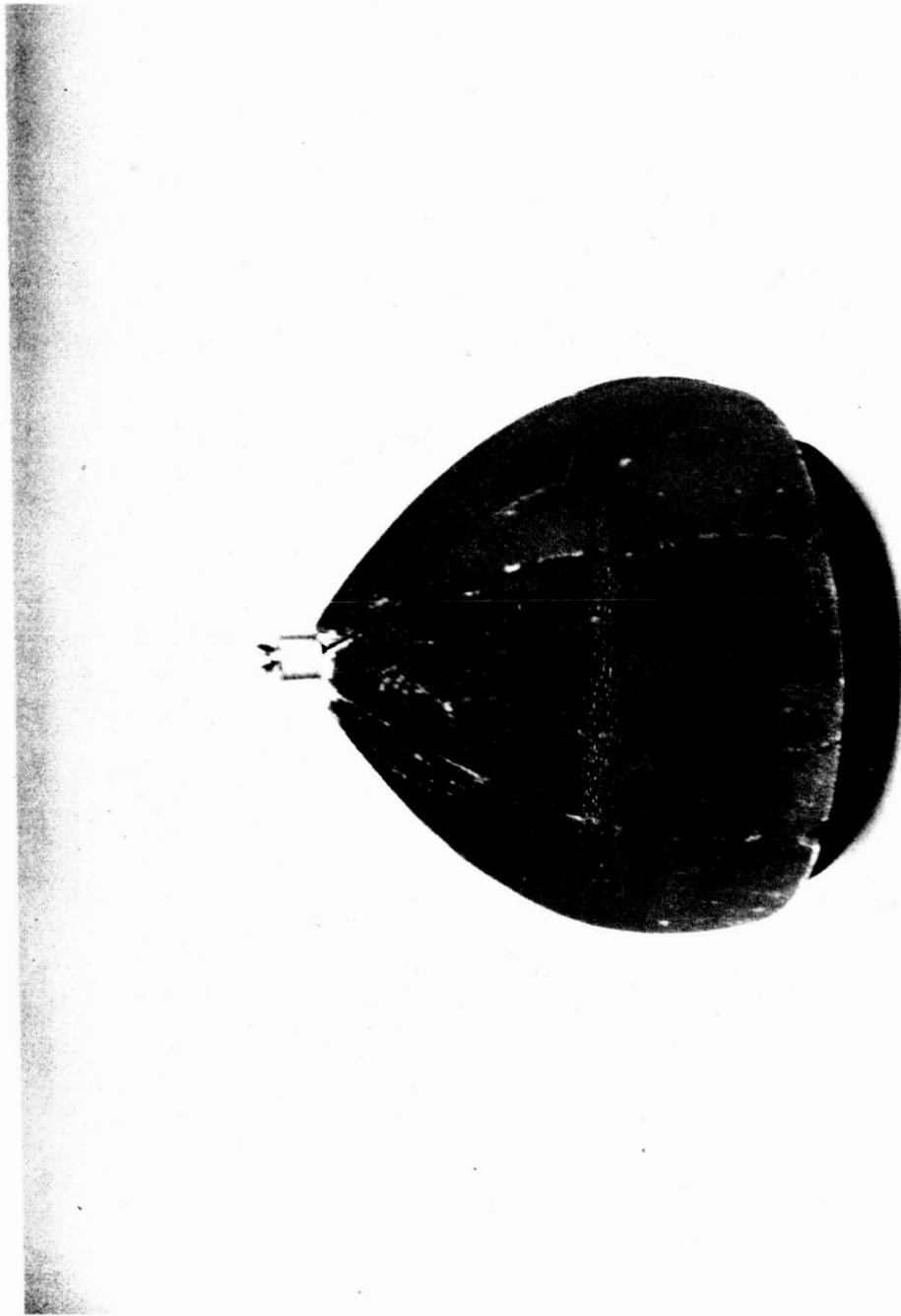


Figure 23 PHOTOGRAPH OF LANDER "ACORN" MODEL

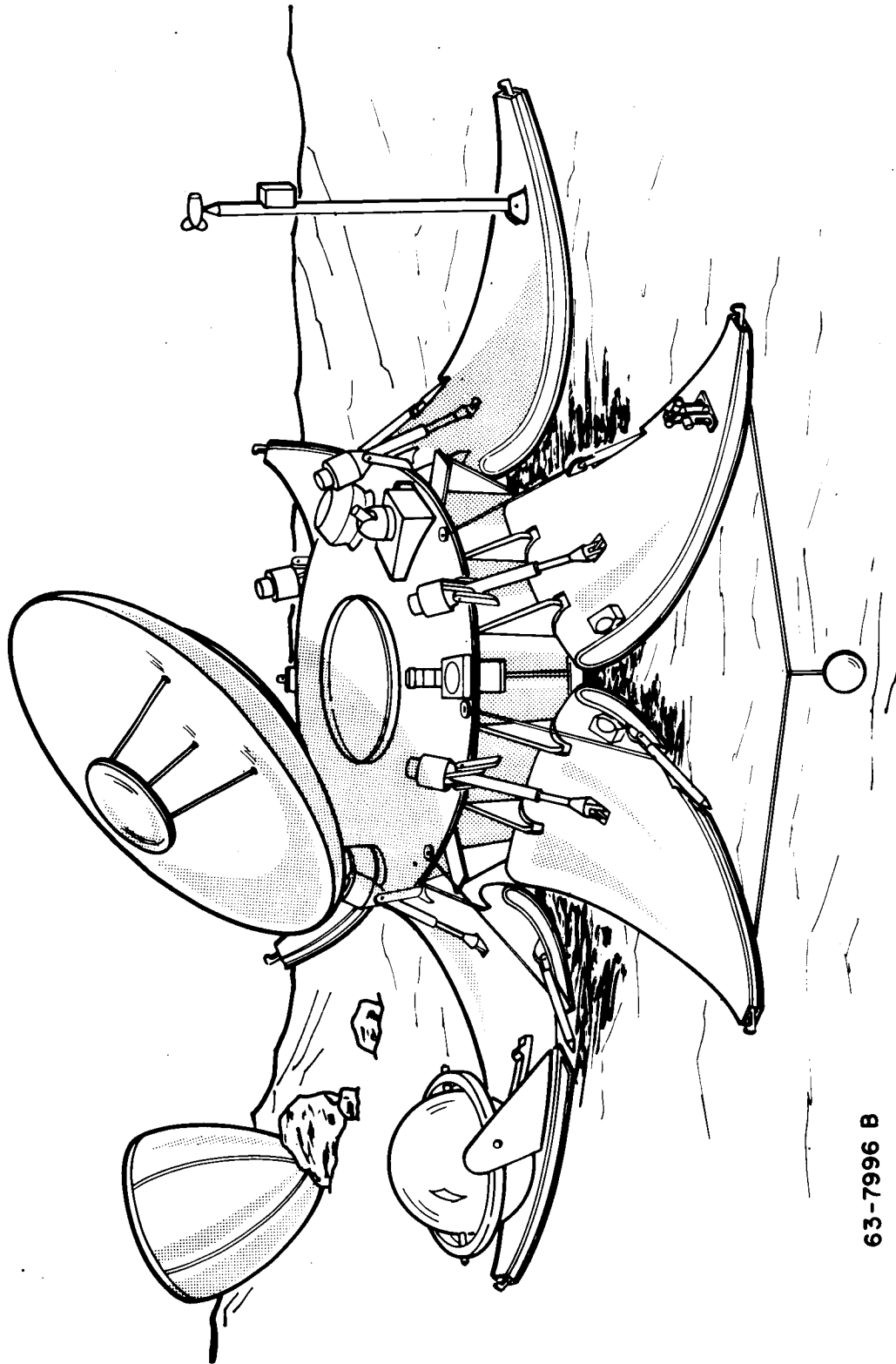


Figure 24 ARTIST'S CONCEPTION OF THE MARS LANDER BEFORE AND AFTER PETAL DEPLOYMENT

63-7996 B

plate to aid in impact load distribution. Local cutouts are provided for the compression struts to the front cap, which in turn bear on the main instrument package. These struts carry the entry inertial loads and prevent the crushup from seeing any load prior to impact.

The parametric study of internal packaging and lander residual weight versus vehicle entry weight showed that the overall vehicle center of gravity moved rearward with decreasing entry vehicle weight, and that for aerodynamic stability there was a minimum entry vehicle weight of about 1000 pounds.

4. Weight summary. The entry vehicle is fabricated of aluminum honeycomb with aluminum inner and outer face sheets. Avcoat 5026 heat shielding material is bonded to the external surface in the thickness required to protect the vehicle.

The reference design has an entry vehicle weight of 1410 pounds, corresponding to an entry vehicle diameter of 6.45 feet, and the total experiment weight of 201.9 pounds. A communications and power supply weight of 456 pounds added to the 302 pounds for package structure, erection system, crushup, planetary navigation and location system, bring the total landed weight, exclusive of main parachute, to 960 pounds. Table 5 shows a complete weight breakdown for the vehicle at Earth liftoff sequentially through the entire mission. Figure 25 shows the external vehicle configuration.

5. Operational sequence. Main and drogue parachutes are packaged within the entry vehicle, but external to the lander. The drogue parachute, in its mortar, is located on the aft end of the vehicle, with its cylinder axis pointing through the vehicle center of gravity. This prevents an overturning or tumbling motion being imparted to the vehicle at mortar firing. Drogue harness lines are in insulated channels from the mortar to the two pickup points on the outer diameter of the vehicle. An insulated cap is also fitted over the outer end of the mortar. At mortar firing and drogue ejection, the cap is pushed out of the way by the drogue, and the harness line covers are jettisoned as the harness becomes taut. The main parachute sits in its container on a shelf between brackets on the outer wall of the entry vehicle and the instrumentation package. The entire main parachute is carried aft with the entry vehicle aft section, due to the drogue's aerodynamic force, when the vehicle separation shaped charge is fired. The parachute riser, attached to a central tiedown at the top of the erection petals, pulls the main parachute lines and then the canopy from the cloth pack, which remains attached to the rear entry vehicle portion.

6. Scientific mission sequence. During the descent phase, atmospheric samples and vertical view television pictures are taken. It is expected that atmospheric temperature, pressure, and composition will be measured, and this data relayed to the oncoming orbiter-bus. The television camera, mounted on the main antenna azimuth scan post, looks down at the ground through a fixed set of optics. The ground view is through a cutout in the load-distributing

TABLE 5

WEIGHT SUMMARY

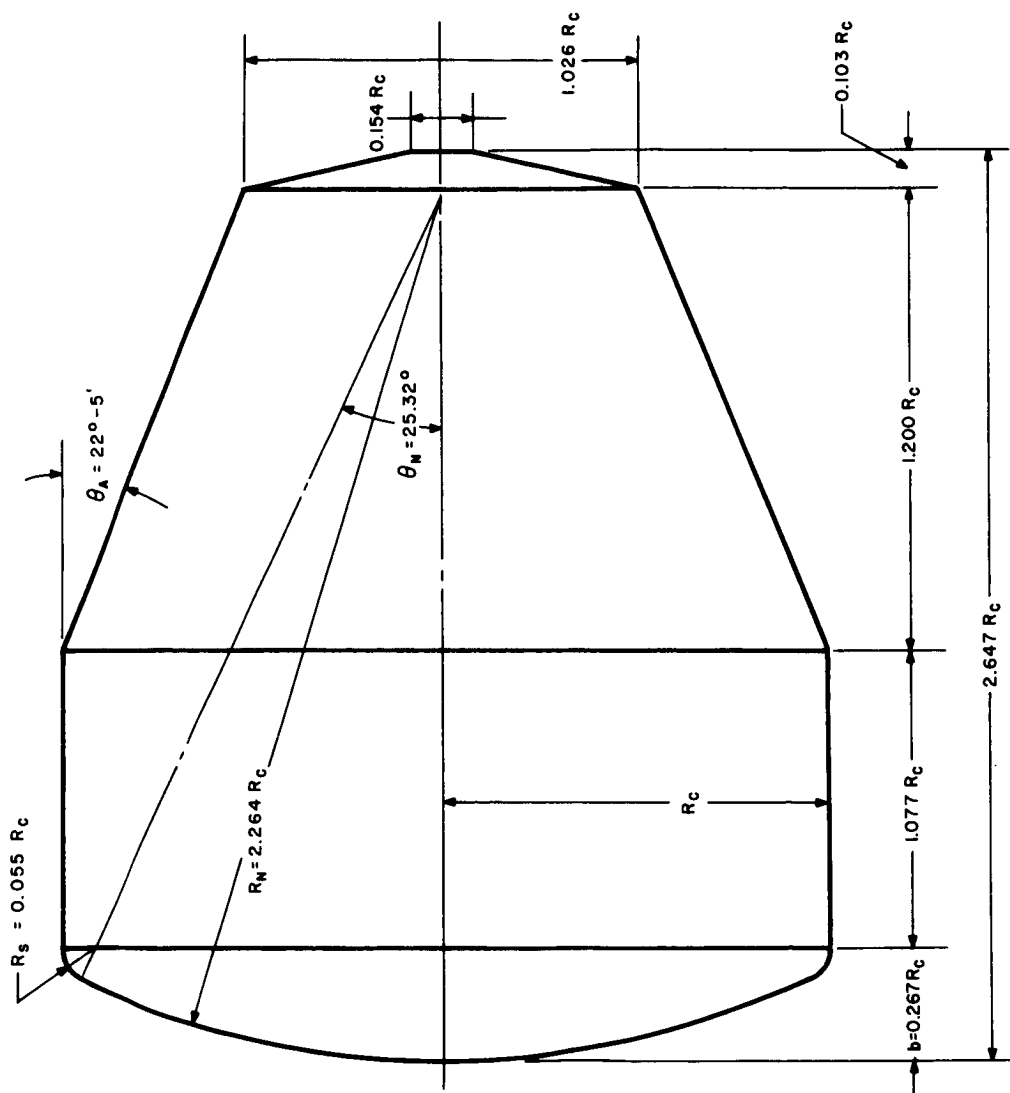
MARS LANDER, REFERENCE DESIGN, SCHILLING ATMOSPHERES--
SELF-ERECTING CONCEPT

$$M/C_D A = 0.9 \quad V_E = 24,000 \text{ ft/sec}$$

		Weight (pounds)	
Total Lander Weight (on Orbiter)			1517.95
Sterilization can and micrometeorite shield		89.	
Aluminum cover sheets and foam metal core			
Spin rocket system			
Four solid rockets at 90 degrees, $\Delta \text{RPM} = 10$.		2.35	
Main propulsion system			
Bipropellant liquid system			
ISP = 315 sec, $\lambda_p = 0.7$, $\Delta V = 100 \text{ ft/sec}$			
Propellant weight (including residuals)		15.9	
Entry Weight (6.43-foot diameter)			1410.7
Heat shield, Avcoat 5026 (0.65 inch on nose cap)		163.0	
$\gamma_E = -20$ deg worst conditions			
Substructure-aluminum honeycomb		135.0	
$\gamma_E = -90$ deg worst conditions			
Heat shield bond - HT-424 bonding compound		49.0	
Drogue chute - HT-1 material - mortar ejection		27.0	
Main propulsion system (dry)		11.0	
Main parachute for 40 ft/sec impact velocity		65.0	
(75.0 foot unloaded dia.)			
(50.0 foot loaded dia.)			
15,000 foot deployment at $M = 0.8$			
Material HT-1			
Landed Weight			960.7
Parachute logic		6.0	
Impact attenuation and payload protection system		61.3	
Aluminum spiral grid crushup pads		14.3	
Petals-lower half aluminum honeycomb		47.0	
-upper half fiberglass honeycomb			
Petal actuation system		44.0	
Ball screw type jacks driven by high speed electric motors			
Internal structure-aluminum sheet metal		130.0	
Navigation system		31.7	
Sun tracker		3	
Computer and power conditioner		28	
Precision frequency reference		0.7	
Miscellaneous		29.3	

TABLE 5 (Concl'd)

		Weight (pounds)	
Residual Weight			658.4
Instruments		201.9	
Camera	17.0		
Pressure	.312		
Density	1.5		
Temperature	.312		
Velocity of Sound	.625		
H ₂ O Detector	1.5		
Anemometer	1.0		
Microphone	.625		
Bio-pack	40.0		
Sun Spectrometer	8.0		
Experiment Cell Growth	4.0		
Gas Chromatograph	7.0		
X-ray Diffractometer	10.0		
Seismograph	34.0		
Experiment Turbidity and pH Growth	4.0		
X-ray Spectrometer	8.0		
Core Drill and Mill	30.0		
Petro Microscope	14.0		
Advanced Mass Spectrometer	20.0		
Communications and Power Supply Equipment		456.5	
VHF Omni Antenna System	6.0		
Parabolic Antenna 5-Foot S-Band Parabola	18.5		
Gimbaled antenna system	10.0		
Antenna Driver Amplifier	5.0		
50w VHF Transmitter	24.0		
Power Amplifier 70w S-Band PA	18.0		
S-Band Transceiver	20.0		
S-Band Command Receiver	14.0		
PCM Command Receiver	11.0		
Low-Speed Recorder	12.0		
High-Speed Recorder	7.0		
Command Decoder	2.0		
Subcarrier Modulator	4.0		
Multiplexer	18.0		
Power Conditioning Equipment	25.0		
Cabling	10.0		
X-Band Altimeter and Antenna	5.0		
110w RTG	55.0		
Battery	192.0		



63-9825

Figure 25 MARS V-2 ENTRY VEHICLE EXTERNAL CONFIGURATION

fiberglass plate beneath the crushup pads. Side-looking pictures between the petals may also be taken during descent, using a mirror and the same optics.

Once landed, as the petals deploy, a three-axis seismograph is deployed by cables attached between the petals' tips. A study of this deployment sequence has shown the capability of putting the seismograph on the ground even though the petal tips may be as much as 2 feet above the local ground contour. The seismograph sensitive elements remain caged throughout the mission until after the deployment sequence has been completed, for protection against shock damage. A separate boom with instrumentation to measure wind velocity and direction as well as a microphone to detect any surface noise, are also deployed at petal opening. On the top of the main instrument box structure, a tracking Sun sensor and Sun spectrometer, with an internal pendulum for vertical sensing, are used to locate the impact site on the planetary surface. Once this has been determined, Earth tracking can be accomplished and the data collection and transmission sequence can be initiated.

Ground specimen samples are ingested into the instrument box by a vacuum system, after being abraded from the surface by a core drill. This unit is located almost centrally in the instrument box (and along the box axis normal to the ground horizontal plane, due to the petal action). An extension capability of about 18 inches below the base of the instrument box is provided, to allow for terrain contour variations. The sample is processed by a pulverizer, then distributed internally to the various experiments. If the petals do not open, or if the final vehicle attitude is such that the central core drill is inoperable, six small sample collector systems have been built into the interpetal spaces. Using the pendulum for information, those systems closest to the ground will be initiated, and samples taken. The remainder of the sequence is as previously described.

1.3 Design Concept for Mars Lander -- Kaplan Atmospheres

The atmospheric model suggested by Kaplan as a minimum for Mars has a sea level density much lower than any of those previously studied. From previous Voyager studies, it has been determined that a greater landed weight may be realized by minimizing descent system weight. This may be done by discarding the external entry vehicle structure and heat shielding material at drogue parachute deployment. Studies conducted included the determination of the largest physical dimensions that could be carried within the Saturn shroud outline. In the normal mounting position, the blunt front cap of the Apollo-type shape is toward the nose of the Saturn. The orbiter-bus is positioned at the aft end of the lander. In this position, a 12.5-foot diameter lander may be packaged. The alternate or inverted mounting position would require a different orbiter design from that now envisioned. If a different orbiter design is incorporated, a 15.5 foot diameter lander could be packaged. As can be seen,

total entry vehicle weights will be limited by the vehicle sizes mentioned, and the aerodynamic performance M/C_{DA} requirements for the low pressure atmosphere.

Figure 26 shows a plot of entry vehicle weight for the Apollo shape versus entry vehicle diameter for M/C_{DA} 's of 0.2 and 0.3 slug/ft.² These values were selected to provide adequate deceleration and descent time prior to impact. Figure 27 shows the heat shield and structural weights as a function of vehicle diameter for M/C_{DA} values of 0.1, 0.2, 0.3 slugs/ft.²

It can be seen from figure 27 that in order to maintain the same lander payload capability as achieved in the Schilling atmosphere, the vehicle performance would have to be $M/C_{DA} \geq 0.3$ slug/ft.² However, trajectory analysis indicate that with this performance level, a Mach 5 or greater light-weight parachute system is required if normal entry is to be permitted. Therefore, restriction of the flight path angle was investigated and it was found that a maximum angle of 45 degrees would permit use of an M/C_{DA} of 0.3 slug/ft.² with a state of the art parachute system.

If a normal entry capability were required from system or reliability aspects, the M/C_{DA} would have to drop to about 0.2 slug/ft.² using state of the art parachute systems, and the maximum entry lander weight would be 1200 pounds using the present spacecraft design. By redesigning the spacecraft, it appears that the necessary vehicle size could be obtained to land the same payload selected for the Schilling atmospheres.

Two sets of data are presented, one based on a nominal entry angle corridor of from -20 to -90 degrees, and the other based on an entry angle corridor restricted to a range of -20 to -45 degrees. With the heat shield and structure weight discarded at drogue parachute deployment, the weights descending during drogue flight, W_{DT} (including the drogue), are shown on figure 28. It may be noted that a considerable increase in W_{DT} may be obtained by going to a higher M/C_{DA} . A tradeoff study between parachute deployment altitude and Mach number, vehicle M/C_{DA} , and required descent time results in a compromise between vehicle performance and parachute system weight.

All vehicles have external entry vehicle structures of aluminum honeycomb, protected by Avcoat 5026 heat shield material. Figure 29 shows a typical low M/C_{DA} packaging arrangement.

Table 6 is a weight summary of a 12.5-foot diameter vehicle. An M/C_{DA} aerodynamic performance parameter of 0.28 slug/ft.² was achieved, landing the same payload as in the Schilling atmosphere case. At an entry angle of -90 degrees, using a Mach 2.5 drogue chute deployment, the main parachute is deployed at slightly above 5000 feet, with a resultant ground level impact velocity of 50 ft/sec. Restriction of the entry angle to -45 degrees, as previously discussed, will enable main chute deployment to take place at an altitude of greater than 15,000 feet.

TABLE 6

WEIGHT SUMMARY

MARS LANDER, REFERENCE DESIGN, KAPLAN MINIMUM ATMOSPHERE--
SELF-ERECTING CONCEPT

$$M/C_D A = 0.28 \quad v_E = 24,000 \text{ ft/sec.}$$

	Weight (pounds)	
Total Lander Weight (On Orbiter)		1976.45
Sterilization can and micrometeorite shield	320	
Aluminum cover sheets and foam metal core		
Spin rocket system		
Four solid rockets at 90 degrees $\Delta \text{RPM} = 10$	3.0	1656.45
Main propulsion system		
Bipropellant liquid system		
$I_{sp} = 315 \text{ sec}$ $\lambda_p = 0.7$, $\Delta v = 100 \text{ ft/sec.}$		
Propellant weight (including Residuals)	18.3	
Entry Weight (12.5-foot diameter)		1635.15
Entry Vehicle Substructure and Heat Shield		
Heat shield, Avcoat 5026 (0.65-inch on nose cap)		
$\gamma_E = -20$ deg worst conditions		
Substructure-aluminum honeycomb		
$\gamma_E = -90$ deg worst conditions		
Heat shield bond - HT -424 bonding compound	491.0	
Drogue chute - HT-1 material - mortar ejection	32.0	
16.5 Foot Diameter		
Main propulsion system (dry)	11.45	
Main parachute for 50 ft/sec. impact velocity	140.0	
(123 feet unloaded dia.)		
(80.0 feet loaded dia.)		
5,000-foot deployment at $M = 0.8$ for $\gamma_E = -90$ deg.		
15,000-foot deployment at $M = 0.8$ for $\gamma_E = -45$ deg.		
Material: HT-1 Textile		
Landed Weight ¹		960.7

1. Same As Reference Design For Schilling Atmospheres -- See table 5.

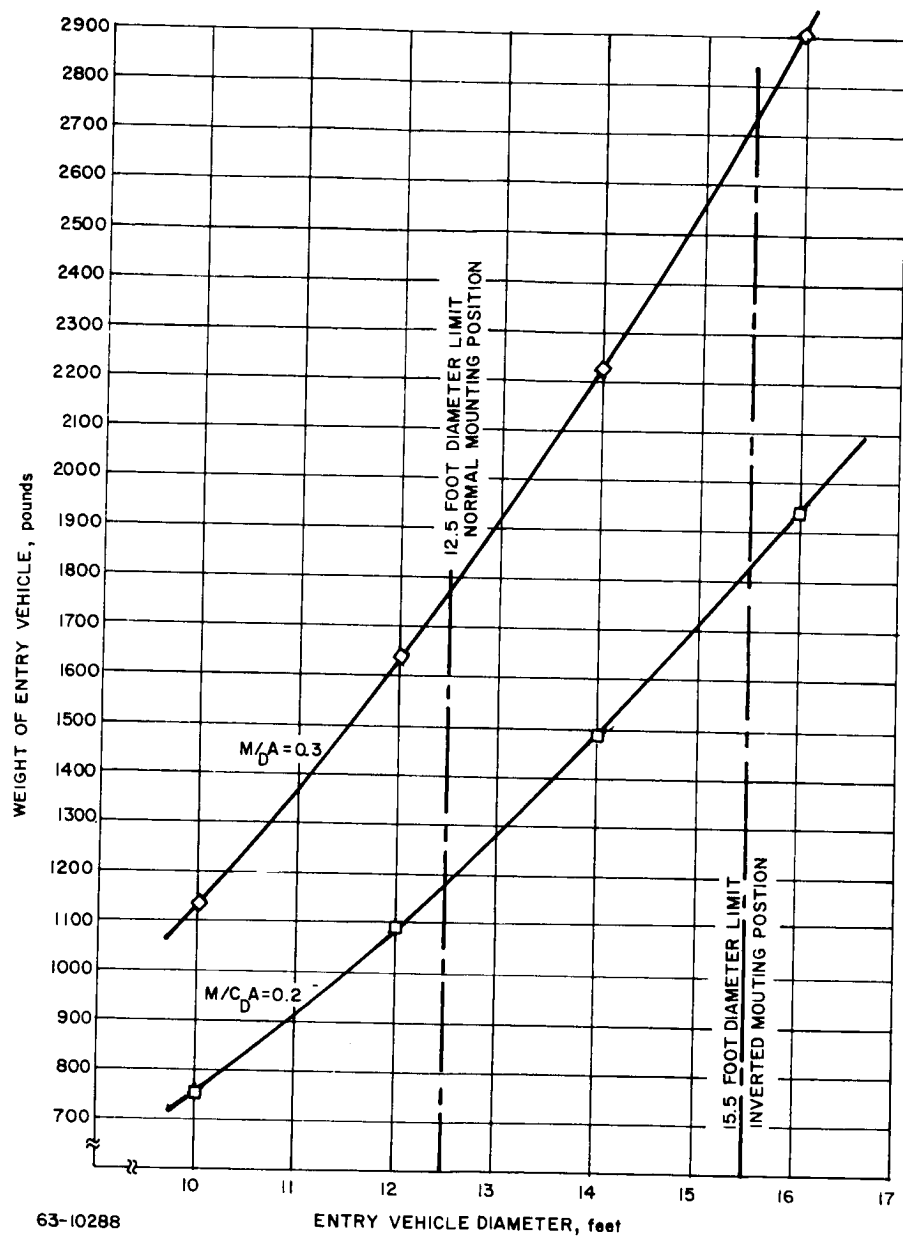


Figure 26 WEIGHT VERSUS DIAMETER FOR MASS LANDER JPL MINIMUM ATMOSPHERE APOLLO SHAPE

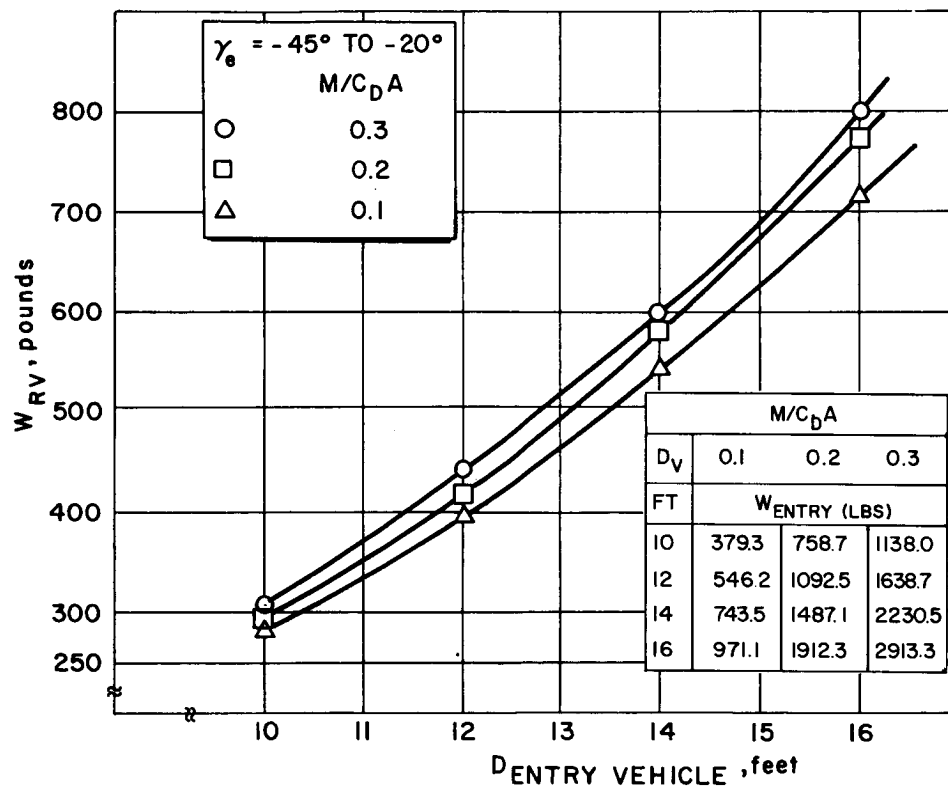
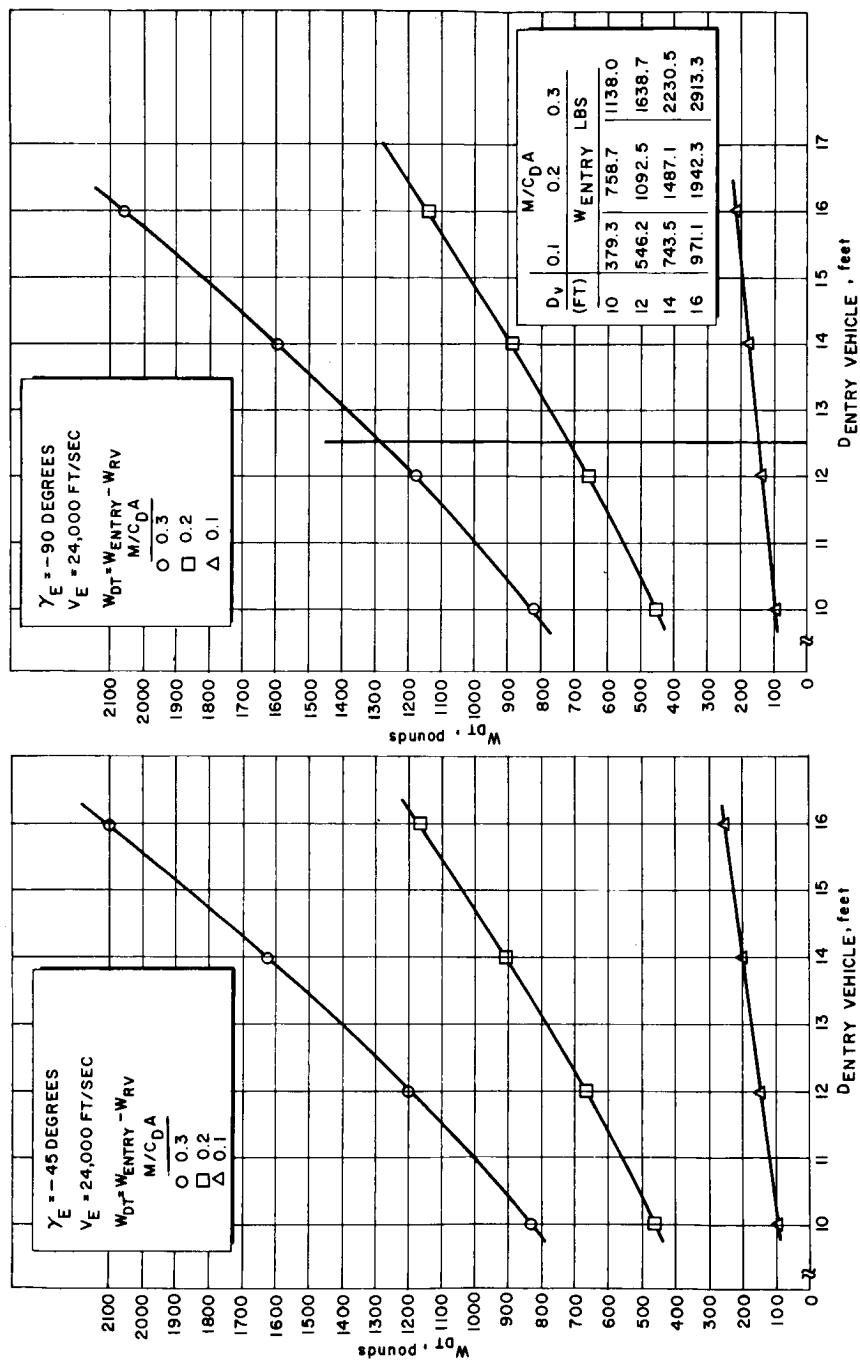


Figure 27 WEIGHT VERSUS DIAMETER FOR MASS LANDER JPL MINIMUM ATMOSPHERE ALUMINUM HONEYCOMB STRUCTURE



63-10261

Figure 28 WEIGHT VERSUS DIAMETER FOR MASS LANDER JPL MINIMUM ATMOSPHERE
ALUMINUM HONEYCOMB STRUCTURE

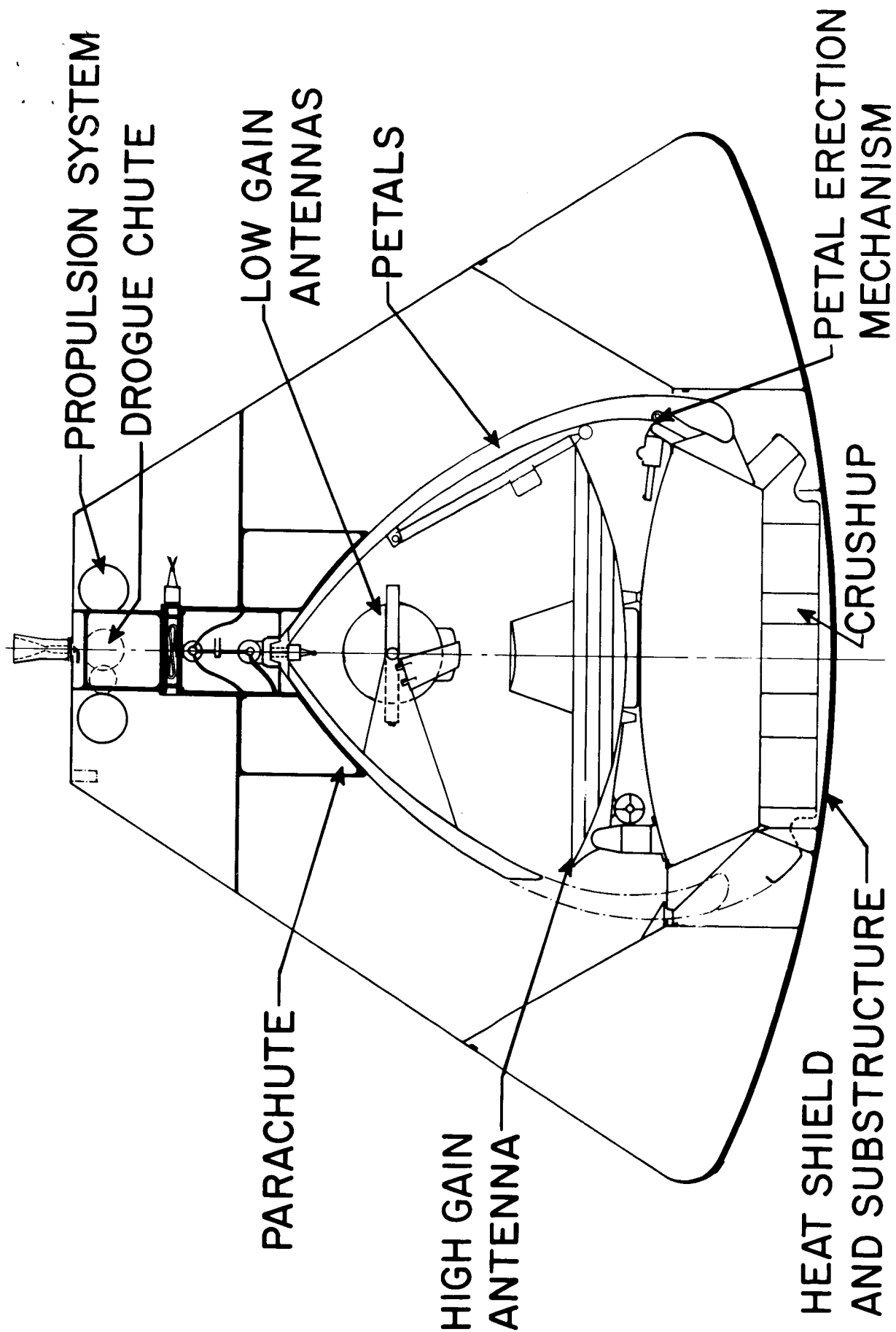


Figure 29 MARS LANDER--KAPLAN ATMOSPHERE

2. DESCENT AND LANDING SYSTEMS

2.1 Parachute System

1. System requirements. This section defines a parachute descent system to fulfill lander retardation requirements. The system outlined herein is a result of studies by Avco RAD and Northrop Ventura Division. A summary of the Northrop Ventura study is given in appendix A. Voyager system requirements which have been considered in the selection of the descent system include:

a. Minimum descent time. Atmospheric measurement and communication requirements dictate a minimum descent time during which data can be recorded and transmitted. This minimum descent time must be obtainable for a "worst" combination of entry conditions and atmospheric model.

b. Descent time variations. A communications relay of information during parachute descent to an orbiter passing overhead requires that the maximum possible time to impact not be excessive.

c. Impact velocities. The impact velocity must be limited so that design landing loads are not exceeded.

d. System weights. The parachute and actuation system directly affects the selection of the lander ballistic coefficient (M/C_{DA}). Since the available payload weight is a function of ballistic coefficient, the payload weight can also be considered a function of the descent system choice.

The entry conditions investigated include an entry angle range of -20 to -90 degrees and entry velocities up to 29,000 ft/sec. The atmospheric models considered are those shown in table 8 (section 32). The state of the art parachute technology, the sensing system for the parachute actuation, the resulting parachute system performance, and the detailed design of the system will be discussed in the following sections.

2. Parachute technology and constraints.

a. Mach number limits. No approach to the retardation function possesses the simplicity and, therefore, potential reliability that is provided by a blunt supersonically stable vehicle having sufficient drag area without augmentation to reach subsonic equilibrium velocity prior to surface impact. Earth landing systems for current manned spacecraft (Mercury, Gemini, and Apollo) are based on this principle of dissipating most of the vehicle's kinetic energy in the ablative heat shield. The remaining function of the retardation system, then, is to provide vehicle stability through the transonic speed range of deceleration

and a terminal descent speed to the planet's surface compatible with atmosphere sampling and data transmitting requirements in addition to touchdown system constraints.

The present state of the art in landing technology is defined by the inner envelope of figure 30 which shows, in a general sense, an initiation limit of Mach 2.5 for parachute systems. Systems are being designed today which will provide highly reliable (man-rated) performance within the Earth's atmosphere with a high confidence level. The use of Mach 2.5 as a limitation represents a designation of convenience, since recent development (ref. 2) of high-speed deployable drag devices has demonstrated effective and stable performance at speeds higher than Mach 2.5. The true limitation appears to be aerodynamic heating, and an increase in availability of lightweight, flexible materials capable of good strength at elevated temperatures should be accompanied by an increase in the limit velocity associated with successful deployment and performance of parachutes. Temperature strength characteristics of nylon and dacron limit today's drogue parachute designs to speeds of Mach 2.5.

Effective advancement in the state of the art is being accomplished in current programs of the Air Force Aeronautical Systems Division (ASD) and industry to produce higher temperature textile materials and the high-speed deployable drag devices to use them. Progress with HT-1 and the Hyperflo parachute indicates that the drogue initiation limit may advance to the region of Mach 4 or better in the near future.

Five years of effort have gone into the development of the organic fiber HT-1 by Dupont and the Air Force. Figure 31 shows comparative strength versus temperature characteristics of various candidate organic fibers. At present, HT-1 yarns (100 and 200 denier) are produced in limited quantity and used for experimental and special applications only. Quantity production will be started next year by Dupont, assuring its availability within the Voyager time scale.

A newer organic material called PBI which possesses better temperature resistant characteristics (900°F) than HT-1, although lower tensile strength, is being developed by ASD into a fiber suitable for parachute textiles. PBI development is 5 years behind HT-1, according to ASD, and will not be available in time for initial Voyager systems development.

Metallic fabrics have been produced in small quantities from drawn fibers (0.5 to 0.7 mil) of Rene and Chromel alloys (1800°F). Without proper mill facilities and special tooling for weaving, metallic fabrics are very expensive.

Drogue parachutes constructed of HT-1 materials have been designed and tested successfully at speeds above Mach 2.5. The Hyperflo, a relatively new design under development, has demonstrated good performance up to Mach 4 in free-flight tests (ref. 3). A drogue device developed for ASD called the Ballute

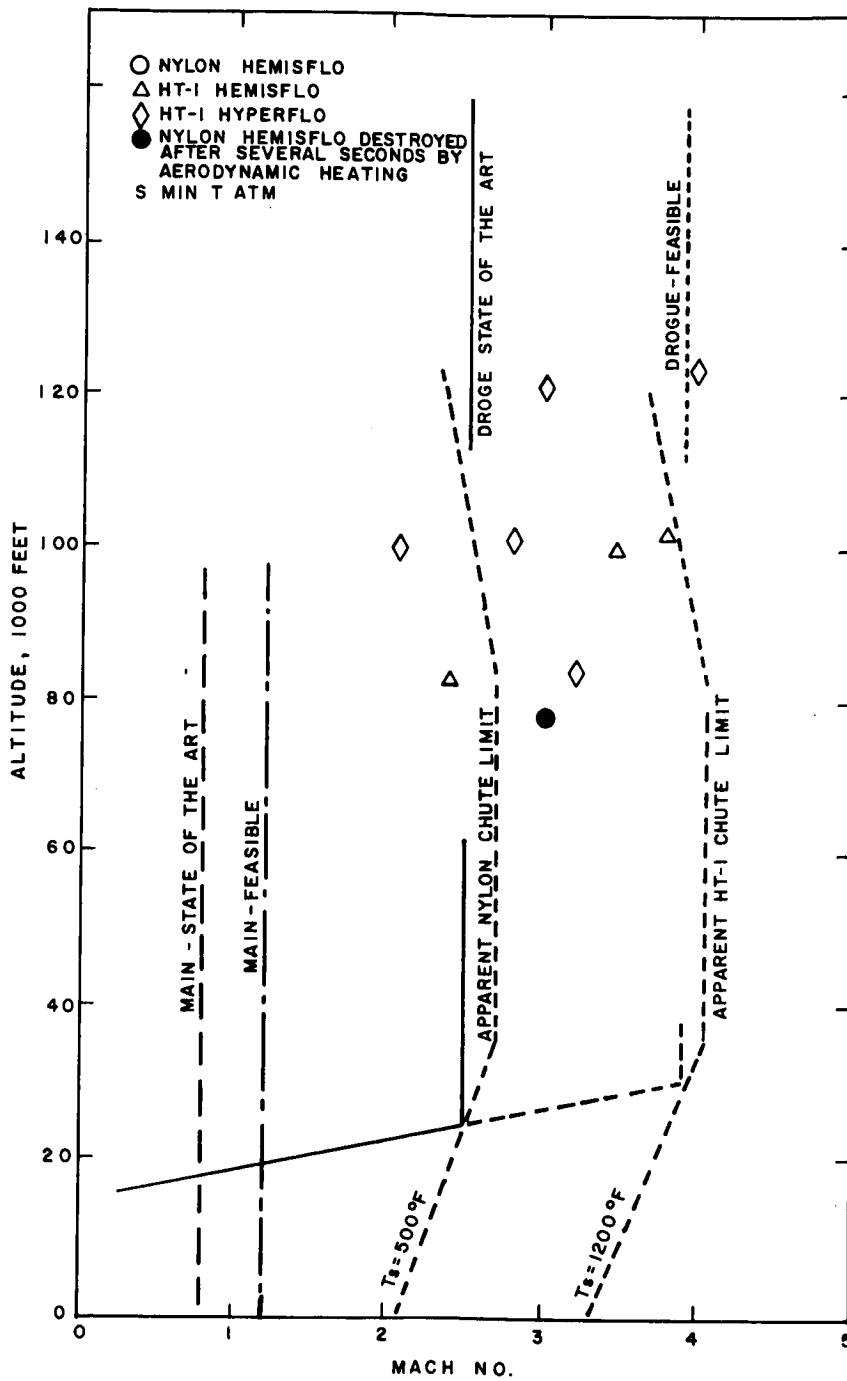


Figure 30 PARACHUTE PERFORMANCE ENVELOPE AND INITIATION LIMITS

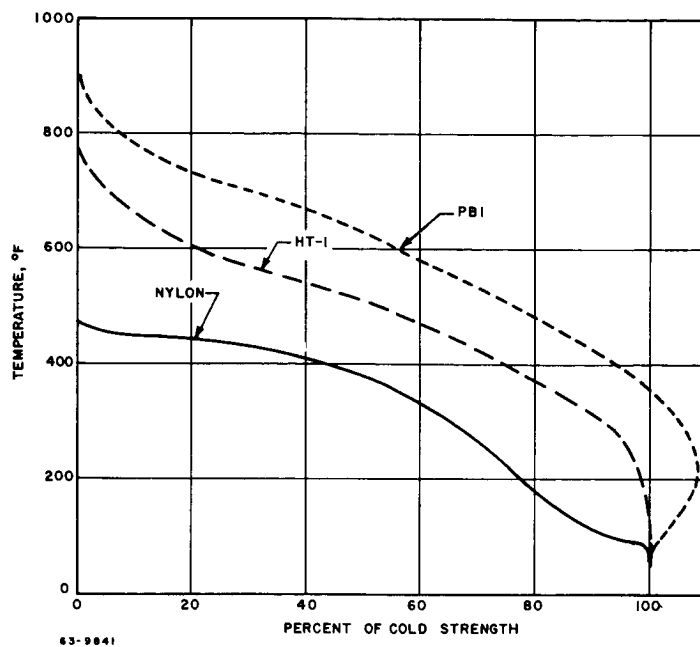


Figure 31a TEMPERATURE CHARACTERISTICS OF ORGANIC FIBERS FOR PARACHUTE FABRICS

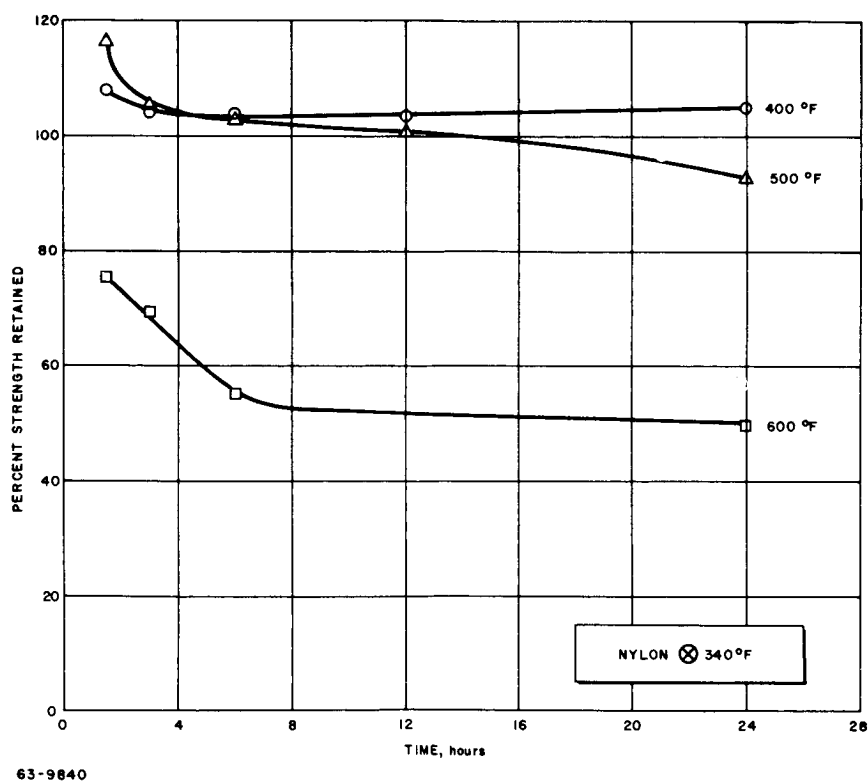


Figure 31b PERCENT STRENGTH RETAINED VERSUS EXPOSURE TIME AT VARIOUS TEMPERATURES FOR MIL-T-5038 TYPE IV HT-1 FABRIC

has been successfully fabricated from silicone ceramic elastomer coated metal fabrics and tested in the wind tunnel to Mach 10. The Air Force has initiated a new program to continue the development and evaluation of the Ballute, Hyperflo and other supersonic drogue parachutes during the next 2 years.

To illustrate the apparent deployment limit of nylon parachutes and the probable limit of HT-1 parachutes, figure 30 shows lines representing a calculable stagnation temperature of 500 and 1200 °F in relation to actual data points from recent tests which represent successful performance up to failure from aerodynamic heating. An allowable velocity, above which equilibrium temperature experienced by the parachute reaches design limits is conservatively approximated by these tentative limits.

b. Environmental limits. The parachute must withstand certain environmental conditions and still be completely effective. Initially, the material must be sterilized at temperatures up to at least 135 °C for times up to 24 hours or more. Then, it must withstand a vacuum environment, although this is not critical as the lander will contain some inert gas. The flight temperature will be controlled by the thermal control system of the lander, and is not a serious problem. Radiation effects need not be considered because the parachute will be enclosed within the sterilization can. Even if exposed, the proposed material is quite stable to ultraviolet irradiation (ref. 2). Tensile strength and elongation at break fell only slightly after exposure to a G30T8 low-pressure mercury arc lamp for times up to 120 hours. The effect of various atmospheres, including nitrogen, oxygen, and high vacuum (10^{-6} mm Hg), was negligible.

The proposed Mars parachute material is HT-1, a recently developed polymer that is essentially an aromatic polyamide. Nylon is the standard parachute material, but nylon possesses very marginal physical properties after thermal aging. For example, nylon loses all strength at 370 °F, and melts at approximately 400 °F. Figure 30 shows the excellent strength retention of HT-1 fabric after exposure to elevated temperatures in an air atmosphere (ref. 3). It can be seen that aging at 400 °F actually increases the tensile strength. A nylon fabric of the same type as the HT-1 fabric retained only 10 percent of its original strength after 24 hours aging at only 340 °F (fig. 31b).

HT-1 fiber is still a developmental fiber, and is not generally available on a commercial scale. However, it should be available in large quantities soon, depending on the demand. No major difficulties are encountered in fabricating fabrics from the HT-1 fibers, and fabrics similar to standard nylon parachute cloth can be readily made (ref. 4).

3. Sensing for parachute actuation.

a. Vehicle M/C_DA and the sensing system. The parachute actuation sensing method and the desired deployment altitude are two major variables in

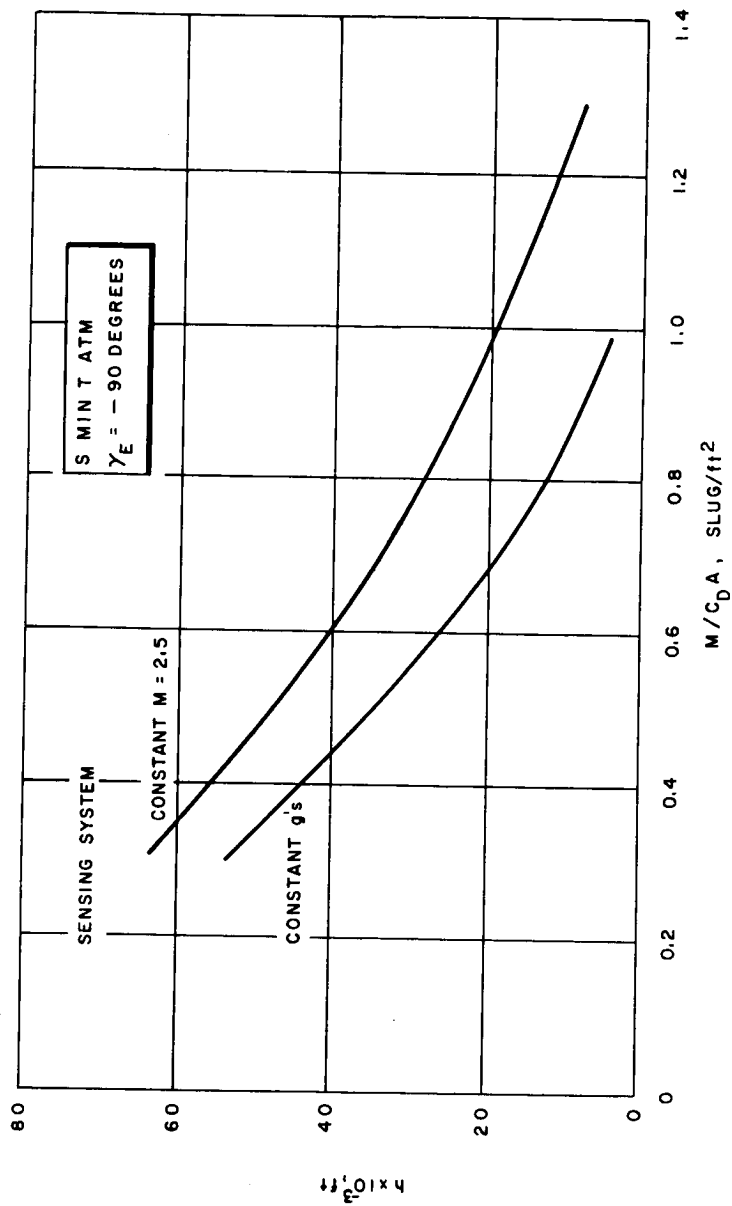
the determination of the vehicle ballistic coefficient. Figure 32 presents drogue chute deployment altitude as a function of vehicle M/C_{DA} for a "worst" combination of entry conditions and atmospheric model ($\gamma_E = -90$ degrees and Schilling's minimum temperature atmosphere). The two methods of actuation which are compared are: 1) a single setting axial accelerometer, and 2) a method which deploys the chute at a constant Mach number of 2.5. The single setting accelerometer is set such that, for any combination of entry conditions, the deployment Mach number is not greater than 2.5. To deploy the drogue chute at an altitude of approximately 25,000 feet (this deployment altitude is necessary to enable a larger main parachute to deploy in the vicinity of 20,000 feet) with a single setting accelerometer, the vehicle M/C_{DA} must be limited to 0.6 slug/ft². A drogue deployment at a constant Mach number of 2.5, however, allows a M/C_{DA} of 0.9 slug/ft². The feasibility of constant Mach number deployment was investigated and then selected due, primarily, to a 25 percent increase in available payload weight with the M/C_{DA} increase.

The possible entry trajectories for the lander with $M/C_{DA} = 0.9$ slug/ft² are presented in figure 33 indicating the effect of entry angle and atmospheric model variation. The drogue chute will then be deployed approximately at a constant Mach number of 2.5 which, as mentioned, places the least severe limitation on M/C_{DA} and also ensures improved dynamic characteristics throughout the low supersonic and transonic Mach number range. The larger main chute will deploy at a constant altitude to avoid the problem of possible excessive descent times.

b. Sensing for drogue actuation. The selection of a sensing system for a Mars lander parachute actuation presents a difficult problem due to the range of entry conditions and atmospheric models considered. The sensing system must be capable of deploying a parachute at an acceptable altitude for a "worst" combination of entry angle and model atmosphere. Another consideration is the fact that high vehicle M/C_{DA} is desirable due to higher available payload weights. Thus, it would be reasonable to maximize the "minimum" deployment altitude for a given vehicle to place the least restriction on M/C_{DA} . Also, a drogue chute which deploys at Mach number greater than 1.5 is preferred to provide stabilization through the transonic range.

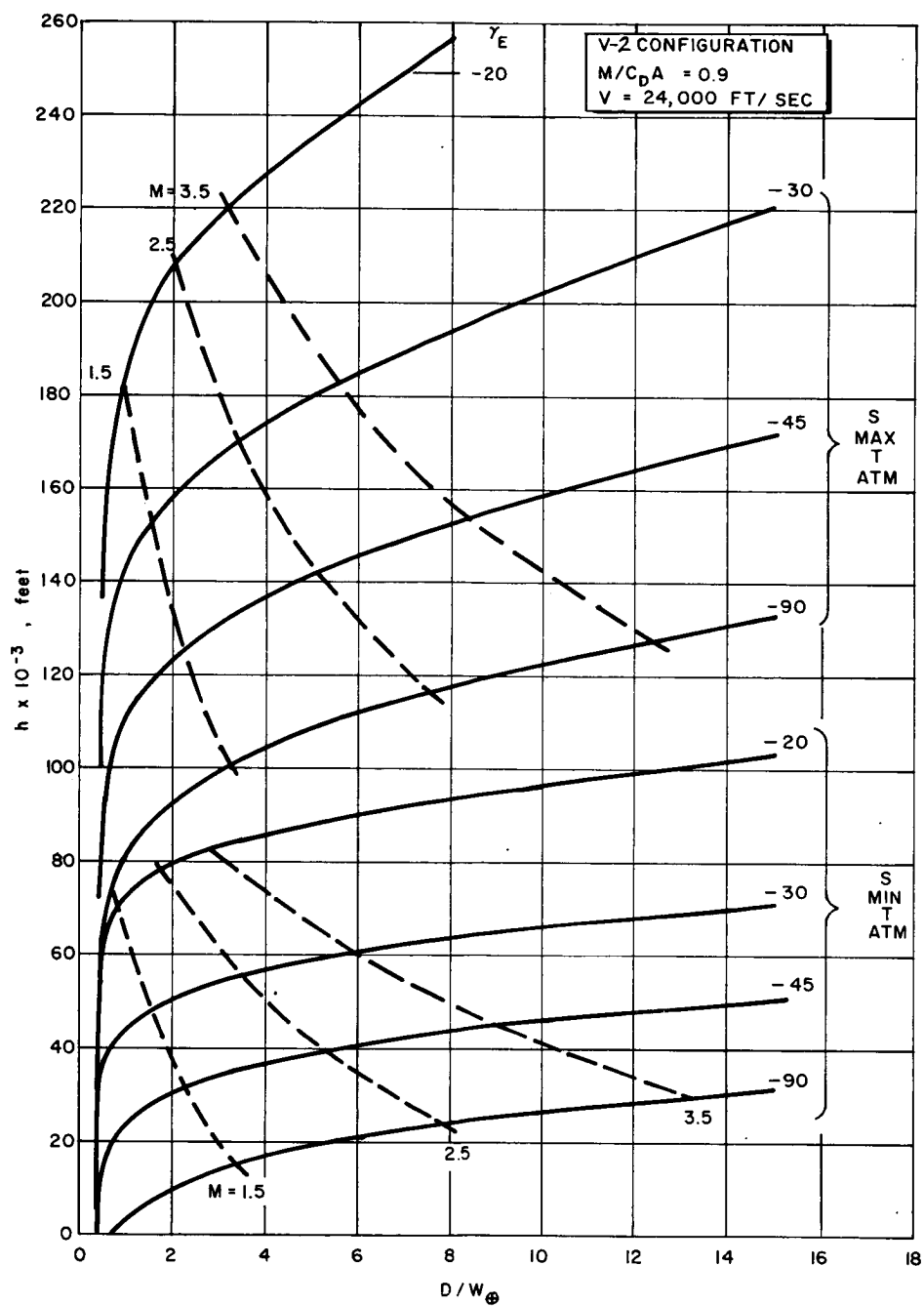
Various sensing method possibilities for the drogue actuation have been investigated and are briefly discussed below. For comparative and illustrative purposes, the vehicle M/C_{DA} is assumed equal to 0.9 slug/ft², the maximum Mach number for drogue deployment is 2.5, dynamic pressure and wake temperature are not assumed critical at deployment, and the atmospheric model is that specified by Schilling's Model II. Figure 34 presents the range of possible entry trajectories as a function of deceleration g 's illustrating the effect of entry angle and atmospheric model variation on Mach number and altitude.

1) Baroswitch. The measured pressure at some point on an entry body can be correlated with experimental data and used to estimate the atmospheric ambient pressure. Utilizing this type of sensing, the parachute deployment



63-9839

Figure 32 TYPICAL DROGUE DEPLOYMENT ALTITUDE VERSUS VEHICLE M/C_{DA}



63-9838

Figure 33 ALTITUDE VERSUS AXIAL DECELERATION FOR LANDER ENTRY

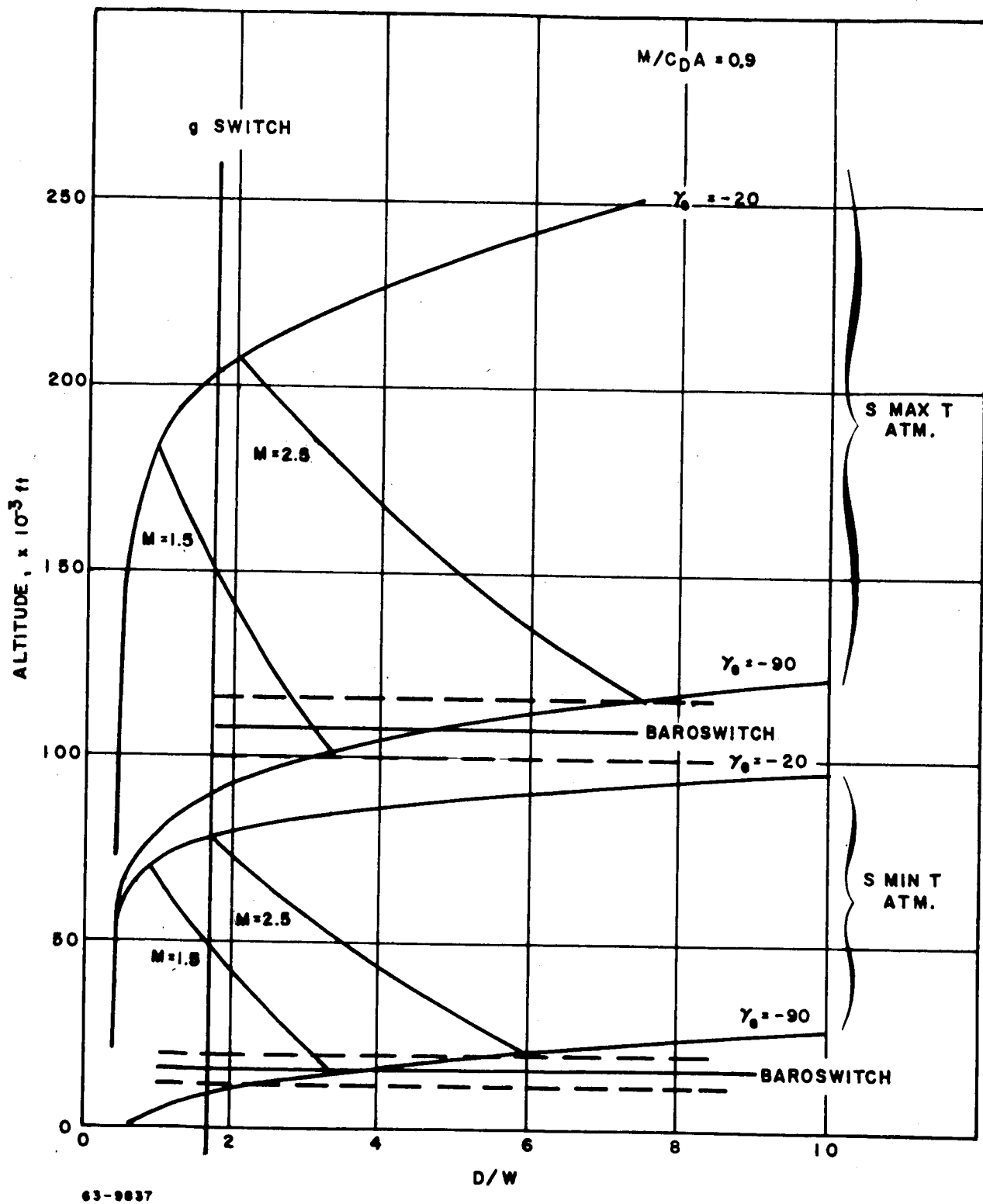


Figure 34 METHODS OF SENSING FOR DROGUE CHUTE DEPLOYMENT

would occur at a constant altitude which would depend on the atmospheric model, experimental simulation accuracy, and the pressure sensing system tolerances. Figure 34 indicates the results of baroswitch sensing with a very optimistic assumption of $\pm 5 \text{ lb/ft}^2$ accuracy in determination of the ambient pressure. The nominal baroswitch setting is represented with a solid line and the effects of the $\pm 5 \text{ lb/ft}^2$ tolerance are indicated with dashed lines.

The baroswitch is set so that the assumed limiting Mach number of 2.5 would not be exceeded in either model atmosphere for the specified sensing system tolerance. The deployment altitudes in each of the two limiting atmospheric models for the same baroswitch setting are indicated. It should be noted that it is only coincidence in this case that the same setting allows a maximum deployment Mach number of 2.5 for the $\gamma_E = 90$ degree entry in both atmospheres. In general, the atmospheric model variation would have to be considered when determining the baroswitch setting.

Considering first the "worst" case of $\gamma_E = 90$ degrees in the "S Min T" atmosphere the sensing tolerance of $\pm 5 \text{ lb/ft}^2$ is shown to allow a deployment altitude variation of approximately 8000 feet. This variation does not allow a deployment at $M \geq 1.5$ for all cases and could possibly result in unacceptable dynamic characteristics. Shallow entry angles also present the same problem in violating the minimum Mach number requirement for deployment.

2) Axial accelerometer. A g switch or axial accelerometer which is set before launch is a simple and common means of sensing for actuation. However, the system has disadvantages for the range of entry angles and atmospheric models under consideration. Also illustrated in figure 34 is the use of an accelerometer. The g switch setting for deployment is determined by the limiting Mach number on a minimum entry angle trajectory, as shown. For steeper entry angles, the deployment occurs at altitudes significantly lower than those allowed by parachute technology. The possible large Mach number variation with this method would again present a possibility of deployment at Mach numbers lower than 1.5.

3) Accelerometer and baroswitch combination. The problem of deployment at low Mach numbers would still be present for this combination but would be relieved somewhat as illustrated in figure 34. Both the baroswitch and accelerometer would be set to avoid deployment above a limiting Mach number for any atmospheric model; the drogue would then be deployed when either of the two settings had been satisfied. The possibility of large minimum deployment altitude variation is still present due to the baroswitch tolerances.

4) Constant Mach number deployment. If a drogue chute could be deployed near the specified limiting Mach number, several definite advantages would be gained. First, the problem of possible deployment at low Mach numbers when the vehicle has begun to tumble would be eliminated. Secondly, for a worst combination of entry angle and atmospheric model, the minimum

deployment altitude would be maximized. Thus, this system would place the least restriction on the vehicle ballistic coefficient. Several methods which would enable approximately constant Mach number deployment are:

a) Integrating accelerometer. When the initial entry velocity is known, an integrating accelerometer may be used to determine the velocity history which, coupled with atmospheric model knowledge, would enable deployment at constant Mach number. It appears at this time, however, that the accuracies required after deceleration from 24,000 ft/sec to approximately 3000 ft/sec are not available with this approach.

b) Radar altimeter. Utilizing the doppler effect, a radar altimeter could theoretically be used for determination of the vehicle velocity. The major drawback to this scheme is the possible vehicle oscillatory and spinning motion which would make interpretation of the signal return difficult.

c) Mach number = $f(D/W_0, \gamma_F)$. With knowledge of the vehicle flight path angle, the drogue can be deployed at approximately a constant Mach number with the use of a variable setting accelerometer. This is the method selected.

The entry angle knowledge can be acquired with Earth-based measurements of the vehicle velocity and range before entry. A radar altimeter could possibly be used for the determination of the entry angle if there were no possibility of vehicle initial tumbling and spinning motion.

c. Reference drogue actuation system. A variable setting axial accelerometer was selected for sensing to actuate the drogue chute at a nominal Mach number of 2.5. The variables required to determine the correct accelerometer setting are the entry angle and the entry velocity (see figure 35). These entry conditions can be predicted within reasonable accuracy with Earth-based velocity and range measurements of the spacecraft (orbiter and lander combination). Since the entry velocity can be estimated to within ± 500 ft/sec and the accelerometer settings as shown in figure 35 are insensitive to changes of this magnitude, the predicted entry velocity will be used without considering accuracy. A typical accuracy to which entry angle is known when the spacecraft is approaching the planet is represented in figure 36. With the predicted nominal entry conditions and estimated accuracies, an accelerometer setting can be determined as shown below, such that the drogue chute does not nominally deploy above a Mach number of 2.5.

Although entry condition predictions do not give drogue deployment nominally above $M = 2.5$, there are other factors which must be considered. For a typical entry trajectory, the Mach number at a given value of deployment D/W setting (decreasing deceleration) is also a slight function of atmospheric model, any possible vehicle angle of attack, and accelerometer tolerances. Figure 37

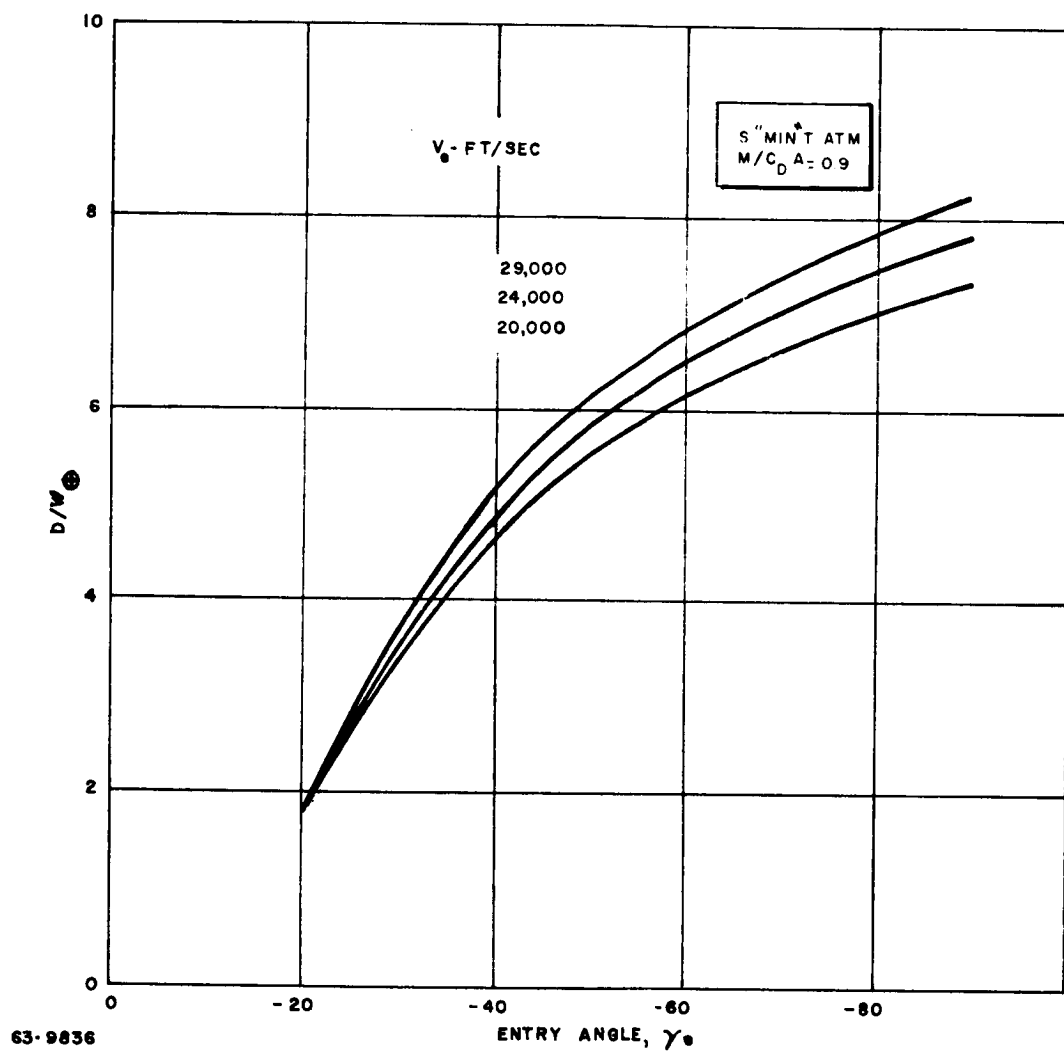
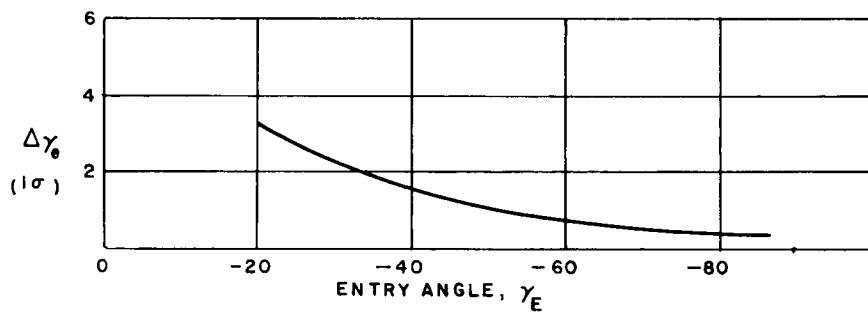
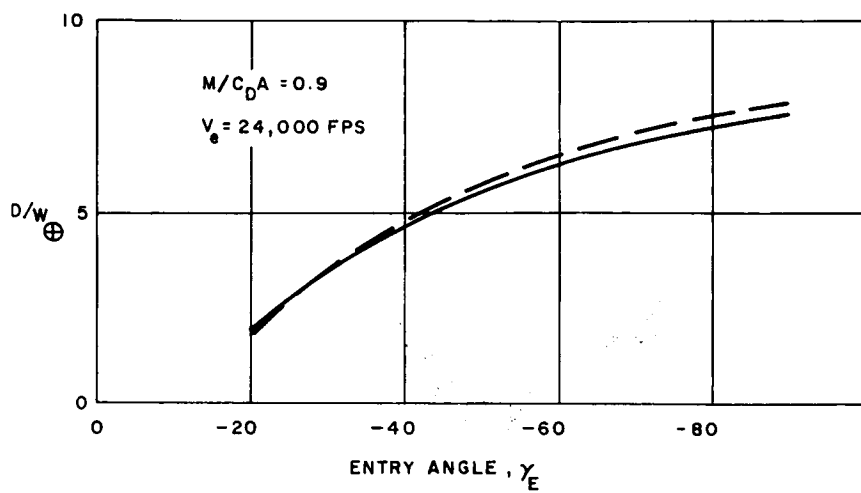
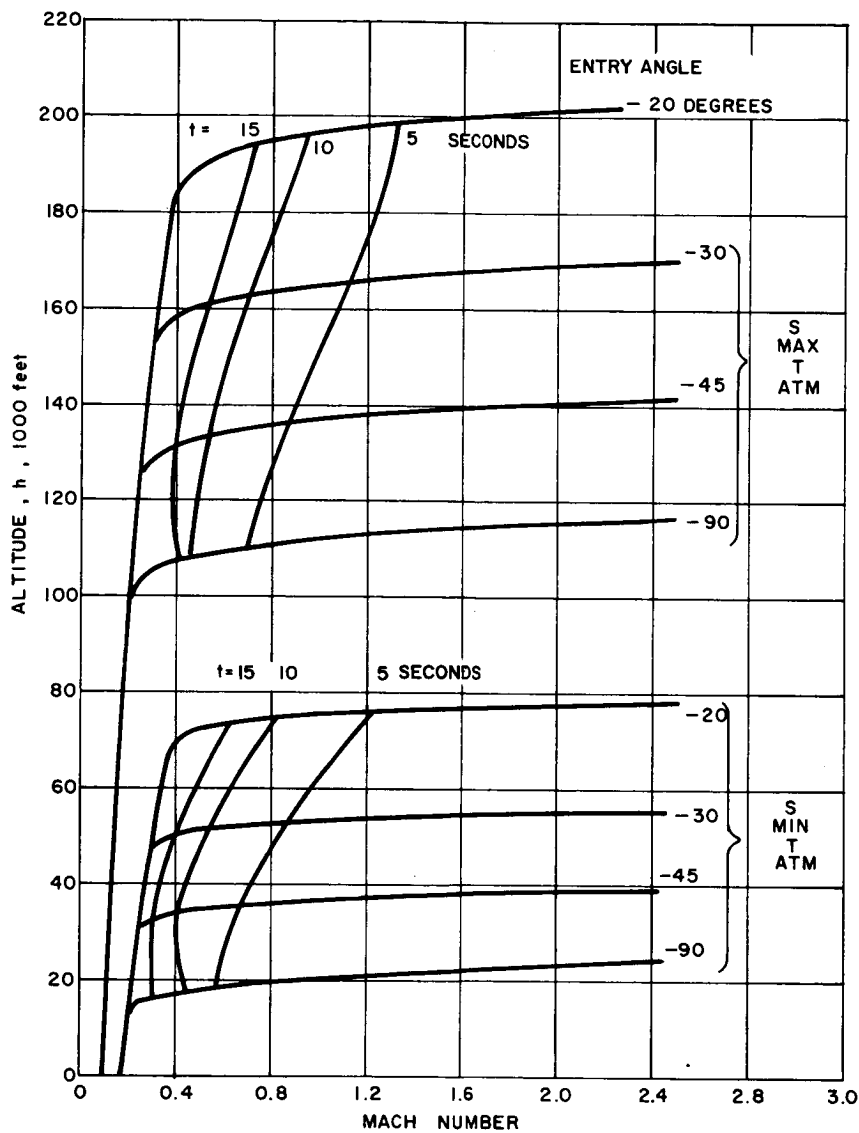


Figure 35 EFFECT OF VELOCITY AND ENTRY ANGLE VARIATION ON DROGUE ACTUATION



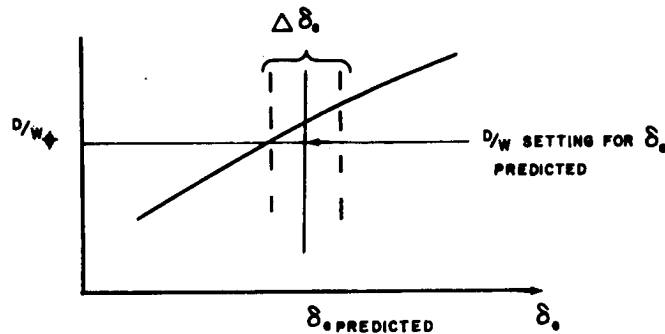
63-9835

Figure 36 EFFECT OF ATMOSPHERIC MODEL D/W FOR $M = 2.5$ VERSUS ENTRY ANGLE



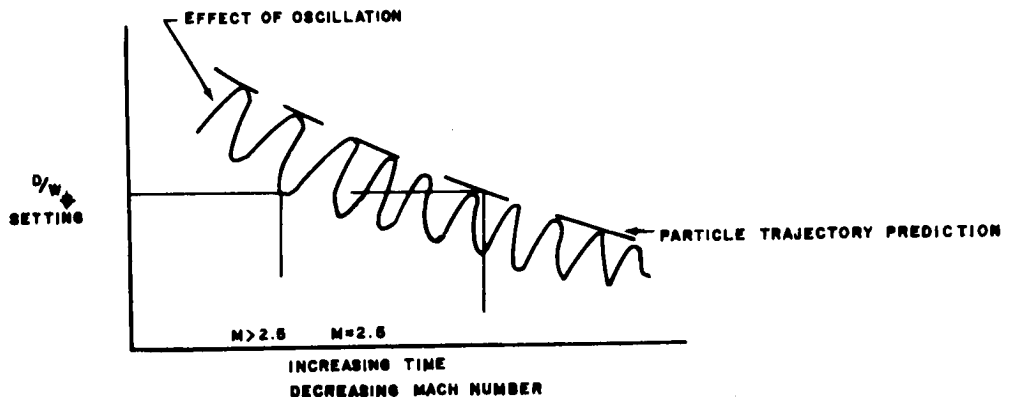
63-9834

Figure 37 ALTITUDE VERSUS MACH NUMBER FOR TYPICAL VOYAGER LANDER DROGUE FLIGHT



63-10292

indicates a maximum variation in D/W of 0.4 g for $M = 2.5$ due to atmospheric model variation. Also, the vehicle maximum angle of attack at parachute deployment can be as great as approximately 30 degrees with the axial force reduction being 15 percent. The measured D/W is then reduced by the same percentage resulting in possible deployment at Mach numbers greater than 2.5, as illustrated below.



63-10293

The above mentioned effects, combined with an accelerometer tolerance of ± 0.5 g can possibly produce a parachute deployment at Mach numbers approaching 3.0. As explained earlier, this would be acceptable since recent tests have proven the feasibility of higher Mach number deployment.

When the predicted nominal entry conditions and estimated prediction accuracies have been calculated on Earth, the correct accelerometer setting would then be determined with the information being sent to the lander by command.

The drogue actuation system is armed during increasing D/W as the lander begins to enter. The mortar used to eject the drogue is then fired when the decreasing deceleration reaches the correct accelerometer setting.

A backup for the drogue deployment is achieved by presetting the accelerometer before launch such that, if no commands are received from Earth, the drogue and main chute will still deploy. For a worst combination of entry conditions and atmosphere, the drogue deployment would occur at a low altitude (9000 feet) but still in sufficient time to allow the main chute to deploy and enable the lander to survive impact.

d. Main parachute actuation. The main parachute will be deployed at a constant altitude with the use of a radar altimeter and a timer initiated at drogue deployment. Possible drogue flight trajectories for a given drogue system are indicated in figure 38. The altimeter and timer will be set such that the main chute will not deploy at a Mach number greater than 0.8. Thus, if a main chute deployment is desired at 20,000 feet, the altimeter switch will be set at 20,000 feet, and the timer will be set at ~10 seconds for the system shown in figure 38. If the vehicle does not decelerate to $M = 0.8$ by 20,000 feet, the time requirement will not allow the main chute deployment until the vehicle reaches the correct Mach number at a lower altitude. There is only a very limited range of entry conditions and atmosphere combinations for which the main chute cannot be deployed at 20,000 feet, with the minimum deployment altitude being 15,000 feet.

If a main chute deployment at higher altitudes is desired, the altimeter switch setting is simply changed to the appropriate altitude. The range of conditions which requires lower deployment altitudes is then expanded as a function of the desired altitude. The parachute performance which is presented in later paragraphs assumes a desired main chute deployment altitude of 20,000 feet.

The timer switch, which can be easily provided in duplicate, acts as a backup for the altimeter and timer combination. A sensing device will determine if the altimeter is functioning after the entry heating pulse. If the altimeter is not operating properly, the main chute is then deployed with the timer alone. Thus, the Mach number of 0.8 is not exceeded by the main chute but the deployment then can occur at higher altitudes.

4. Parachute system performance.

a. Selected reference system. The parachute deployment altitudes and descent times for the selected system have been determined. For the purposes of obtaining descent time variations, the effect of the atmospheric model variation on the drogue deployment accelerometer setting was considered, but the variable effects of entry angle prediction accuracy, vehicle angle of attack, and accelerometer tolerances were neglected. Inclusion of the neglected effects would not significantly change the presented results and trends.

The entry angle is a major variable in the determination of deployment altitudes and descent times, but an entry velocity variation is shown in figure

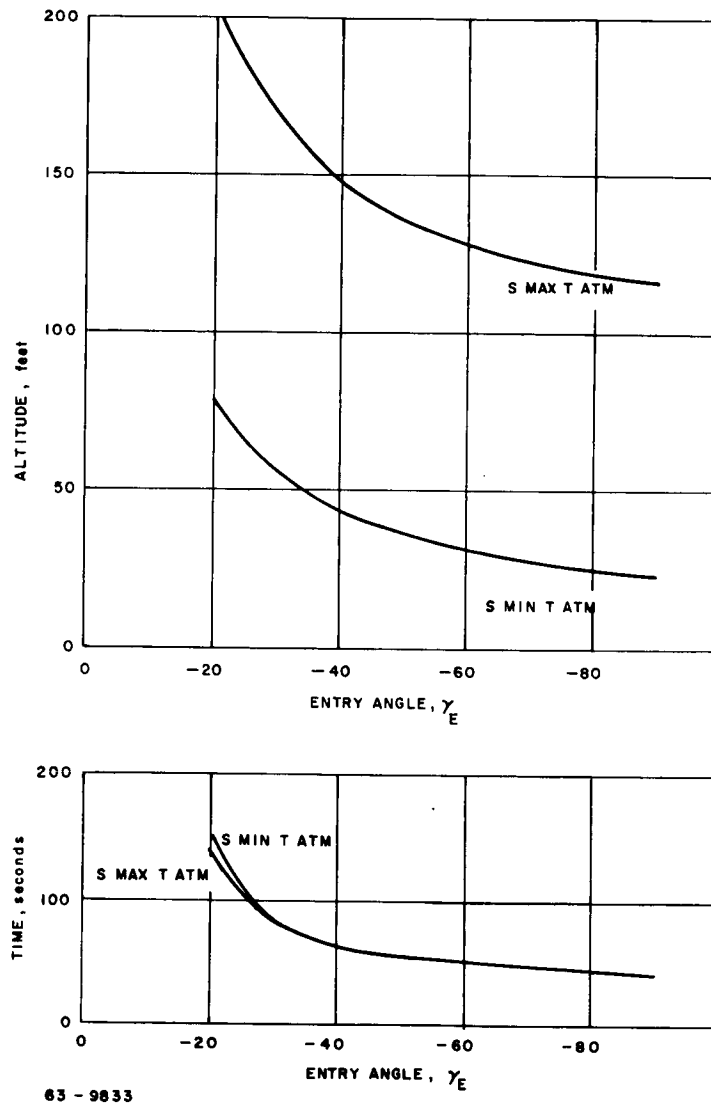


Figure 38 DROGUE DEPLOYMENT ALTITUDE VERSUS ENTRY ENTRY ANGLE

35 to have little effect. Therefore, the results have been obtained for a nominal entry velocity of 24,000 ft/sec and are not considered significantly different for other entry velocities. The graphical results show the effect of atmospheric model variation which is represented by Schilling's limiting atmospheres of "maximum temperature" atmosphere (SMAXT) and "minimum temperature" atmosphere (SMINT).

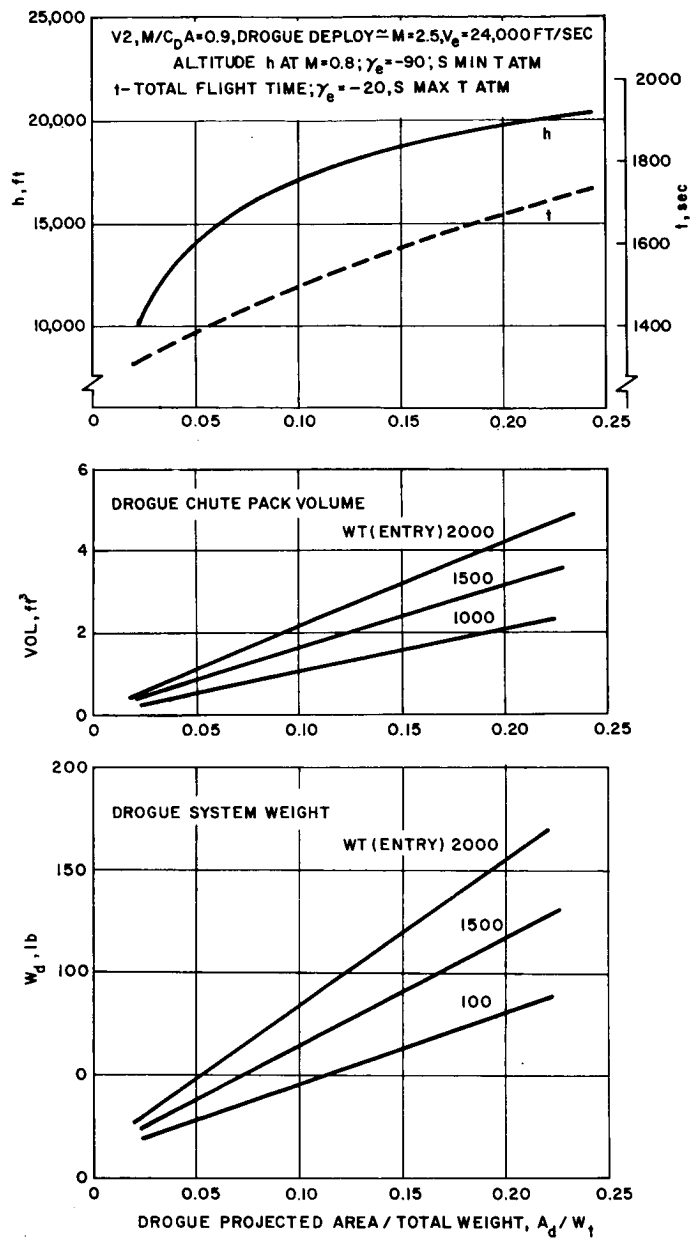
The drogue parachute deployment altitude variation is shown in figure 38 with the large effect due to the atmosphere variation being indicated. Vehicle flight times from entry to drogue deployment are also given in figure 38. The drogue chute must decelerate the vehicle to a Mach number of 0.8 or less so that the main parachute can be deployed. Since the deceleration obtained during drogue flight is a function of the ratio of drogue chute area to total (suspended plus parachute) weight (A_d/W_t), the maximum chute deployment altitude is determined by A_d/W_t and the flight conditions at drogue deployment. Figure 39 indicates the tradeoff study required to properly select the drogue A_d/W_t (or size for a given vehicle). The main chute deployment altitude ($M = 0.8$) for a worst combination of entry conditions and atmosphere, the drogue system weight, and the required system packaging volume are all functions of A_d/W_t , as shown. To keep drogue weights and volume relatively low, a value of $A_d/W_t = 0.063$ was selected. Thus, the minimum deployment altitude is 15,000 feet. This altitude increases rapidly as the entry angle becomes shallower (see figure 40) or as the atmosphere becomes denser until deployment at 20,000 feet is possible. The constant main chute deployment altitude is then 20,000 feet for all remaining trajectory possibilities.

Drogue flight times from deployment to main chute deployment are shown in figure 41. Main parachute descent times are presented in figure 42 as a function of deployment altitude with the chute sized for a minimum descent time of 10 minutes for a 20,000 ft. deployment. The resulting impact velocities range from 24 to 33 ft/sec. These velocities are compatible with the impact attenuation system.

Figure 43 shows the possible variation of total flight time (from entry to impact) as a function of entry angle and atmospheric model.

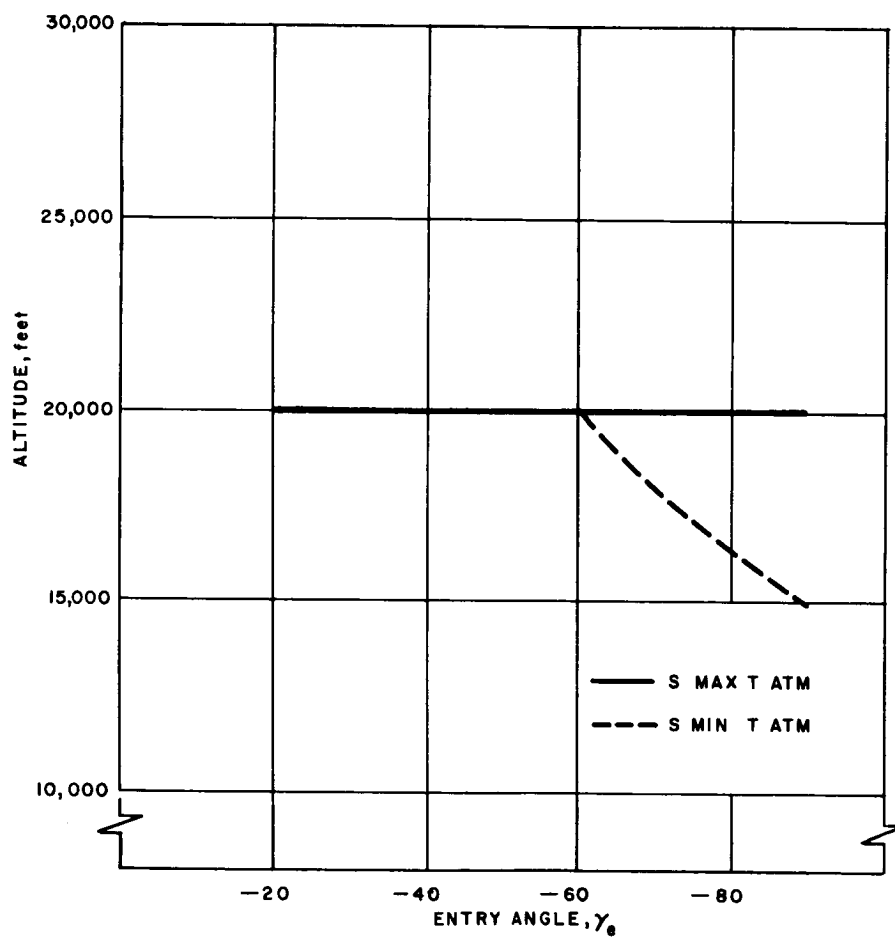
b. Descent time calculations. An approximate relationship was utilized to determine the main chute descent times for the parametric study. The assumptions involved include vertical descent, adiabatic atmosphere, and equilibrium descent. The descent time is given by the expression:

$$\Delta t = \frac{C_1}{V_{sl}} \left(\frac{g \sigma}{\rho_{sl}} \right)^{1/2} \quad (\text{seconds})$$



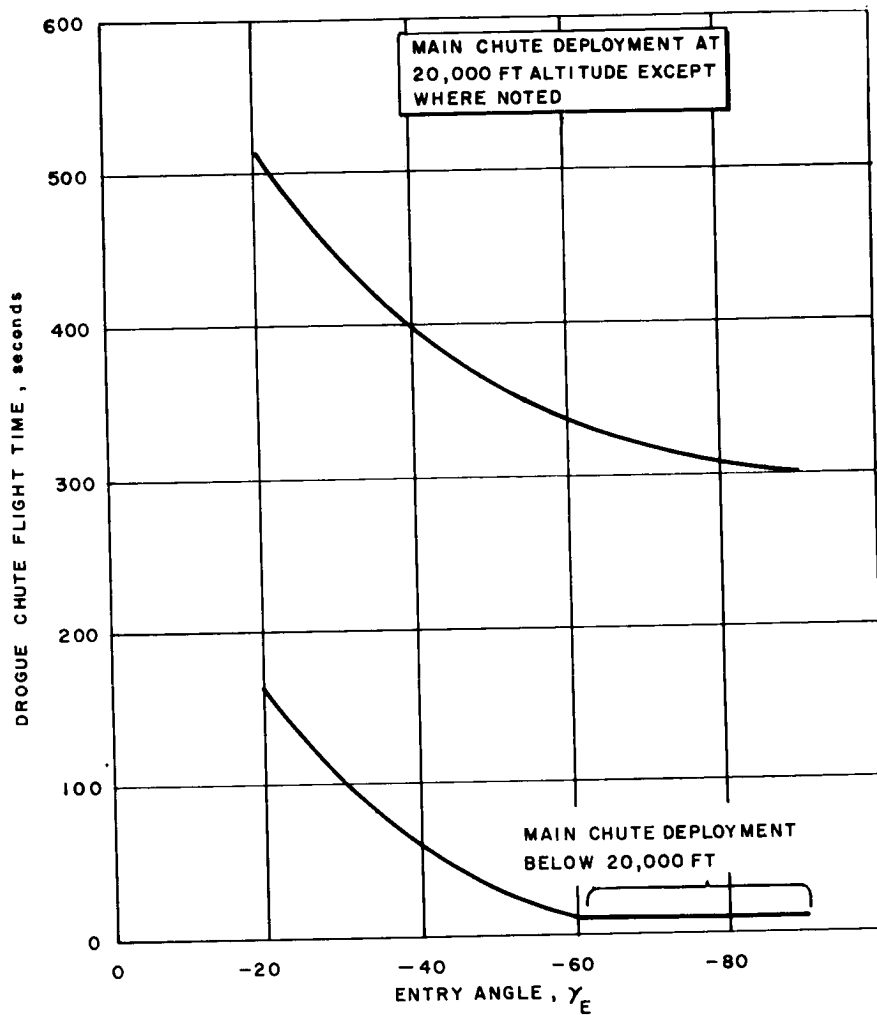
63-9832

Figure 39 DROGUE CHUTE AREA TRADEOFF



63-9831

Figure 40 MAIN PARACHUTE DEPLOYMENT ALTITUDE VERSUS ENTRY ANGLE



63-9830

Figure 41 DROGUE FLIGHT TIME TO MAIN CHUTE DEPLOYMENT VERSUS ENTRY ANGLE

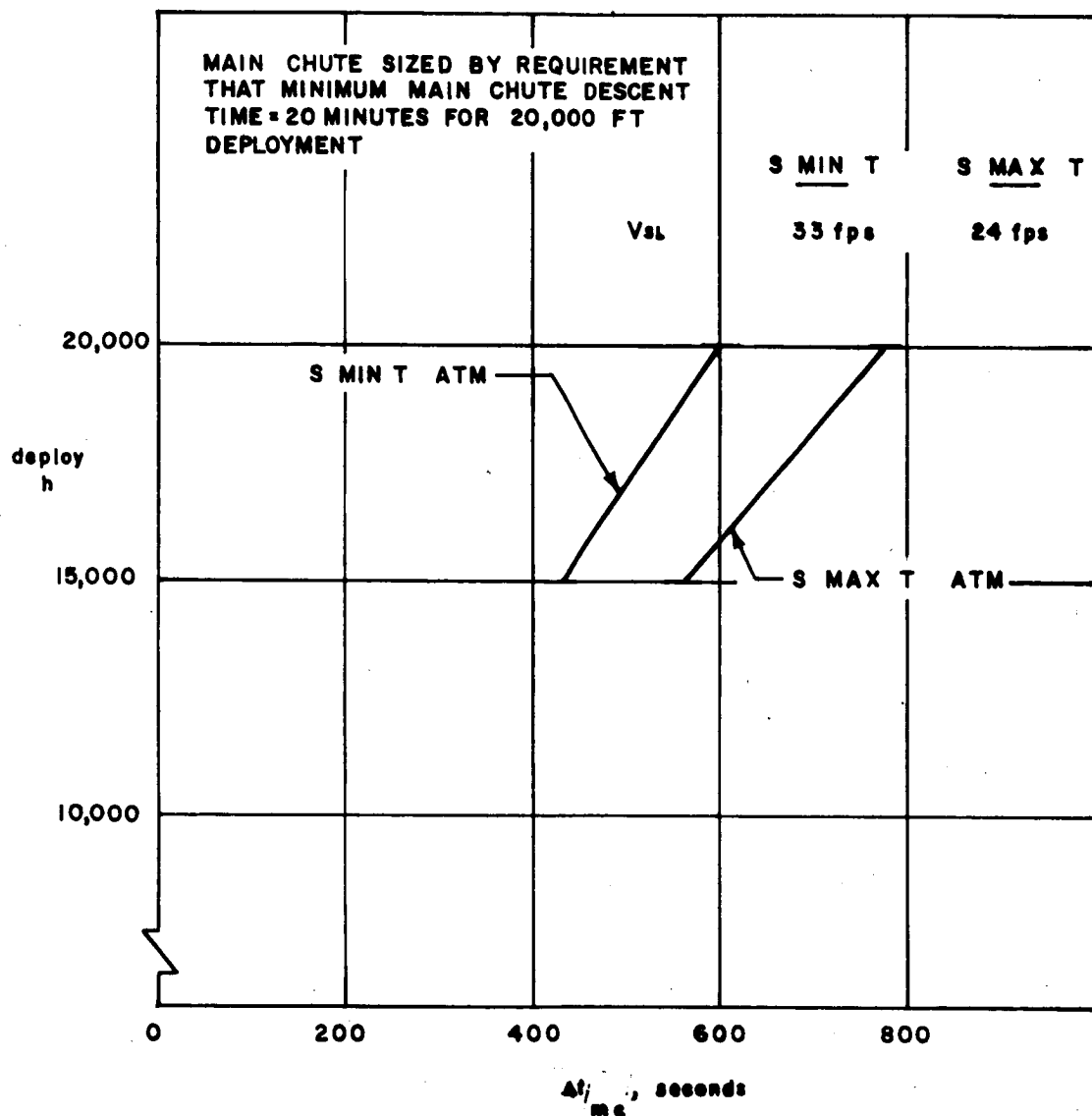


Figure 42 MAIN CHUTE DESCENT TIME VERSUS MAIN CHUTE DEPLOYMENT ALTITUDE

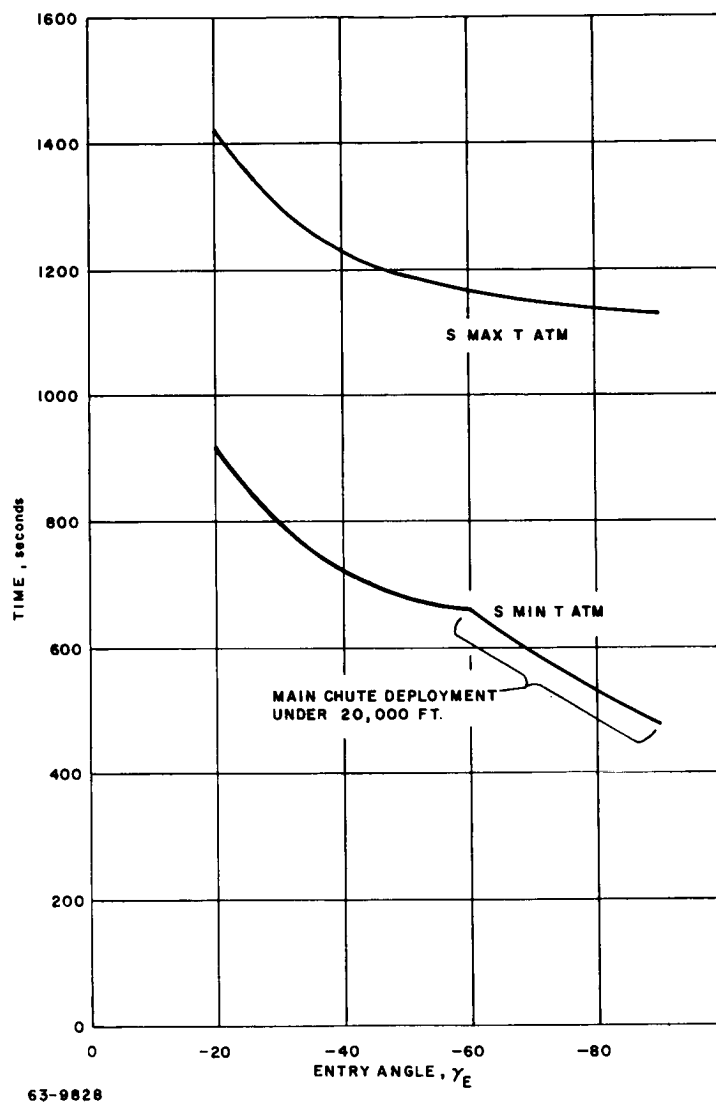


Figure 43 TOTAL FLIGHT TIME FROM ENTRY TO IMPACT VERSUS ENTRY ANGLE

where

$$C_1 = \frac{\gamma R T_{sl} \rho_{sl}^{1-\gamma}}{3/2} [\rho_{sl}^{\gamma-1/2} - \rho^{\gamma-1/2}]$$

$$g \mathcal{O}^{\gamma} (\gamma - 1/2)$$

v_{sl} = velocity at sea level ft/sec

$g \mathcal{O}^{\gamma}$ = gravitational constant (ft/sec²)

ρ_{sl} = sea level density (slug/ft³)

T_{sl} = ambient temperature at sea level (°K)

ρ = density at deployment altitude

γ = ratio of specific heats.

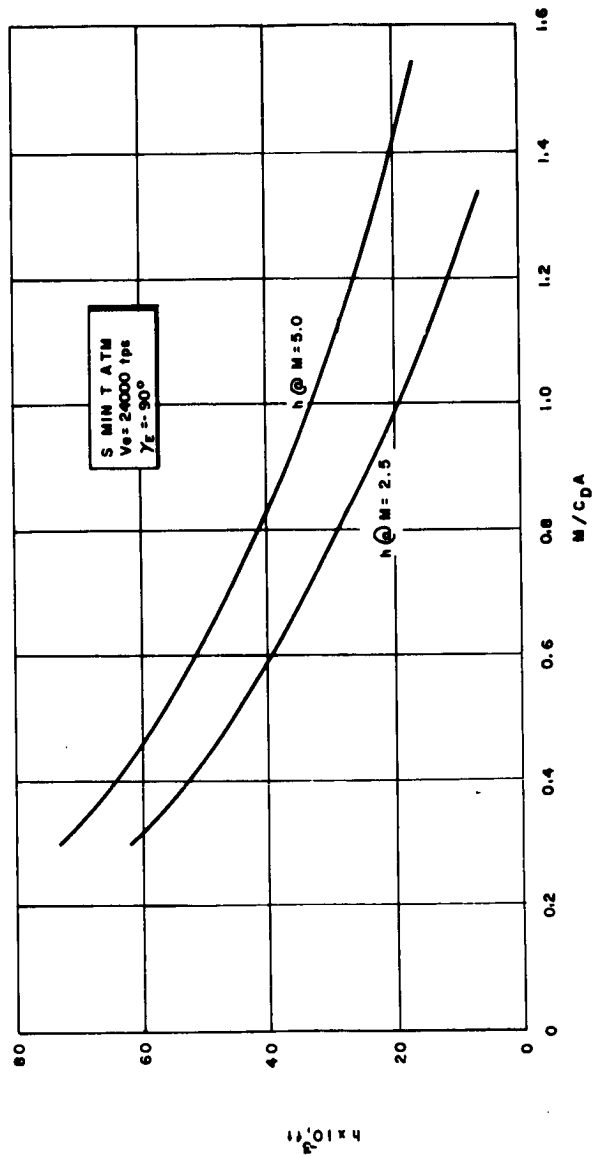
The sea level velocity can then be related to the main chute size by

$$1/2 \rho_{sl} v_{sl}^2 C_D A = \text{descent weight}$$

Descent times for the drogue flight portion of the trajectory were determined with a particle trajectory computer program.

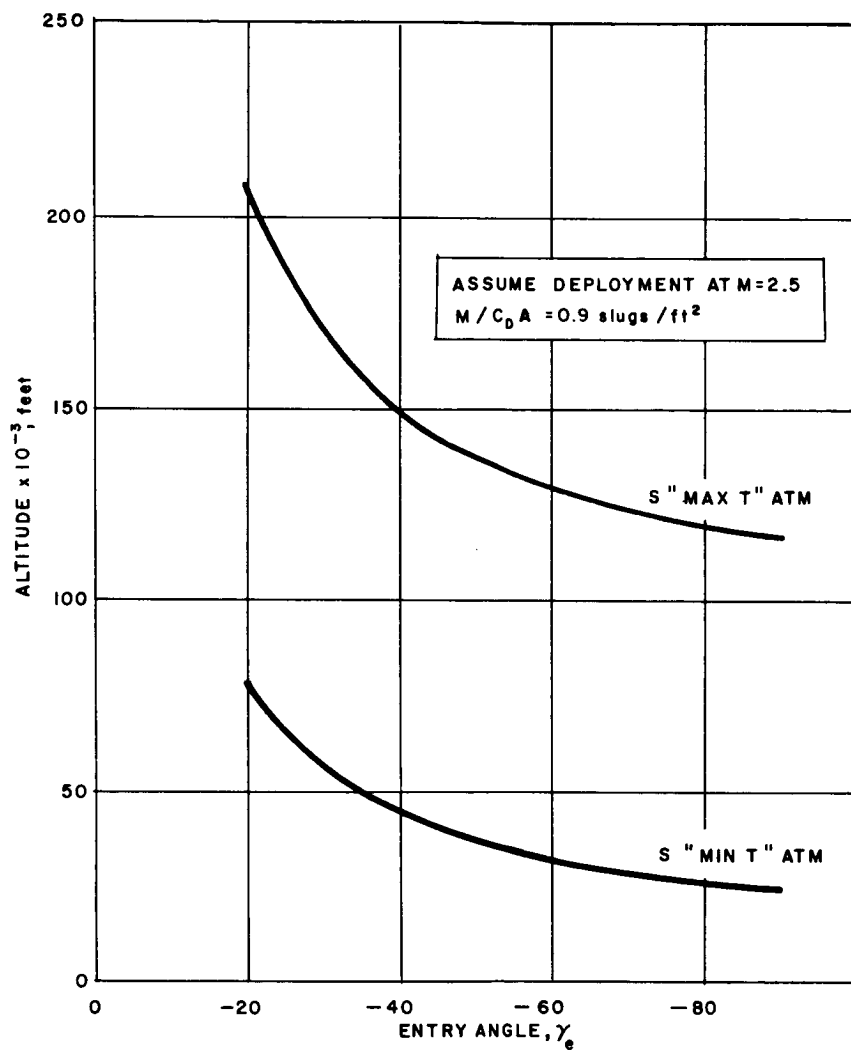
c. Possible tradeoffs. The performance of a parachute system can be varied to fulfill changing lander system requirements. Assuming the vehicle ballistic coefficient is to remain constant, descent time and deployment altitudes can be increased by state of the art parachute technology advances, entry angle restrictions, and variation of the drogue chute and main chute sizes. For example, if a drogue deployment at Mach number of 5.0 were feasible, the gain in deployment altitude would be as shown in figure 44. Thus, for a given M/C_{DA} of 0.9 slug/ft², the minimum deployment altitude is increased from 24,000 to 37,000 feet for the higher velocity deployment. The limitations on vehicle M/C_{DA} can also be relieved.

Gains in drogue deployment altitudes can be achieved by restriction of the entry angle as shown in figure 45. Assuming a maximum entry angle of -45 degrees, the gain in minimum deployment altitude is 16,000 feet. The main parachute deployment altitude can be changed by varying the drogue chute size, as was shown in figure 41, and by an increase in main chute deployment velocity. The major portion of the descent time then, of course, can be varied with variation in main chute sizes with the impact velocity varying.



63-9827

Figure 44 ALTITUDE VERSUS M/C_{DA} FOR MASS ENTRY



63-9826

Figure 45 GAIN IN DROGUE DEPLOYMENT ALTITUDE WITH VARIATION IN ENTRY ANGLE

5. Effects of Kaplan's atmospheric model. The descent system selected for the study consisted of a high speed drogue chute capable of deployment at Mach numbers approaching 3.0 and a main chute with a Mach number limitation of 0.8. The use of a drogue chute deployment at $M = 5.0$ (representing an advance in parachute technology state of the art) was investigated to determine possible gain. It was found that the small gain in the possible main chute deployment altitude with an earlier drogue deployment did not justify the higher parachute weights needed for the higher drogue opening loads.

The drogue actuation sensing method will be the same as utilized for the "Schilling atmosphere" reference design; i. e., a variable accelerometer set with knowledge of the entry angle to achieve nominal deployment at a constant Mach number of 2.5. The drogue actuation backup would be performed with a preset accelerometer. The main chute would then be deployed with the use of an altimeter and timer with the timer acting as backup if needed. Parachute system weights required to allow 1) a minimum main chute deployment altitude of 10,000 feet and 2) various main chute descent times, are shown in figure 46 as a function of vehicle M/C_{DA} . Combination of heat shield and structural weights with these parachute weights indicates that a ballistic coefficient of ~ 0.25 slug/ft² is desirable.

The parachute analysis considered the worst possible combination of entry angle and atmospheric model. If the vehicle were to enter at a shallow entry angle and/or into a denser atmosphere, longer descent times would result. Also, if it were decided to design the vehicle for a restricted entry angle range (i. e., $\gamma_e = -20$ to -45 degrees), the possible vehicle ballistic coefficient could be increased by approximately a factor of two resulting in more available payload weight for a given entry weight.

2.2. Landing System

1. Environment management.

a. Environment features. A literature search was made to ascertain the topography estimates of the surface of Mars. The pertinent bibliography is included in paragraph b. It is generally felt that the surface of Mars is relatively smooth, with less relief than the Earth or the Moon. There are no mountains higher than 3,000 feet, and any vast negative features, i. e., pits and craters, are probably filled with dust and sand. That there is some relief on the surface is shown by the retention of ice on certain areas as the polar caps recede in the Martian summer, indicating plateaus or mesas about 3,000 feet high. Also, white patches (probably frost or low clouds) are sometimes seen in the tropics, often recurring in the same areas, further indicating relief.

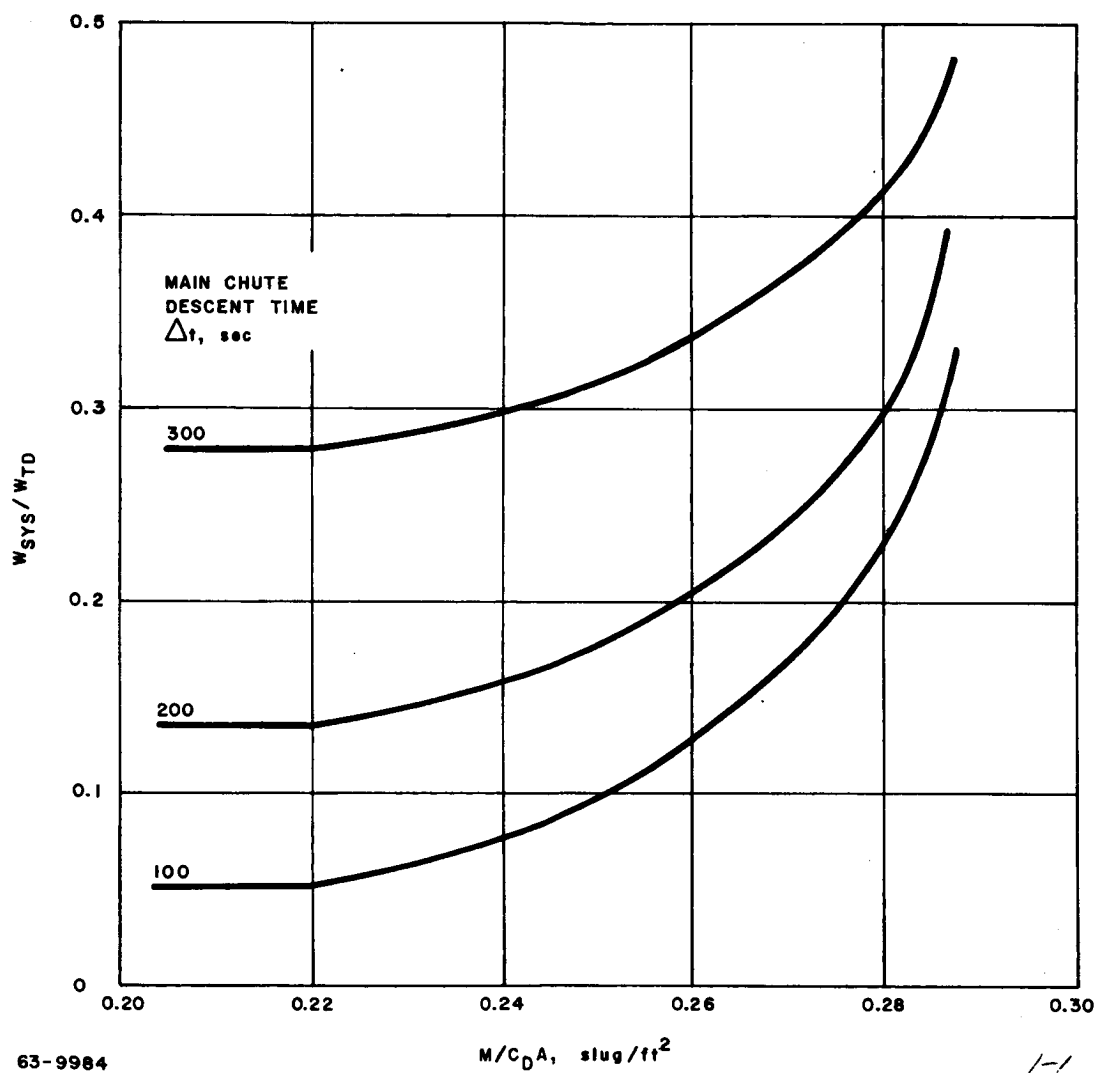


Figure 46 RATIO OF PARACHUTE SYSTEM WEIGHT TO TOTAL WEIGHT DURING DROGUE FLIGHT

There are no large bodies of water on the surface. It has been estimated that a lake less than a mile across would have been detected by the reflection of the Sun from its surface. In the geological past, water may have been present in quantity, and the resulting oceans and glaciers may have performed much of the eroding of the surface. In recent geological times, however, erosion has been by wind, sand, and desiccation.

As shown by study of yellow dust storms, winds can be as high as 60 mph for brief periods. An average wind speed is about 20 miles per hour.

There is, at present, a lack of extensive radar data pertaining to Mars. Therefore, lander design criteria must be based on adapting terrain information about the Earth and the Moon to Mars.

The rms slope of the Moon, as judged from radar returns, ranges from 6 to 14 degrees on a scale of from 2 to 20 feet. Further, studies made at Avco on Earth terrain have shown that the Berkshires, an area which represents an originally rough, mountainous terrain which has been eroded and smoothed over a very long time, has a $1-\sigma$ slope of 6 degrees on a scale of 20 feet. Since Mars is probably smoother than the Earth and Moon at this scale, a very conservative value for rms slope of Mars should be about 10 degrees.

It will be assumed that the distribution of slopes on a surface is a normal distribution (the Avco studies indicate that this is a valid assumption). For initial design purposes, the $3-\sigma$ value will be used. Thus, since the rms (or, equivalently, $1-\sigma$) slope of Mars has been assigned a probable upper bound of 10 degrees, the initial slope will be 30 degrees.

In summary, then, the "reference" Martian surface is a dry, sandy desert with some bare rock, vegetation growing on the desert over large areas of the surface, winds blowing at 20 mph with gusts to 60 mph, and with slopes of up to 30 degrees.

b. Bibliography

Kiess, C. C. and K. Lassovsky: The Known Physical Characteristics of the Moon and the Planets; ARDC-TR-58-41; ASTIA DOC. NO. AD 115-617. (1958).

de Vaucouleurs, G.: Physics of the Planet Mars, Faber & Faber Ltd. (1954).

Johnson, R. W.: Terrain and Soil of Mars, AAS Interplanetary Missions Conf. (15-17 January 1963).

Speed, et al Geological Exploration of the Moon and Planets, in "Lunar and Planetary Sciences in Space Exploration", NASA SP-14 (December 1962).

Proceedings of Lunar and Planetary Exploration Colloquium, NAA 513W2.

Tombaugh, C.: Where to Land on the Moon, Vol. 1, No. 3 (24 October 1958).

Richardson, R. S.: Observations on Mars and Venus, Vol. 1, No. 3 (29 October 1958).

Urey, H. C., The Atmospheres of the Planets; Encyclopedia of Physics; ed. by Flugge, S, Vol. L11 - Astrophysics; III, The Solar System; 363-418.

Salisbury, F. B.: Martian Biology, Science Vol. 136, No. 3510; 17-26 (6 April 1962).

Barabashov, N. P.: Basic Results of Observations of Mars During the Favorable Opposition of 1956; Soviet Astronomy, Vol. 2, No. 1 (1958).

Wanders, A. J. M.: The Physical Conditions on the Planet Mars; Ninth International Astronautical Congress, Proceedings; 1959, Vol. I, 394-404.

Sinton, W. M.: Spectroscopic Evidence for Vegetation on Mars, Astro. J. Vol. 126, No. 2; 231-239 (September 1957).

Moore, P.: The Planet Mars; "Realities of Space Travel", ed. by Carter, L. J.; McGraw-Hill, 1957.

Opik, E. J.: Surface Conditions on the Nearest Planets; Am. J. Phys., Vol. 28; 618-622 (1960).

Evans, J. V., G. H. Pettengill: The Scattering Behavior of the Moon at Wavelengths of 3, 6, 68, and 784 Centimeters; J. Geophys. Res.; Vol. 68, No. 2; 423-447 (15 January 1963).

Daniels, F. B.: Radar Determination of the Root Mean Square Slope of the Lunar Surface; J. Geophys. Res.; Vol. 68, No. 2, 449-453 (15 January 1963).

Clarke, A. C.: The Exploration of Space; Pocket Books, Inc. 1951.

Jones, H. S.: Life on Other Worlds; Macmillan; 1940.

Shaw, J. H.: Natural Environment of the Planet Mars, Ohio State Univ., Research Foundation Phase Tech. Report 847-1; ASTIA AD 242-175 (February 1959).

Loomis, A. A.: Some Geological Problems of Mars; JPL Tech. Report No. 32-400 (4 March 1963).

2. Lander vehicle impact stability and operation analysis. To permit the lander vehicle to transmit the data its instruments collect while on the surface of the planet, it is essential that the vehicle be properly oriented after impact. Proper orientation implies that the vehicle is in such a position that its transmitting antenna or antennas are capable of providing either direct transmission to Earth, or indirect transmission to an orbiting parent vehicle.

To provide proper orientation of the vehicle after impact with the planet's surface, four possible vehicle design approaches are considered. These approaches are:

- a. A vehicle with inherent stability such that landing in any position on any terrain conditions within the range of conditions anticipated for the planet surface will result in the vehicle's regaining its proper orientation,
- b. A vehicle with design features which, after landing on the planet surface, act to upright or self-erect the vehicle to its proper orientation,
- c. A vehicle with design features such that it is capable of performing its mission, no matter what position it may assume after impact, and
- d. A vehicle equipped with stabilizing devices which, having been deployed before or at impact, acts to hold the vehicle in the proper orientation, despite the perturbations imposed on the vehicle during and after impact.

While a complete analysis of each of these design approaches is beyond the scope of this report, a few general remarks on each approach can be made.

Approach (a) is usually quite difficult to achieve on an actual hardware vehicle. Even if it is possible to locate the center of gravity very low in the vehicle, a particular set of terrain conditions can usually be found within the range of anticipated conditions, which will act to overcome the inherent stability of the vehicle.

Approach (b) requires additional fixtures, appurtenances and a source of power in order to perform its function. Its applicability will depend to a large extent on the ingenuity of the design and the ability of the vehicle to accommodate the additional components and equipments necessary to provide the self-erecting feature.

Approach (c) requires redundancy of equipment, particularly antennas, necessary to provide proper operation no matter what the vehicle orientation. Space and weight considerations are again paramount.

Approach (d) requires the deployment of devices, normally mechanical, in order to stabilize the vehicle during and after impact, until the vehicle comes to rest. The factors influencing the design of the stabilizing devices for this method of approach include the surface terrain at impact area, surface winds, the center-of-gravity location of the vehicle, and the magnitude of the gravity force at the planet's surface.

Because approaches (a) and (c) require a detailed knowledge of the design of the vehicle itself (its payload requirements, structural requirements, and the distribution of weight in the vehicle), analysis of impact stability and orientation for these cases has not been considered.

For approach (d), an analysis has been performed to determine whether this technique is feasible for the case of the Mars lander. Specifically, a flat disc shaped vehicle was selected and equipped with horizontal, extendable legs which were assumed to be deployed before impact. It was further assumed that the vehicle impacts on a 30-degree inclined Mars surface, with a velocity down the surface varying from 0 to 100 ft/sec. (It was assumed that the velocity component of the vehicle normal to the surface is removed by the touchdown system, with no toppling moment introduced by the action of impacting.) The result of the analysis was the determination of the leg length to prevent toppling. The necessary leg length was found to vary from 35 feet for a velocity of 20 ft/sec to 840 feet for a velocity down the slope of 100 ft/sec. This analysis indicates that extendable legs are impractical for the range of Mars landing conditions presently anticipated.

In a more general sense, an analysis was carried out to determine the relative dynamic stability of a vehicle landing on Venus with a vehicle landing on Mars. The analysis shows that the dynamic stability of a vehicle is proportional to the gravity force of the planet. Since the gravity force of Venus is 2.23 times that of Mars, a vehicle that is stable on Mars will be stable on Venus.

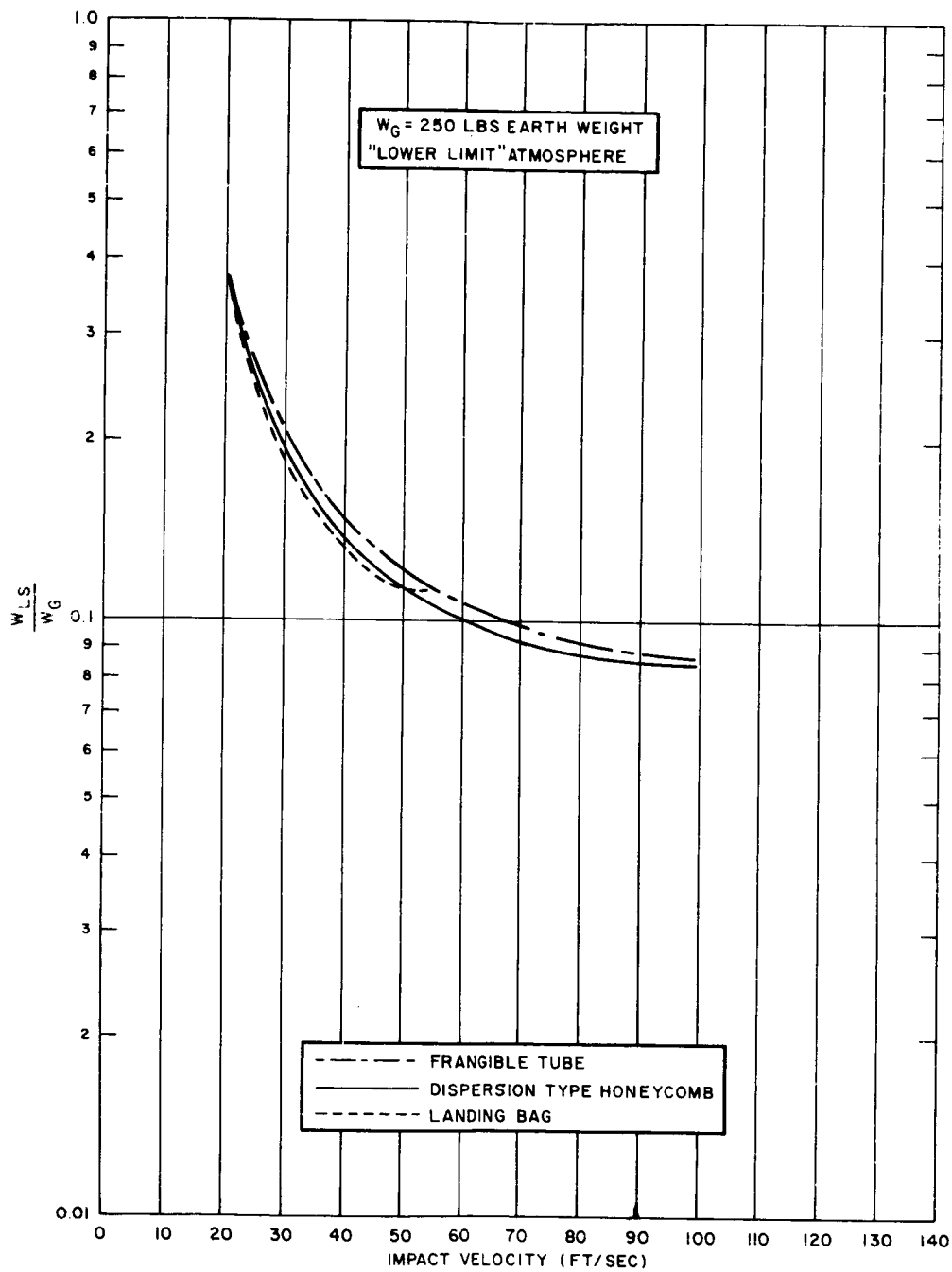
3. Optimization of descent and landing system. A mutual study by Avco RAD and Northrop Ventura Division was made concerning a range of energy absorber materials and lander design. The results of the study are:

For the parachute-landing bag combination, the optimum impact velocity is approximately 50 ft/sec. For the parachute-dispersion type honeycomb system, the optimum impact velocity is between 85 and 100 ft/sec. For the parachute-frangible tube system, the optimum impact velocity is greater than 100 ft/sec.

While it is evident that for all the landing systems considered, a relatively high impact velocity seems desirable to minimize the landing system weight, it remains to examine impact velocity from the operational point of view, as it affects the time of descent of the vehicle for various entry and atmospheric conditions.

To determine the optimum impact velocity, based on a minimum landing system weight, the parachute descent system weight fraction was combined with each of three representative touchdown system weight fractions, to provide a landing system weight fraction (w_{ls}/w_n). The landing system weight fraction for each of the three combinations is plotted versus impact velocity for 250-, 1000-, and 5000-pound vehicle for each of the three Schilling atmospheres in figures 47 to 55.

The results of the stability analysis on the length of legs required to prevent tumbling on a 30-degree slope are shown in figure 56. The calculation was based on the concept that the lower leg could butt up against an obstacle. The surprisingly large leg sizes required for a terrain which is easily conceivable led to the reerectable concept.



63-10276

Figure 47 LANDING SYSTEM WEIGHT FRACTION VERSUS IMPACT VELOCITY

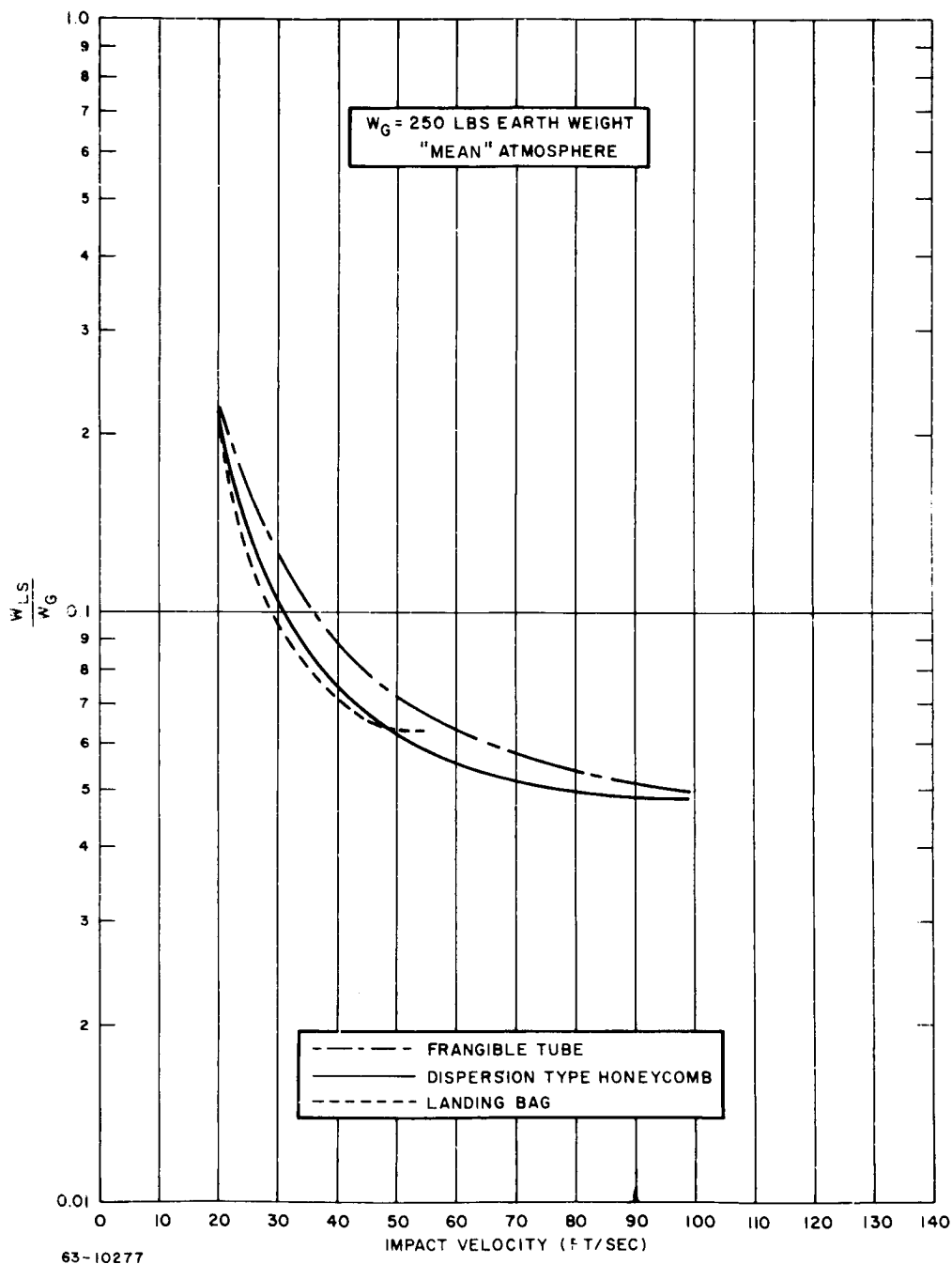
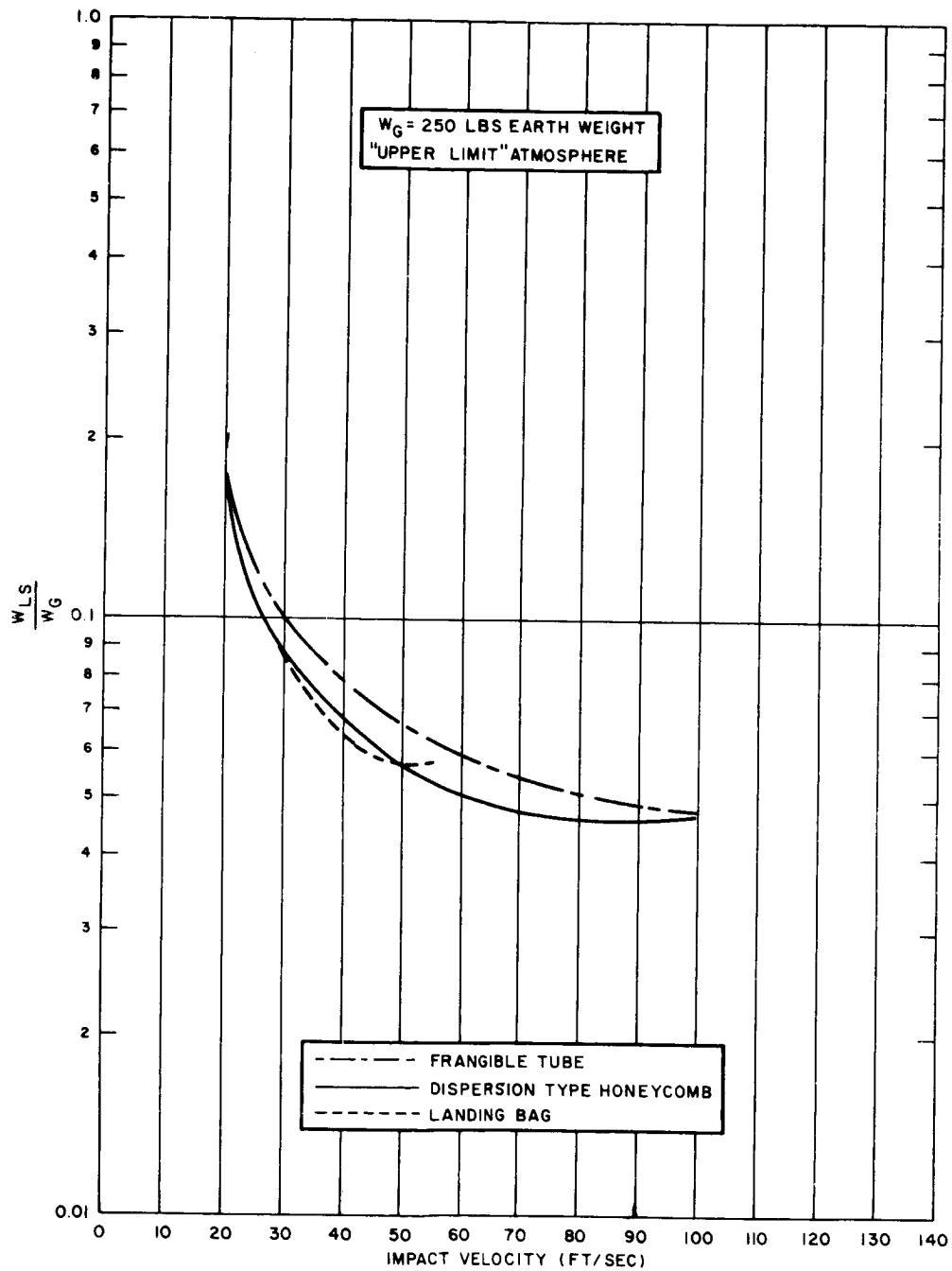
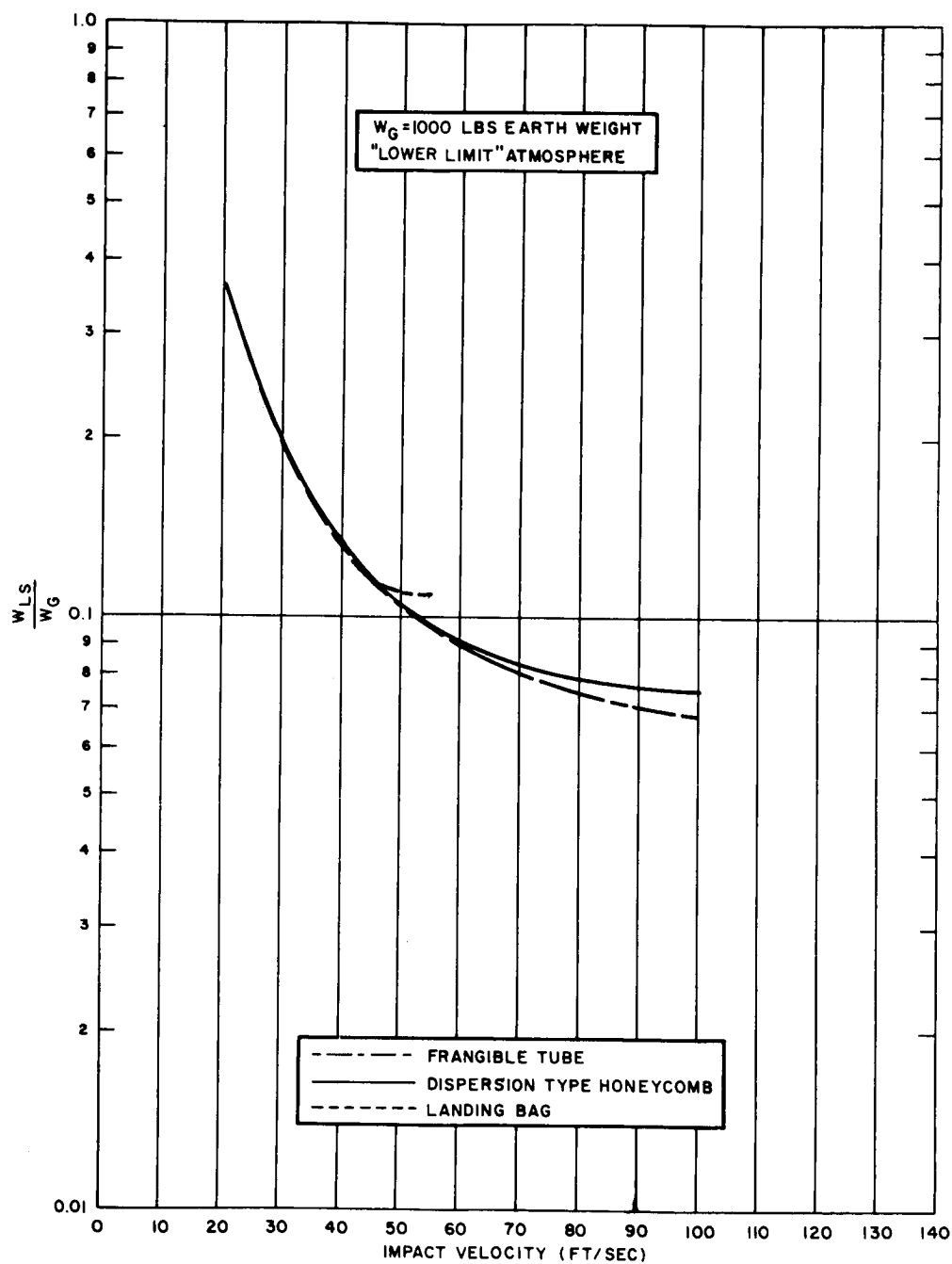


Figure 48 LANDING SYSTEM WEIGHT FRACTION VERSUS IMPACT VELOCITY



63-10278

Figure 49 LANDING SYSTEM WEIGHT FRACTION VERSUS IMPACT VELOCITY



63-10279

Figure 50 LANDING SYSTEM WEIGHT FRACTION VERSUS IMPACT VELOCITY

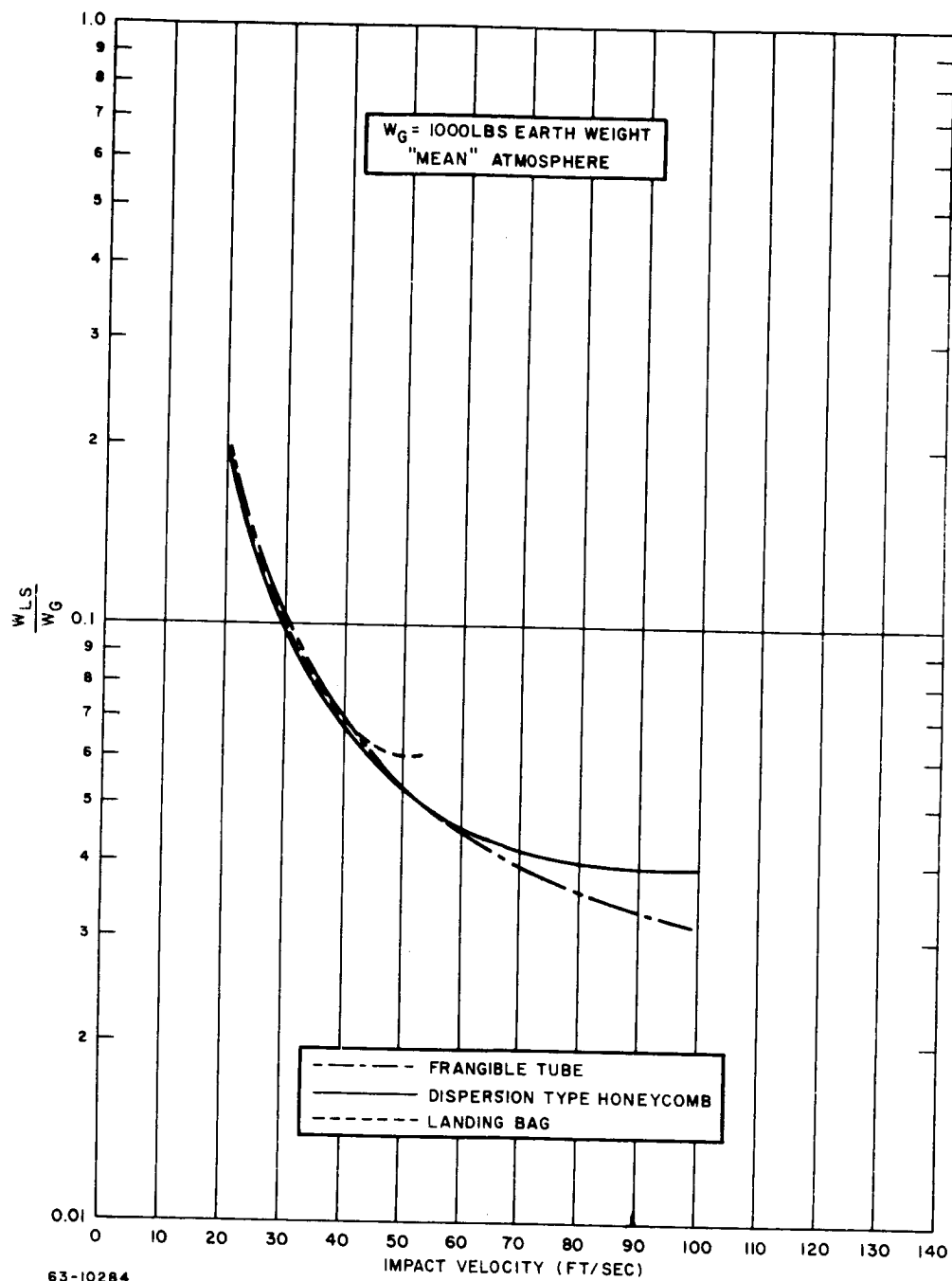
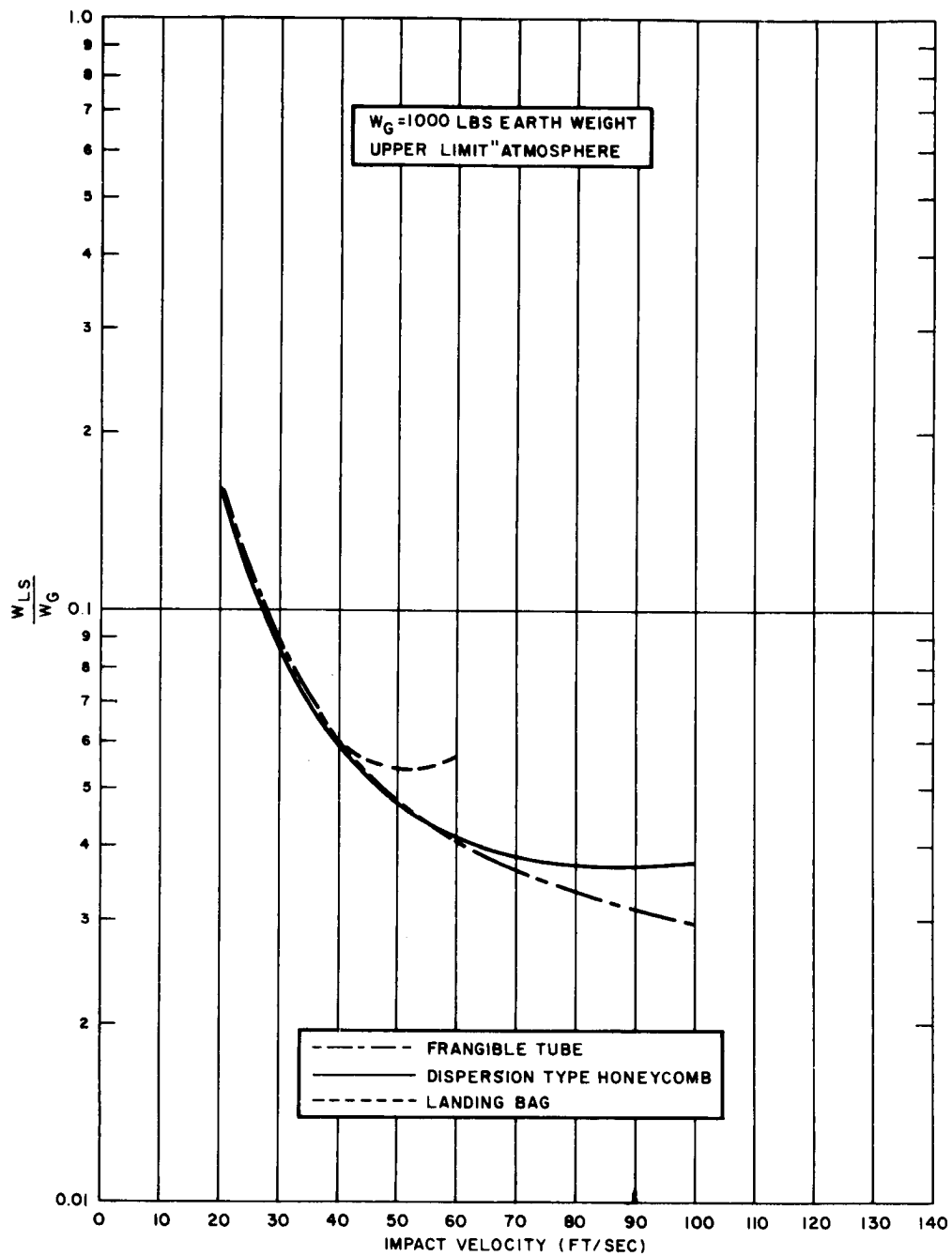
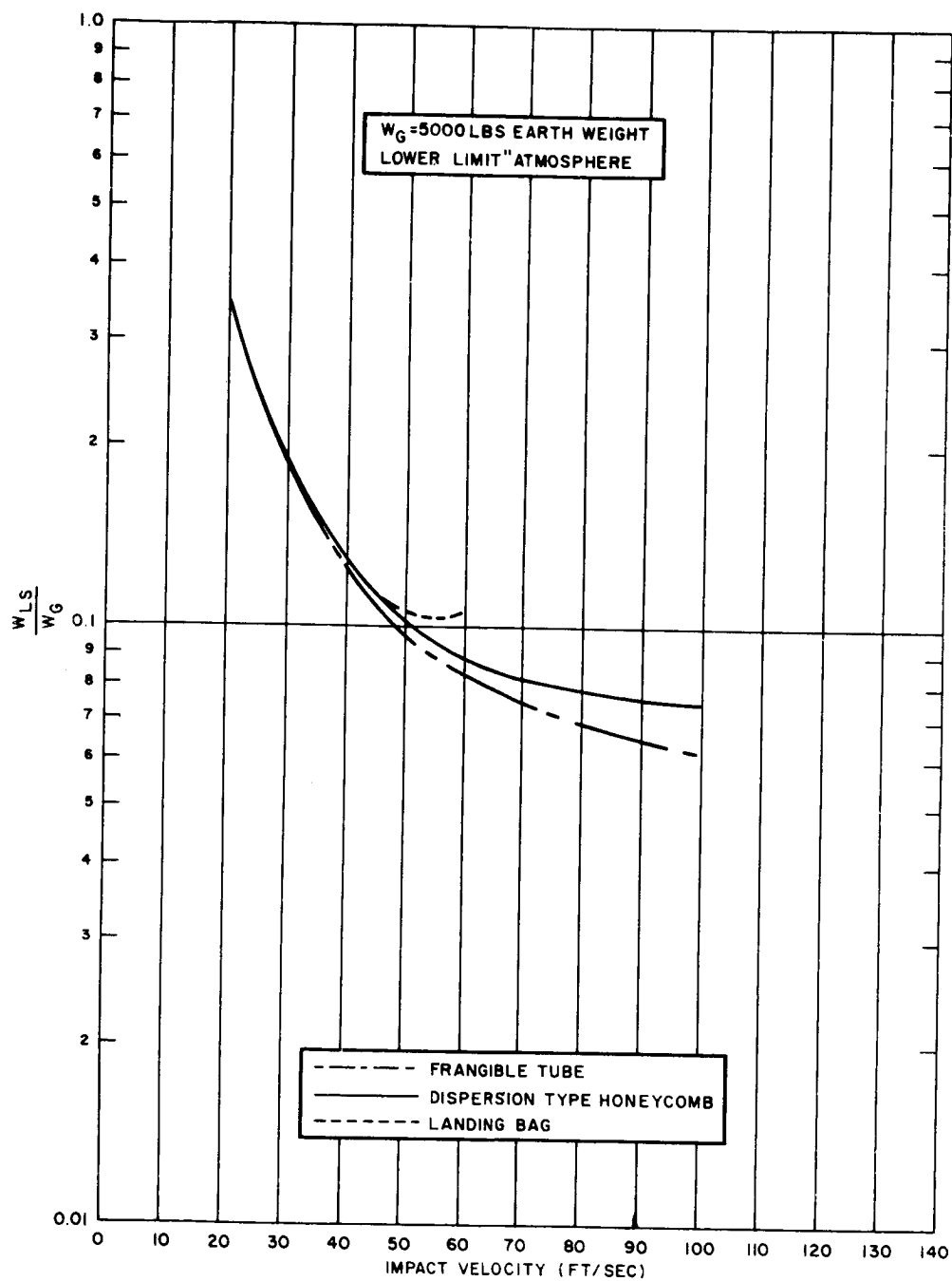


Figure 51 LANDING SYSTEM WEIGHT FRACTION VERSUS IMPACT VELOCITY



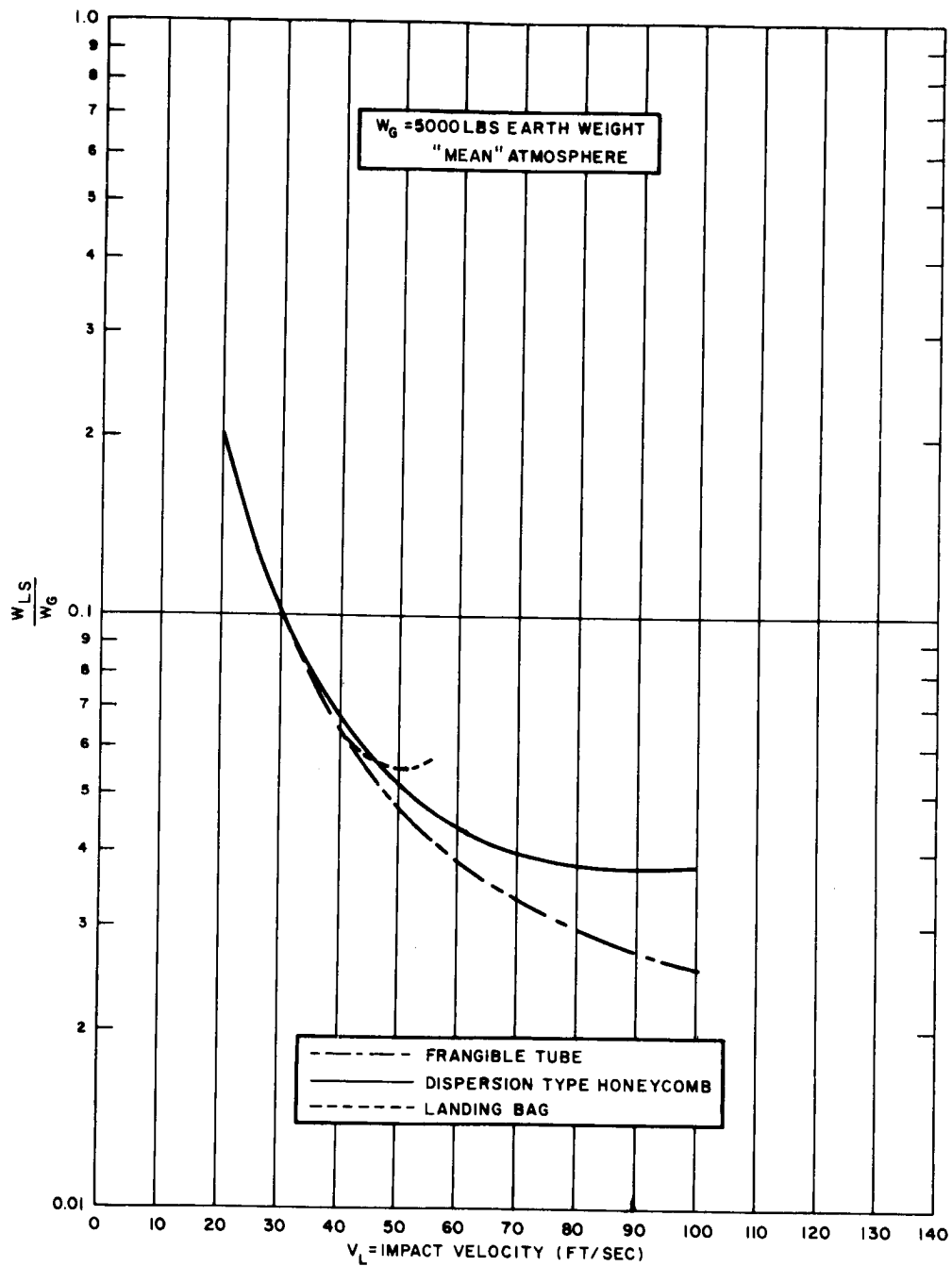
63-10280

Figure 52 LANDING SYSTEM WEIGHT FRACTION VERSUS IMPACT VELOCITY



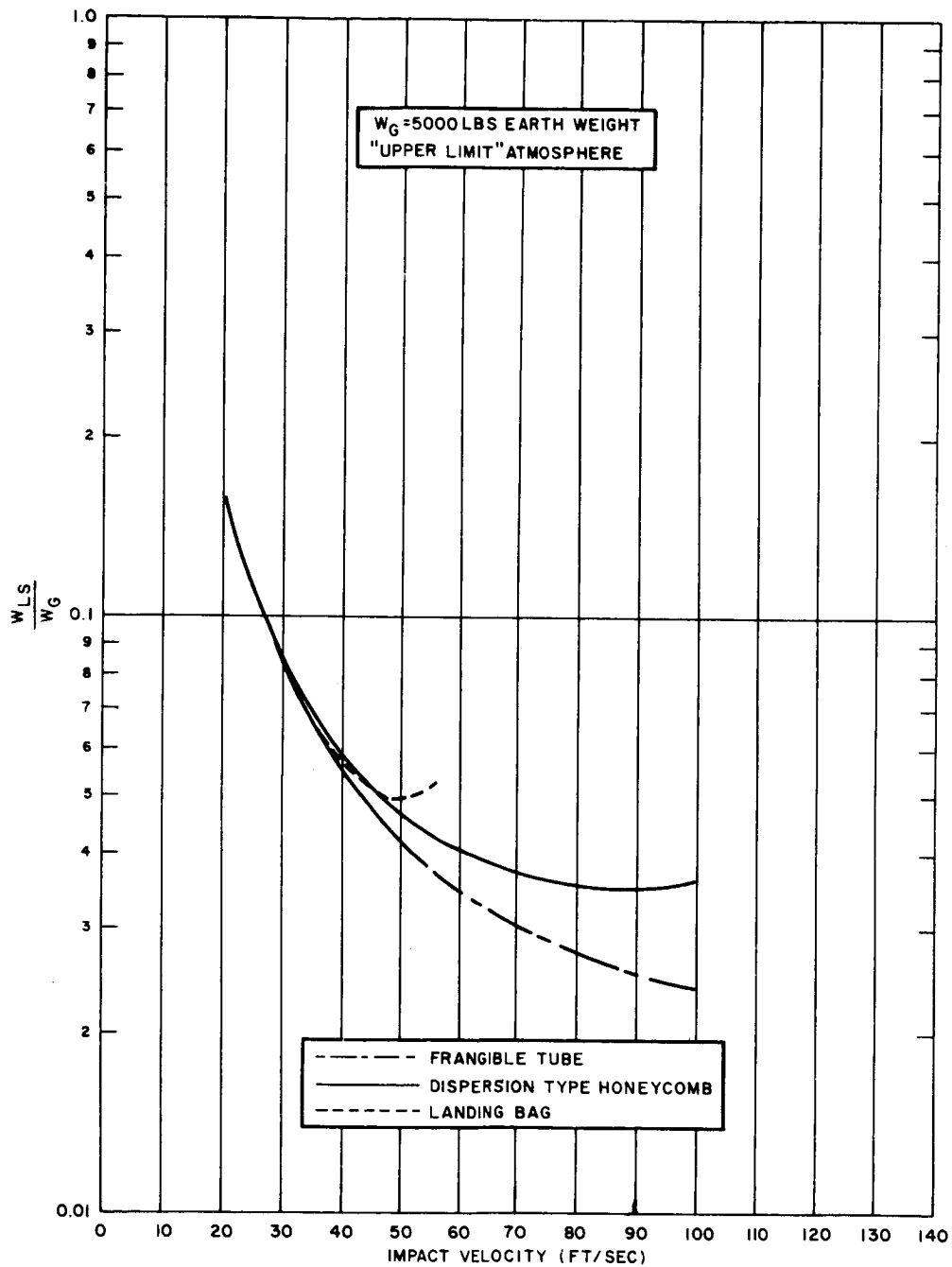
63-10281

Figure 53 LANDING SYSTEM WEIGHT FACTOR VERSUS IMPACT VELOCITY



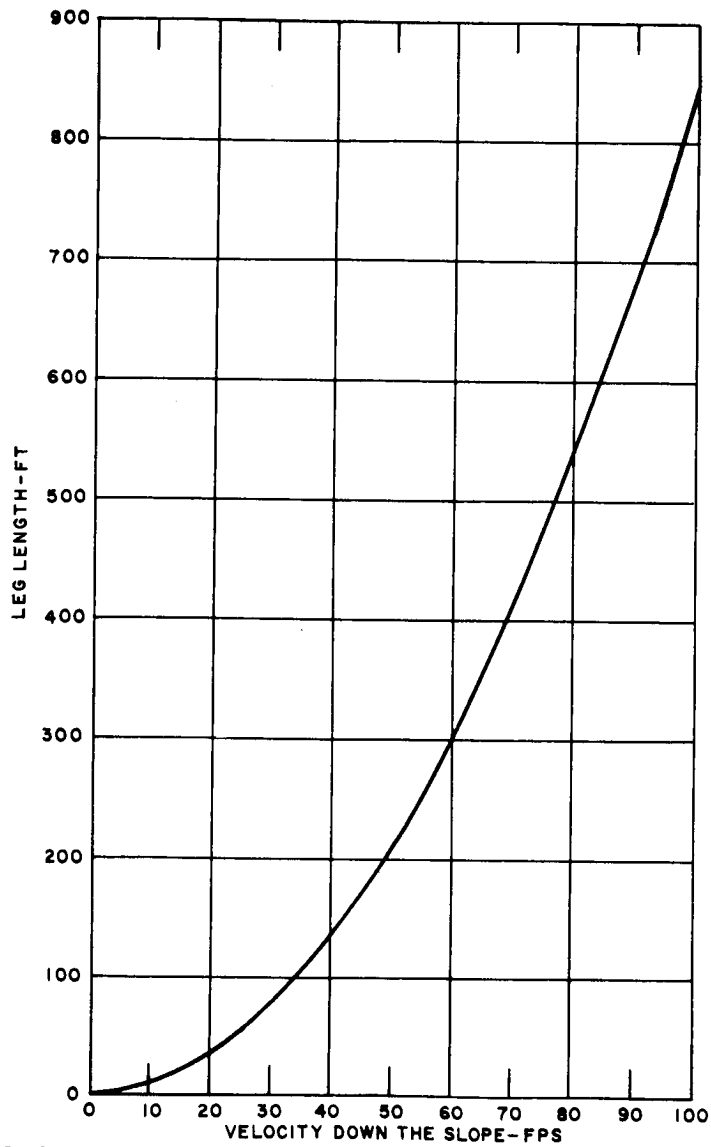
63-10282

Figure 54 LANDING SYSTEM WEIGHT FACTOR VERSUS IMPACT VELOCITY



63-10283

Figure 55 LANDING SYSTEM WEIGHT FACTOR VERSUS IMPACT VELOCITY



63-10286

Figure 56 LEG LENGTH TO PREVENT VEHICLE TOPPLING ON A 30-DEGREE MARS SLOPE VERSUS VELOCITY DOWN THE SLOPE

3. AERODYNAMIC DESIGN--MARS

3.1 Vehicle Configuration

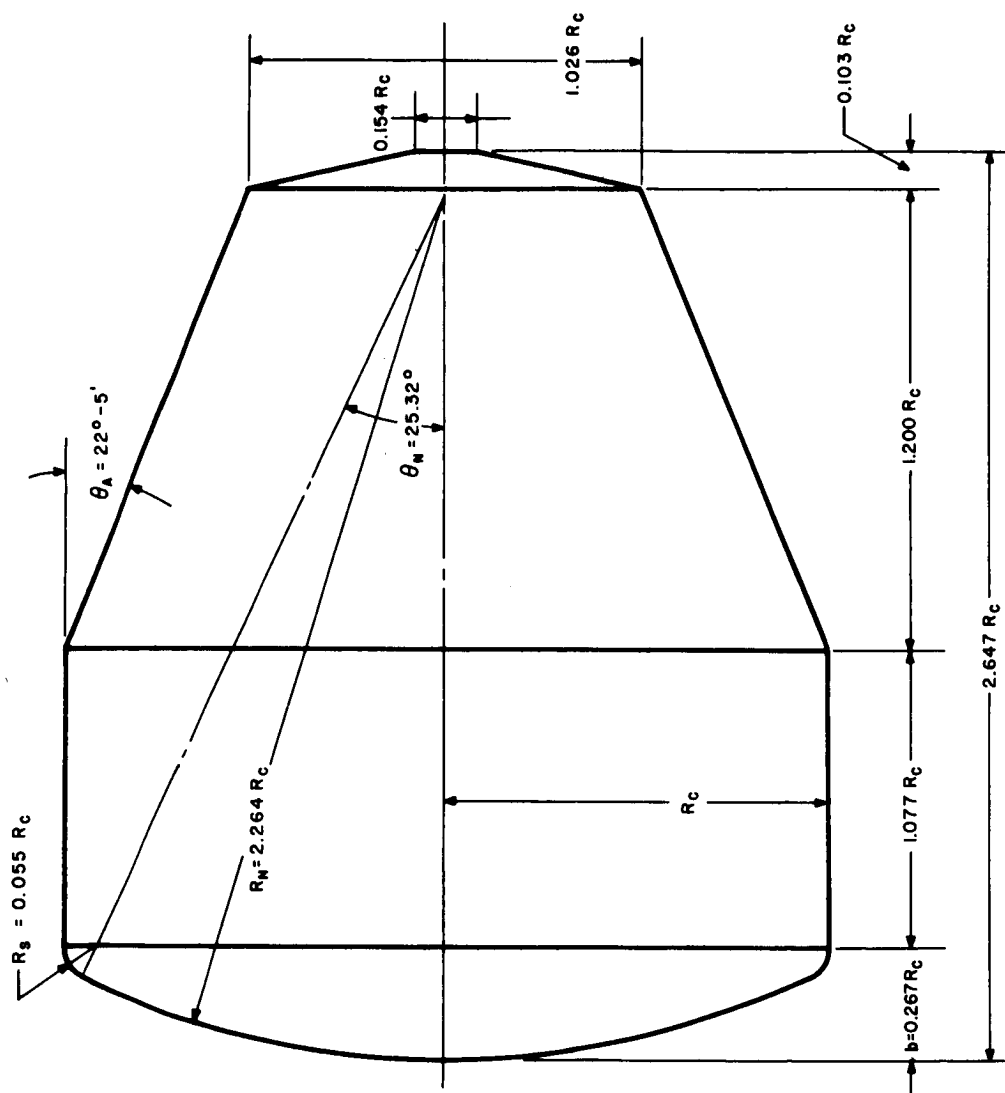
1. Configurations investigated. The two lander shapes which have been investigated in detail are: 1) a high drag vehicle developed by Avco RAD which is designated the V-2 shape (see figures 57 and 58), and the basic Discoverer-Nerv shape which is denoted as the V-1 vehicle (figure 58). The aerodynamic characteristics of both of these shapes are well defined by wind tunnel, shock tube, and ballistic range test programs.

Studies were conducted to determine the impact of lander shape on the design areas of heat shield analysis, instrumentation packaging, external and internal structural design, and the parachute descent system. The vehicle parameters (size, weight, and ballistic coefficient) were varied and all critical combinations of entry conditions and atmospheric model were investigated to allow a selection of the shape for the lander reference design.

2. Reference vehicle selection. The configuration chosen for the reference design is the high drag V-2 shape. One of the primary reasons for the selection is due to the relatively thin Martian atmosphere. The lander system requirements of adequate time for atmospheric measurements and low velocity impact make it necessary for an entry vehicle to decelerate sufficiently for a parachute deployment. It is noted in figure 49 that the hypersonic drag coefficient of the V-2 shape is more than twice that of the V-1 configuration. Thus, for a given vehicle weight and base area, the V-1 ballistic coefficient ($M/C_D A$) is greater than that for the V-2 by the same factor of 2. Figure 59 in section on (Descent system) indicates a typical parachute deployment altitude versus $M/C_D A$ for a worst combination of entry angle and atmospheric model. It is seen that a factor of 2 in $M/C_D A$ can make a difference of 30,000 feet in the deployment altitude. It then appears that the blunter V-2 shape presents a much less severe problem to the design of a retardation system.

Heat shield and structure weight studies for the two shapes resulted in comparisons as shown in figure 59. For a constant $M/C_D A$ vehicle, the V-2 heat shield and structure weights are lower by approximately 30 percent. The weight which is saved with the V-2 vehicle can, of course, be utilized for scientific payload weight.

The V-2 blunt cylindrical shape is suitable for easy packaging of the scientific payload. Also, experimental investigation of the static stability has indicated that the center of gravity location can be placed as far rearward as the centroid of the internal volume, thus showing a high degree of compatibility with the packaging requirements.



63-9825

Figure 57 MARS V-2 ENTRY VEHICLE EXTERNAL CONFIGURATION

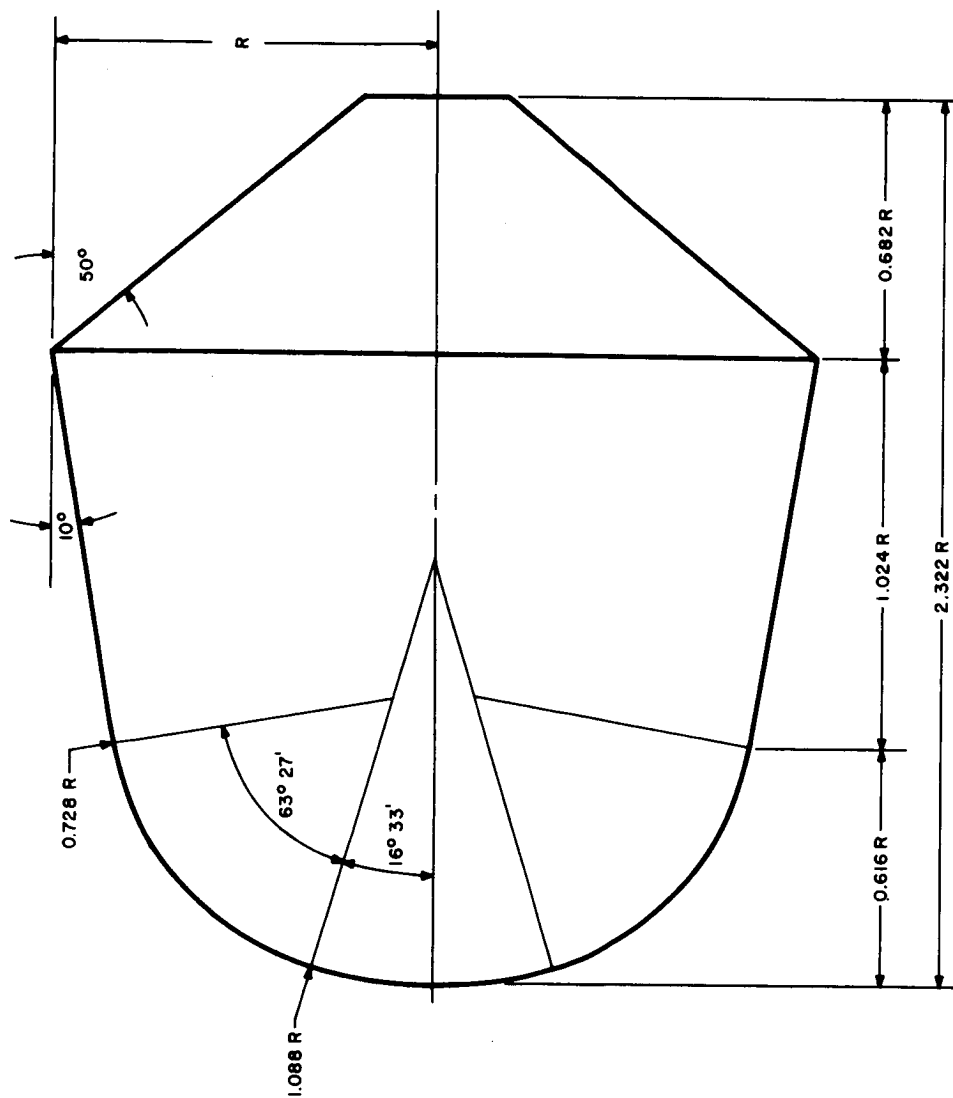


Figure 58 V-1 VEHICLE CONFIGURATION

63-9824

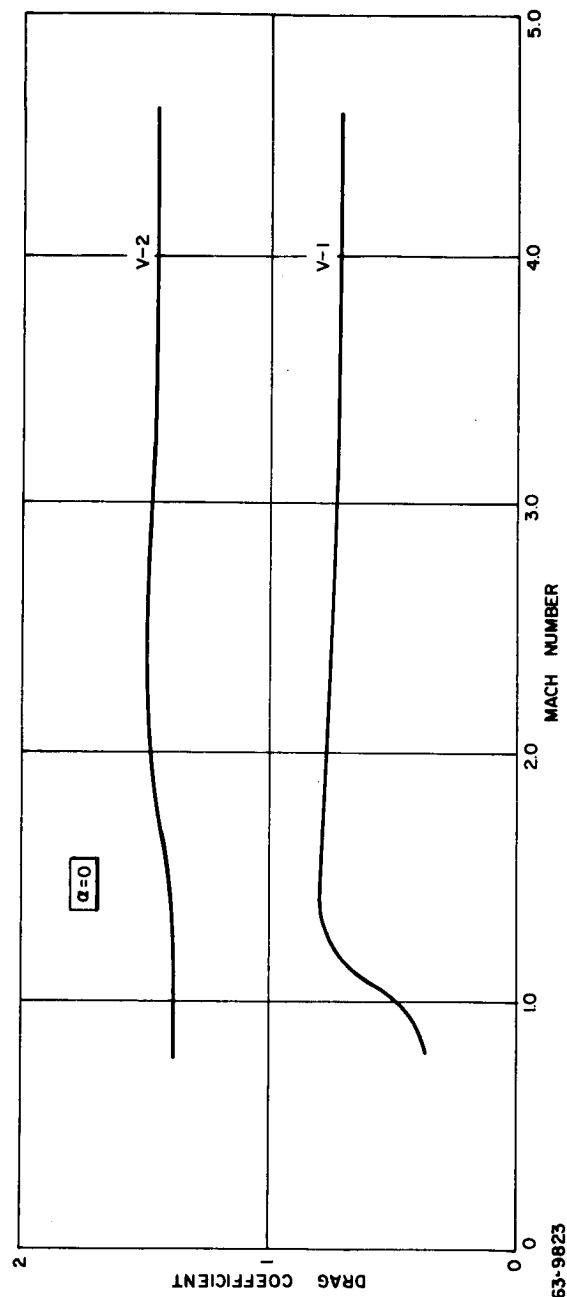


Figure 59 DRAG CURVE COMPARISON FOR V-1 AND V-2 SHAPES

The V-2 vehicle dynamic characteristics were investigated with a six-degree-of-freedom trajectory program and were found to be satisfactory. The results, presented in another section, were used in the vehicle design.

Due to required relatively low ballistic coefficients, the development of a high drag vehicle for the Mars mission could prove beneficial in the future. As higher weight landers are planned, vehicle dimensions would rapidly become excessive for low drag shapes. The ballistic coefficient of 0.9 slug/ft^2 for the reference design was determined with a tradeoff between the parachute descent system requirements and available payload weights. Figure 60 presents the lander residual weight (defined as total minus heat shield, structure, and retardation) as a function of $M/C_D A$ for a given total weight. Assuming a desired minimum drogue chute deployment altitude of approximately 25,000 feet, the $M/C_D A$ limitations as determined by two actuation sensing systems (constant g and constant Mach number deployment) are noted on the plot. The significant increase in residual weight with $M/C_D A$ indicates that the choice of a retardation system which places the least restriction on $M/C_D A$ is desirable. The retardation system with drogue deployment at an approximately constant Mach number was investigated along with other possibilities and found to be satisfactory (see section on (Descent system) resulting in the selection of a vehicle ballistic coefficient of 0.9 slug/ft^2 .

The available payload weight for the lander as a function of total entry weight was then determined and, with the specification of a desired scientific package weight, resulted in the selection of a total entry weight of 1410 pounds and a vehicle diameter of 6.45 feet.

3. Aerodynamic coefficients. The V-2 shape aerothermodynamic characteristics have been defined in test programs as listed in table 7.

The static aerodynamic coefficients for an angle of attack range of 0 to 110 degrees are derived from experimental data with the results comparing well with Newtonian predictions. Newtonian theory was utilized for the remaining angle of attack range. The vehicle center of pressure variation indicates that the limiting center of gravity location is governed by the stability limits at zero angle of attack. The reference vehicle has only the single trim point at zero angle of attack and is thus acceptable for a tumbling entry.

The dynamic damping coefficients are obtained from wind tunnel and ballistic range tests at angles of attack up to 20 degrees and Mach numbers to 7.5. Satisfactory damping is indicated at Mach numbers above 1.5 with the measured coefficients being much more favorable than Newtonian predictions. Further testing is required to determine possible changes in the dynamic stability characteristics due to afterbody modifications. Higher angle of attack and Mach number tests are also required.

TABLE 7

SUMMARY OF AEROTHERMODYNAMIC TESTS

Mach No.	Facility and Test No.	Angle-of-Attack Range	Type Tests	Purpose of Tests
1.4 < M < 4.8	JPL 20-400	$-4^{\circ} < \alpha < 20^{\circ}$	3-component static force	Define force characteristics and pressure distributions in low Mach number range.
		$-4^{\circ} < \alpha < 20^{\circ}$	Pressure distribution	
1.4 < M < 4.8	JPL 20-407	$\alpha = +12^{\circ}$	Free oscillation, dynamic stability	Define in low Mach number range. 1. Dynamic stability. 2. High angle-of-attack effects. 3. Effect of corner radius on pressure distribution.
		$30^{\circ} < \alpha < 110^{\circ}$	3-component static force	
		$-4^{\circ} < \alpha < 20^{\circ}$	Pressure distribution	
5. < M < 9.5	JPL 21-18	$-4^{\circ} < \alpha < 20^{\circ}$	Pressure distribution	Define force characteristics and pressure distributions in the medium Mach number range
M \approx 20	AEDC Hot Shot II	$0^{\circ} < \alpha < 20^{\circ}$	Pressure distribution	Define pressure distribution and force characteristics in the hypersonic Mach number range.
.7 < M < 5.0	NASA	$0^{\circ} < \alpha < 15^{\circ}$	Force oscillation, dynamic stability	Define damping coefficients at angle-of-attack in low Mach number range.
M \approx 18	CAL 24" Shock Tunnel	$0^{\circ} < \alpha < 180^{\circ}$	3-component static force	Define viscous, force effects and heat transfer rates at high angles-of-attack in the hypersonic Mach number range.
		$0^{\circ} < \alpha < 110^{\circ}$	Pressure and heat transfer	
1. < M < 6	AVCO Ballistic Range		Qualitative	Check gross static stability in low Mach number range.

Mach No.	Facility and Test No.	Angle-of-Attack Range	Type Tests	Purpose of Tests
1.2 < M < 3.7	BRL		Static coefficients and dynamic stability	Define dynamic characteristics in low to medium Mach number range. Also check wind tunnel results.
4.6 < M < 6.2	NOL		Static coefficients and dynamic stability	Define dynamic characteristics in low to medium Mach number range. Also check wind tunnel results.

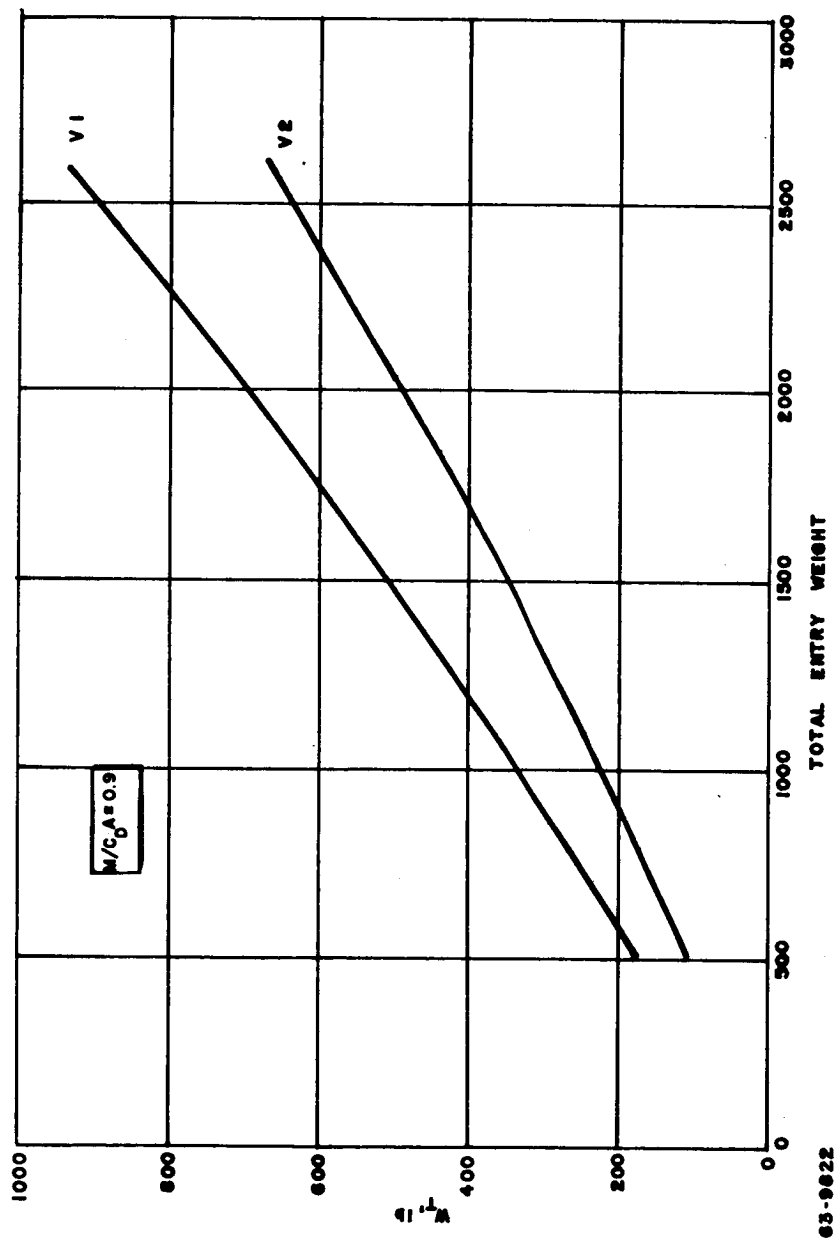


Figure 60 MARS LANDER COMPARISON BETWEEN V-1 AND V-2 VEHICLES WEIGHT OF HEAT SHIELD, BOND, AND STRUCTURE ($M/C_D = 0.9$)

The aerodynamic coefficients were utilized for both particle trajectory and six-degree-of-freedom trajectory computer programs with the results being presented in the following section.

3.2 Vehicle Performance

1. Entry trajectories. A study of the lander entry characteristics was conducted with the use of particle trajectory and six-degree-of-freedom trajectory programs. The range of entry conditions investigated included an entry velocity variation of 16,000 to 29,000 ft/sec and an entry angle of -20 to -90 degrees. The minimum entry angle of -20 degrees was selected to avoid possibilities of excessive integrated heating input and flight times due to aerodynamic skipping. The entry altitude was considered to be 800,000 feet due to the lack of significant aerodynamic effects above this altitude.

The basic philosophy with respect to entry conditions variation and vehicle design was to determine the possibility and penalties of a single lander design for all launch dates under consideration. For the general study, the entry angle was not restricted due to reliability and landing site selection considerations. Thus, the effect of entry velocity variation on a lander designed for a full entry angle velocity variation on a lander designed for a full entry angle range was determined. The higher entry velocity possibilities for type I launches in 1969 proved to penalize the heat shield design rather severely. A vehicle designed to the maximum entry velocity of 29,000 ft/sec would therefore be inefficient for the bulk of the launch possibilities. The heat shield and structure for the reference vehicle has instead been designed for entry conditions which cover the greatest portion of the likely launch possibilities ($V_e = 24,000$ ft/sec).

Atmospheric variations are considered to be represented by the limiting atmospheric models as given by Schilling (ref. 5). The extreme range of temperatures were used and combined with the molecular weight estimates to provide the extreme range in scale height. The atmospheric parameters used in the study are given in table 8. The aerodynamic characteristics utilized are discussed in the previous paragraph 3. The velocity and altitude histories obtained with the particle trajectory program did not differ significantly from six-degree-of-freedom results. Therefore, the general parametric studies involving loads, heating, and the descent system utilized the more economical particle trajectory program. In addition to entry condition and atmospheric model variations, the effects of change in vehicle ballistic coefficient and size were determined.

The results of the entry study are presented primarily in summary form in other sections (i.e., loads, heating, angle of attack effects, and retardation system). Several time histories of flight conditions, total angle of attack envelope, and loads are shown in figures 61 through 66 to indicate some typical six-degree-of-freedom entry trajectories for the reference design. The results

TABLE 8
ATMOSPHERIC DATA USED FOR MARS

	Minimum Temperature	Maximum Temperature
Surface Temperature	200°K	300°K
Stratosphere Temperature	102°K	263°K
CO ₂ Concentration	12.5%	1.0%
N ₂ Concentration	87.5%	99.0%
Sea Level Density	1.44 x 10 ⁻⁴ slug/ft ³	2.89 x 10 ⁻⁴ slug/ft ³
Lapse Rate	Adiabatic	Adiabatic

shown in figures 61 and 62 are for a trajectory which has been run to impact without a stabilization chute deployment. It is noted that the rapid angle of attack divergence occurs at a Mach number of about 1.5 (vehicle dynamic damping coefficient becomes positive) whereas the selected retardation system deploys a drogue chute at approximately a Mach number of 2.5. Figure 63 shows the effects of initial pitch rate, c.g. offset, and moment of inertia cross products on the same trajectory. Similar time histories for different entry conditions are shown in figures 64 and 65. Figure 66 is of interest as it compares the total angle of attack and dynamic pressure histories for the two limiting atmospheric models. The fact that the dynamic pressure peaks occur at altitudes that are 200,000 feet apart illustrates the large atmospheric variation considered in the Voyager study.

2. Dynamics study results. The vehicle dynamics study was conducted with the six-degree-of-freedom trajectory program presented (ref. 6). The possible vehicle initial motion at entry is defined by the approach geometry and lander separation from the orbiter with maximum values of 90 degree angle of attack, 1 rad/sec spin rate, and 0.1 rad/sec pitch rate being used for the vehicle design. The study also determined effects of extensions of these limits. The lander parametric weight studies were used to determine the inertia characteristics which were utilized.

The results from the vehicle dynamics study have been utilized to determine angle-of-attack effects on the lander design. The angles of attack at peak heating, peak loads, and parachute deployment have been determined as a function of initial vehicle motion, flight path entry angle, entry velocity, atmospheric model, and vehicle size. Factors were calculated for use in the design of the heat shield, structure, and parachute activation sensing system.

The vehicle investigated was the V-2 shape with a ballistic coefficient of 0.9 slug/ft² with total weight being varied from 500 to 4000 pounds. The total angle of attack envelopes ($\bar{\alpha}$) at peak heating, peak loads, and Mach number of 2.5 (parachute deployment) is shown to be relatively insensitive to a weight variation in figures 67 and 68. Therefore, results for a 2000-pound lander have been taken to apply for the reference design (1410 pounds). Figures 69 to 77 contain $\bar{\alpha}$ as a function of the vehicle initial motion and entry conditions. With the initial conditions range as stated previously, the following maximum or design angles of attack were determined:

maximum $\bar{\alpha}$ at peak heating \approx 25 degrees
maximum $\bar{\alpha}$ at peak loads \approx 25 degrees
maximum $\bar{\alpha}$ at chute deployment \approx 32 degrees

For the required parametric study, relatively simple methods were used to determine angle-of-attack effect design factors. The heat shield analysis factor assumed a nonspinning vehicle in planar oscillation. The heating at various

longitudinal locations on the body is available as a function of angle of attack (ref. 7) and has been time weighted throughout an oscillation. The resulting heat factor for two body stations is shown in figure 77 as a function of the angle-of-attack envelope.

The structural design factors are simply the vehicle normal acceleration and pressure distribution increase for a given maximum angle of attack (ref. 7).

The effect of a possible angle of attack at parachute deployment must be taken into consideration when determining an axial accelerometer setting for actuation sensing. An angle of attack of approximately 30 degrees causes an axial drag reduction of 85 percent for the V-2 vehicle; thus, if a maximum deployment Mach number of 2.5 is specified, the accelerometer setting must be lowered to insure that the Mach number limitation is not exceeded.

3.3 Effects of Kaplan Atmosphere

1. Atmospheric model. The significant atmospheric parameters of a new atmospheric model variation as proposed by NASA are presented in table 9. The effects on required vehicle performance and descent system selection due to consideration of this new model will be discussed in the following paragraphs.

2. Required vehicle performance. Consideration of the new low density atmosphere (specified as "JPL worst") dictates a lower vehicle ballistic coefficient to enable sufficient retardation for atmospheric sampling and survival of impact. Figure 79 indicates typical parachute deployment altitudes as a function of M/C_{DA} for a "worst" combination of entry angle and atmospheric model. Whereas $M/C_{DA} = 0.9$ slug/ft² was acceptable for the atmospheric variation as specified by Schilling, a M/C_{DA} in the range of 0.2 to 0.3 is required for the new atmosphere. Figures 80 to 82 present velocity, altitude, and deceleration histories in the new atmosphere to indicate typical entry performance for a vehicle with the required ballistic coefficient.

For a given entry weight, the vehicle dimensions tend to become very large for the range of M/C_{DA} under consideration. Thus, the required heat shield and structural weight increases rapidly as M/C_{DA} is decreased. A descent system must then be selected which places the least restriction on the selection of the ballistic coefficient while not becoming excessively heavy. A tradeoff of parachute, heat shield, and structural weight versus vehicle M/C_{DA} should then determine the exact value of the ballistic coefficient for the vehicle design.

3. Vehicle shape. The required low $M/C_D A$'s result in large vehicle dimensions for a given entry weight. A blunt shape would thus be desired to prevent the dimensions from becoming excessive. The basic Apollo configuration (figure 83) was selected due to 1) the blunt shape, 2) the weight saving conical afterbody, and 3) the availability of experimental aerodynamic data.

TABLE 9

MARS JPL ATMOSPHERE AND
UNCERTAINTIES

Property		Worst			Nominal	Best
Surface Pressure, (mb)	P _o	11				30
Stratosphere Temperature °K	T _s	130	230		180	130
Surface Temperature °K	T _o	260			230	210
Acceleration of Gravity at Surface (cm/sec ²)	ϕ	375			375	375
Composition, molar concentration percent						
CO ₂		65			43	11
A		35			32	13
N ₂		0			25	76
Molecular Weight	M	42.7			38.7	31.2
Specific Heat Ratio		1.40			1.42	1.42
Adiabatic Temperature Lapse Rate Troposphere Γ °K/km)		5.30			4.81	3.93
Tropopause Altitude, km	h _T	24.5	5.66		10.4	23.5
Inverse Scale Height, km ⁻¹	β	0.148	0.0838	0.0838	0.0970	0.108
Surface Density, gm/cm ³	ρ _o /10 ⁻⁵	2.17			3.04	5.36
Artificial Surface Density gm/cm ³	ρ _o ¹ /10 ⁻⁵	13.2	2.53		4.37	14.1
Density at Tropopause, gm/cm ³	ρ _{TP} /10 ⁻⁵	0.347	1.57		1.60	1.55

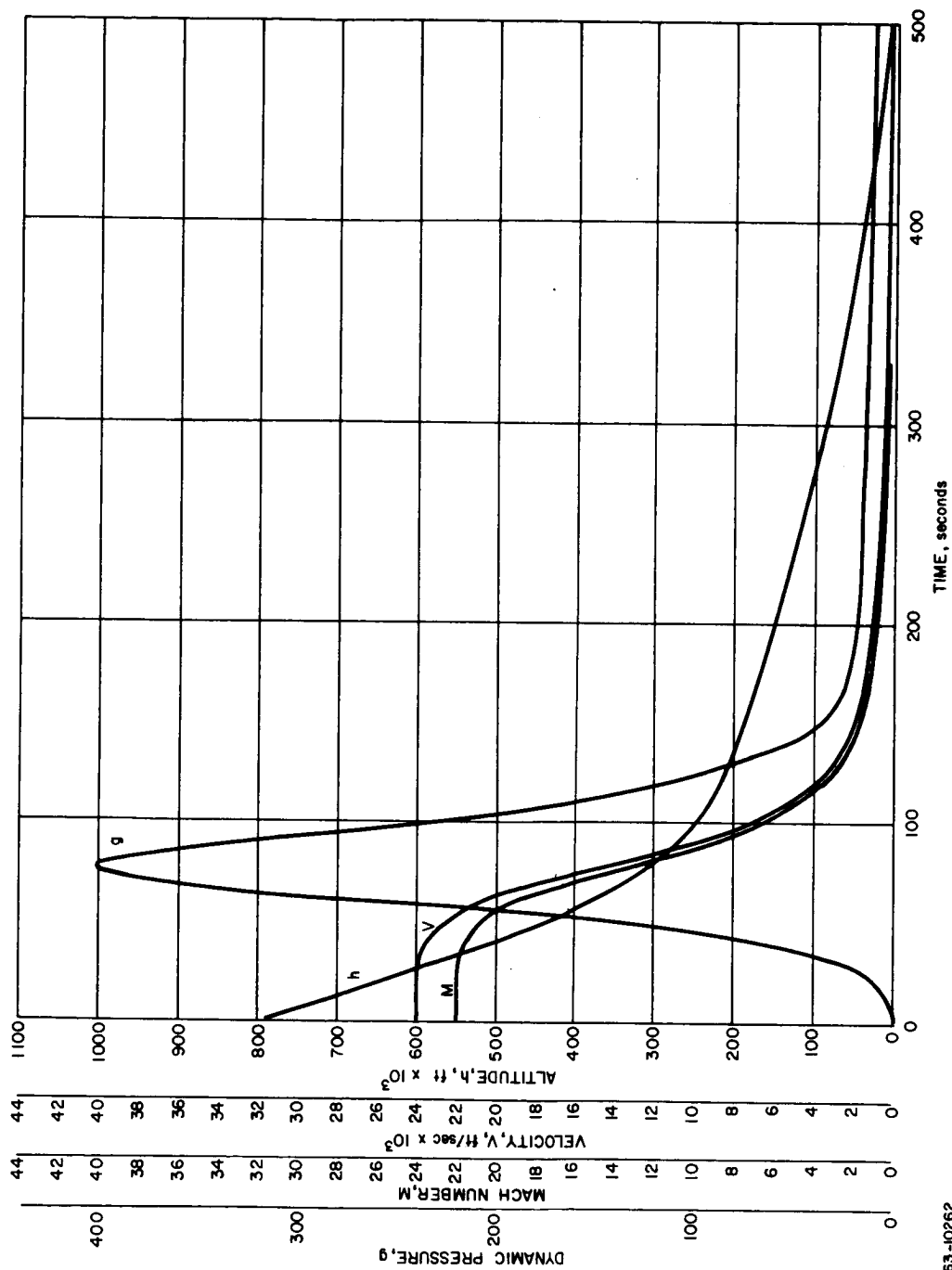
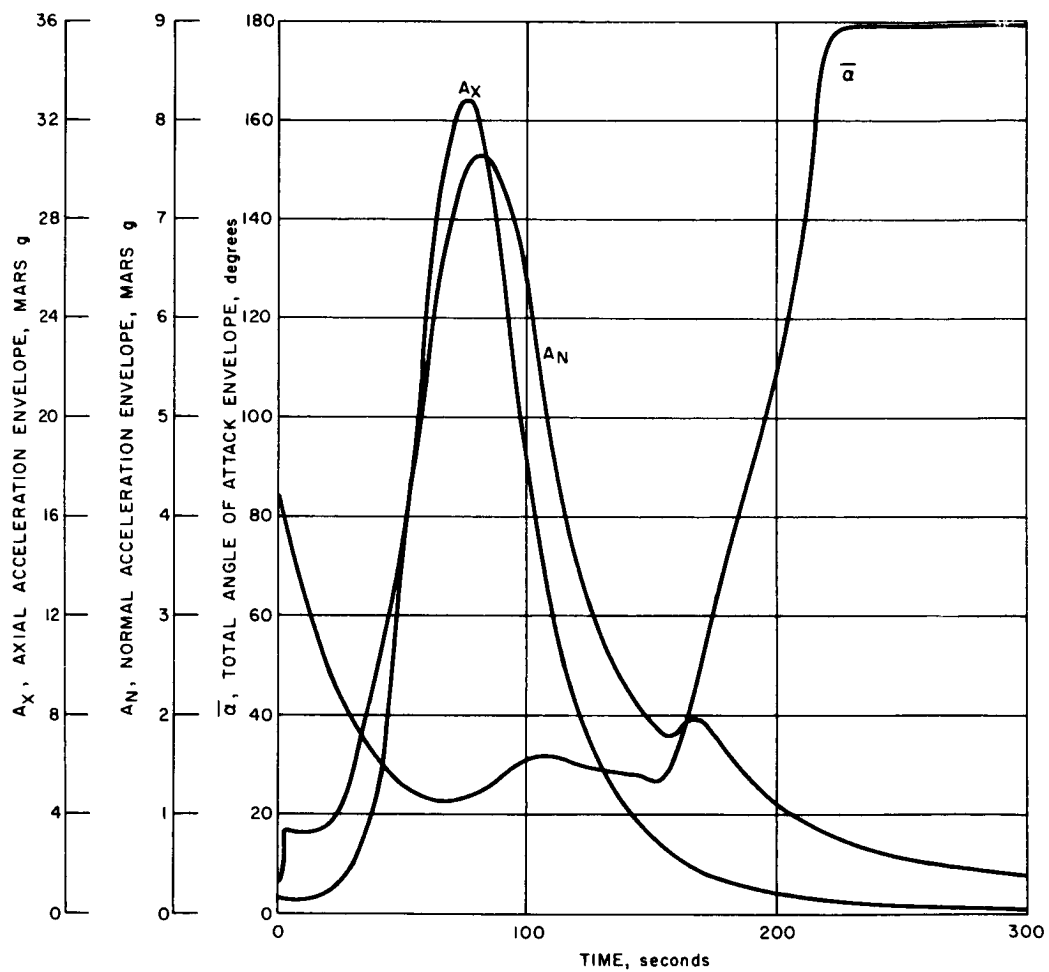


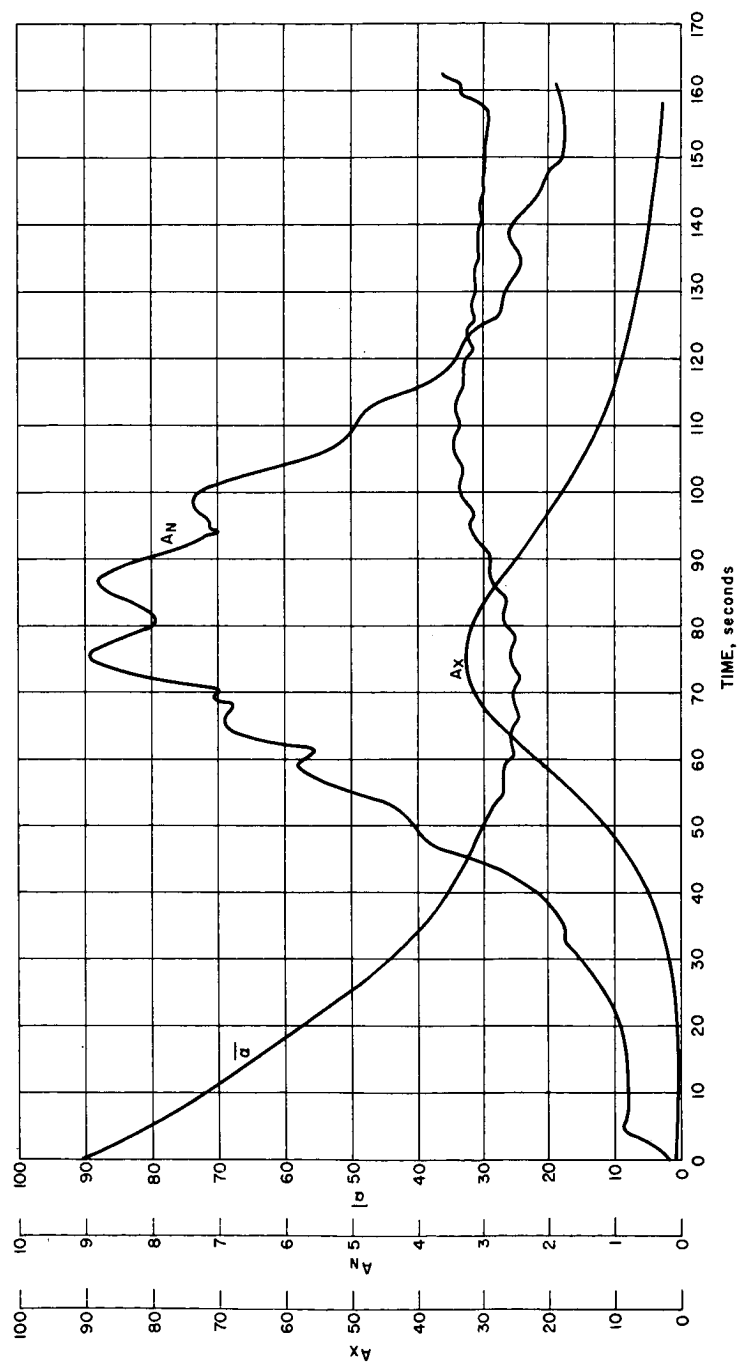
Figure 61 RESULTS OF VEHICLE DYNAMIC ANALYSES

63-10262



63-10263

Figure 62 RESULTS OF VEHICLE DYNAMIC ANALYSES



63-10264

Figure 63 RESULTS OF VEHICLE DYNAMIC ANALYSES

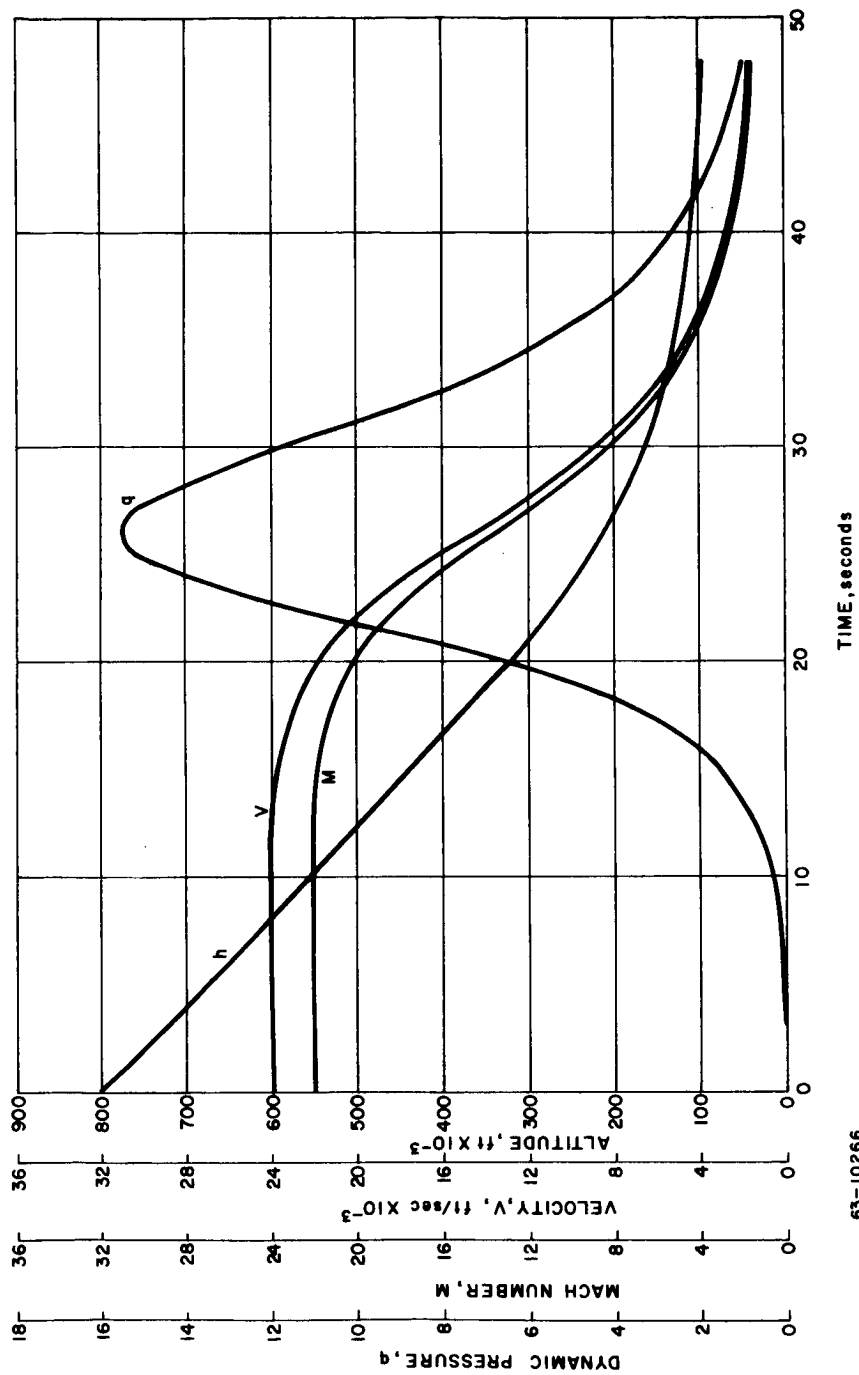


Figure 64 RESULTS OF VEHICLE DYNAMIC ANALYSES

63-10266

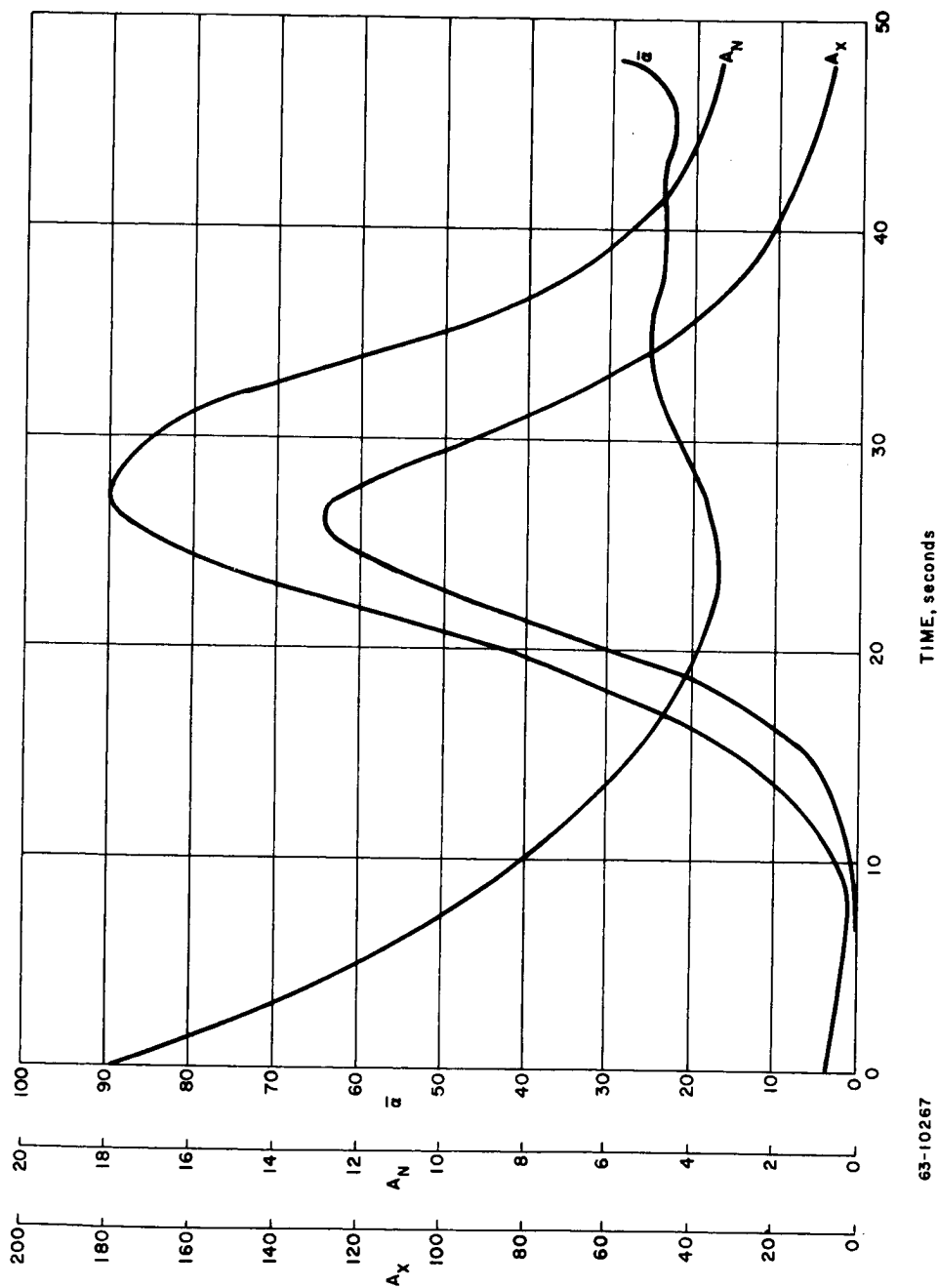
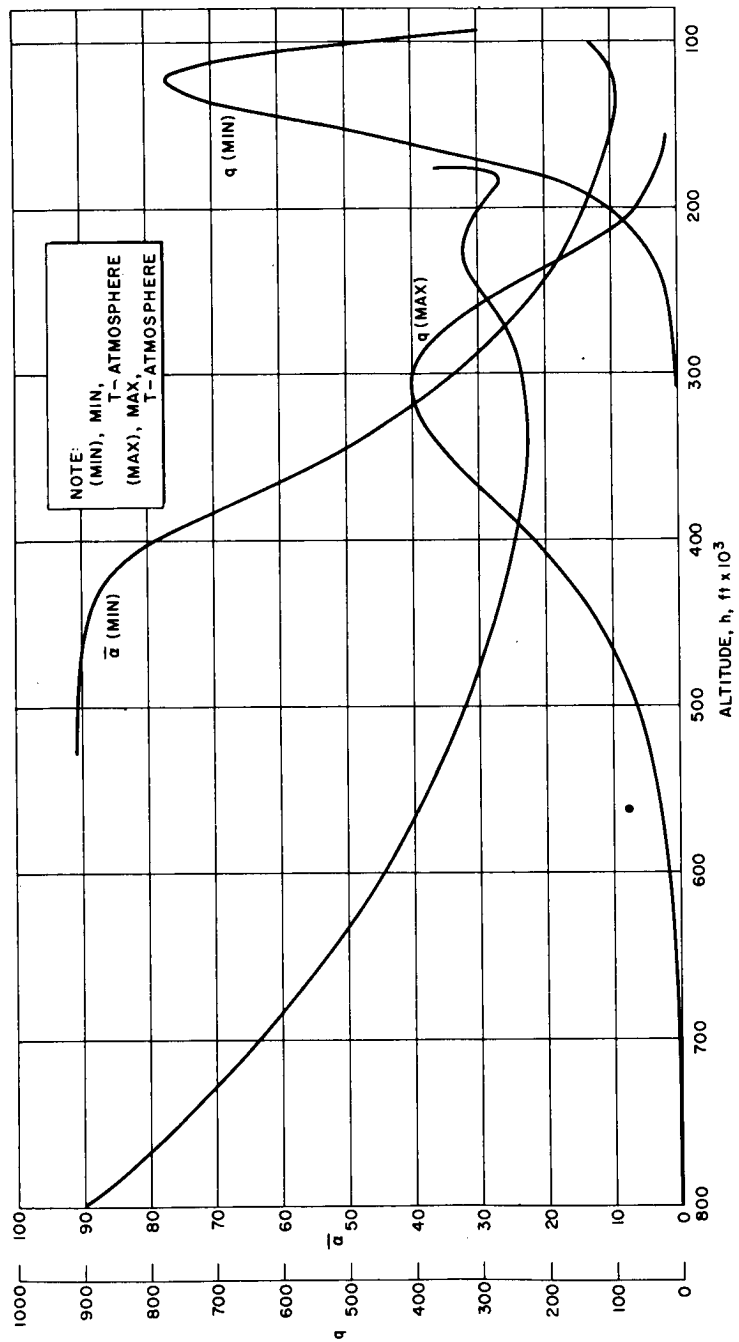
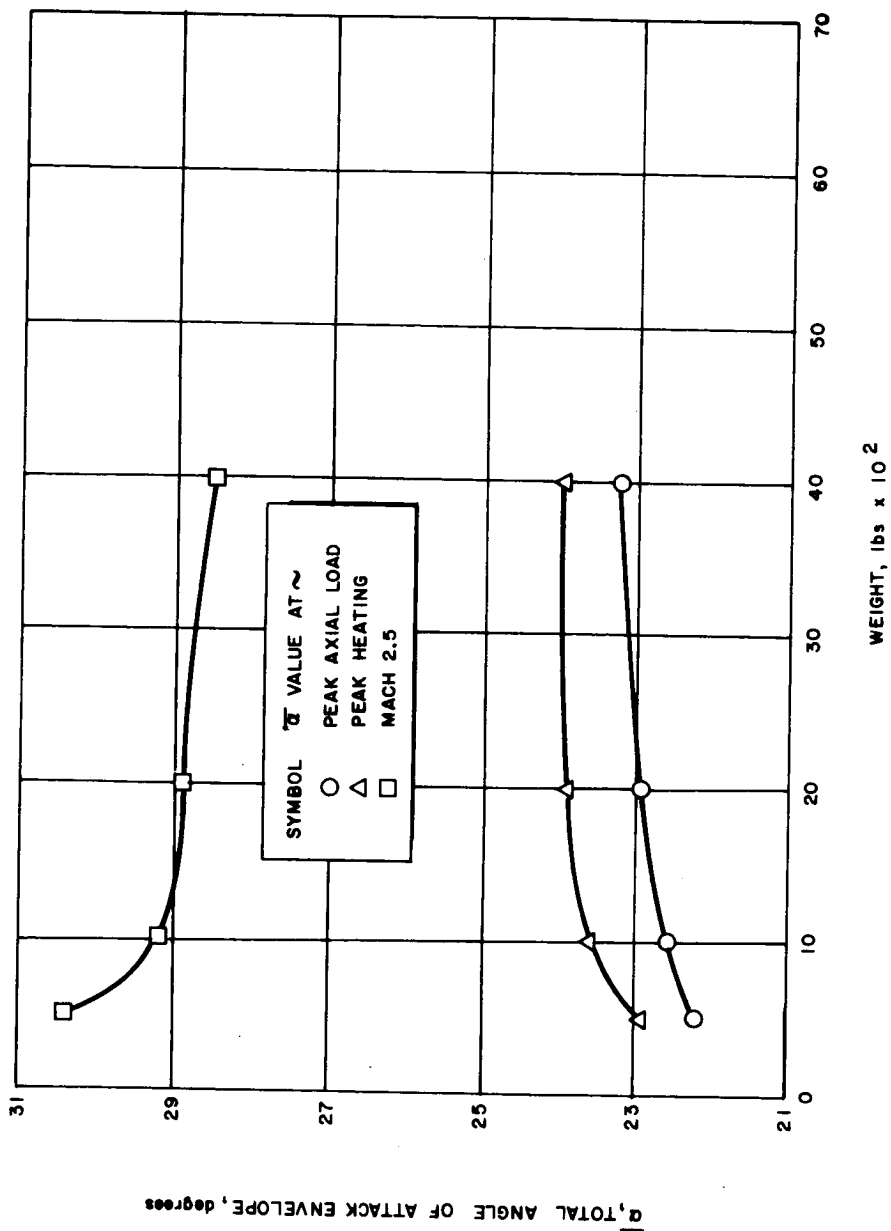


Figure 65 RESULTS OF VEHICLE DYNAMIC ANALYSES



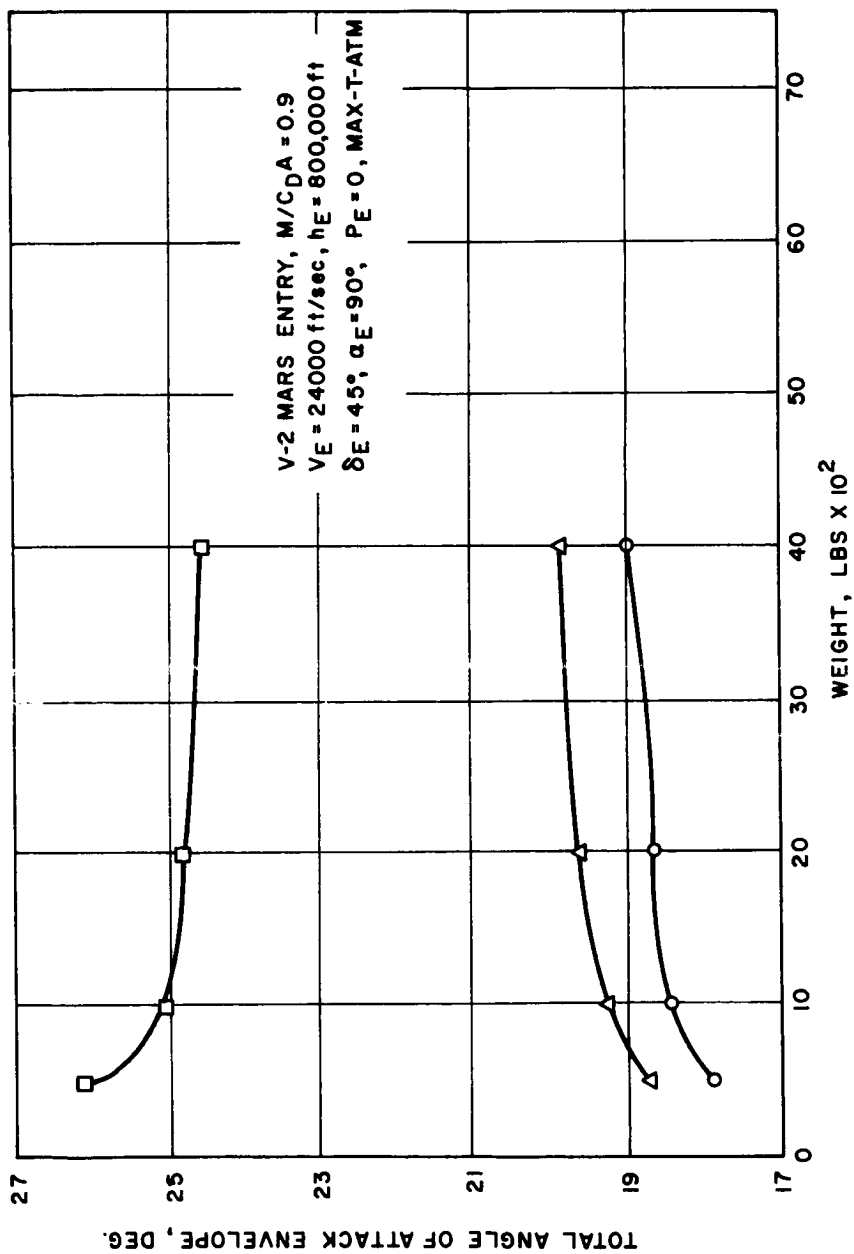
63-10265

Figure 66 RESULTS OF VEHICLE DYNAMIC ANALYSES



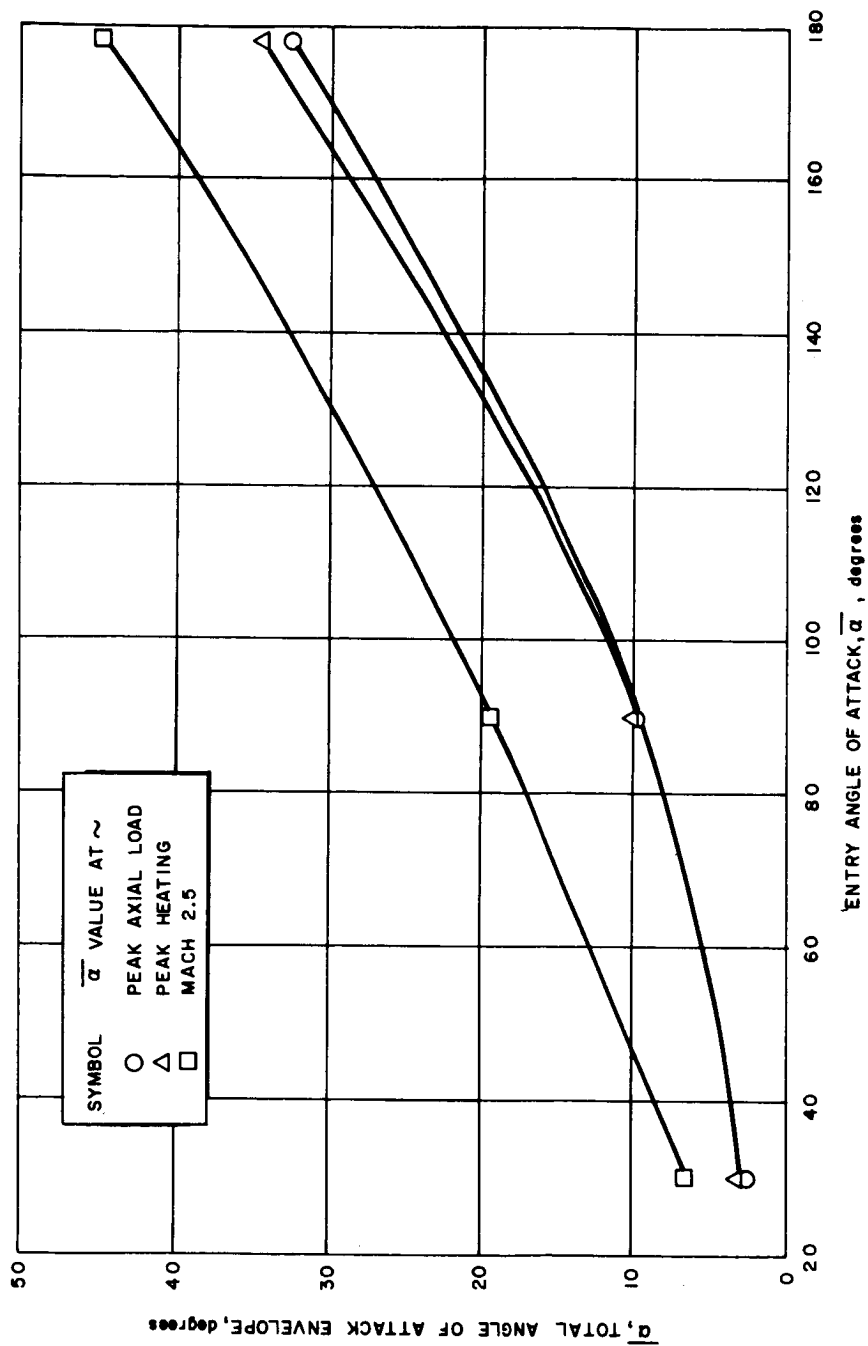
63-10086

Figure 67 TOTAL ANGLE OF ATTACK ENVELOPE VERSUS WEIGHT FOR V-2 MARS ENTRY



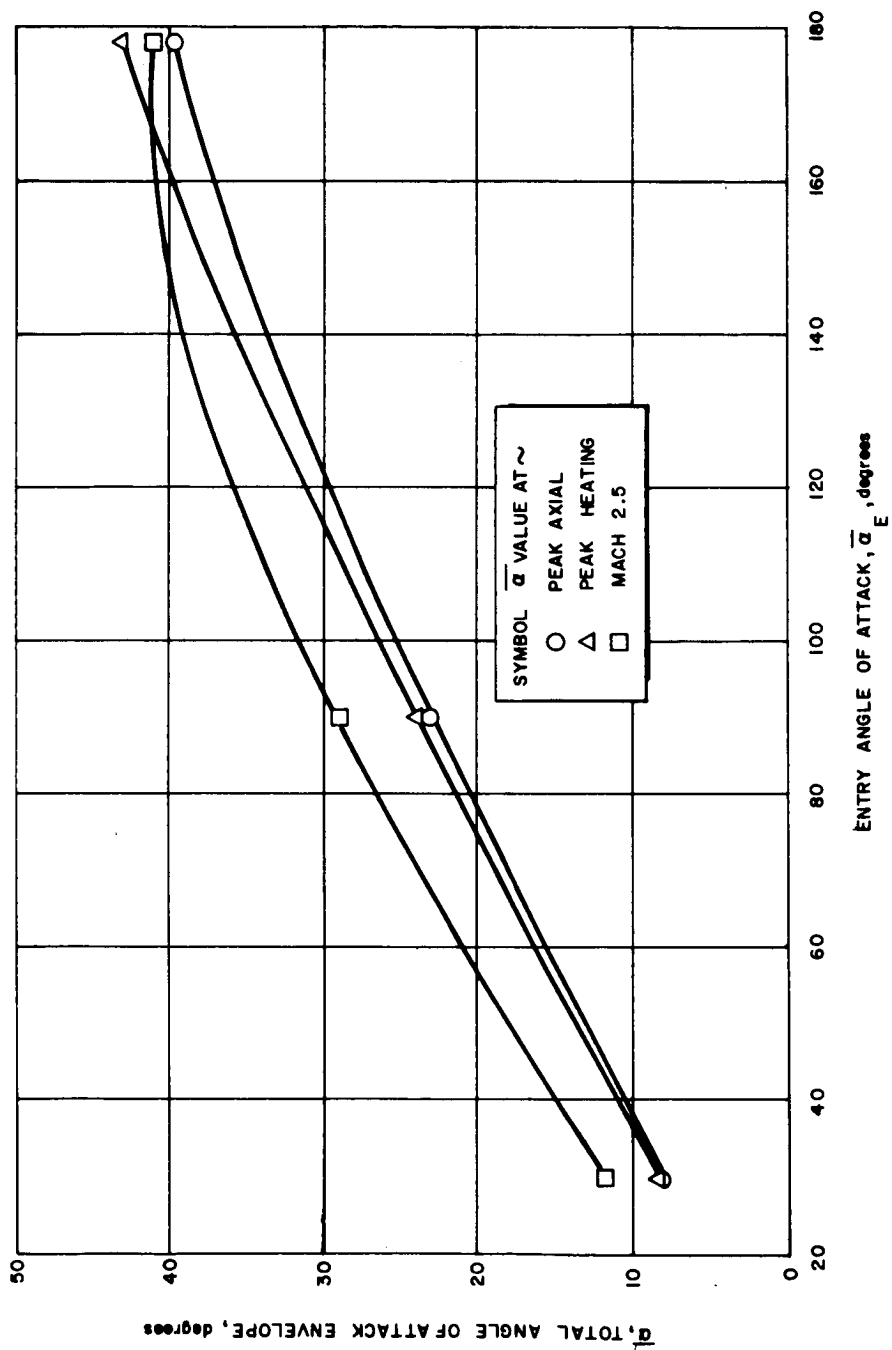
63-10289

Figure 68 TOTAL ANGLE OF ATTACK ENVELOPE VERSUS WEIGHT FOR V-2 MARS ENTRY

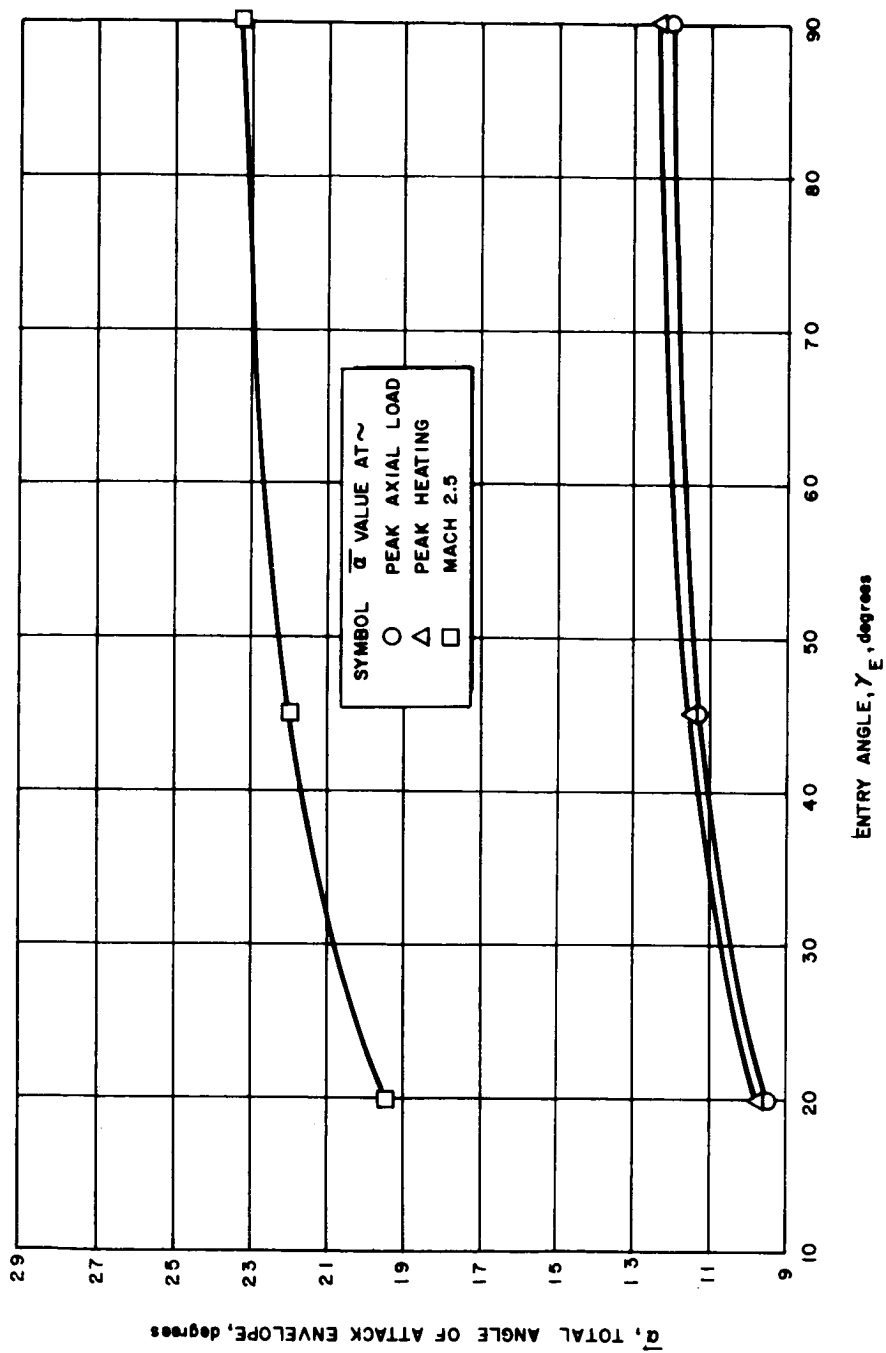


63-10079

Figure 69 TOTAL ANGLE OF ATTACK ENVELOPE VERSUS ENTRY ANGLE OF ATTACK FOR V-2 MARS ENTRY

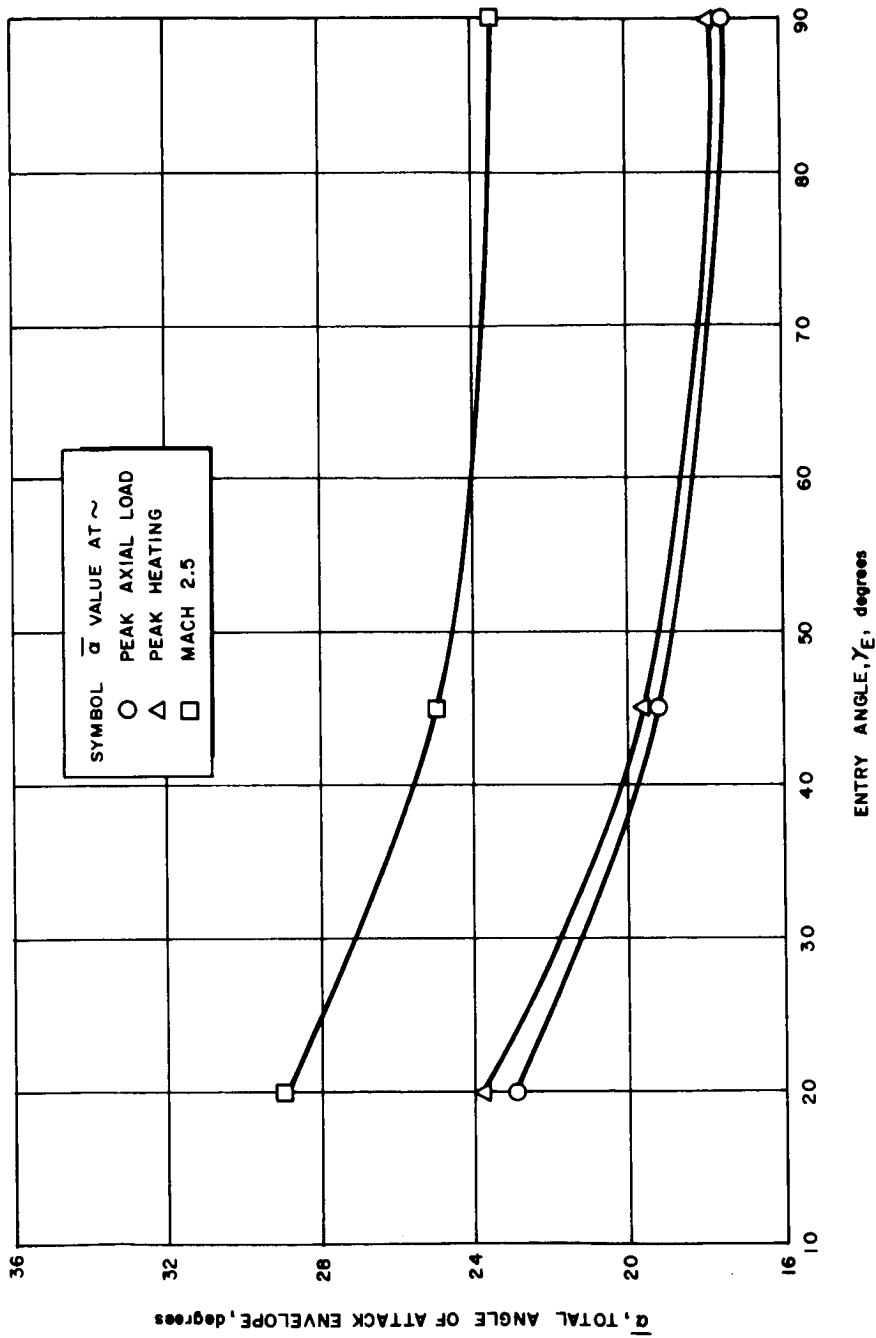


63-10080 Figure 70 TOTAL ANGLE OF ATTACK ENVELOPE VERSUS ENTRY ANGLE OF ATTACK



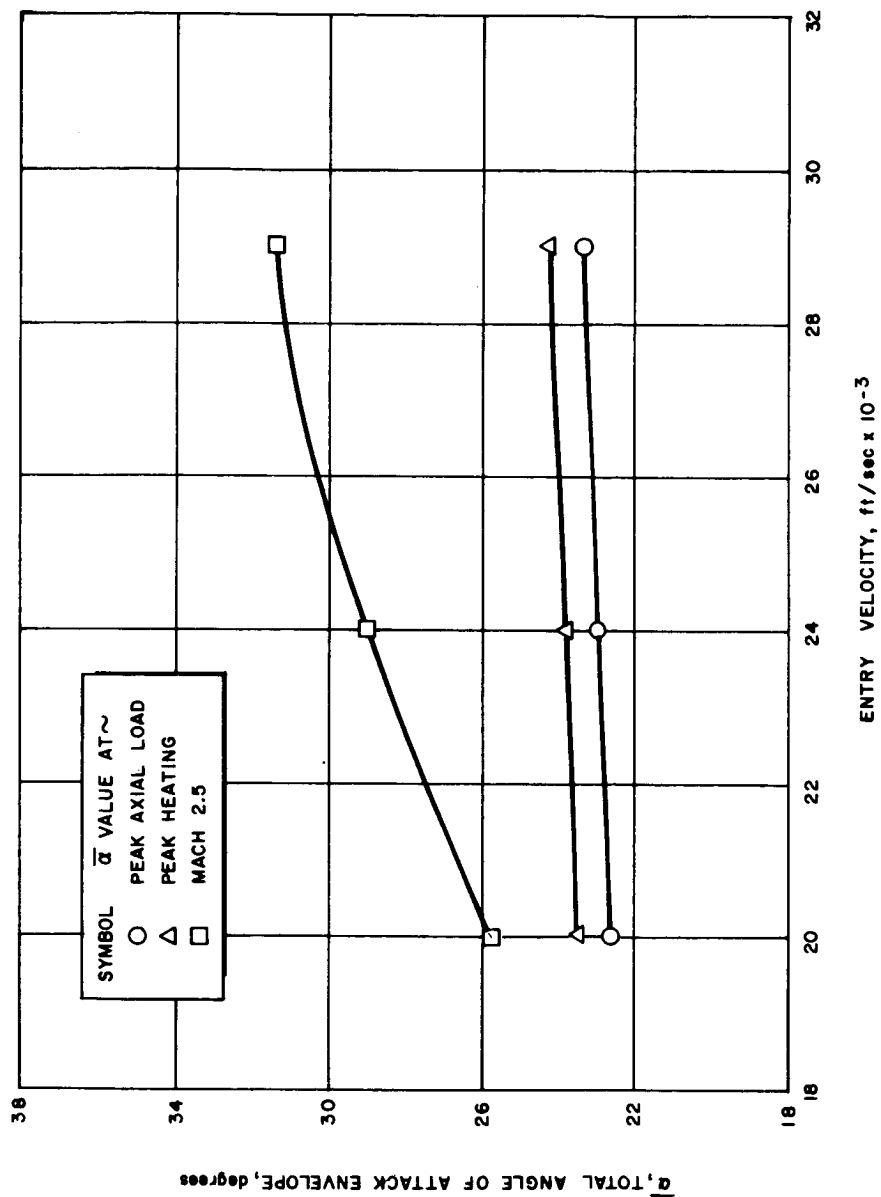
63-10078

Figure 71 TOTAL ANGLE OF ATTACK ENVELOPE VERSUS ENTRY ANGLE FOR V-2 MARS ENTRY



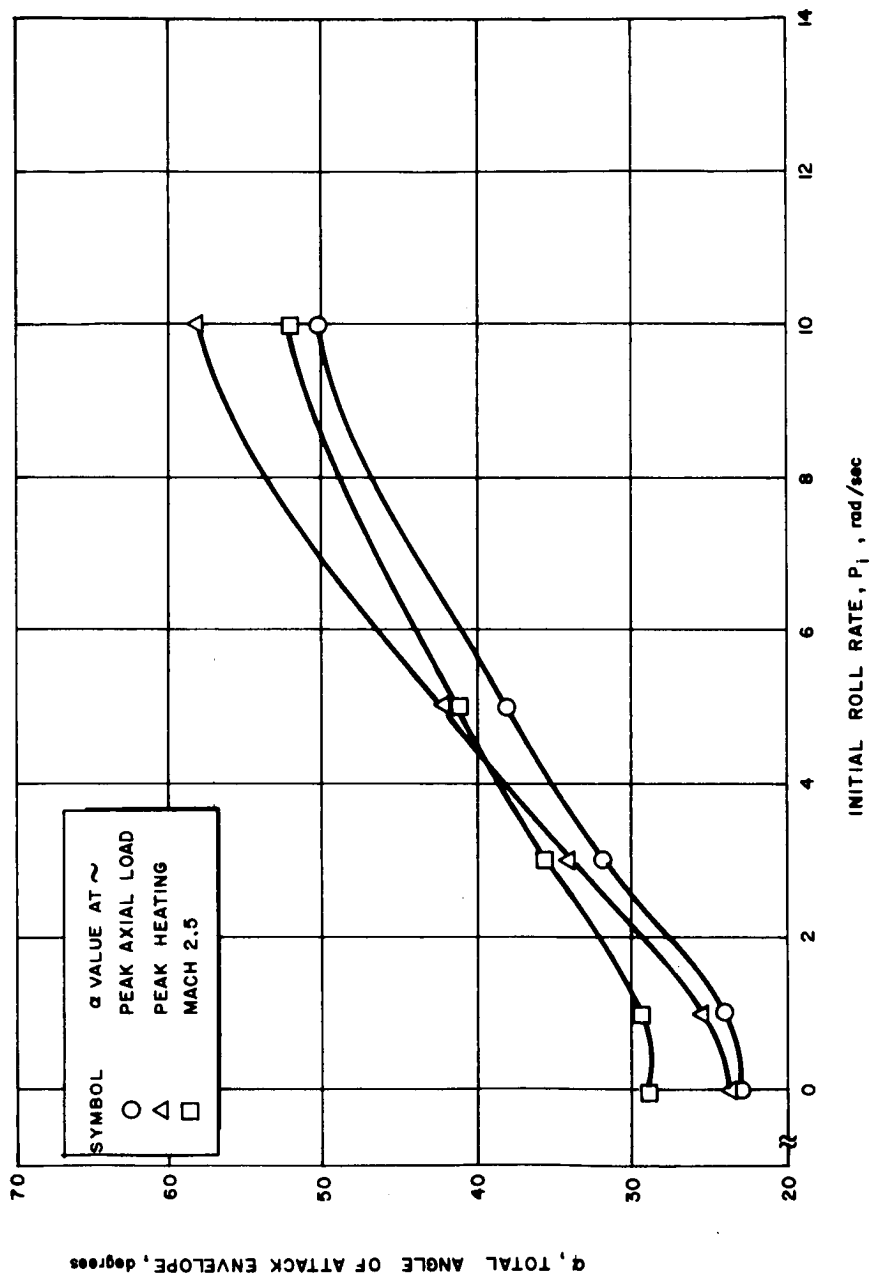
63-10077

Figure 72 TOTAL ANGLE OF ATTACK ENVELOPE VERSUS ENTRY ANGLE FOR V-2 MARS ENTRY



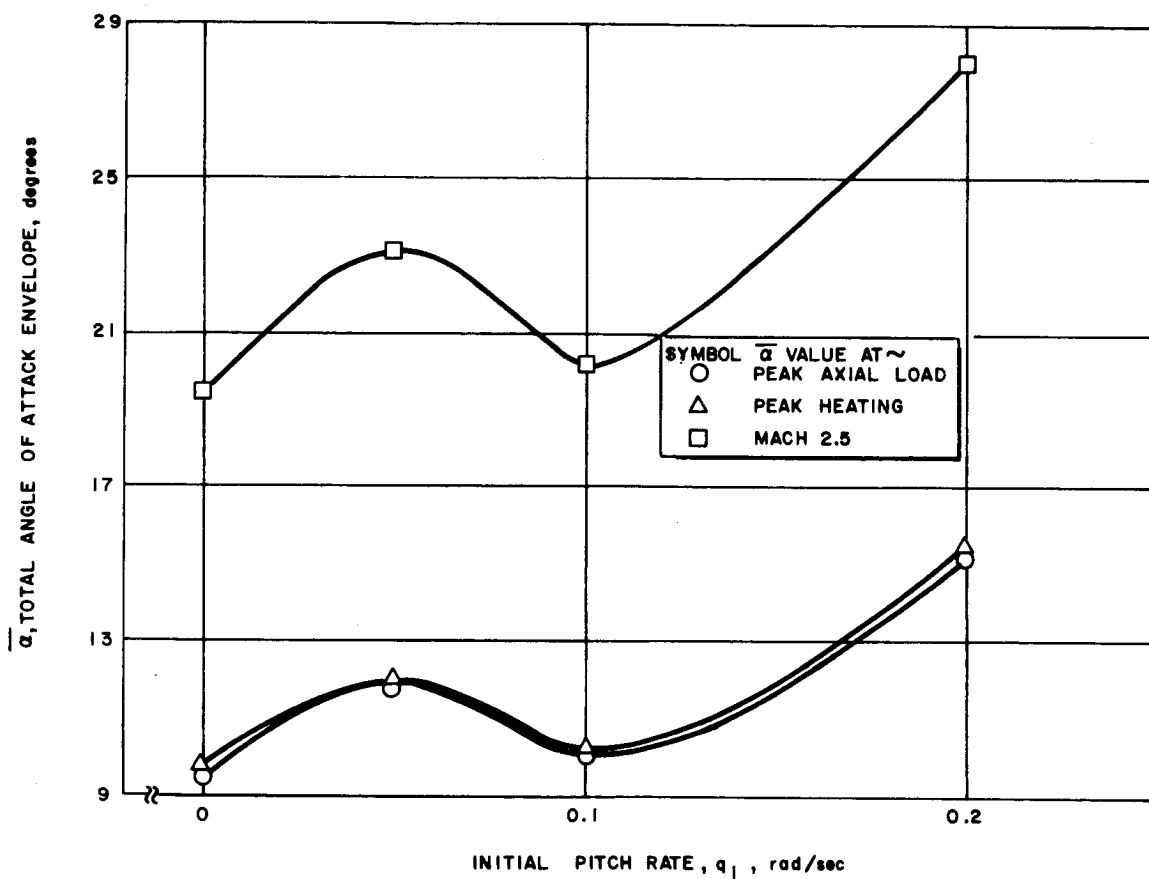
63-10076

Figure 73 TOTAL ANGLE OF ATTACK ENVELOPE VERSUS ENTRY VELOCITY FOR V-2 MARS ENTRY



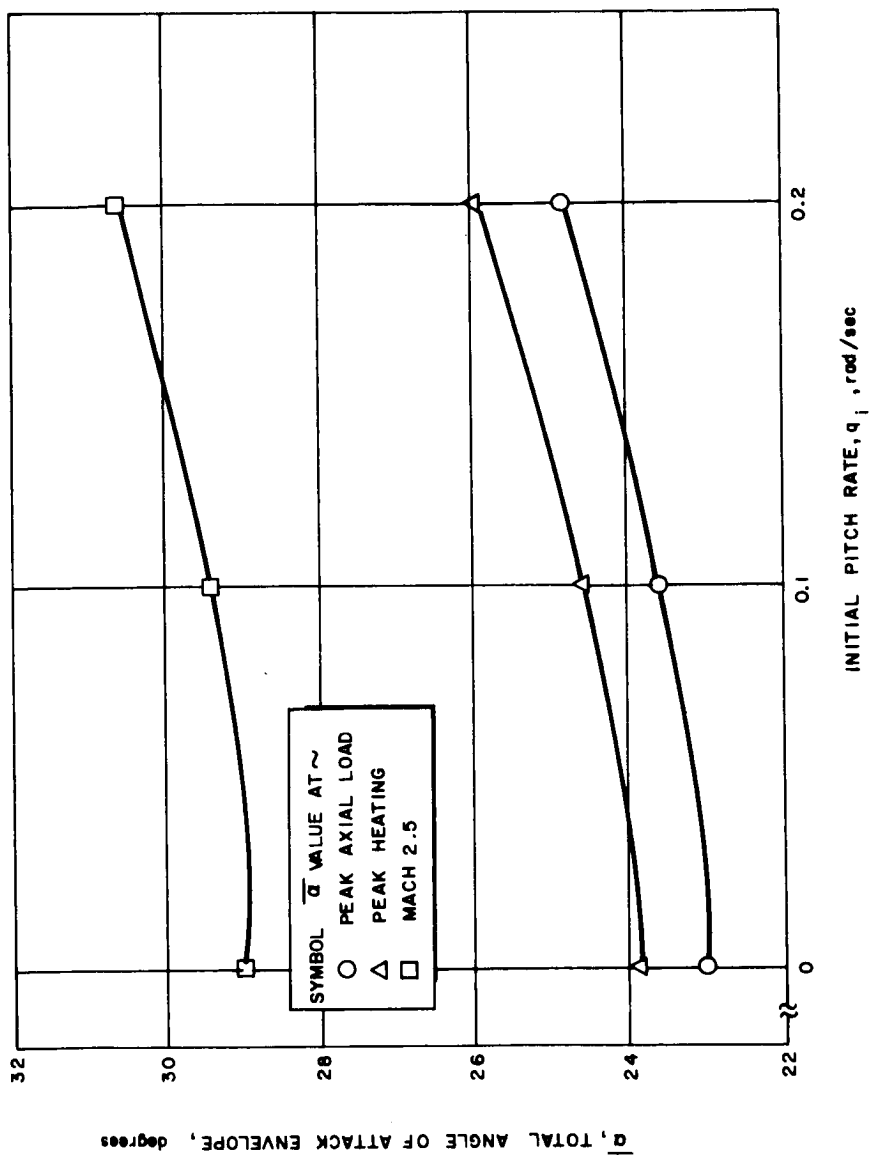
63-10094

Figure 74 TOTAL ANGLE OF ATTACK ENVELOPE VERSUS INITIAL ROLL RATE FOR V-2 MARS ENTRY



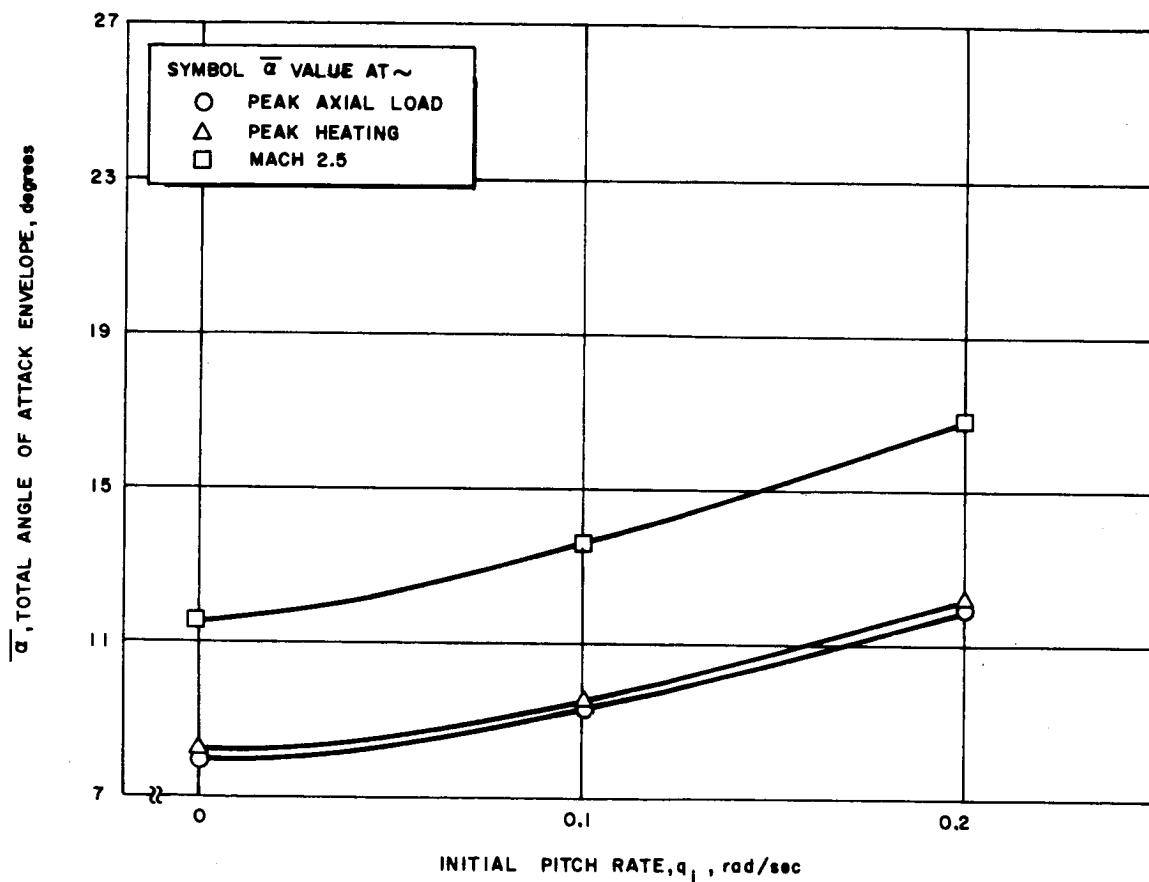
63-10085

Figure 75 TOTAL ANGLE OF ATTACK ENVELOPE VERSUS INITIAL PITCH RATE FOR V-2 MARS ENTRY



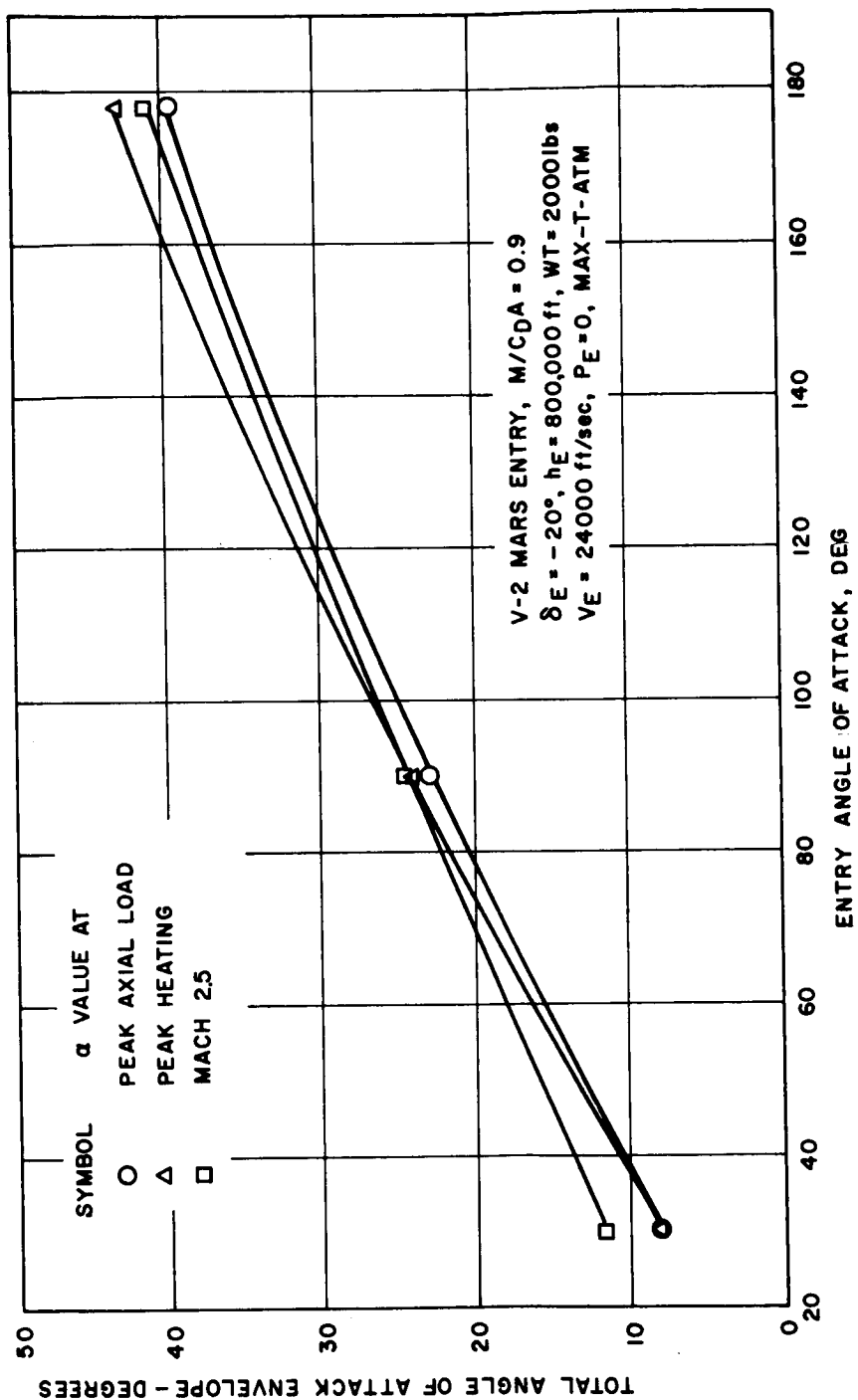
63-10082

Figure 76 TOTAL ANGLE OF ATTACK ENVELOPE VERSUS INITIAL PITCH RATE FOR V-2 MARS ENTRY



63-10081

Figure 77 TOTAL ANGLE OF ATTACK ENVELOPE VERSUS INITIAL PITCH RATE FOR V-2 MARS ENTRY



63-10287

Figure 78 TOTAL ANGLE OF ATTACK ENVELOPE VERSUS ENTRY ANGLE OF ATTACK

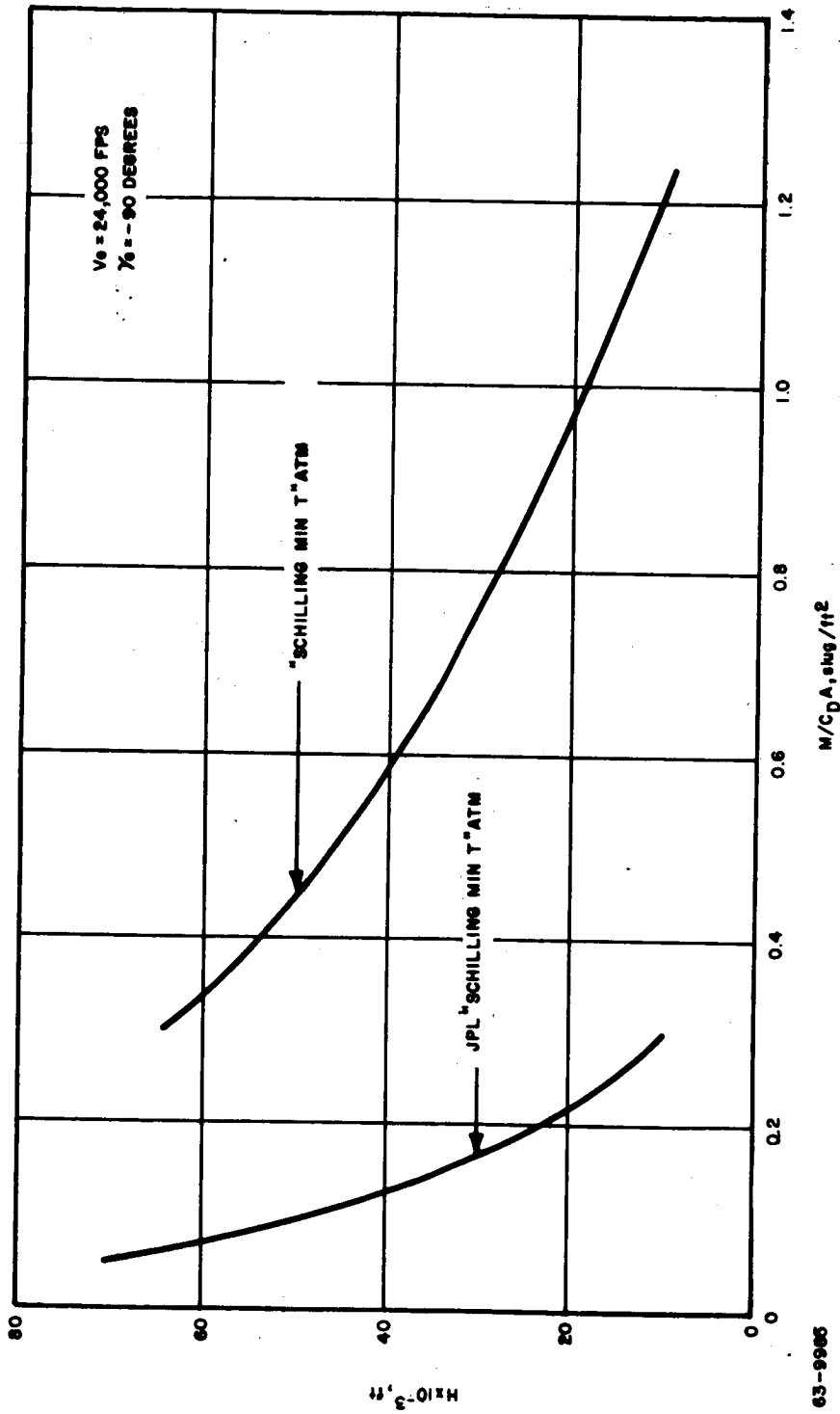


Figure 79 EFFECT OF MODEL ATMOSPHERE CHANGE ALTITUDE AT $M = 2.5$ VERSUS $M/C_D A$

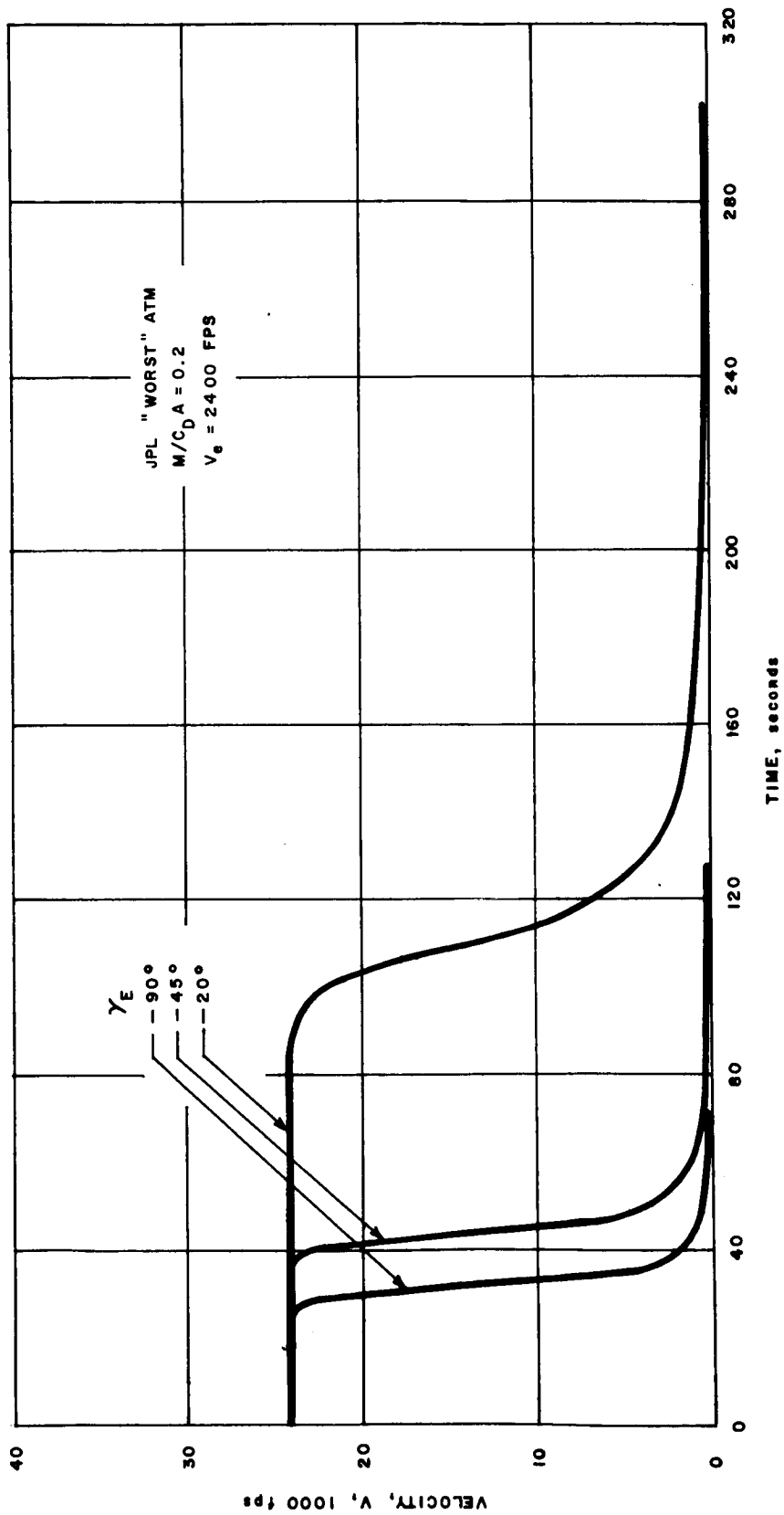


Figure 80 VELOCITY VERSUS TIME FOR MARS LANDER

63-9981

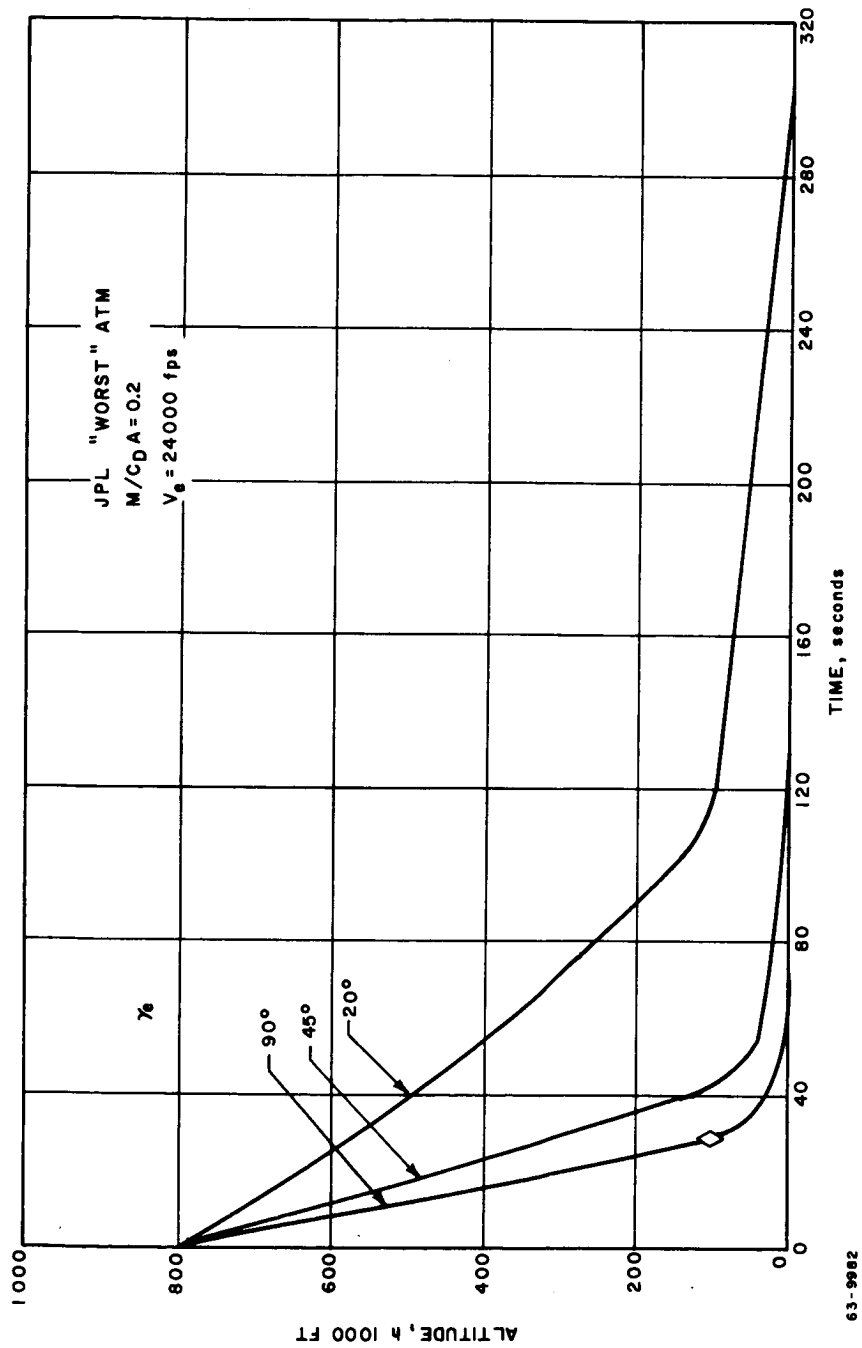


Figure 81 ALTITUDE VERSUS TIME FOR MARS LANDER

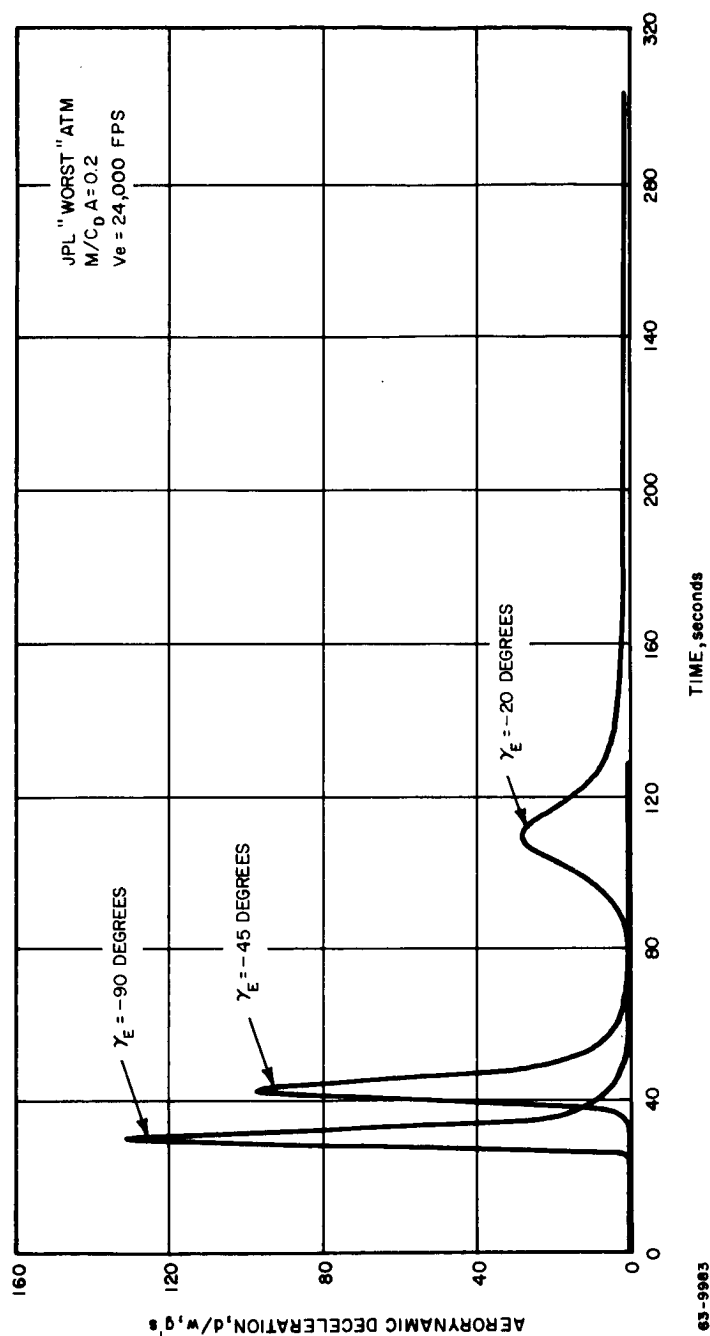
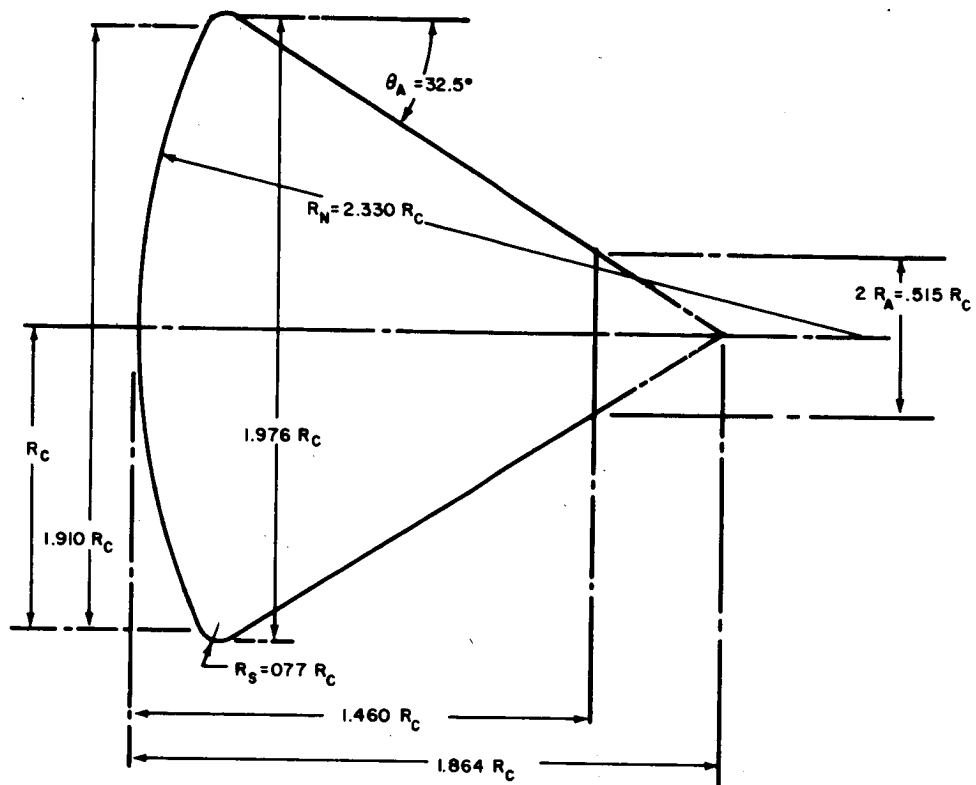


Figure 82 AERODYNAMIC DECELERATION VERSUS TIME FOR MARS LANDER



63-10286

Figure 83 VOYAGER APOLLO-TYPE ENTRY VEHICLE (MARS LOW-DENSITY ATMOSPHERE) CONFIGURATION

4. HEAT SHIELD DESIGN -- MARS

4.1 Thermal Analysis

1. Entry Heating.

a. Convective heating. Relatively simple heating relationships were used to facilitate the handling of the many variables involved in the study. For the calculation of stagnation point heating, the following correlation by Detra (ref. 10) was used:

$$\dot{q}_s = \frac{865}{\sqrt{R}} \left(\frac{V}{10^4} \right)^{3.15} \left(\frac{\rho}{\rho_{\infty SL}} \right)^{0.5} \left(\frac{H_s - h_w}{H_s - h_{w300}} \right) \quad (1)$$

This expression is derived from the theoretical prediction of

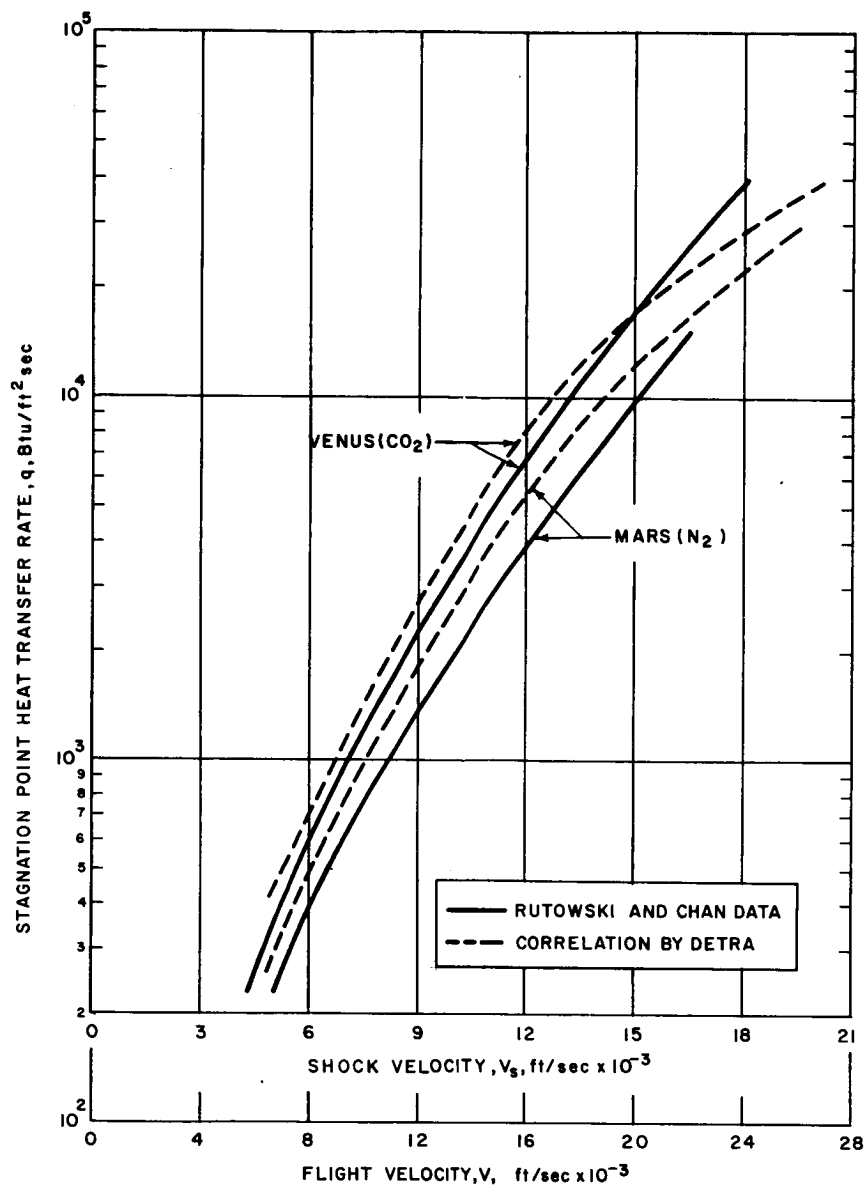
$$\dot{q}_s = \frac{0.76}{\sigma^{0.6}} \left\{ (\rho u)_{ws}^{0.1} (\rho \mu)_{es}^{0.4} \left[1 + (L^{0.5} - 1) \frac{h_{Ds}}{H_s} \right] (H_s - h_{ws}) \sqrt{\left(\frac{du_e}{dx} \right)_s} \right\} \quad (2)$$

by Fay (ref. 11) with the assumptions of a Newtonian velocity gradient at the stagnation point, the viscosity temperature dependence given by Sutherland, a Lewis number of 1.4, a Prandtl number of 0.71, and a wall temperature of 300 °K.

The correlation is estimated to be accurate to 10 percent for air over a velocity range of 6000 to 26,000 ft/sec and a density $\frac{\rho_{\infty}}{\rho_{\infty SL}}$ ratio of 1 to 8×10^{-5} .

A comparison of the predicted results using the above expression and the data of Rutowski and Chan is given in ref. 13 and is reproduced in figure 84. The comparison is quite satisfactory for the purposes of the study.

Equation (1) has been coupled to a particle trajectory program to give as output the stagnation point heating (neglecting the wall enthalpy correction) for a 1-foot radius sphere. The results were then scaled according to the factor:



63-9875

Figure 84 VELOCITY VERSUS STAGNATION POINT HEAT TRANSFER RATE

$$\left\{ \frac{\left[\left(\frac{du}{dx} \right)_s \right]_{\text{shape}}}{\left[\left(\frac{du}{dx} \right)_s \right]_{\text{sphere}}} \right\}^{1/2}$$

where the ratio of velocity gradients (ref. 13) is a function of the normal shock stagnation point density ratio $\frac{\rho_\infty}{\rho_s}$ as is indicated in figure 85. The $\frac{\rho_\infty}{\rho_s}$ ratios for equilibrium flows were computed for nitrogen

and carbon dioxide with the calculations being based on the results of refs. 14, 15, 16, and 17. For the V-2 shape, the velocity gradient ratio does not vary greatly for the range of density ratio of interest and has been assumed constant in the study.

b. Radiative heating. Calculations of the equilibrium radiative heat flux for the variety of vehicle shapes, entry conditions and atmospheric models of this study, were carried out using the following equations and assumptions.

Any attempt to compute a radiative heat flux must deal with both the microscopic or geometric aspects of the transfer of radiant energy and the microscopic or the absorption and emission of the radiant energy by the individual molecules or atoms.

With respect to the microscopic aspect of the radiant transfer, the so-called "plane parallel" approximation was used. This consists of replacing the actual curved shock layer by a slab of radiating gas having a thickness equal to the detachment distance of the shock in a direction normal to the vehicle surface and extending to infinity perpendicular to this normal. For blunt nosed vehicles of the type considered in this study, the plane parallel layer geometry is a good approximation. This is because the radiation from the "wings" of the slab is attenuated to some extent by the intervening layer of gas, and the radiant flux absorbed by the vehicle has a cosine dependence. The reason for the use of the plane parallel slab approximation is the simplification that it introduces into the transfer equation. The appropriate equation for the above case is:

$$-\cos \theta \frac{dI}{dr} = K [I - B] \quad (3)$$

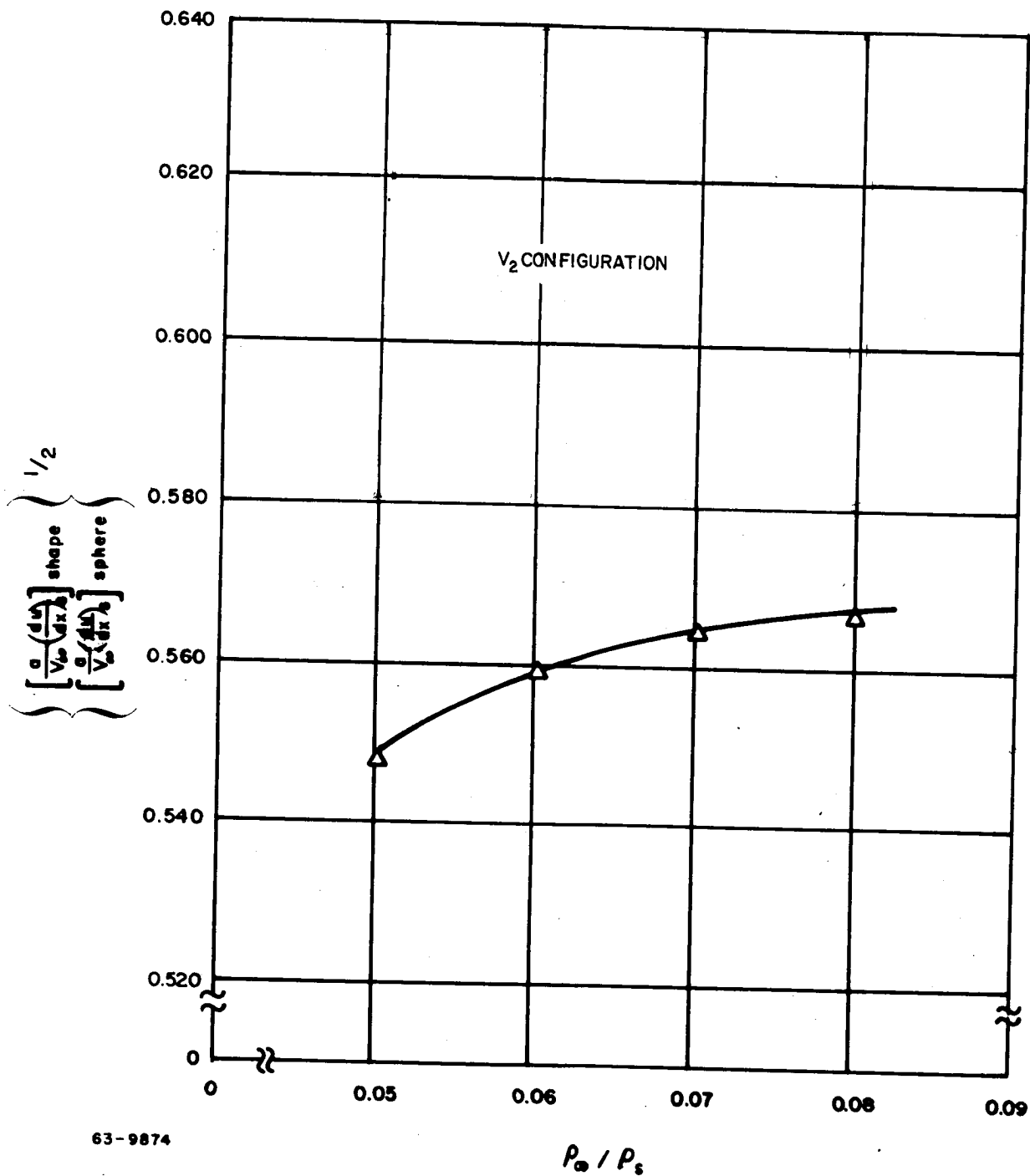


Figure 85 STAGNATION POINT HEATING RATE VELOCITY GRADIENT CORRECTION FACTOR (V-2 CONFIGURATION)

where:

K is the mass absorption coefficient

I is the radiant intensity

B is the Planck blackbody function

θ is the azimuthal angle to the normal

τ is the optical thickness defined as: $\tau = \int_Z^{\delta} K dZ$ (4)

where:

δ is the detachment distance

Z is the geometric variable normal to the body.

From the definition of the intensity (I), the radiant flux crossing a unit area is (ref. 18)

$$q_r = \int_{\Omega} I \cos \theta d\Omega \quad (5)$$

where Ω is the solid angle.

Solving equations (3), (4), and (5) with the addition restrictions that the temperature and density in the slab be constant results in:

$$q_N = \sigma T^4 [1 - 2 E_3(\tau)] \quad (6)$$

where:

$$E_3(\tau) = \int_0^1 e^{-\tau/\mu} \mu d\mu \quad (7)$$

and

σ is the Stephan-Boltzmann constant

T is the temperature of the slab.

For a detailed derivation of equation (6) see ref. 19. Equation (6) is the equation used in the present study.

In the limiting case where $\tau \ll 1$, equations (6) and (7) reduce to

$$q_r = 2K \delta \sigma T^4 \quad (8)$$

For a detailed derivation of equation (8), see ref. 19. In the case of Mars, calculations indicate that $\tau \ll 1$, therefore, the approximations leading to equation (8) are valid. On the other hand, calculations for a Venus entry indicate that the approximation $\tau \ll 1$ is not valid for the higher temperature range only when $\tau \ll 1$, radiative heating is proportion to body size.

The microscopic aspect of radiation has to be appealed to in order to obtain values of the mass absorption coefficient K . There are two processes of emission and absorption of radiation; those due to the rotational, vibration and electronic transitions in molecules and the "Kramers" radiation in atoms. A number of mathematical models have been formulated for the absorption coefficient for molecules (ref. 20). For the molecular species and temperatures of interest, the different models give essentially the same results. The one large uncertainty in all these models is the value of the electronic oscillator strength, f_e , which is defined as:

$$f_e = \frac{8\pi^2 \mu c}{3h \epsilon^2 d_n} \tilde{\nu} |R_e(r)|^2 \quad (9)$$

where:

μ is the reduced mass of the molecule

C is the speed of light

h is Planck's constant

$\tilde{\nu}$ is the frequency in wave numbers

d_n is the degeneracy of the absorbing state.

The quantity $R_e(r)$ is the electronic transition moment and for many molecules varies for the different vibrational transitions. This quantity could, in theory, be calculated from quantum mechanical considerations, but in practice the complexity and number of the calculations rendered such a process impossible. Therefore, the value of f_e is obtained from experimental measurements

of the intensity or of the radiative lifetime of the excited molecule. Both of these experimental methods are difficult and result in uncertainties in the electronic oscillation strength. These, in turn, are reflected in the absorption coefficient.

Presently, Kramers free-free radiation is on a fairly firm basis but the free-bound is not. Most calculations of the free-bound Kramers' radiation have used a formula postulated by Unsold (ref. 21). Recently Biberman and Norman (ref. 22 and 23) have obtained corrections for the Unsold formula using the quantum defect method of Burgess and Seaton (ref. 24).

Kivel and Bailey (ref. 25) have presented an empirical equation for the emissivity per unit length whose form has been dictated by the reasoning of ref. 20 and 21. This equation gives the emissivity per unit length of a plane parallel slab of gas at a constant temperature and density. From the arguments of ref. 19, it may be seen that for a plane parallel slab, the relation between the absorption coefficient K and the emissivity per unit length ϵ/L is:

$$K = \frac{1}{2} \frac{\epsilon}{L} \quad (10)$$

The expression for the absorption coefficient used in the present study uses equation (9) combined with the equation presented in ref. 25.

$$K = \frac{1}{2} C_i \left(\frac{N_i}{5.4 \times 10^{19}} \right) \frac{e^{-T_i/T}}{(T \times 10^{-4})} n_i \quad (11)$$

where:

N_i is the number of molecules or atoms of species i

and

C_i , T_i , and n_i are empirical constants determined from shock tube experiments and theoretical considerations.

The values of C_i , T_i , and n_i listed in ref. 14 were used in this study with the exception that the oscillator strength of $CN(A_{\pi}^2 \rightarrow X\Sigma^2)$ was taken as 6.3×10^{-3} and for $CN(B^3\Sigma \rightarrow X^2\Sigma)$, 2.7×10^{-2} was used. The value for the red system ($A_{\pi}^2 \rightarrow X^2\Sigma$) is thought to be low due to the incomplete spectrum from which it was measured.

With the exception of the uncertainties in the oscillator strengths, equation (10) is in good agreement with the more detailed calculation for the diatomic molecules. However, the values of radiant intensity from Kramers' radiation are thought to be too high at the temperatures of interest. One reason could

be that they are based on an equation of the form of ref. 21 which does not account for a wave length variation of the radiation. A number of calculations for Kramers' radiation from nitrogen at temperatures from 8000 to 12,000 °K and 1 atm pressure have been computed using equation (10) and also using the equations of ref. 22. These were then compared to measurements of radiation from an arc heated nitrogen plasma. The results have been reported in ref. 26. The results computed from equation (10) appear too low up to 9000 °K. From 9000 to 12,000 °K, the values computed from equation (8) become increasingly higher than the experimental data to where they are approximately a factor of 4 higher at 12,000 °K. The values computed using the equations of ref. 22 match the experimental data well when the free-free and the estimated contribution of N is subtracted from the experimental data.

Atomic line radiation has been excluded from the calculations since at the temperatures of interest it is negligible in comparison to the molecular and Kramers' radiation. This is because at the temperatures of interest, the line width is only a few Angstroms and is highly self-absorbing.

c. Results of heating study. Several heating time histories for the reference vehicle are shown in figures 86 and 87 illustrating the effect of atmospheric model and entry angle variation. For the low density Mars atmosphere (Schilling's minimum temperature atmosphere), the maximum radiative rates are significantly higher than convective rates for all entry angles. Only for shallow entry angles and the denser (Schilling's maximum temperature) atmosphere are the convective rates higher.

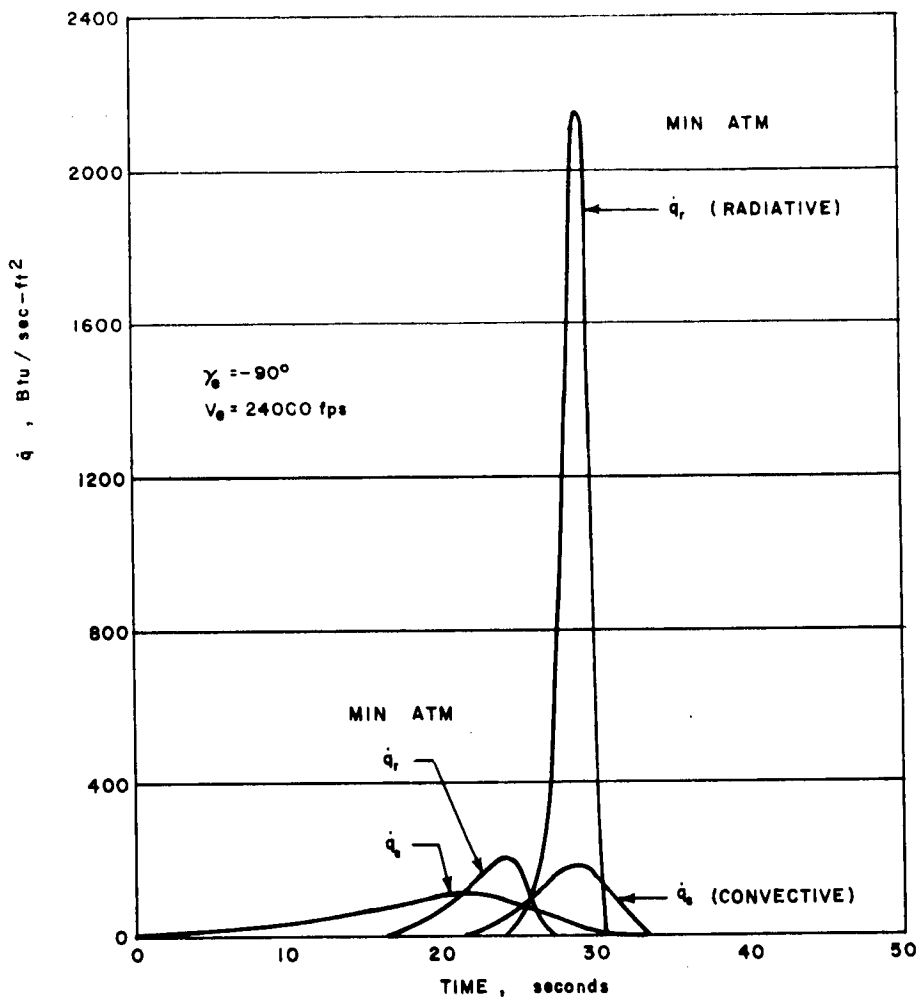
The reference vehicle stagnation point convective and radiative heating (maximum rates and total integrated input) is summarized in figures 88 to 91 as a function of entry velocity, entry angle, and atmospheric model.

It is noted that the atmospheric model variation allows a large variation in the maximum radiative heating rates. Figure 92, presenting the ratio of integrated radiative heating to integrated convective heating, illustrates the predominance of radiative heating for many of the entry possibilities.

A general heating study for a 1-foot radius sphere has been conducted to determine the effect of variation of $M/C_D A$ in addition to entry conditions and atmospheric model. The results of the stagnation heating (maximum rates and total integrated input) and the ratio of integrated radiative to integrated convective heating are presented in figures 93 to 107.

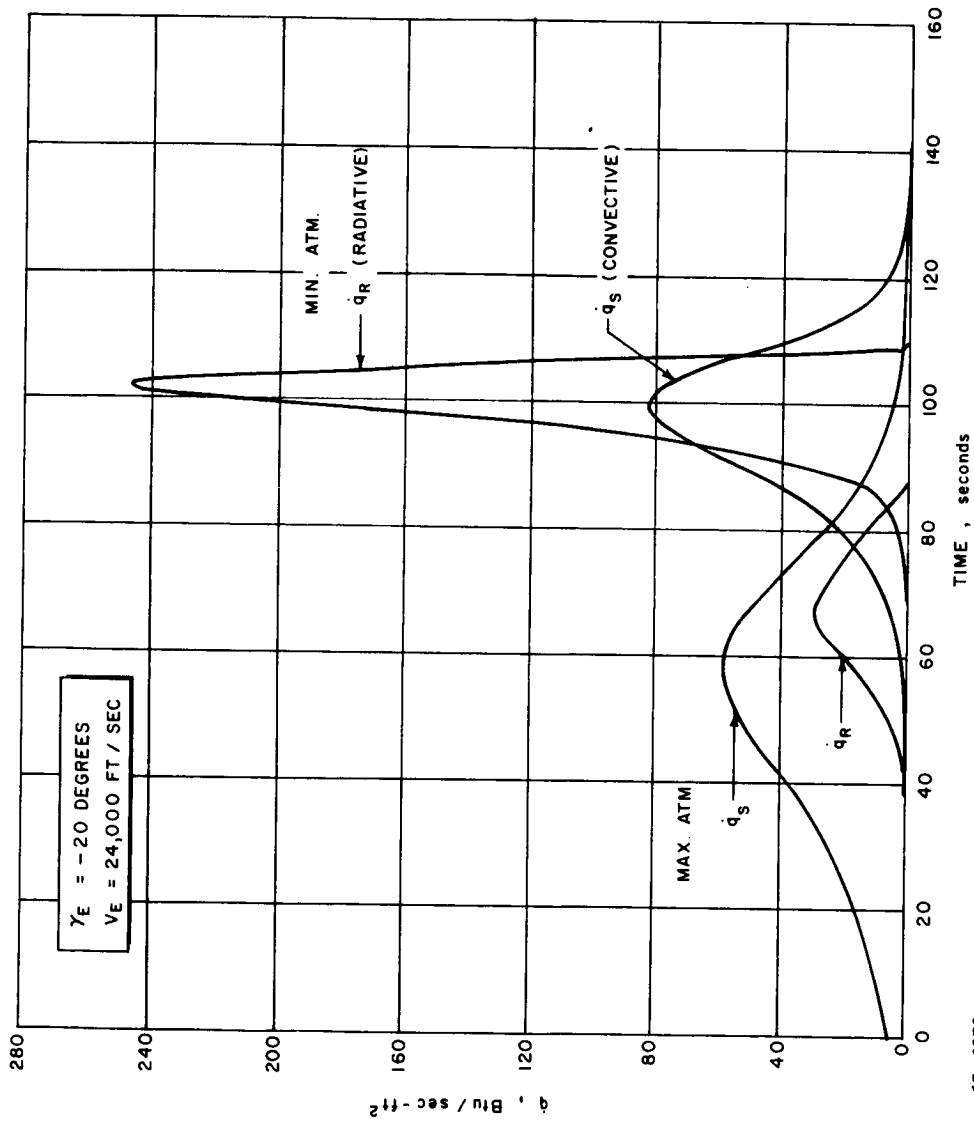
2. Heat shield analysis.

a. Method of calculation. In order to determine the heat shield material requirements for the lander, a knowledge of the convective and radiative thermal environment is required. The heat input load is a function of the vehicle trajectory and the body flow field. The manner in which these quantities are calculated is discussed in section 4.1.



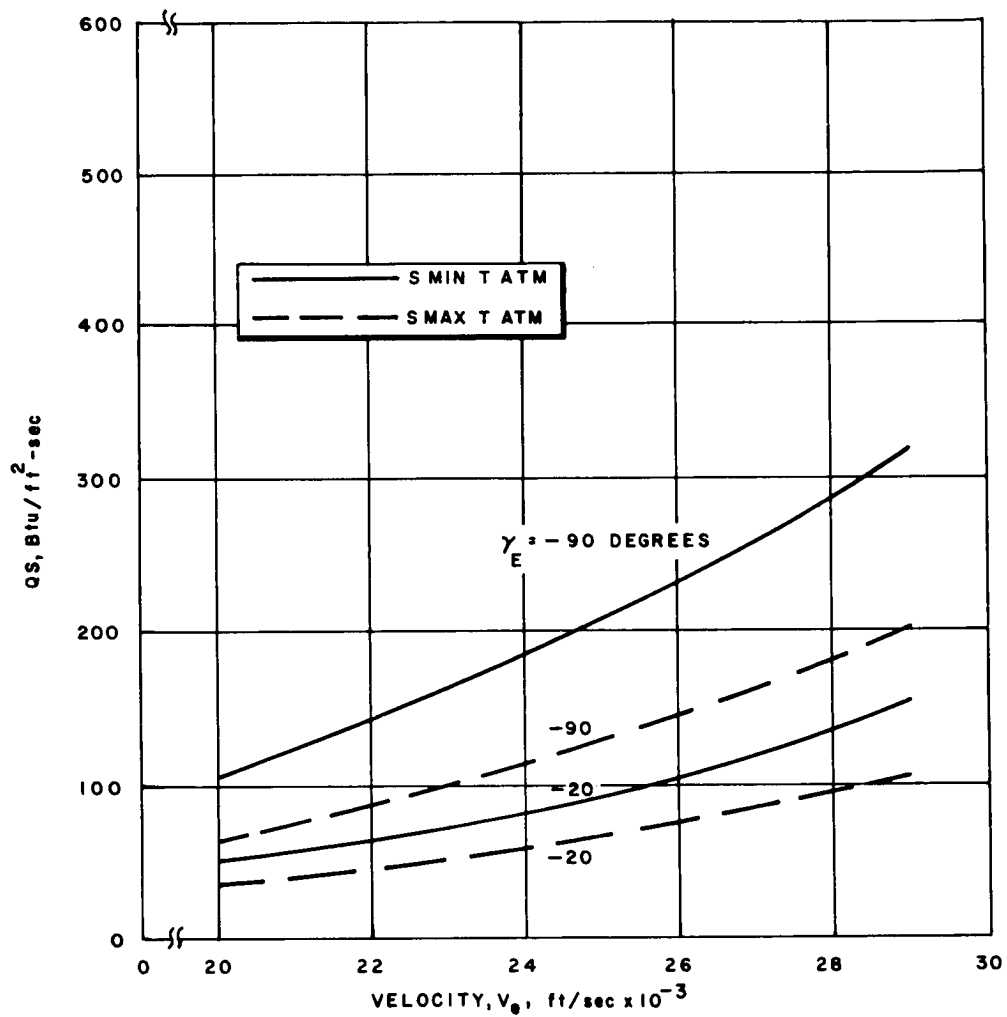
63-9873

Figure 86 STAGNATION CONVECTIVE AND RADIATIVE HEATING TIME HISTORIES
($\gamma_e = -90$ DEGREES)



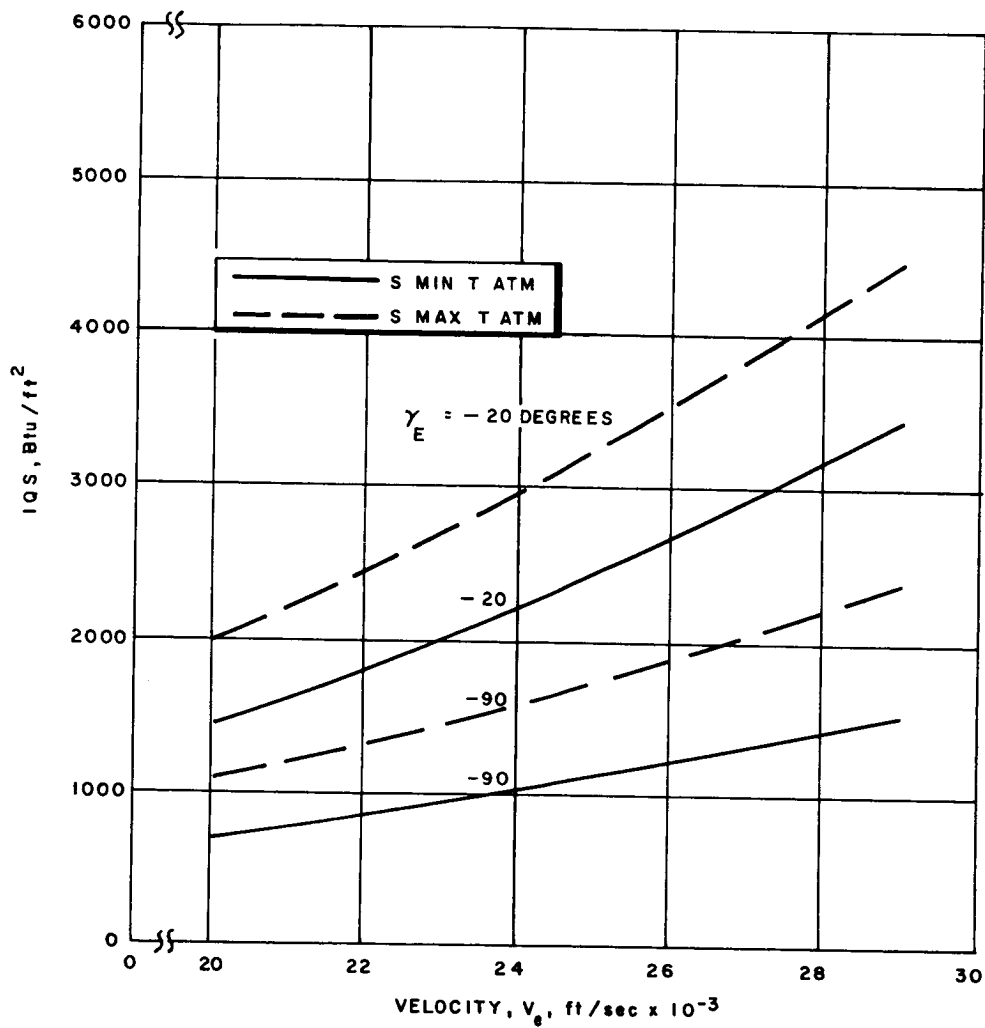
63-9872

Figure 87 STAGNATION CONVECTIVE AND RADIATIVE HEATING TIME HISTORIES ($\gamma_e = -20 \text{ DEGREES}$)



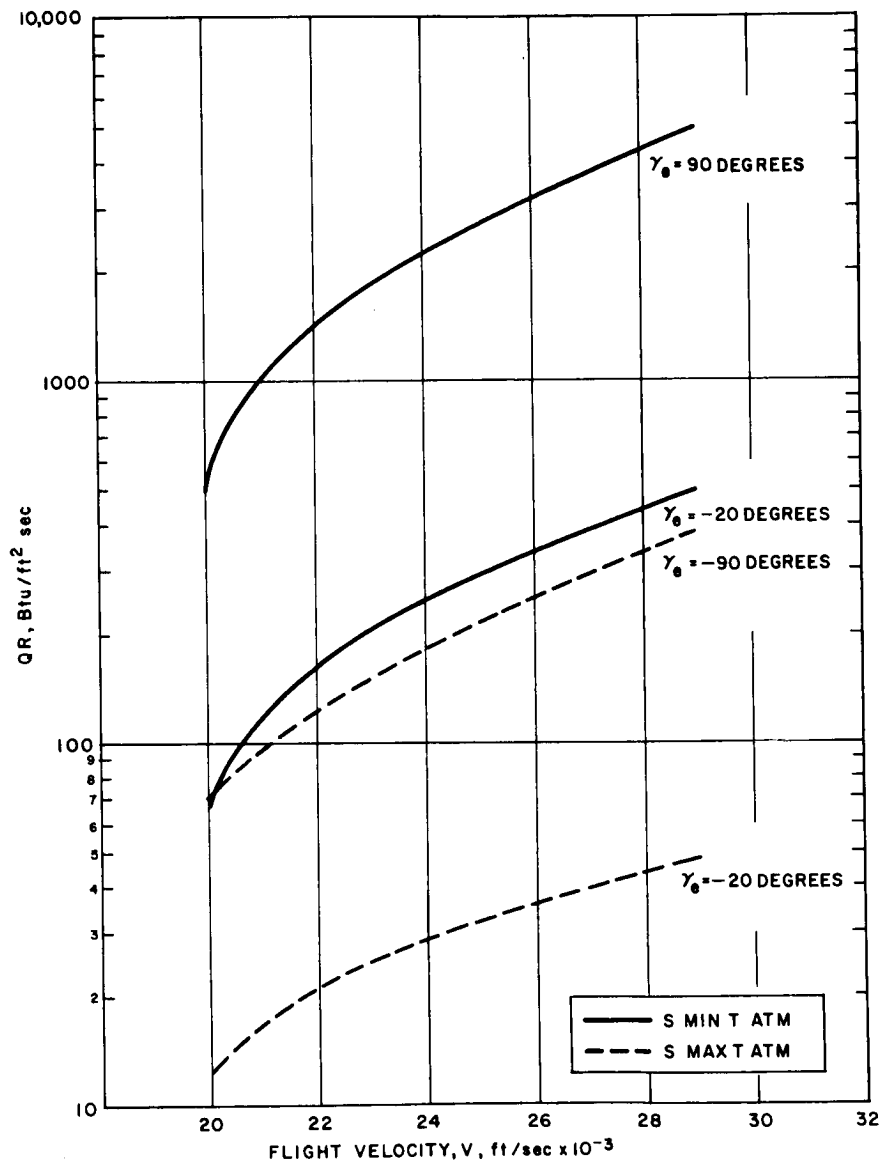
63-9871

Figure 88 MARS ENTRY MAXIMUM CONVECTIVE STAGNATION HEATING RATE



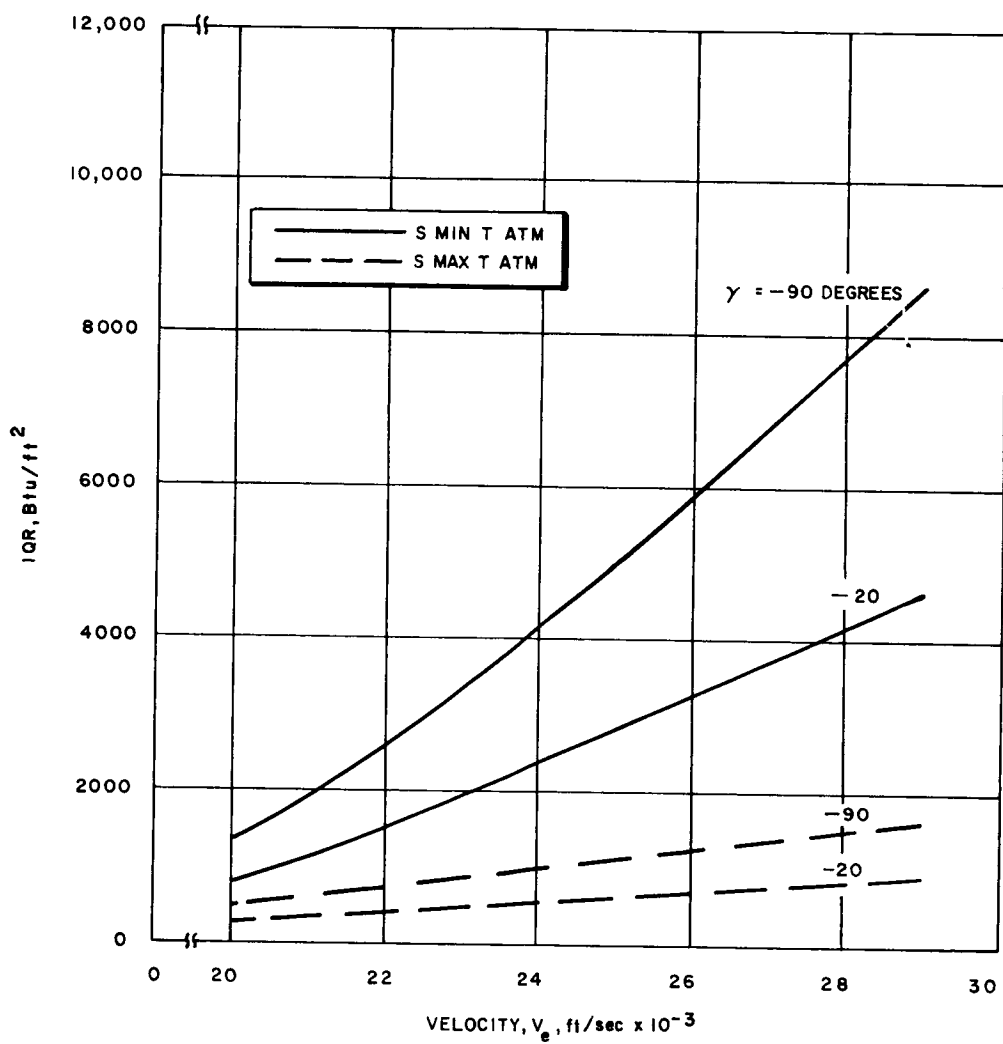
63-9870

Figure 89 MARS ENTRY INTEGRATED CONVECTIVE STAGNATION HEATING



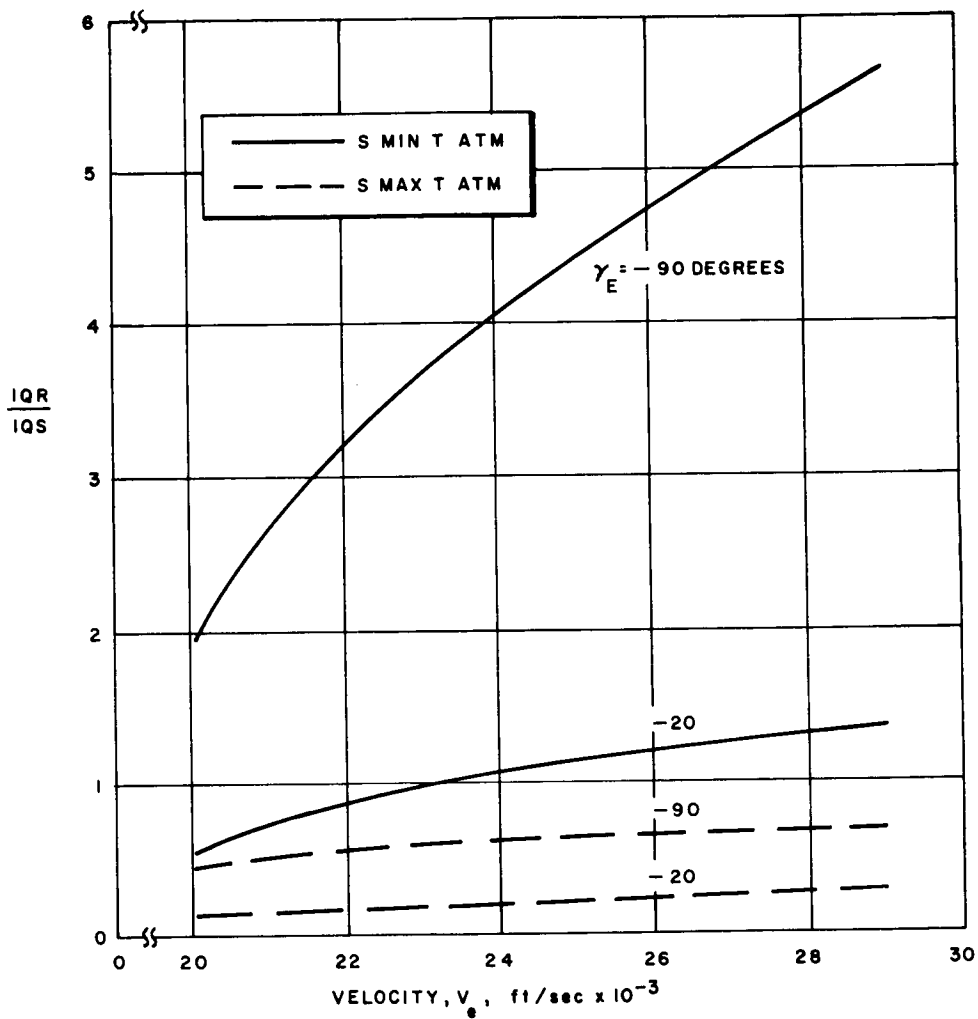
63-9869

Figure 90 MARS ENTRY MAXIMUM RADIATIVE STAGNATION HEATING RATE



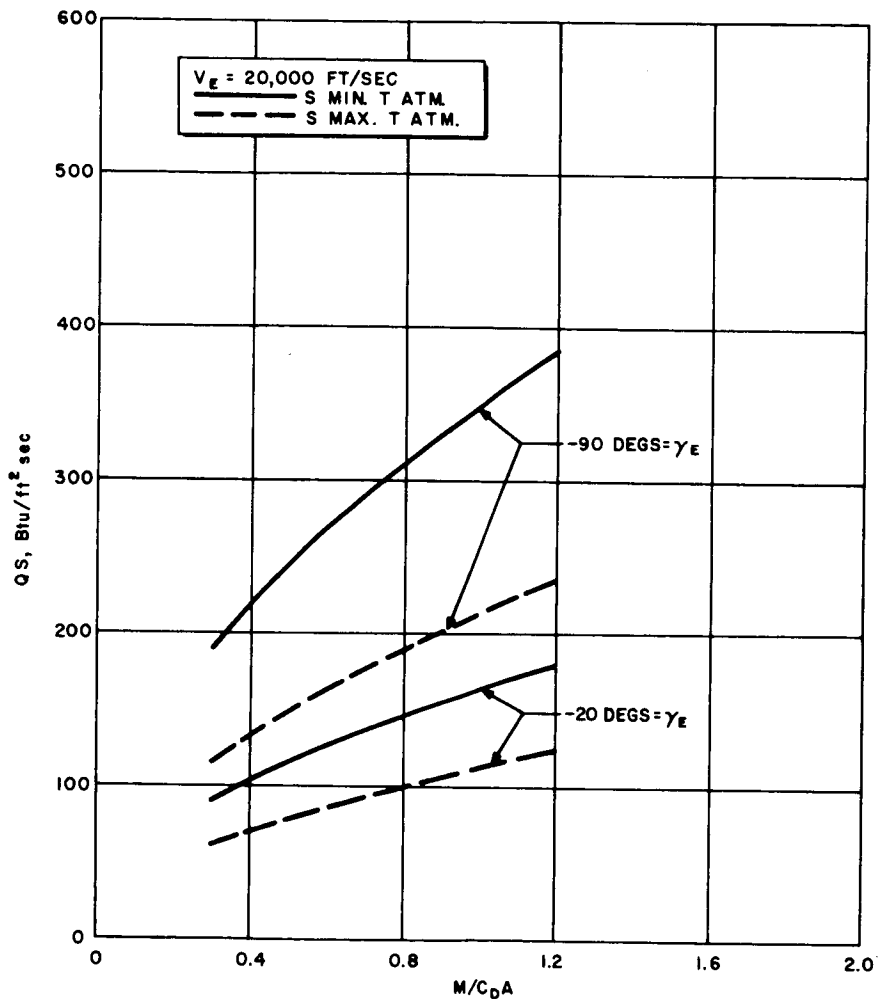
63-9868

Figure 91 MARS ENTRY INTEGRATED RADIATIVE STAGNATION HEATING



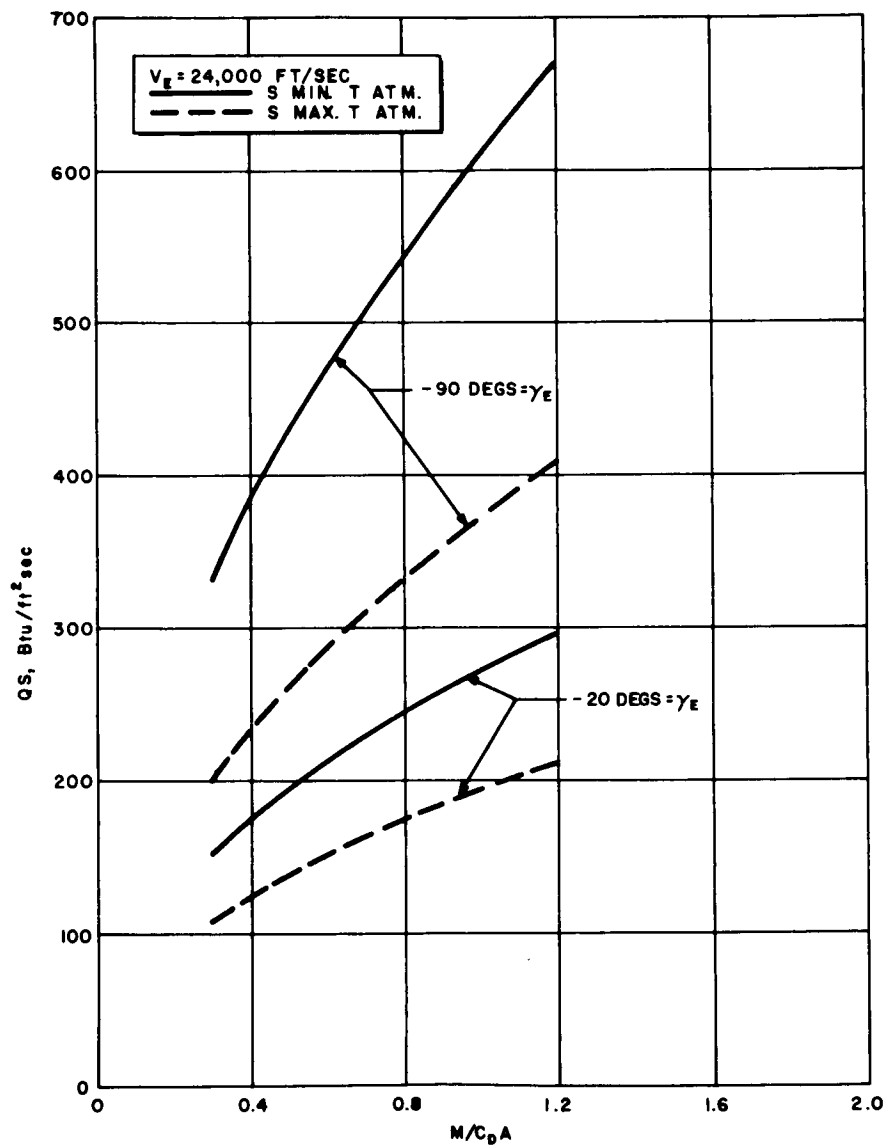
63-9867

Figure 92 MARS ENTRY RATIO OF INTEGRATED RADIATIVE STAGNATION HEATING TO CONVECTIVE STAGNATION



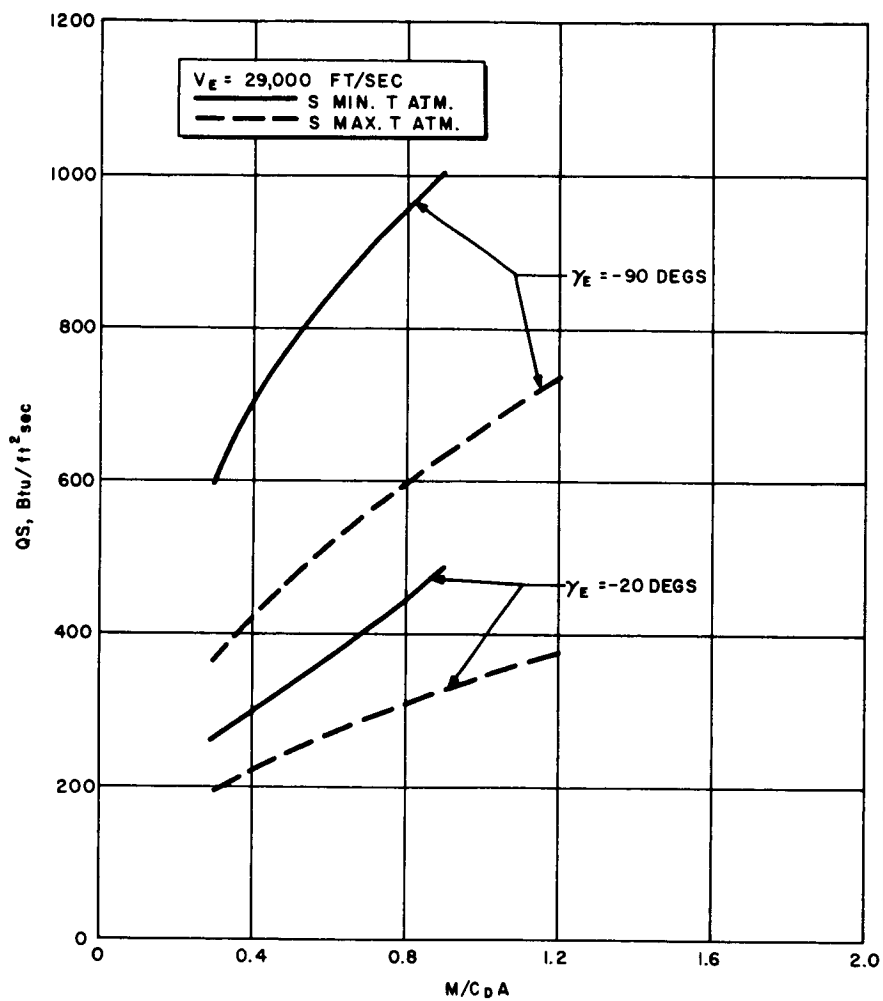
63-9866

Figure 93 MARS ENTRY MAXIMUM CONVECTIVE STAGNATION HEATING RATE



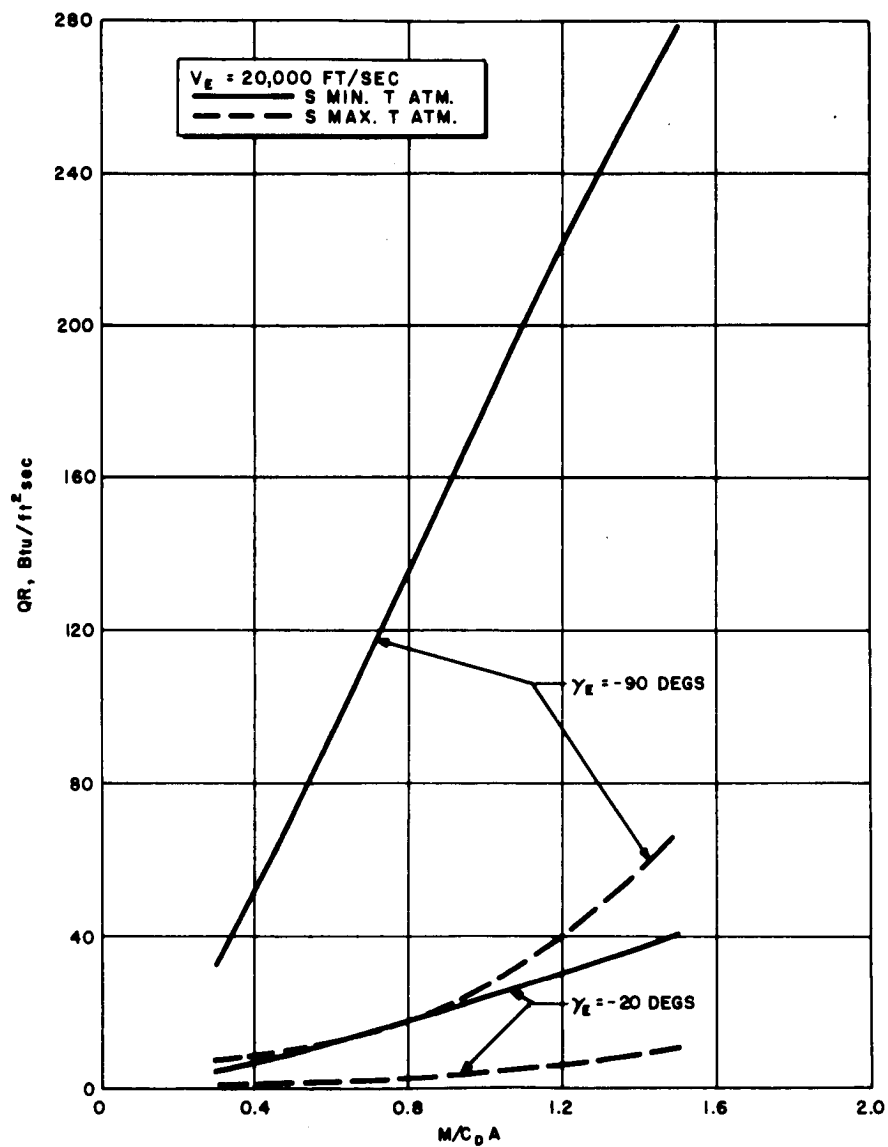
63-9865

Figure 94 MARS ENTRY MAXIMUM CONVECTIVE STAGNATION HEATING RATE



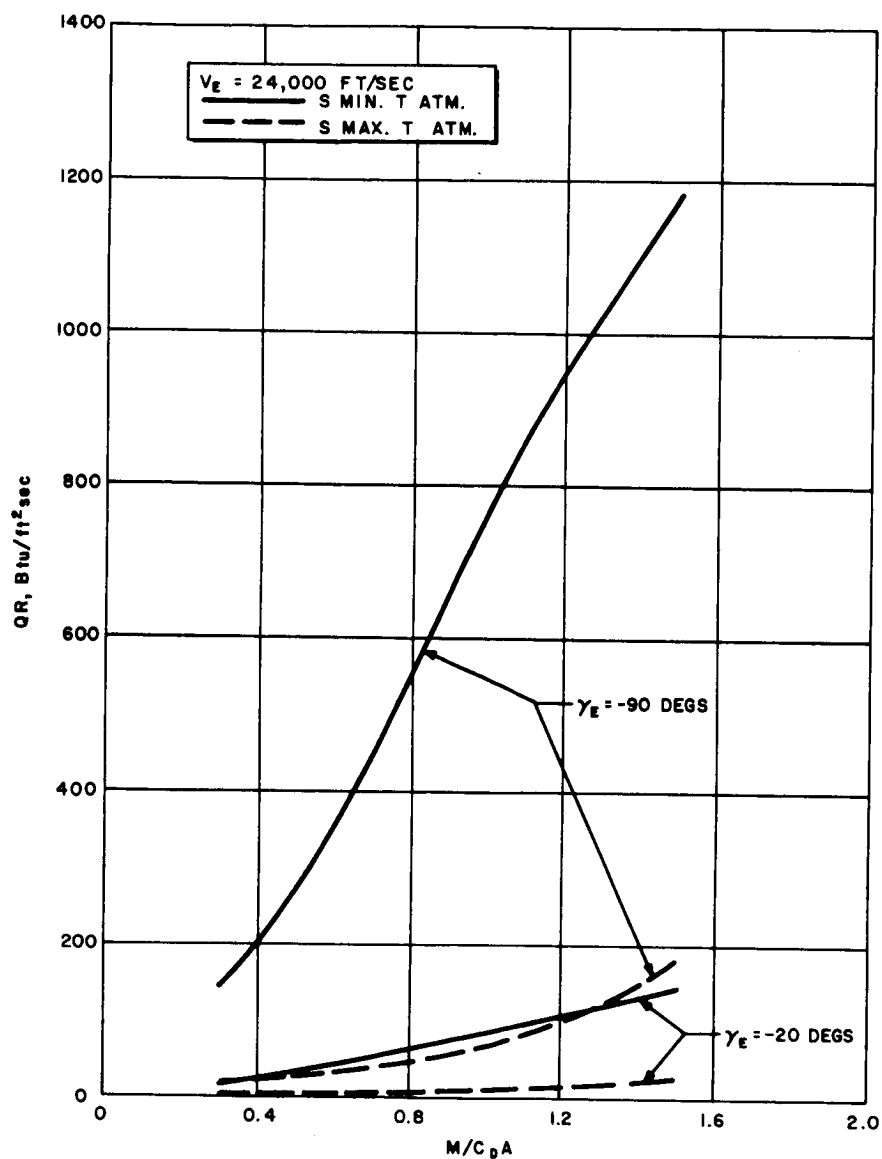
63-9864

Figure 95 MARS ENTRY MAXIMUM CONVECTIVE STAGNATION HEATING RATE



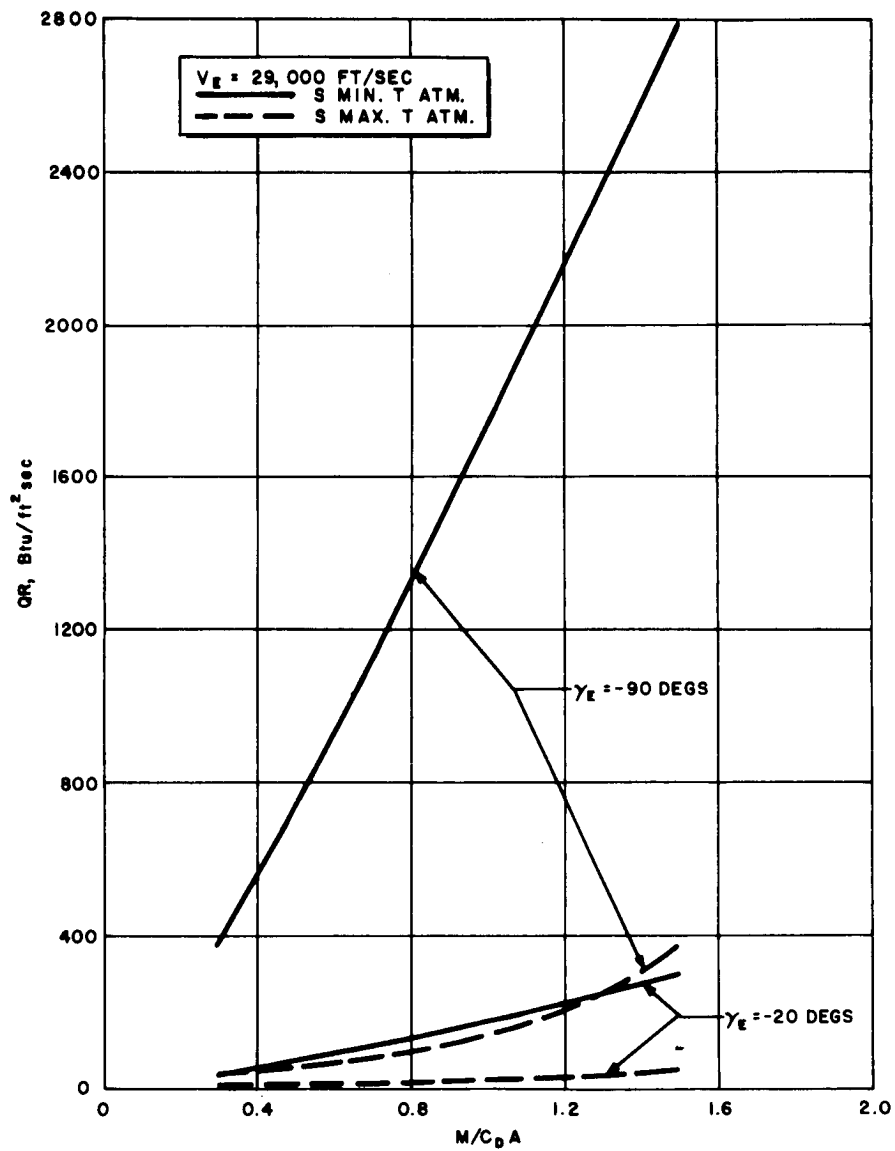
63-9863

Figure 96 MARS ENTRY MAXIMUM RADIATIVE STAGNATION HEATING RATE



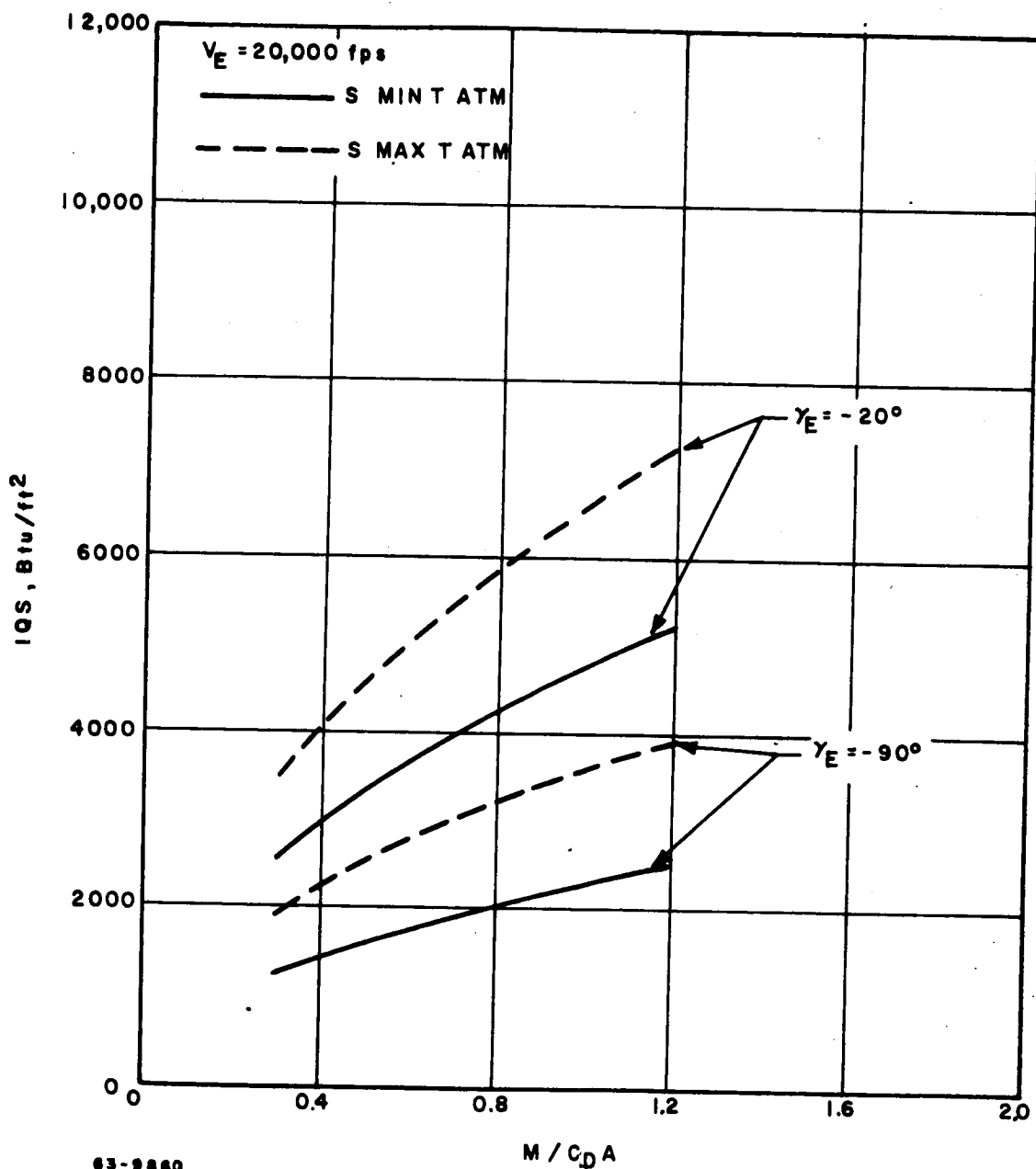
63-9862

Figure 97 MARS ENTRY MAXIMUM RADIATIVE STAGNATION HEATING RATE



63-9861

Figure 98 MARS ENTRY MAXIMUM RADIATIVE STAGNATION HEATING RATE



63-9860

Figure 99 MARS ENTRY INTEGRATED CONVECTIVE STAGNATION HEATING RATE

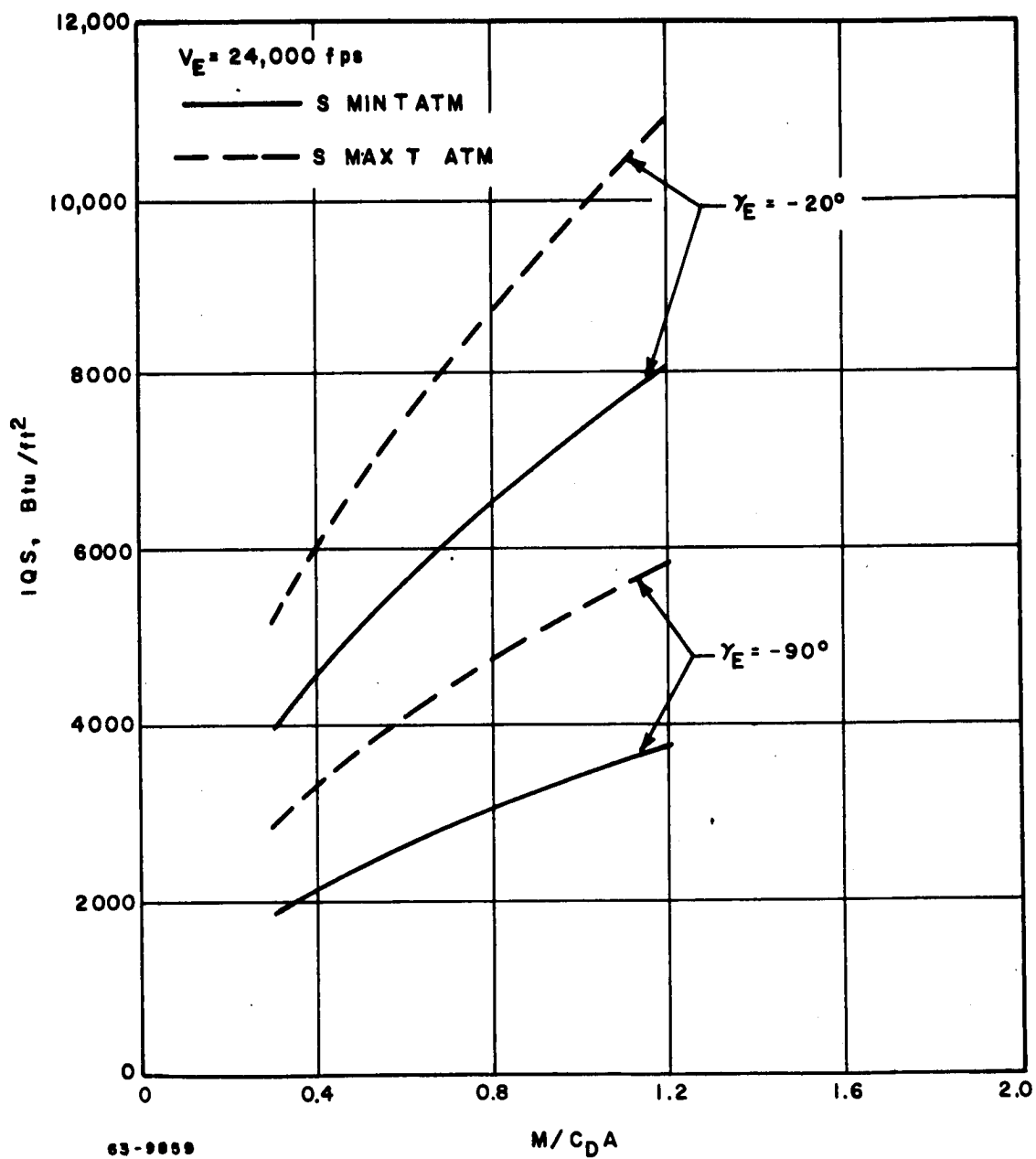
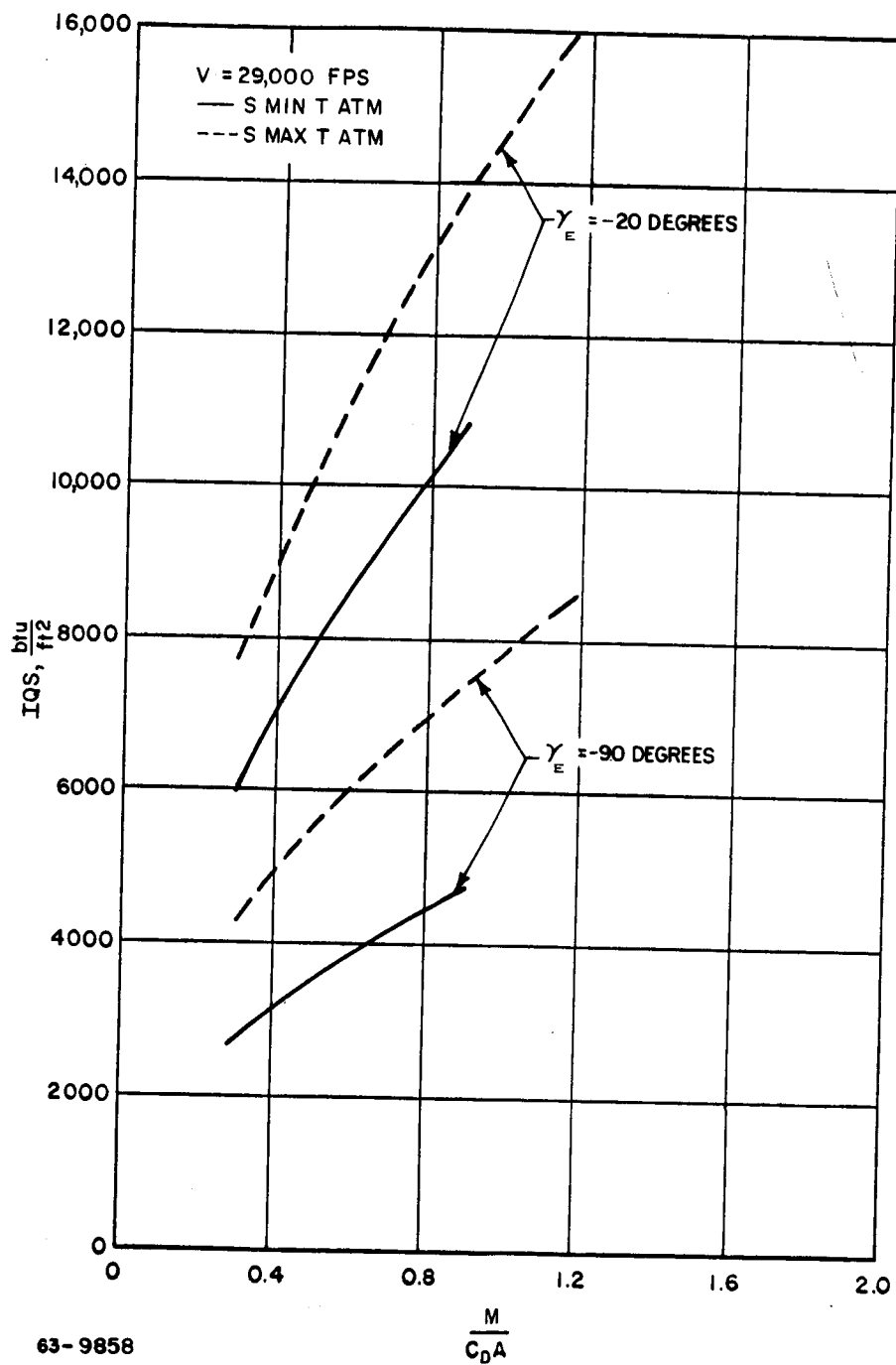
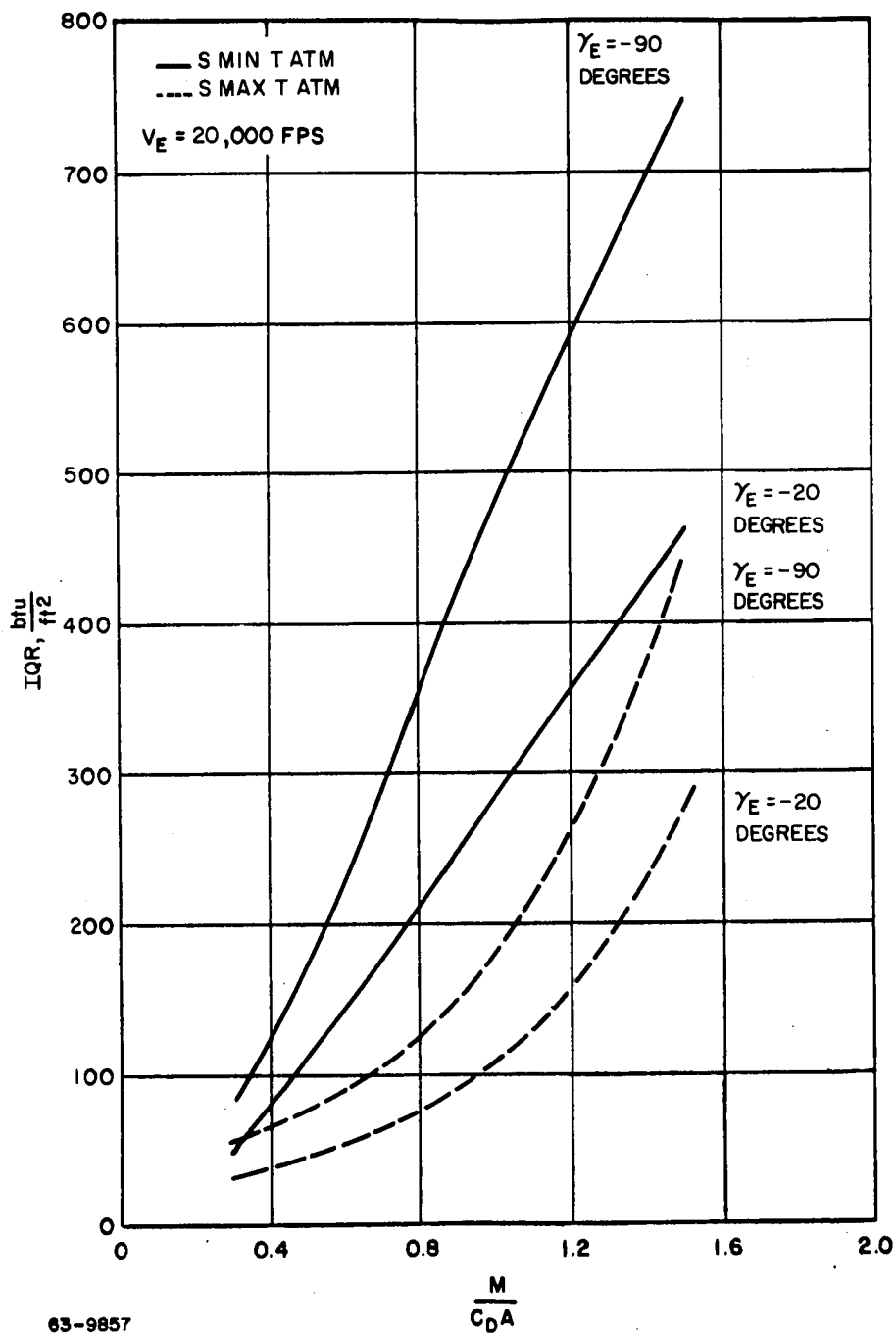
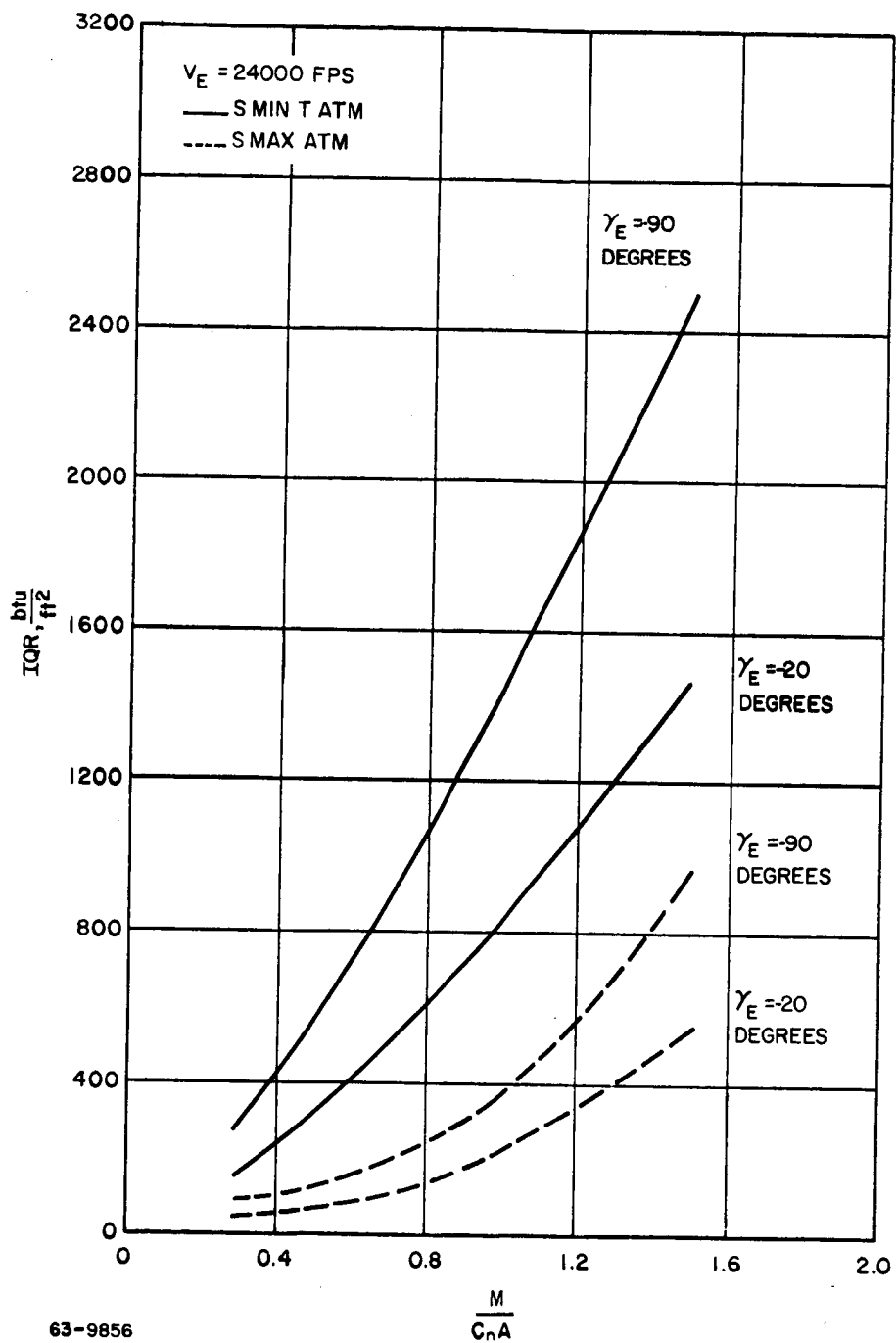


Figure 100 MARS ENTRY INTEGRATED CONVECTIVE STAGNATION HEATING RATE



63-9858
 Figure 101 MARS ENTRY INTEGRATED CONVECTIVE STAGNATION HEATING RATE





63-9856

Figure 103 MARS ENTRY INTEGRATED RADIATIVE STAGNATION HEATING

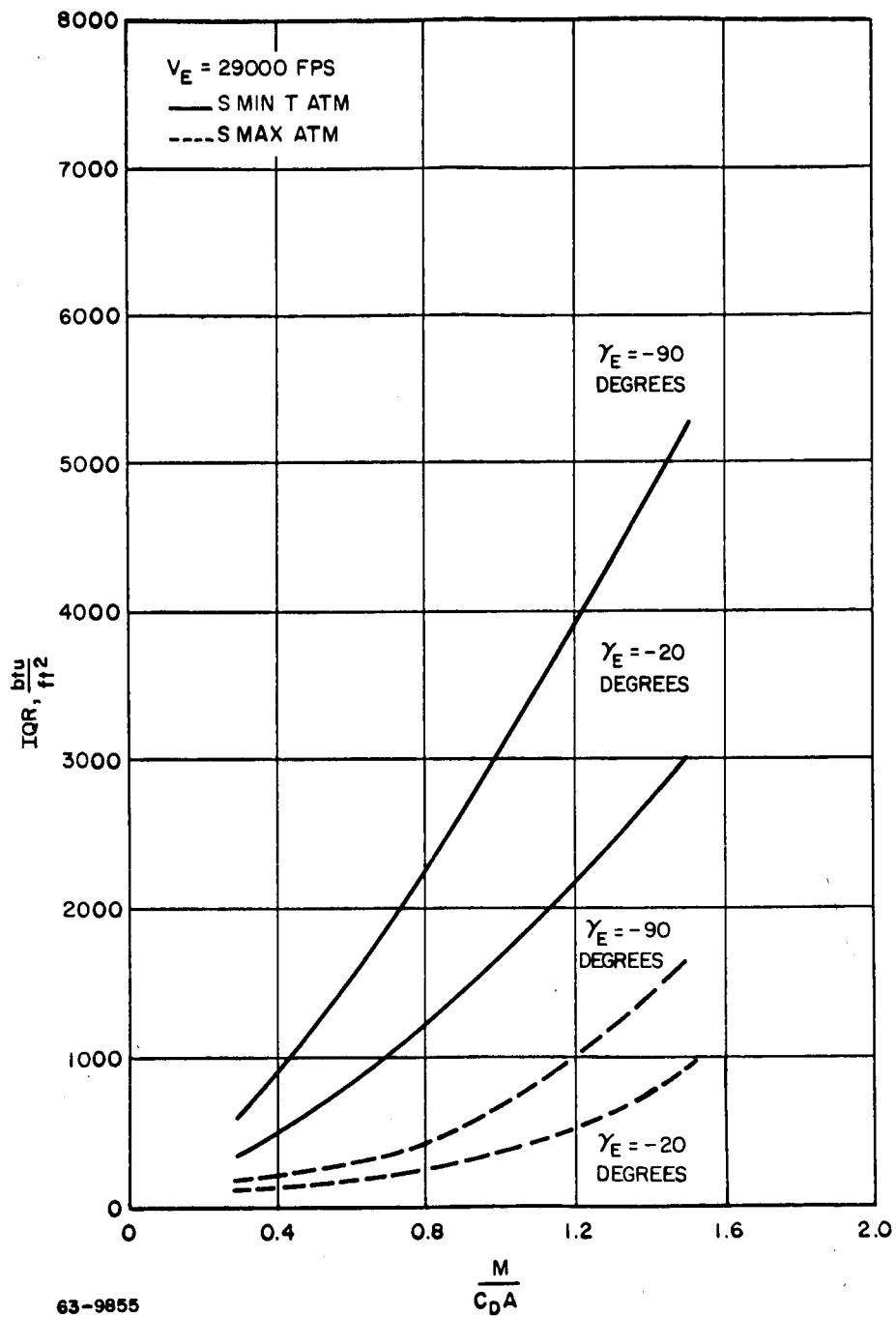
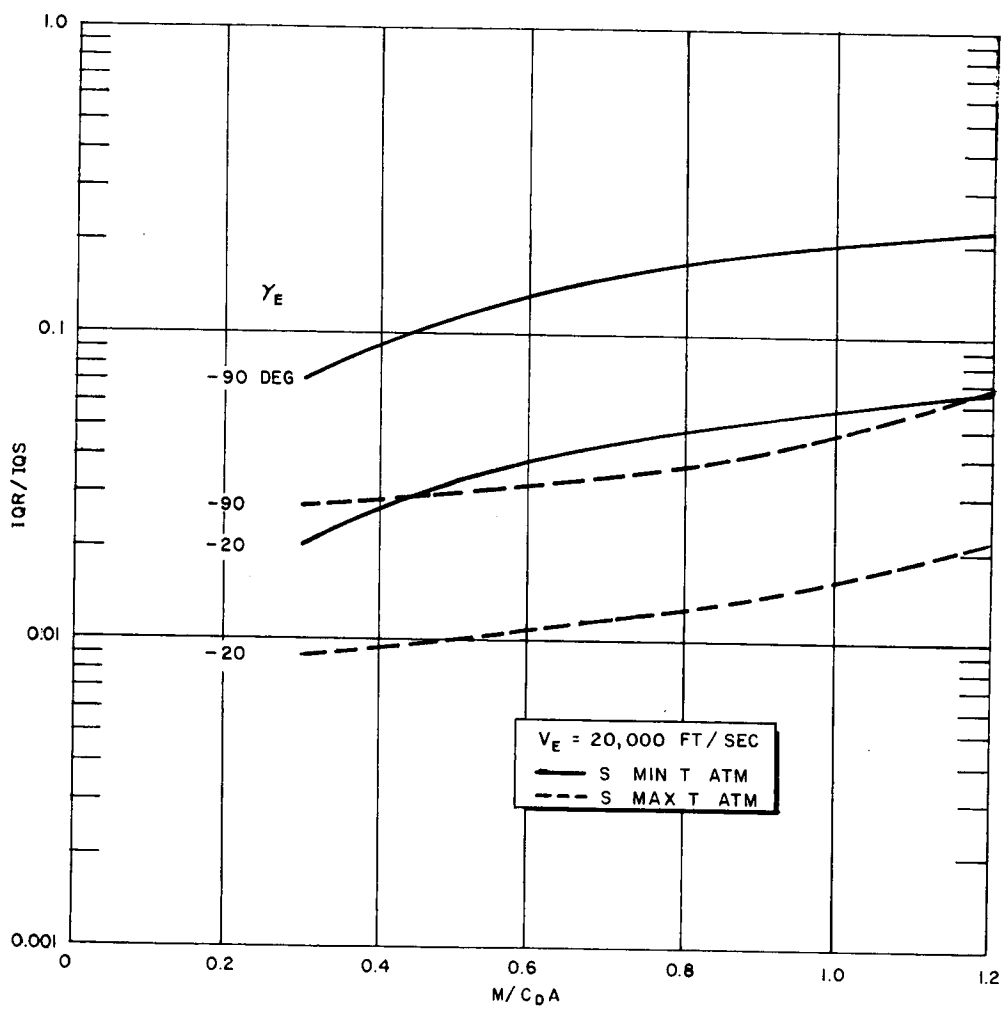


Figure 104 MARS ENTRY INTEGRATED RADIATIVE STAGNATION HEATING



63-9854

Figure 105 MARS ENTRY RATIO OF INTEGRATED RADIATIVE STAGNATION HEATING TO CONVECTIVE STAGNATION HEATING

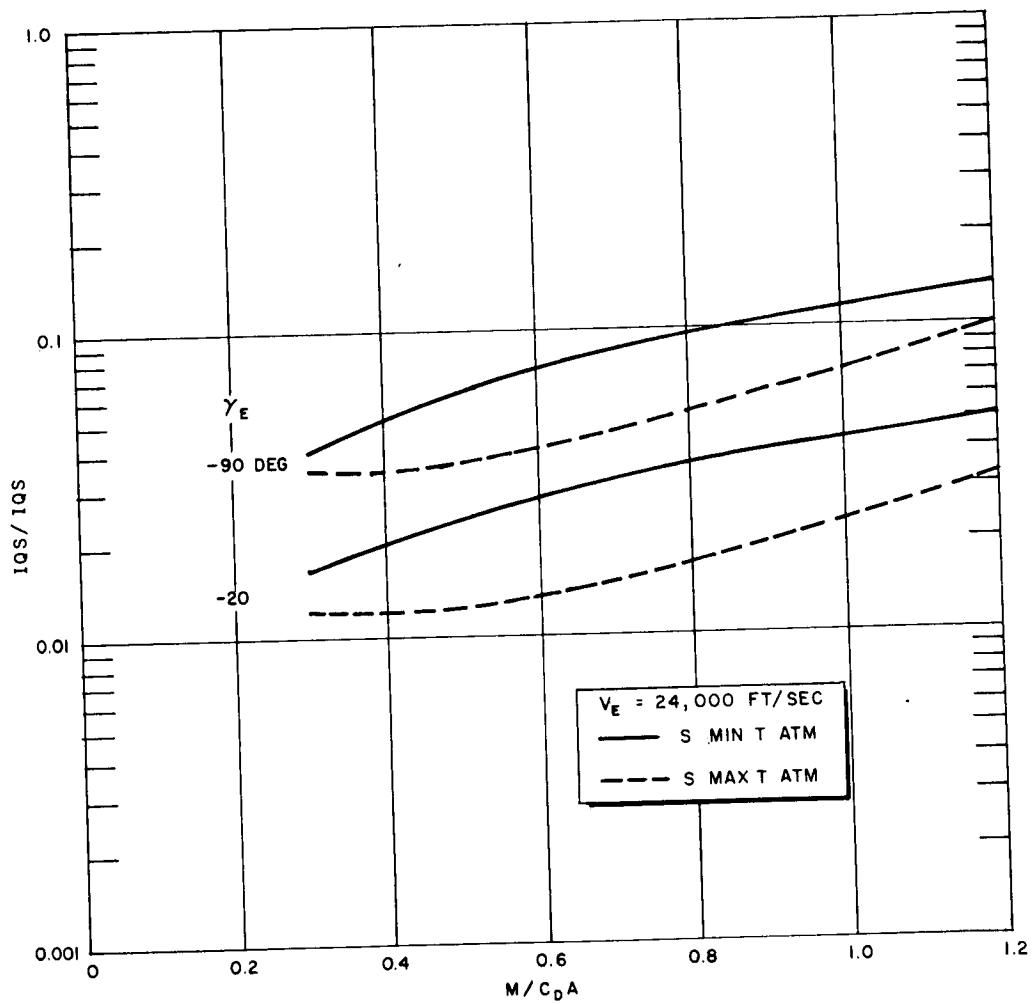


Figure 106 MARS ENTRY RATIO OF INTEGRATED RADIATIVE STAGNATION HEATING TO CONVECTIVE STAGNATION HEATING

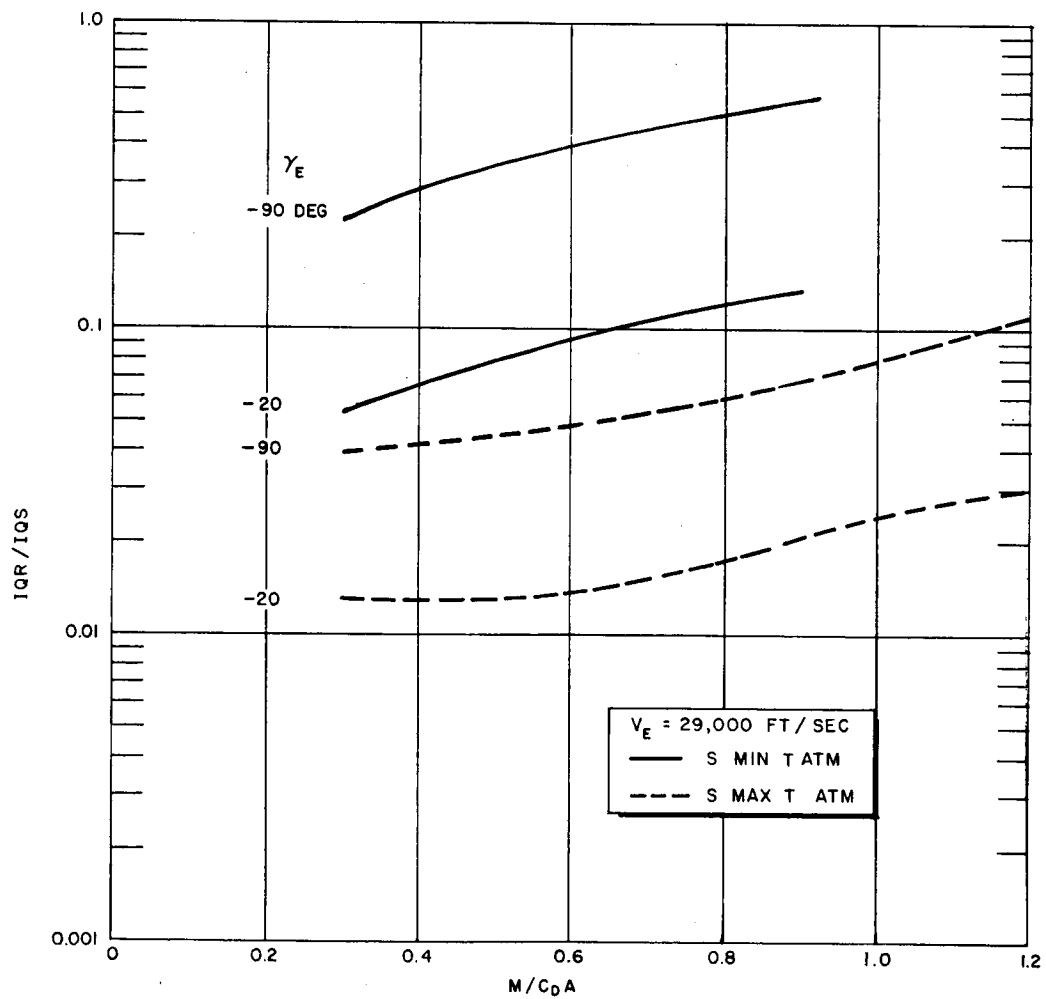


Figure 107 MARS ENTRY RATIO OF INTEGRATED RADIATIVE STAGNATION HEATING TO CONVECTIVE STAGNATION HEATING

With the heating rates known as a function of time at each station, the problem is to determine the heat shield thickness required to maintain a structure temperature above a specified value. Although accurate methods of solution are available at Avco RAD for determining the thermal response of charring ablator (ref. 27 and 28), they are far too cumbersome for a parametric study. Fortunately, a simplified method, which has also been programed on a high speed computer (ref. 29), has been previously developed. This simplified approach has been used in the present study and spot checks using more accurate calculations were made.

One of the major assumptions in the analysis was that the boundary layer gases are transparent to the radiation from the high temperature gases behind the bow shock. When the mass injection produced by convection and radiation is large enough to block the convective heating completely, the transpiration term in the q^* expression and the convective heating input are set equal to 0; radiation is then the only mode of heat transfer, and vaporization heat capacity and reradiation are the methods by which the structure is shielded.

b. Scope of study. The heat shield parametric study for entry into the Martian atmosphere included the following:

- 1) Reference configuration -- V-2.
 - a) M/C_{DA} Variation -- 0.6, 0.9, and 1.5 slugs/ft²
 - b) Entry Velocity -- 20,000 24,000 and 29,000 ft/sec
 - c) Vehicle Size -- 500, 2000, and 4000 pounds
 - d) Entry Angle -- -20, -45 and -90 degrees
 - e) Schilling's maximum and minimum temperature atmospheres.
- 2) NERV shape -- V-1.
 - a) M/C_{DA} -- 0.9 slug/ft²
 - b) Entry Velocity -- 20,000, 24,000 and 29,000 ft/sec
 - c) Vehicle Size -- 500, 2000, and 4000 pounds
 - d) Entry Angle -- -20, -45 and -90 degrees
 - e) Schilling's maximum and minimum temperature atmospheres.
- 3) Apollo shape.
 - a) M/C_{DA} -- 0.2, 0.3 slugs/ft²
 - b) Entry Velocity -- 20,000, 24,000 and 29,000 ft/sec
 - c) Vehicle Size -- 1,000 and 2,000 pounds
 - d) Entry Angle -- -20, -45, and -90 degrees
 - e) JPL's maximum and minimum atmospheres (ref. 28).

In all cases, structural requirements limited the maximum backface temperature to 500° F. The methods used for the analysis are described in detail in ref. 29. The calculations accounted for the presence of the structure by the method described in ref. 29. This method assumes that the structure is a pure capacitor and that the mean temperature of the structure is identical to the backface temperature of the heat shield.

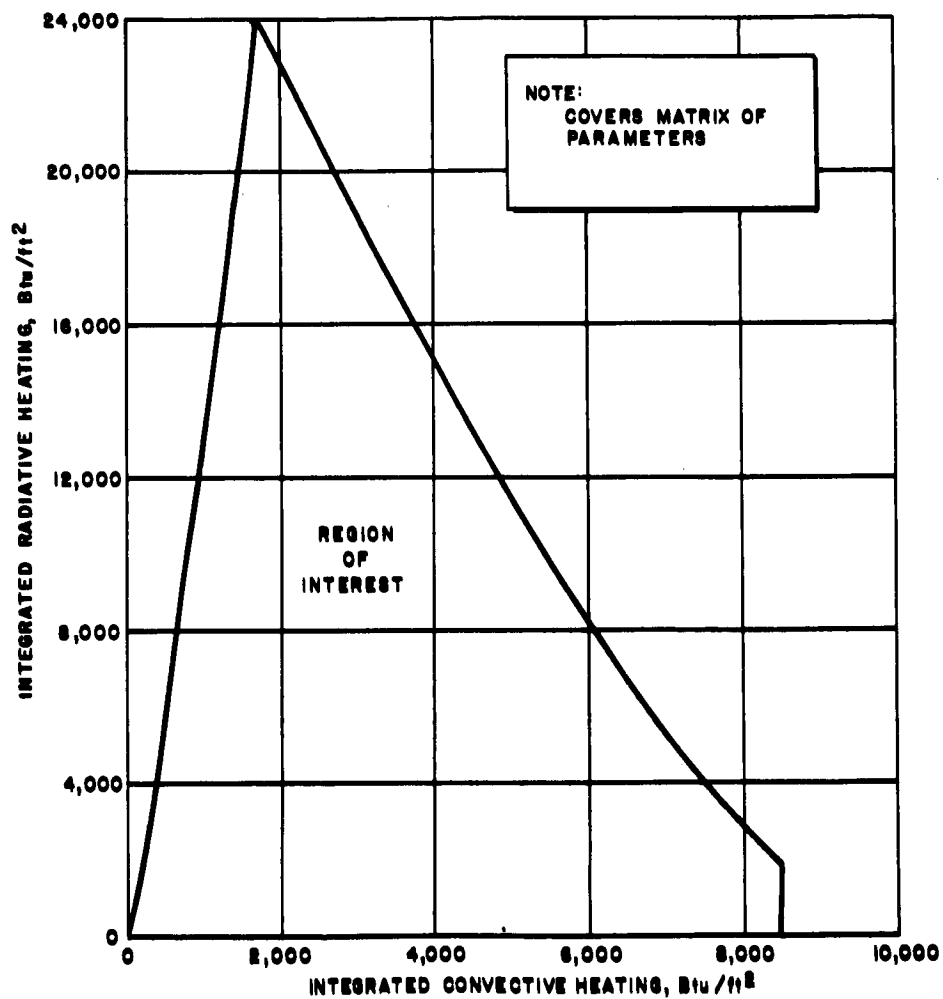
The structure weights employed in the heat shield calculations were obtained for the worst possible entry conditions, that is for the entry angle and atmosphere that produced the largest structural loading. However, the structural weights still varied with entry velocity, $M/C_D A$ and vehicle size and shape.

c. Material selection. The variety of heat pulses produced by the entry conditions made material selection an extremely complex task. Figure 108 shows all possible combinations of integrated convective and radiant heating at the stagnation point. Figure 109 shows all possible combinations of maximum rates. The material Avcoat 5026-39 was found to be the best available material, because of its high ablation temperature, excellent ablation properties, extremely low thermal conductivity and density, and high specific heat. It is a charring material composed of organic resins and silica fibers. A high ablation temperature material is suitable if the conductivity is low so that reradiation can be employed as a heat protection mechanism.

Low thermal conductivity supplements a high ablation temperature in that it limits the penetration of heat. This results in a high surface temperature, but low backface temperature. This combination has been found to be more effective than a low temperature ablator which will generally ablate more, even though the high temperature ablator requires more insulation thickness.

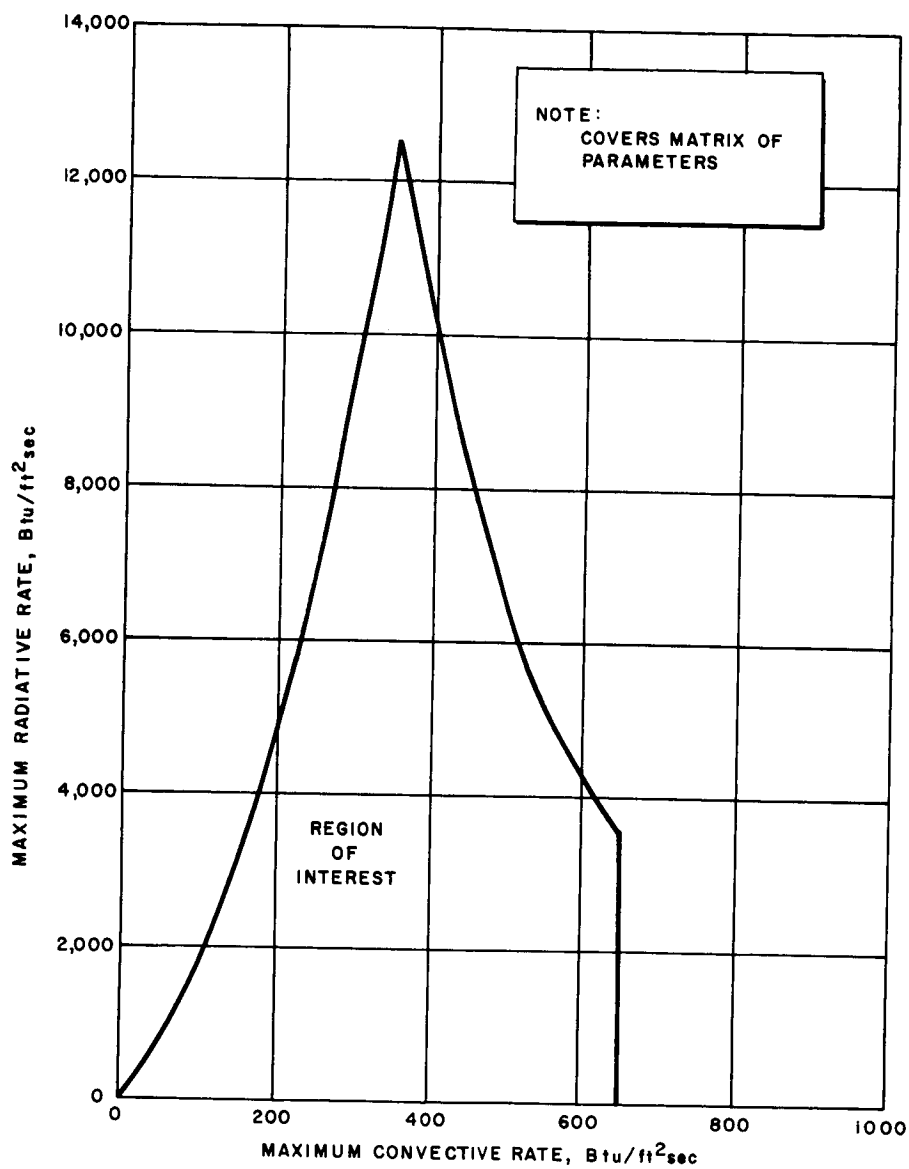
Other materials were also considered, but were found to be less efficient because of their low ablation temperatures and/or high thermal conductivity and density. Results for several existing heat shield materials are shown in Figure 110. It can be seen that the low temperature ablators are the heaviest. Low temperature ablators are also generally unable to withstand the sterilization temperatures.

The properties of Avcoat 5026 are reported in ref. 31 for air. Ref. 31 reports a value for the thermochemical heat of absorption as measured in air. The measured heat of absorption is dependent on the oxygen concentration in the boundary layer which combusts at the surface and in the boundary layer. Combustion was assumed to occur at the surface in the Mars entry case to the extent that oxygen can be obtained from the dissociation SO_2 vaporizing at the surface, and in the boundary layer to the extent that carbon will react with CO . Based upon these assumptions, a value of 85.0 Btu/lb was calculated.



63-8923

Figure 108 POSSIBLE COMBINATIONS OF INTEGRATED STAGNATION POINT
CONVECTIVE AND RADIATIVE HEATING RATES FOR MARS ENTRY



63-8922

Figure 109 POSSIBLE COMBINATIONS OF MAXIMUM STAGNATION POINT
CONVECTIVE AND RADIATIVE HEATING RATES FOR MARS ENTRY

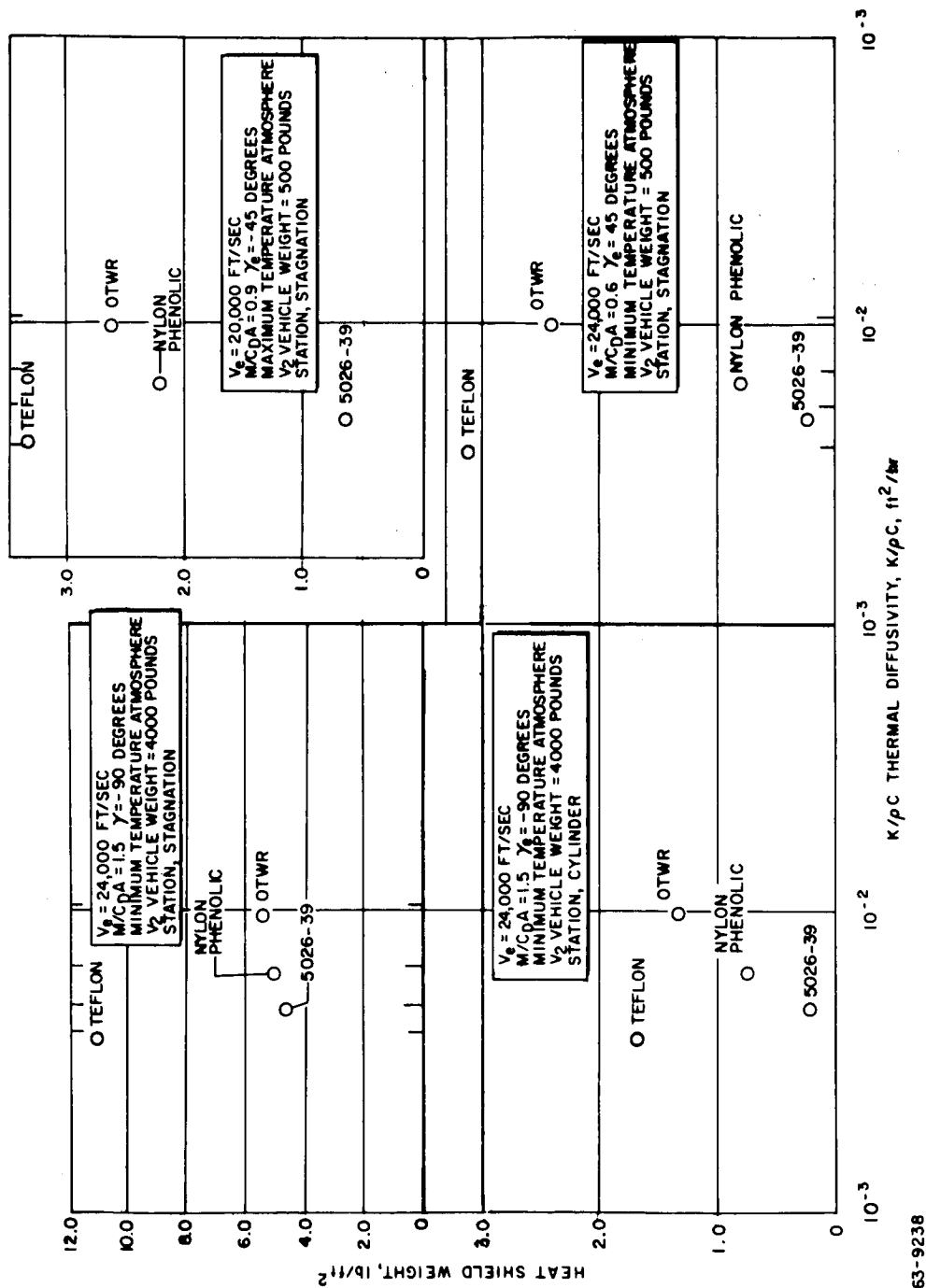


Figure 110 MATERIAL SELECTION CHART

63-9238

d. Parametric study results.

1) Reference design -- V-2. Curves showing the variation of heat shield weight (lb/ft^2) at the stagnation point with M/C_{DA} entry velocity, entry angle, and atmosphere are shown in figure 111 for a 2000-pound vehicle. These weights account for the variation of structure weight, heating rates, and integrated total heating.

Weights calculated for trajectories (with entry angles of -20 degrees) with the maximum temperature atmosphere were generally higher than those calculated with the minimum temperature atmosphere, except for the $29,000$ ft/sec entry case. For the high velocity cases, ablation resulted from the large increase in radiation, and hence the worst heating trajectories became those for the normal entry path angle ($\gamma = -90$ degrees). Ablation rates for other velocities (if ablation occurs) were relatively low, resulting in lower heat shield weights than for a nonablation case. For the low velocity nonablating cases, the material can gasify and char. Convective heating is blocked by the gasification products, and also rejected by reradiation. For a 2000-pound vehicle, the total integrated heating is slightly higher in the minimum temperature atmosphere due to the increase in the proportion of radiative heating as vehicle size increases.

Integrated heating summaries are shown in figure 112. For trajectories where the heat rates were not high enough to cause ablation, the heat shield weight is proportional to the integrated heating. However, for trajectories where ablation was observed, the heat shield requirement was dependent on the radiative rates. Therefore, with ablation, the heat shield weight rapidly increases for a 2000-pound vehicle with increasing entry velocity, entry angle, and M/C_{DA} . As these parameters increase, the minimum temperature atmosphere becomes the critical atmosphere. Figure 113 shows the rapid increase of radiative rates with entry velocity, entry angle and M/C_{DA} in the minimum atmosphere.

For other size vehicles, the critical atmosphere will change, depending on the ratio of convective to radiative heating. For smaller vehicles (500 pounds) the maximum temperature atmosphere was usually found to be worse. The exception is at $29,000$ ft/sec for steep entry (-45 and -90 degrees). However, the trend usually reversed for the 4000-pound vehicle, because of the greater ratio of the radiative to convective heating, resulting in larger ablation rates. This is due to the radiative rates being proportional to R_C and the convective rates proportional to $1/\sqrt{R_C}$. Figure 114 shows the heat shield weight variation with vehicle size for a trajectory that does not result in ablation in the maximum atmosphere, for 500 to 4000-pound vehicles, but for which ablation occurs slowly in the minimum temperature atmosphere for the 500-pound vehicle and more rapidly for the 400 - pound vehicle.

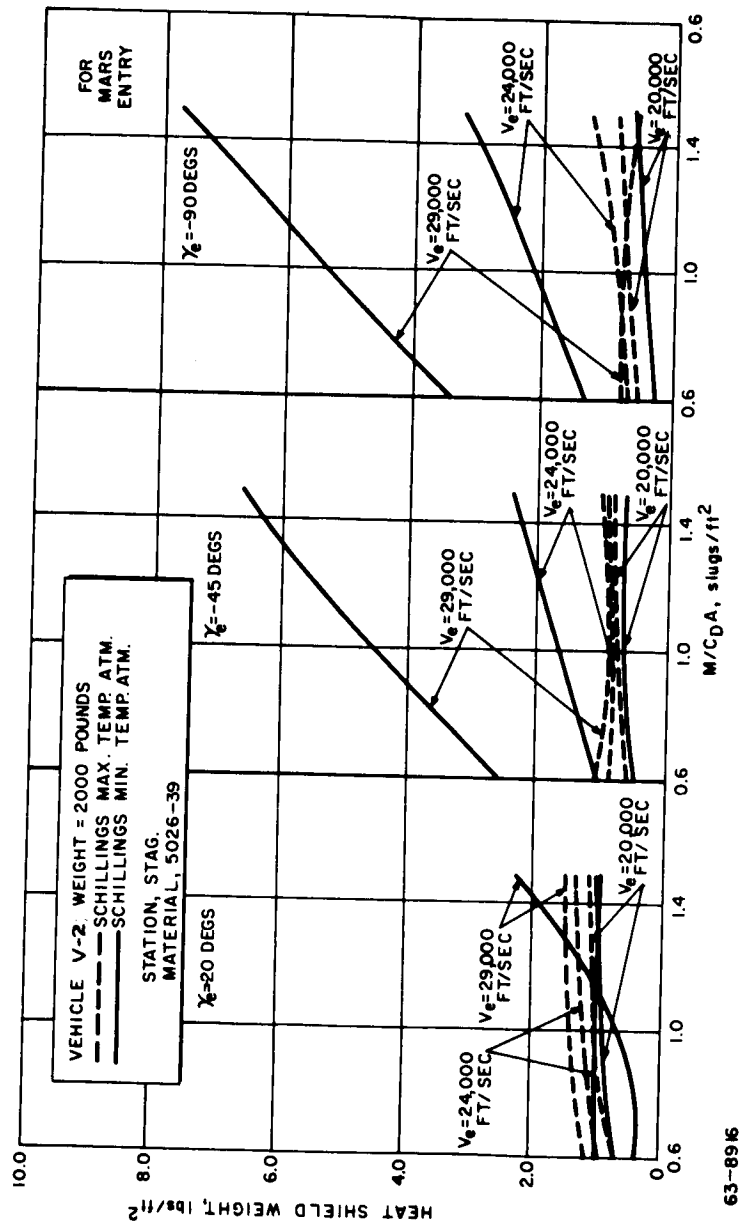


Figure 111 HEAT SHIELD WEIGHT VERSUS $M/C_p A$,
REFERENCE VEHICLE

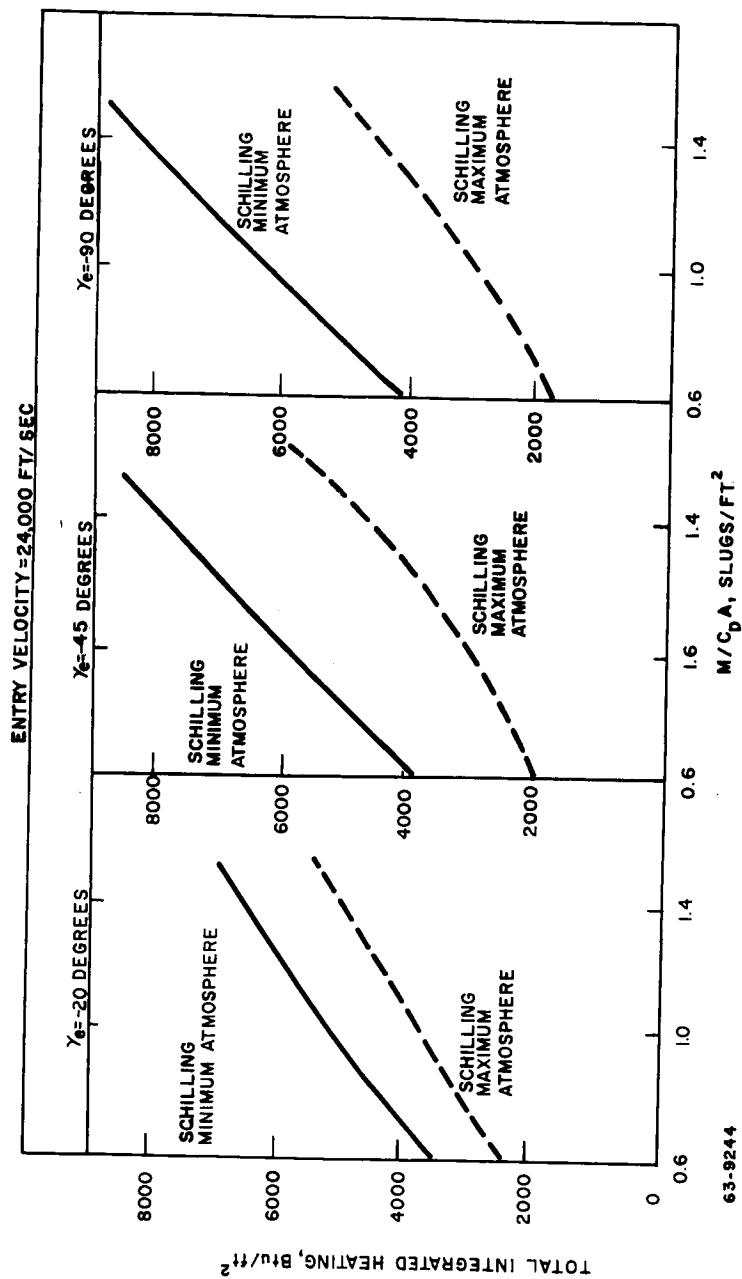


Figure 112 TOTAL INTEGRATED HEATING VERSUS $M/C_p A$ FOR STAGNATION POINT OF 2000-POUND REFERENCE VEHICLE

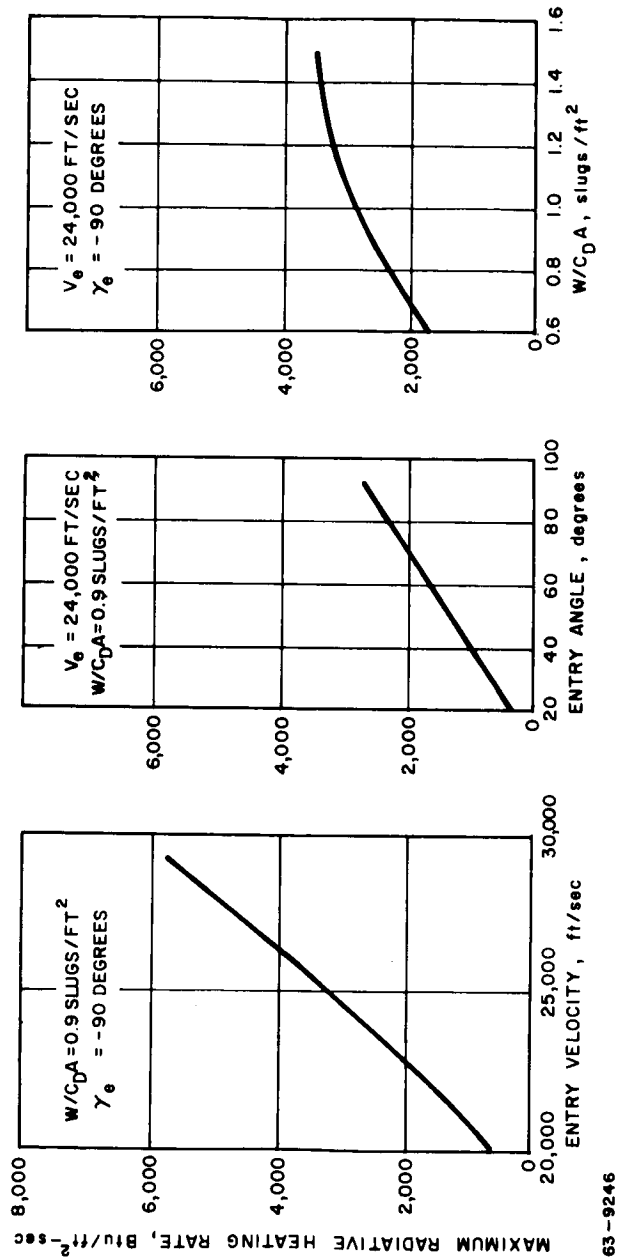


Figure 113 MAXIMUM RADIATIVE HEATING RATE VERSUS ENTRY VELOCITY, ENTRY ANGLE, AND W/CDA FOR 2000-POUND REFERENCE VEHICLE

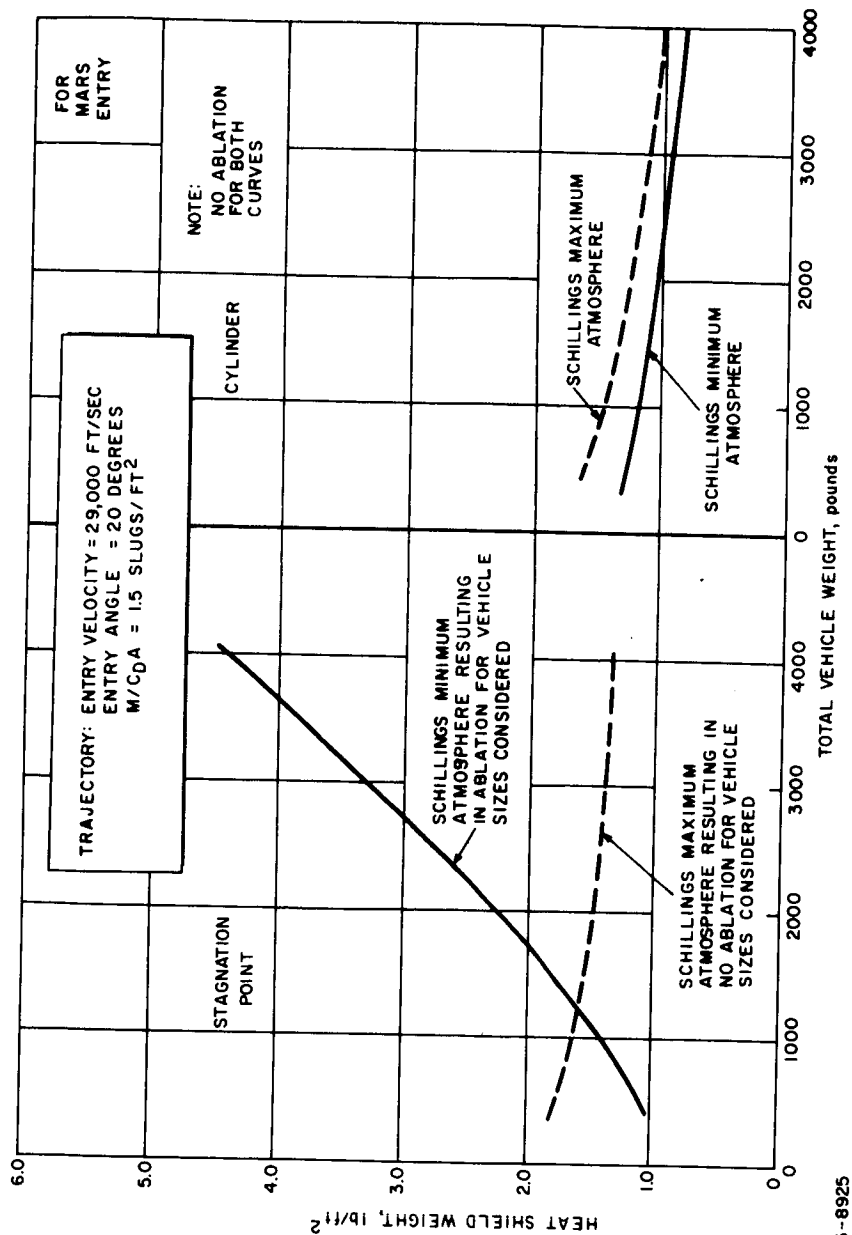


Figure 114 HEAT SHIELD VARIATION WITH VEHICLE SIZE FOR
REFERENCE VEHICLE

The heat shield requirement for the cylinder and boat-tail are directly dependent on the integrated convective heating since there is no ablation and essentially no radiant heat input. Figures 115 and 116 show the dependency of heat shield weight with M/C_{DA} , entry velocity, entry angle, and atmosphere. Like the nonablating cases on the stagnation point of the vehicle, and heat shield weight requirement is greatest for shallow entry angles and increases with entry velocity. Figure 117 shows the performance dependency variation with vehicle size. Note the tendency for the increase in heat shield weight for the cylinder to relax with increasing vehicle size. This results partially from the increase in structure weight with increasing vehicle size. The rear closure was designed as a fiberglass structure for all trajectories to absorb and re-radiate the heat load without additional protection.

2) V-1 shape. The nose of the V-1 shape was divided into two stations, the stagnation region and spherical section. The stagnation point heat shield weights are presented in figure 118. Magnitude and trends are similar to the reference shape. In general, there tends to be less ablation since the radiative pulses are smaller in magnitude (the reference shape is a blunter vehicle producing more radiative heating). However, the convective pulses are greater primarily because of the vehicle shape.

Figure 119 shows the heat shield weights for the spherical section. They generally follow the same trends as the curves for the stagnation point, but are somewhat smaller in magnitude and tend to ablate less.

Unlike the reference design, there is some radiation on the side section of the V-1 vehicle. However, its magnitude is less than 20 percent of the convective heating. Ablation of the heat shield on the conical areas never occurs. Therefore, the heat shield weight trends shown in figure 120 are very similar to the reference design cylinder weights.

3) Apollo shape. The Apollo shape was analyzed in reference to Kaplan's JPL atmospheres. The stagnation point heat shield variations shown in figure 121 again follow the same basic trends as for the reference design, except that they are lower and tend to vary less with atmospheric variations. This is due to a lower integrated heating and maximum rates for the lower M/C_{DA} required in these atmospheres.

Since the afterbody angle of the Apollo shape is 32.5 degrees, the ratio of heating on the afterbody to the stagnation point will be lower than for the reference or V-1 vehicles. The lower stagnation point heating results in a much lower heat load on the afterbody for the Apollo shape. Therefore an all-beryllium structure was analyzed and found suitable for all the convective heating loads.

e. Conclusions and recommendations. A reference design was selected with an $M/C_{DA} = 0.9$ slug/ft² and a 24,000 ft/sec entry velocity for

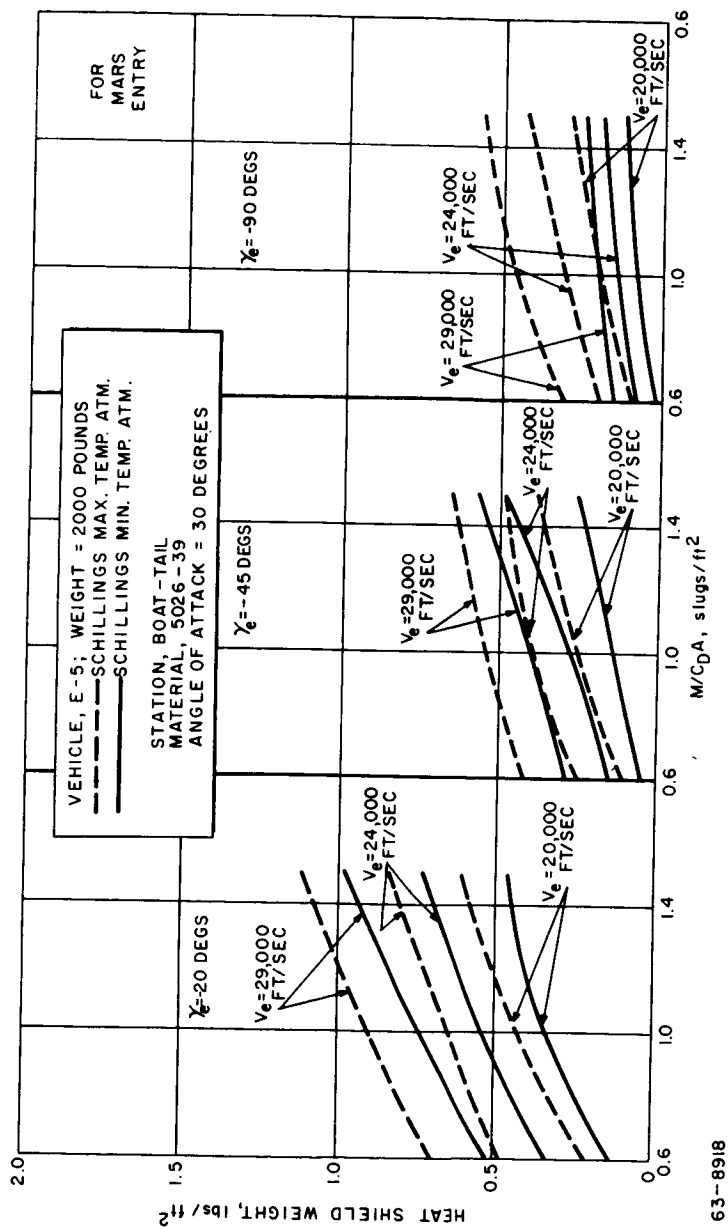
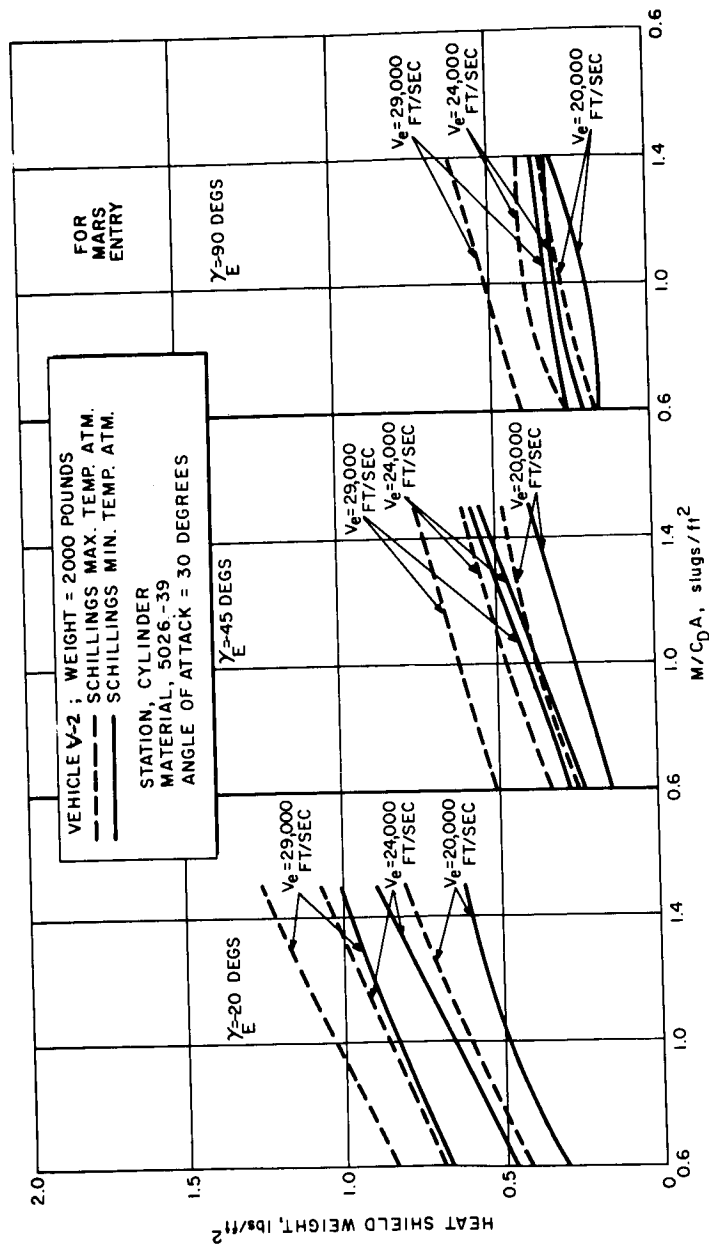


Figure 115 HEAT SHIELD WEIGHT VERSUS $M/C_D A$ REFERENCE VEHICLE

63-8918



63-8917

Figure 116 HEAT SHIELD WEIGHT VERSUS M/C_{pA} A REFERENCE VEHICLE

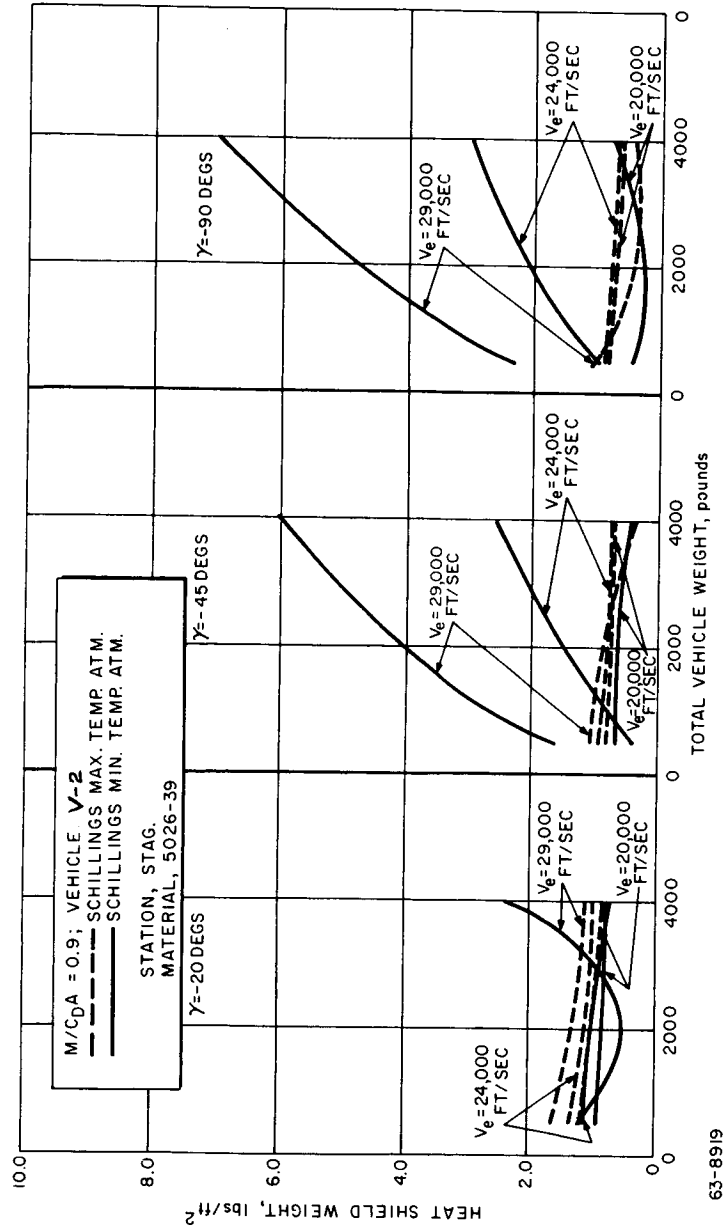


Figure 117 HEAT SHIELD WEIGHT VERSUS TOTAL VEHICLE WEIGHT

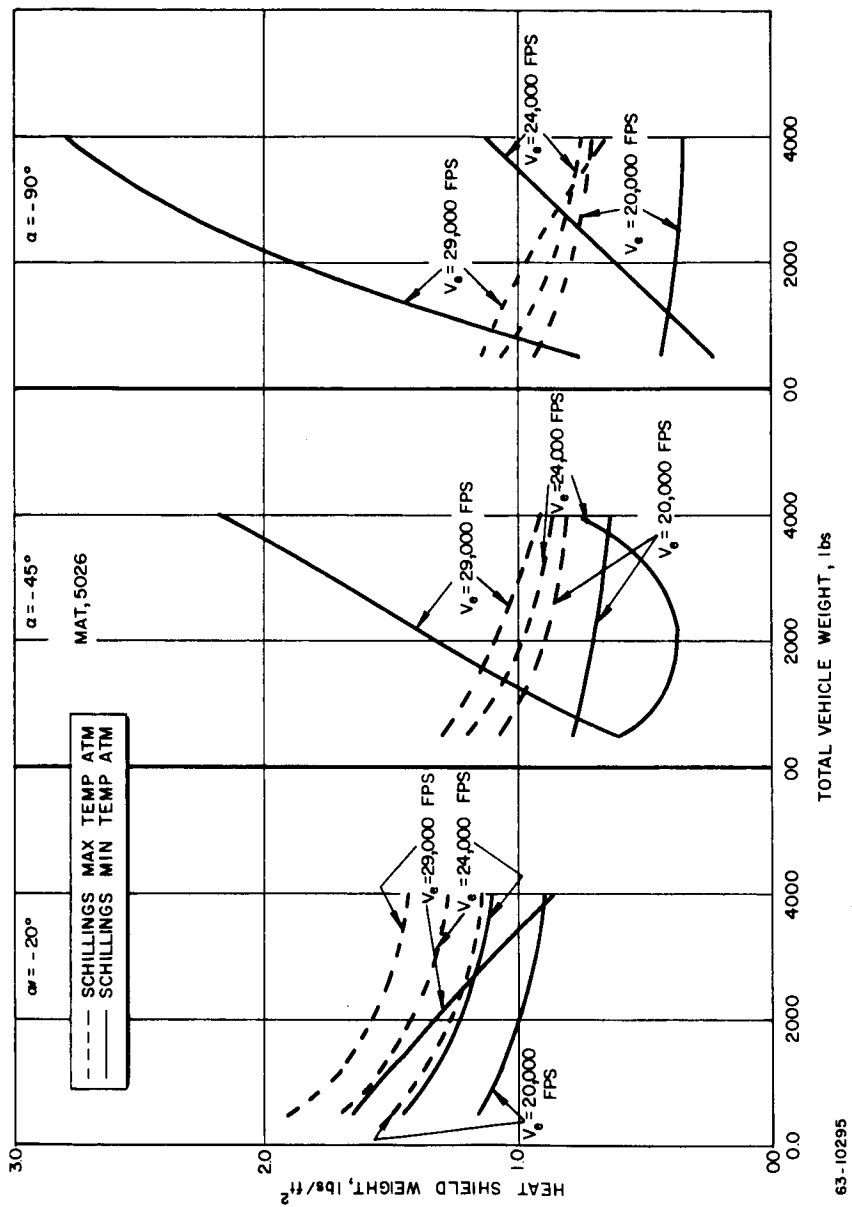


Figure 118 HEAT SHIELD WEIGHT VERSUS TOTAL VEHICLE WEIGHT -- NERV SHAPE

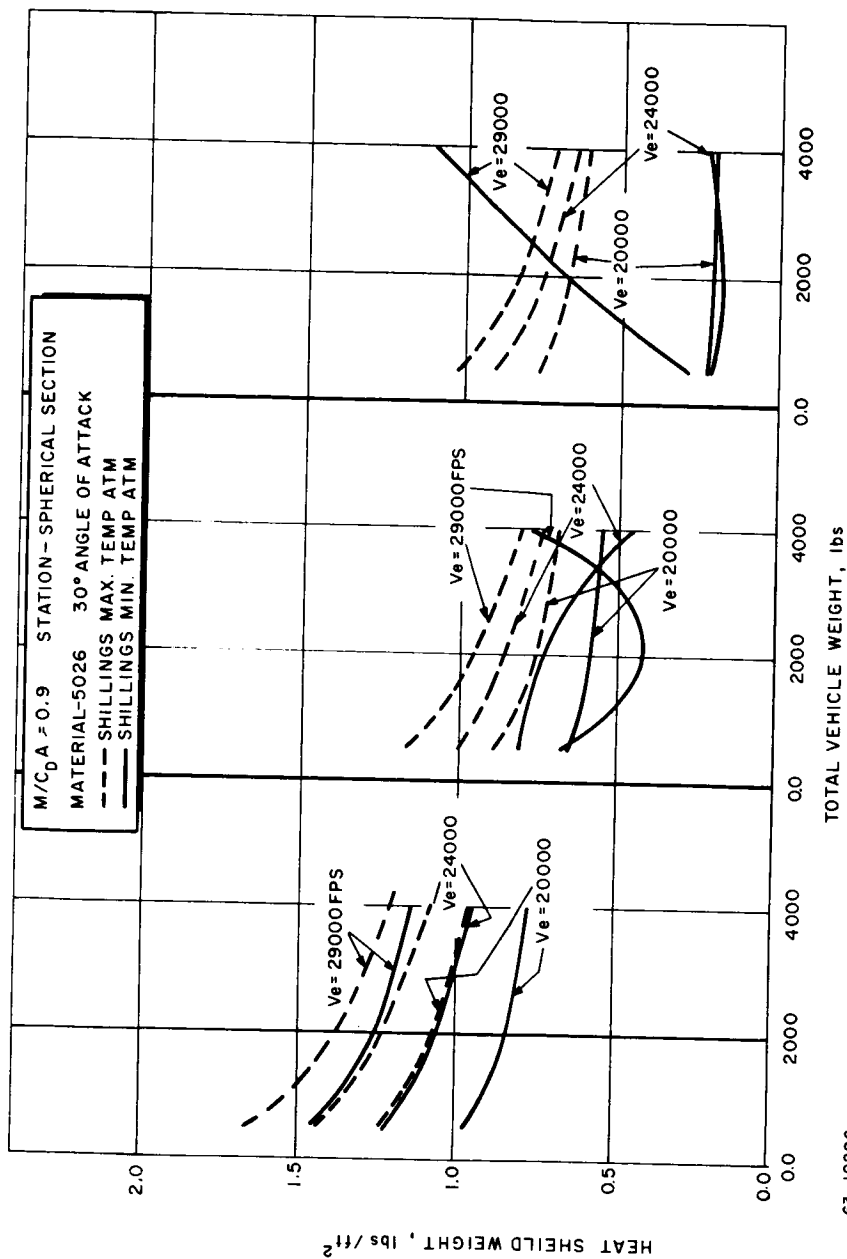


Figure 119 HEAT SHIELD WEIGHT VERSUS TOTAL VEHICLE WEIGHT -- NERV SHAPE

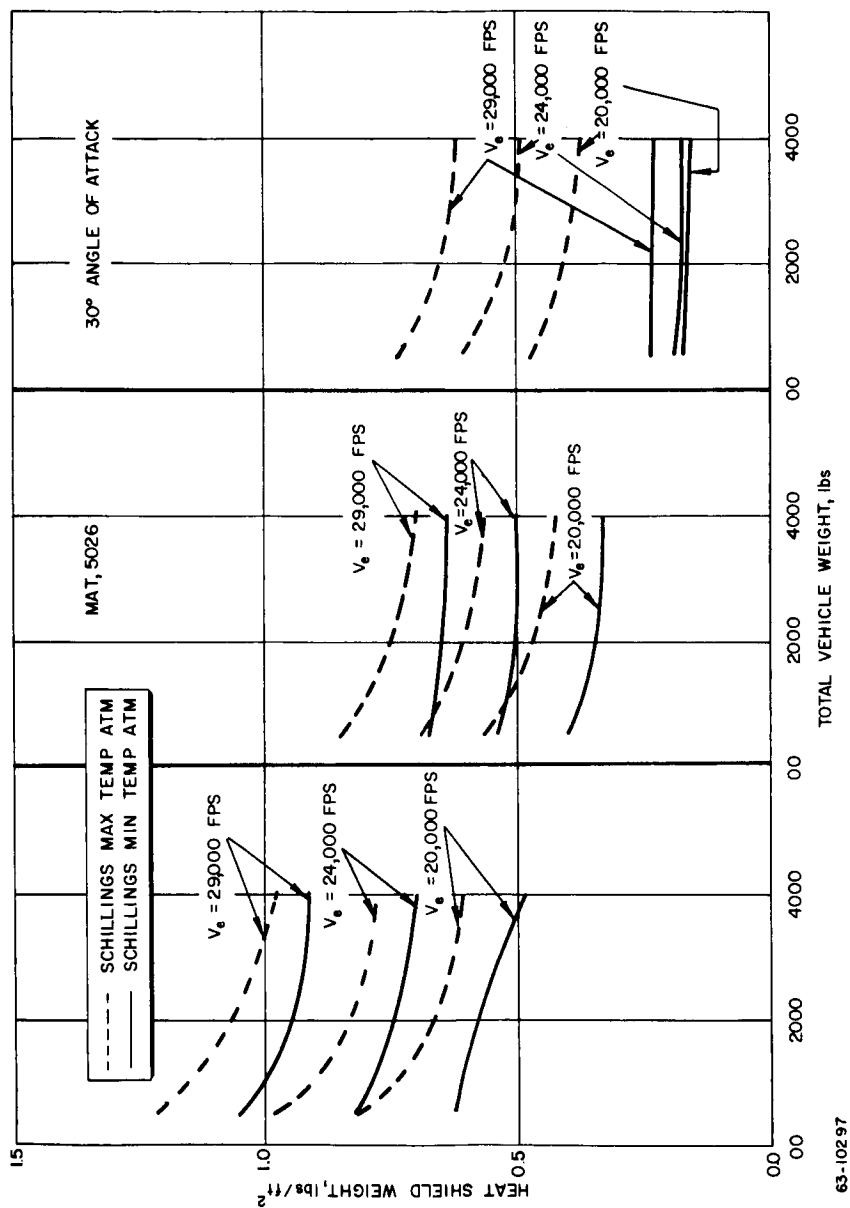


Figure 120 HEAT SHIELD WEIGHT VERSUS TOTAL VEHICLE WEIGHT--NERV SHAPE

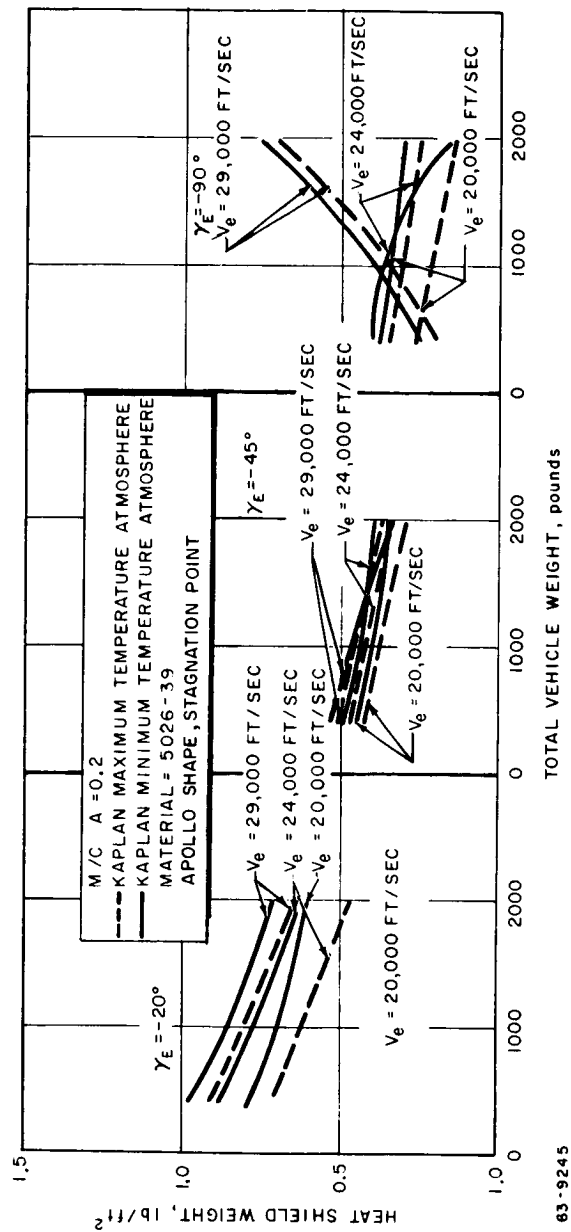


Figure 121 HEAT SHIELD WEIGHT VERSUS TOTAL VEHICLE WEIGHT--APOLLO SHAPE

the Schilling atmospheres. The total vehicle weight was approximately 1500 pounds. Heat shield weights were selected to enable the vehicle to survive entry in any of Schilling's model atmospheres and for entry path angles between -20 and -90 degrees. Thus the -90-degree minimum temperature atmosphere trajectory designed the stagnation point and the -20-degree maximum atmosphere trajectory designed the cylinder and boat-tail sections. This is due to the predominance of radiation at the stagnation point and the absence of radiation on the cylinder and boat-tail. Radiation predominates in the minimum temperature atmosphere and convection in the maximum temperature atmosphere.

Figure 122 shows the survival limits and safety margin for the stagnation point of a 2000 pound vehicle with an $M/C_D A = 0.9$ slug/ft², flying the same matrix of trajectories as the reference design vehicle. It is evident from the curve on the left in figure 122 that if the reference design were to fly the entire matrix of entry possibilities in the worst Schilling heat shield atmosphere, the payload would be penalized highly in the low velocity regime. In addition, it would not survive in the high velocity, steep entry angle regime. The second curve in figure 122 shows a similar comparison against atmosphere for a constant entry angle. Similar trends will occur for the cylinder and boat-tail sections. The total heat shield weight for the reference design is approximately 175 pounds and the payload (scientific and communication instruments) is approximately 650 pounds. Therefore, for many trajectories, half the heat shield weight would be excess. This is 14 percent of the payload, a significant portion.

It is therefore evident that design optimization requires narrowing the band of entry conditions by designing for each launch window separately and incorporating probability limits for entry angle and atmospheric possibilities. Probability limits on the entry angle can be accomplished by studying guidance control system limitations and reliability.

Little is known about the behaviour of a charring ablator in a planetary environment that produces large amounts of radiative heating and which has a different chemical composition than air. The physical model assumed for the present analysis reflects the state of the art. Considerable testing as well as more analysis is needed to better understand this phenomenon for reliable planetary entry heat shield design.

4.2 Heat Shield Material For Mars

1. Reference material for Mars. Of the several general types of materials available for use as heat shields, a low density, low conductivity, charring ablator has been selected as the reference material for the Mars lander. The reference material has been developed at Avco and is designated as Avcoat 5026-39. The other general types of materials investigated for application to the Mars lander are:

a. High glass or silica containing materials that form a molten glass or silica surface during ablation,

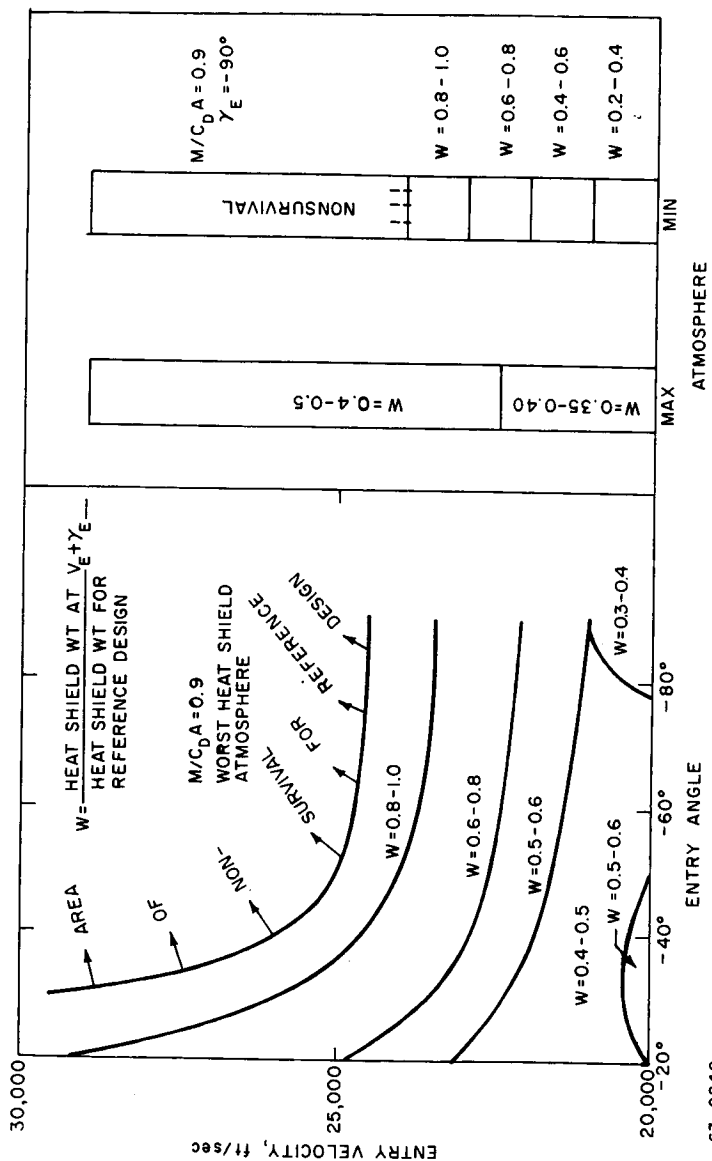


Figure 122 HEAT-SHIELD PERFORMANCE ENVELOPE FOR REFERENCE DESIGN

b. Pure sublimers that leave no residue upon ablation and possess relatively low ablation temperatures,

c. High temperature resistant metals possessing good heat sink and structural properties.

Charring materials have been studied extensively as heat shield materials. A recent analysis of ablative materials (ref. 27) describes the formation of the char layer for those silica-organic resin composites with silica/resin ratios of less than 1. The organic resin decomposes and deposits carbon on the silica fibers. Under proper conditions, this carbon is deposited in the form of pyrolytic graphite, resulting in a hard, dense, stable char layer. The silica (or glass) fibers provide a site for graphite deposition. Pyrolytic graphite may be deposited from epoxy, phenolic, and polyester resins. Fabrication and physical properties considerations indicate that epoxies possess the most desirable combination of properties for many heat shield uses.

The reference material has an appreciable epoxy resin content, which gasifies as the material decomposes. The resultant outward flow of gases has a strong blocking effect on the convective heating. A substantial amount of gasification and char formation can be found during a Mars entry without a significant recession of the surface. The material behaviour adjusts to the level of heating, e. g., at low heat rates it acts as a pure insulator; as the heat rates increase the material gasifies; further increase in the heat rate results in ablation of the complete virgin material and recession of the surface. Hence, the material is attractive for planetary entry where the entry flight path angles vary markedly resulting in a wide range of heating rates that the shield must withstand. The low density and thermal conductivity reduce the heat shield weight and establish a steep temperature gradient for maximum thermal insulation efficiency.

Avcoat 5026-39 has been evaluated in a variety of laminar and turbulent plasma arcs under convective heating. It has been exposed to low heat flux radiant heating. Mechanical and thermal properties have been obtained and fabrication procedures have been extensively developed. The material has been exposed to simulated space environment and its physical properties measured before and after exposure. A complete description of this material is available in ref. 28.

2. Thermal properties. The preponderance of the material testing has been carried out with convective heating because of test requirements in other programs and the availability of facilities. Studies are underway on the effect of combined radiant and convective heating on the reference material but the apparatus available is presently limited to a radiant heat flux of 125 Btu/ft²-sec. An arc-image furnace is now being constructed capable of generating radiant heat fluxes up to 10,000 Btu/ft²-sec.

Parametric studies of the entry into Mars indicate wide ranges of possible radiant and convective heat fluxes. The usual method of evaluating a material's performance under simulated planetary entry conditions in an electric arc is the heat of ablation, as defined below

$$Q^* = H_v + C_p \Delta T + \eta (H_s - H_w) + q_r$$

$$Q^* = \text{Heat of ablation}$$

$$H_v = \text{Heat of vaporization}$$

$$C_p = \text{Specific heat}$$

$$\Delta T = \text{Temperature change up to material degradation}$$

$$\eta = \text{Transpiration factor}$$

$$H_s = \text{Stagnation enthalpy}$$

$$H_w = \text{Wall enthalpy}$$

$$q_r = \text{Heat lost by reradiation}$$

The transpiration factor represents the heat lost by mass injection into the boundary layer. The term $(H_s - H_w)$ represents the "hot wall correction," and q_r is proportional to the fourth power of the measured surface temperature. In practice, the net heat transfer to the wall is measured, and divided by the mass loss, giving the heat of ablation (at steady state) in Btu/lb. A plot of Q^* versus enthalpy gives the $(H_v + C_p \Delta T)$ term from the Y-axis intercept, and (η) from the slope.

a. Convective heating. The following discussion is based on ablation tests of the reference heat shield material in three arc facilities: the OVERS arc, the Model 500 arc, and the 10-megawatt arc. These facilities are capable of producing convective heating, both laminar and turbulent, which can simulate the Mars entry completely. The use of gas mixtures in these arcs presents no major problem. The materials tested are either the reference heat shield, or some minor variations of the material. In general, these variations do not change ablative properties significantly.

1) OVERS arc. Avco RAD's OVERS (orbital vehicle reentry simulator) facility can generate gas enthalpies of approximately 250 to 20,000 Btu/lb and heat fluxes up to 800 Btu/ft² -sec. A schematic of the arc configuration is shown in figure 123. It operates with any combination of nitrogen, oxygen, and carbon dioxide, and the test chamber static pressure is approximately 1.2 mm Hg prior to arc firing. The exhaust jet is supersonic. The facility is programed so that pulsed test conditions can be obtained by varying the enthalpy and heat flux during one test.

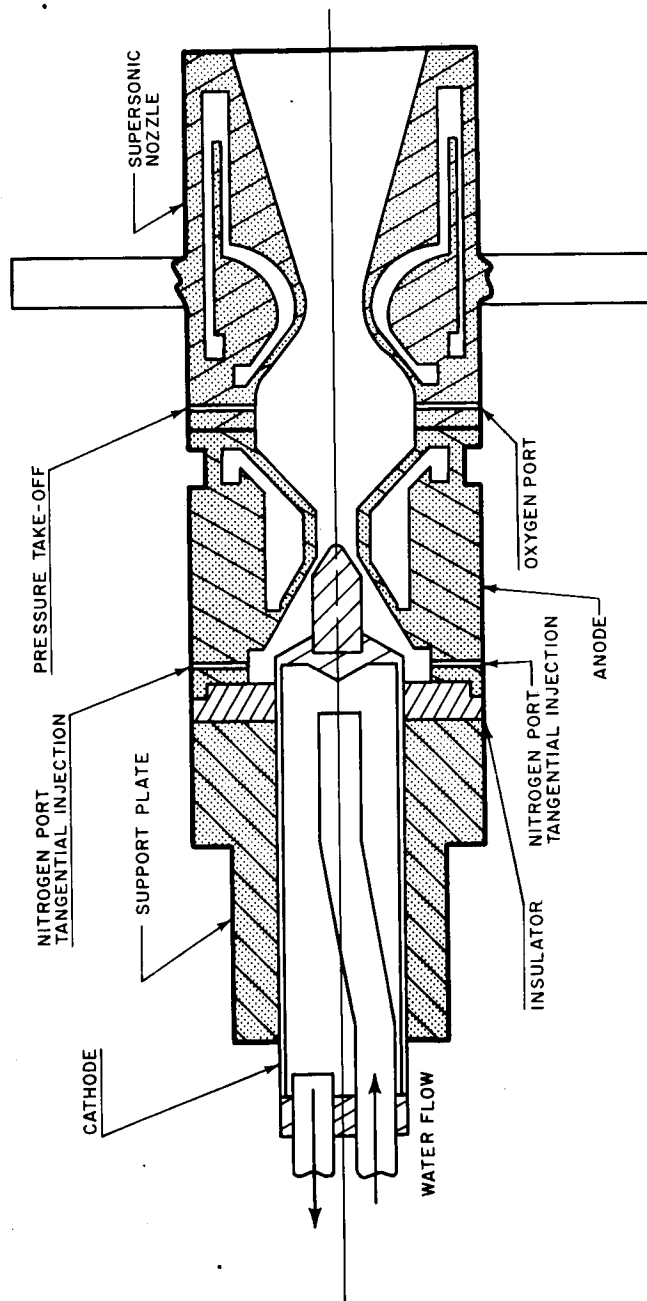
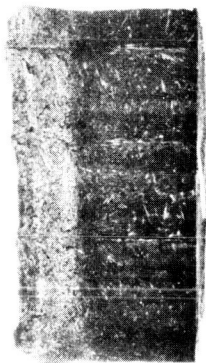


Figure 123 SCHEMATIC OF OVERS ARC CONFIGURATION

63-8716

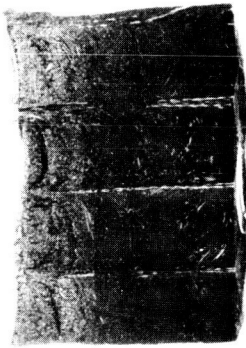


AP 1341-A1

$H = 20,000 \text{ BTU/lb}$

$\dot{q} = 270 \text{ BTU/ft}^2\text{-sec.}$

$t = 360 \text{ sec.}$



AP 1341 - A2

$H = 10,000 \text{ BTU/lb}$

$\dot{q} = 36 \text{ BTU/ft}^2\text{-sec}$

$t = 120 \text{ sec.}$



AP1341-A3

$H = 18,400 - 9,400 \text{ BTU/lb.}$

$\dot{q} = 270 - 36 \text{ BTU/ft}^2\text{-sec.}$

$t = 60 - (36) - 300 \text{ sec.}$

5026-39 3/8 H.C.
From Gunned Panel

Figure 124 PROPOSED MARS HEAT SHIELD MATERIAL AFTER TESTING AT LOW
HEAT FLUXES IN OVERS ARC

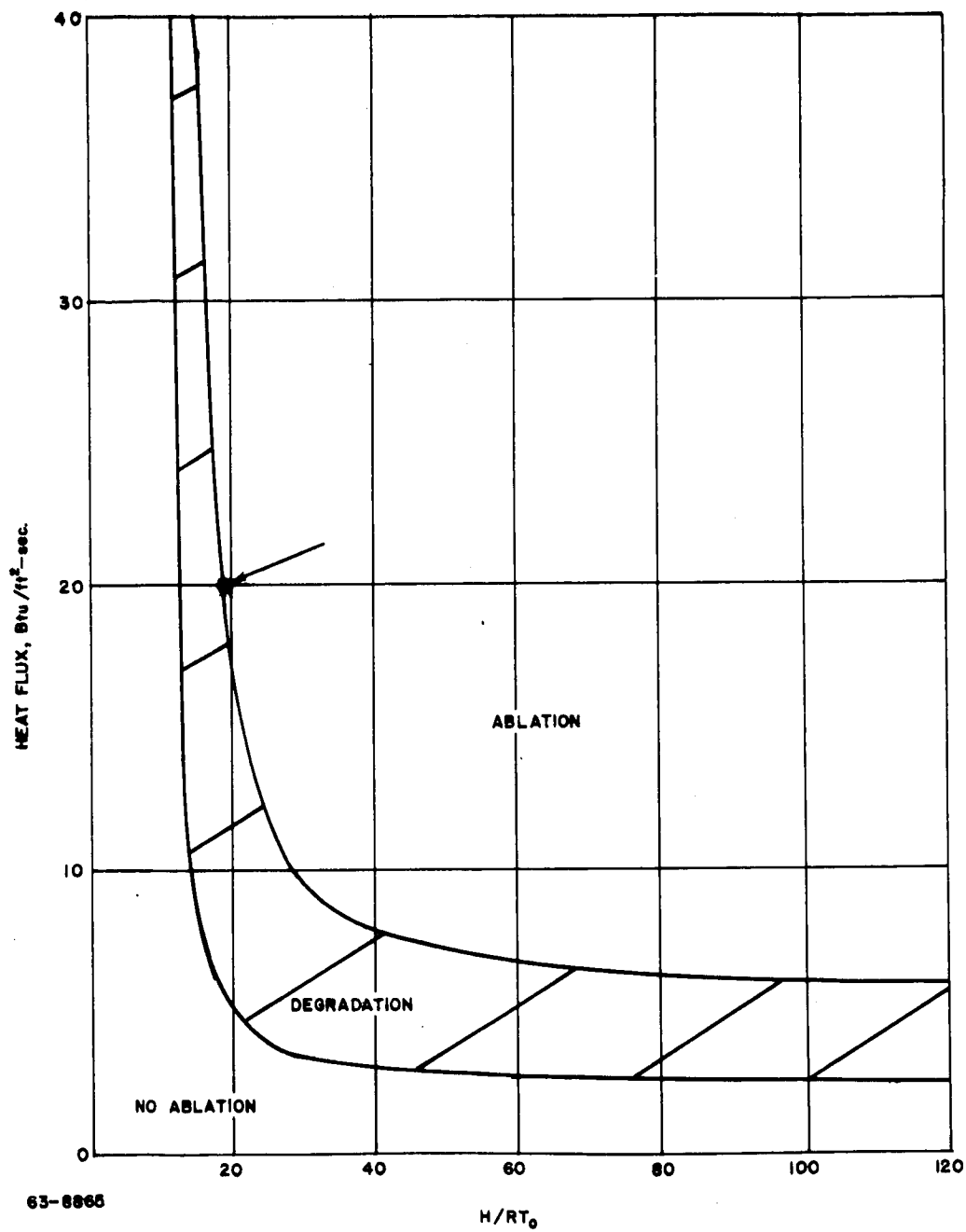


Figure 125 DIMENSIONLESS ENTHALPY VERSUS HEAT FLUX

Many samples of the reference heat shield have been tested in this facility. Figure 124 illustrates the charring characteristics of this material during exposure to low heat fluxes and high enthalpies, as well as one test "pulsed" between two heat fluxes. Microscopic studies with polarized light show that pyrolytic graphite exists in the char layer.

In an effort to evaluate in a preliminary manner the effect of different atmospheres on the proposed material, a series of tests were conducted in the OVERS facility on the Avcoat 5026-39 ablator where the working gas was three different mixtures of nitrogen and carbon dioxide (0, 5, and 10 percent CO_2) (ref. 30). The enthalpy was about 8,500 Btu/lb, and the heat flux near 100 Btu/ft²-sec. The test time in all cases was 2 minutes. For comparative purposes, two essentially noncharring ablators (Teflon and an unfilled epoxy-polyamide) were tested at the same conditions. It was found that increasing the CO_2 content of the working gas increased mass and length loss of the charring material. The noncharring materials were relatively insensitive to CO_2 content. These results are in agreement with the oxygen-diffusion controlled theory of ablation for charring materials proposed by John (ref. 30). Combining known densities and backface temperature rise during the tests for all materials, a figure of merit was calculated for each material. The Avcoat 5026-39 material was far superior to the other two materials, with Teflon being the most inefficient insulator.

2) Model 500 arc. The Model 500 plasma arc generates convective heating over wide heat flux and enthalpy ranges from which effective heats of ablation may be calculated. Two different plasma generators are used to cover an air enthalpy range of 200-10,000 Btu/lb with heat fluxes from 20 to 250 Btu/ft²-sec in the low enthalpy arc (200 to 3000 Btu/lb) and 800 to 1500 Btu/ft²-sec in the high enthalpy arc (3000 to 10,000 Btu/lb). On the basis of calculated convective heat pulses, the low enthalpy tests are the most meaningful for Mars entry. Heats of ablation measured from low to high enthalpies indicate that the proposed heat shield material is a good ablative insulator (ref. 28). Figure 125 illustrates possible ablation-degradation-nonablation areas calculated for Avcoat 5026-39 (ref. 31). A test at a heat flux of 20 Btu/ft²-sec and enthalpy of 20 H/RT₀ (675 Btu/lb) showed weight loss and charring, but no ablation (erosion or length loss). This point is in agreement with the estimates given in figure 126, and the test point is indicated.

2) 10-megawatt arc. The 10-megawatt arc is capable of heat fluxes up to 4000 Btu/ft²-sec and shear stresses to 100 lb/ft². If the proper pipe specimen is used, a turbulent gas flow is created. Figure 127 illustrates the type of stable, uniform char layer produced by the Avcoat 5026-39 material. Tests using shear forces of 3 to 20 lb/ft² indicate that the material's ablative characteristics are insensitive to these shear forces. The heats of ablation calculated from these tests are relatively high, but somewhat less than those obtained in laminar gas flow tests at the same enthalpy.

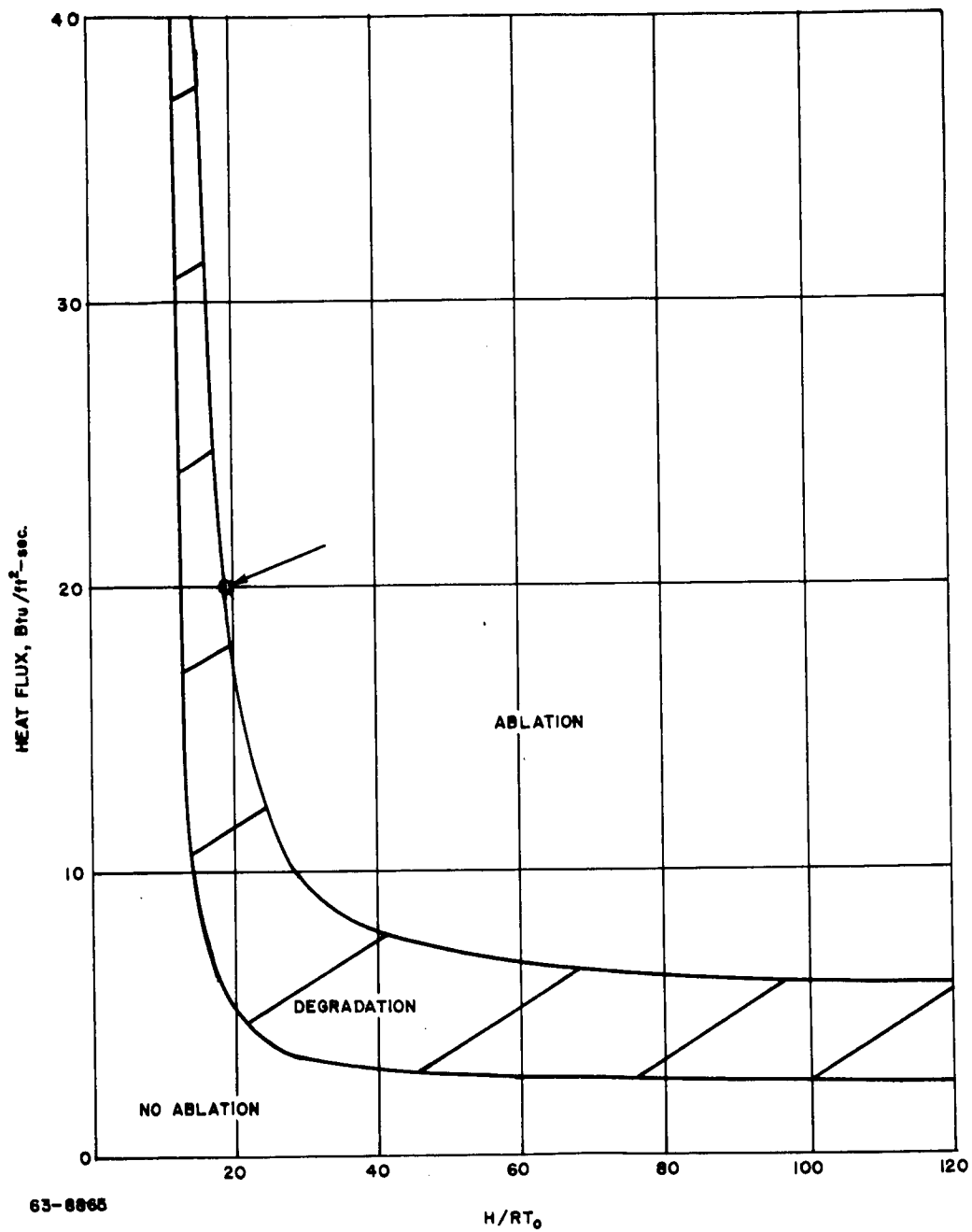
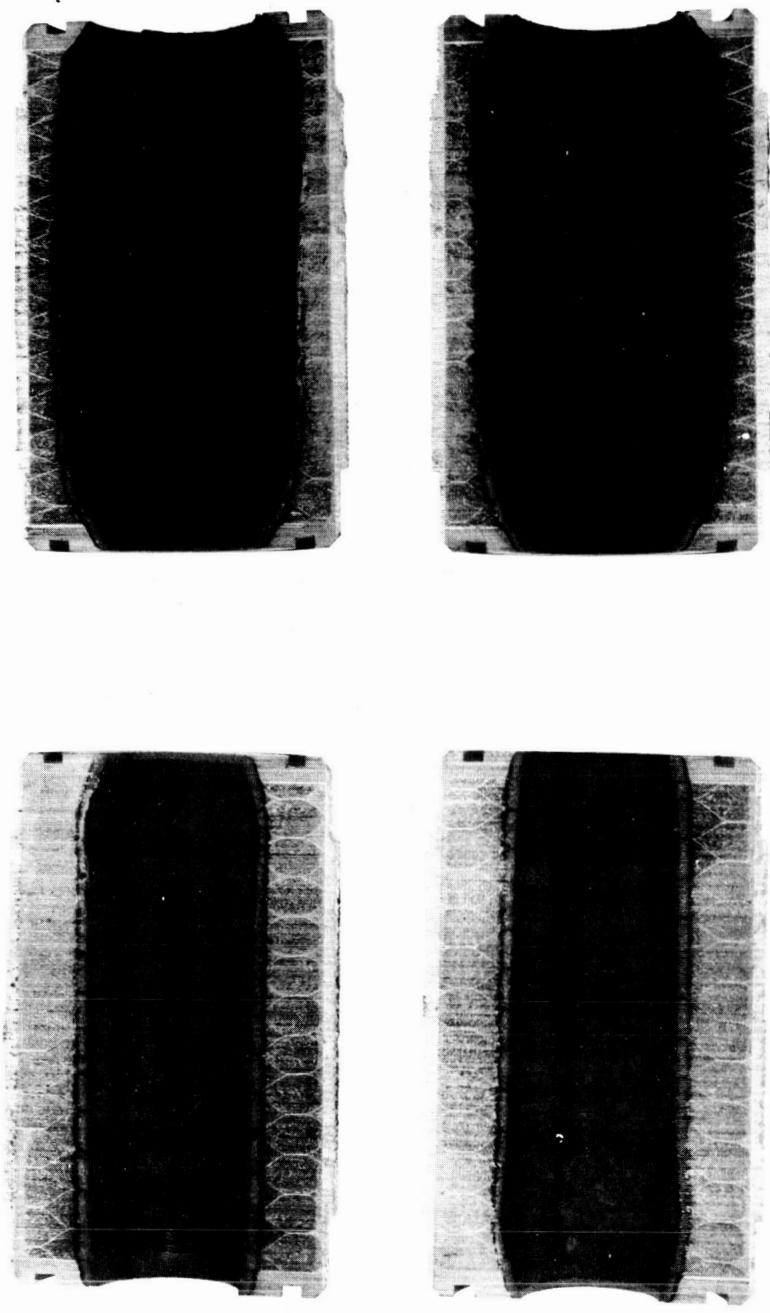


Figure 126 DIMENSIONLESS ENTHALPY VERSUS HEAT FLUX



RUN NO. 1899
AP-1349-3
ENTHALPY 125
HEAT FLUX 885 BTU/FT.²-SEC.
SHEAR 7.3 LB./FT.²
RUN TIME 14.60 SEC.

FLOW →
5026-39 - 3/8 IN. HONEYCOMB
ARC TEST 53

RUN NO. 1899
AP-1349-3
ENTHALPY 125
HEAT FLUX 885 BTU/FT.²-SEC.
SHEAR 7.3 LB./FT.²
RUN TIME 14.60 SEC.

0 1 2 3 4 5 6

Arco Research and Advanced Development

Figure 127 PROPOSED MARS HEAT SHIELD AFTER TESTING IN THE
10-MEGAWATT ARC
P-9598F

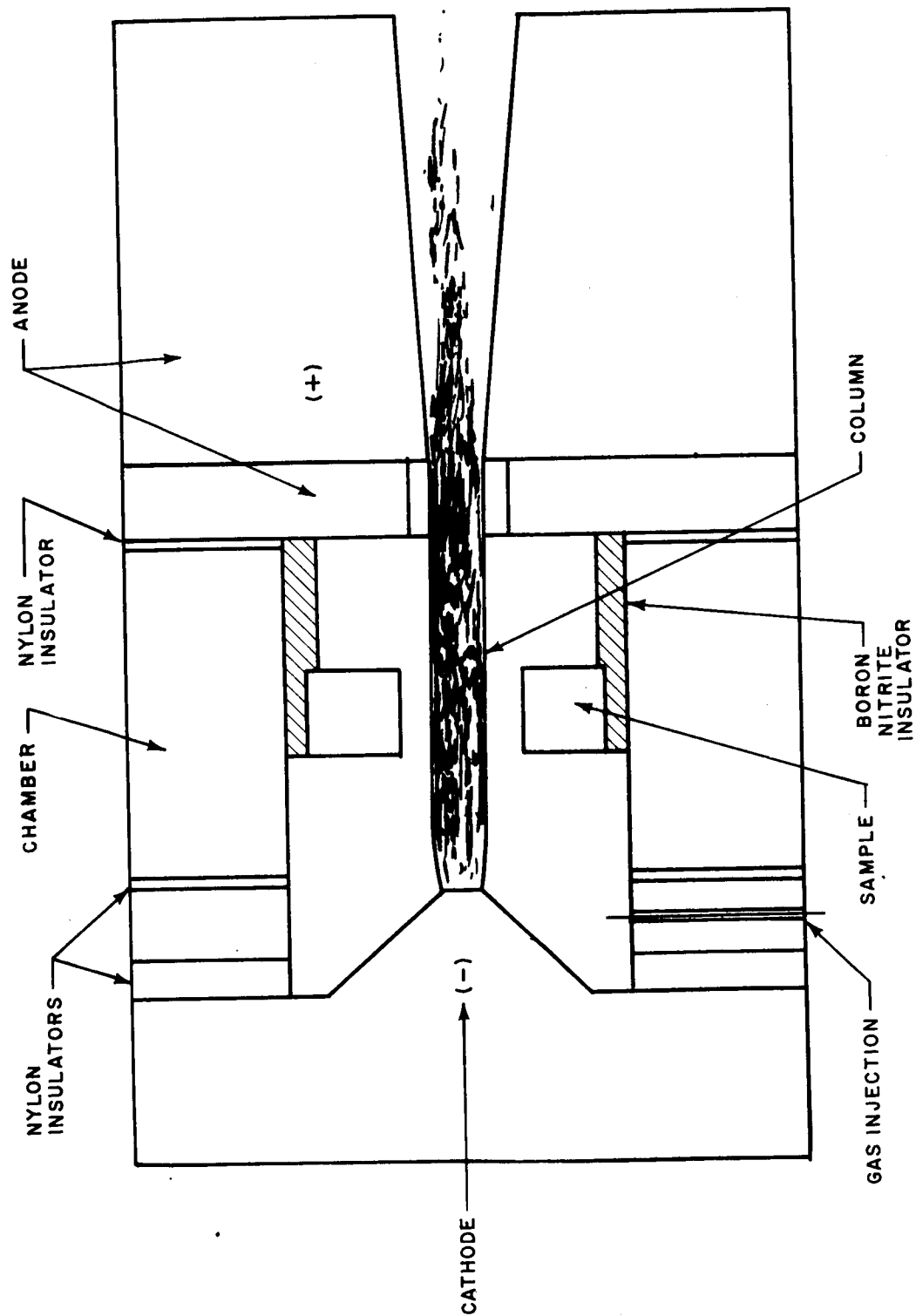
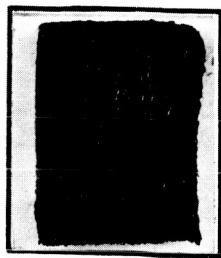
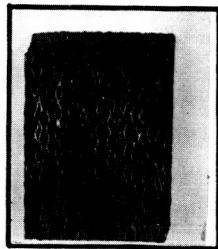


Figure 128 GAS-STABILIZED ARC FOR RADIATION STUDIES

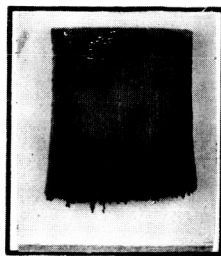
63-8718



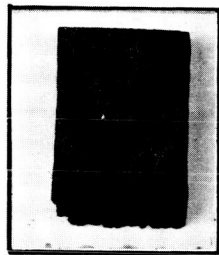
2 Graphite cloth
Epoxy resin



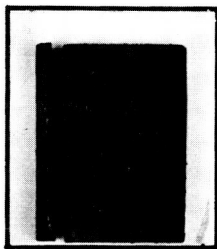
12 Graphite cloth
Phenolic resin



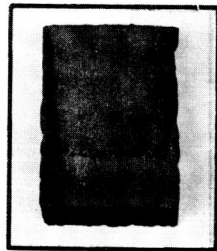
13 Astrolite



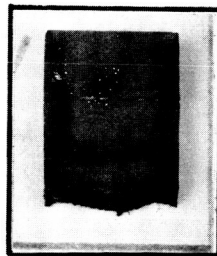
5 Proposed Mars Heat Shield
No Honeycomb



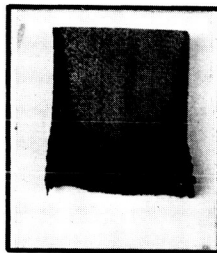
15 Precharred Graphite cloth
Epoxy resin



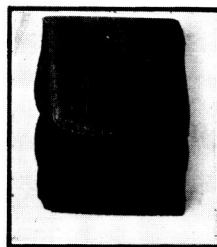
7 Variation of Proposed
Mars Heat Shield



16 RAD 60 PMTS
(Silica - Epoxy resin)



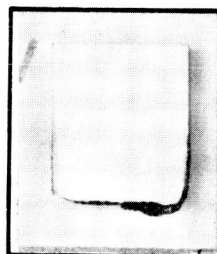
10 Astrolite (Silica cloth -
Phenolic resin)



17 Carbon and HT-1 Fiber
Epoxy resin



8 RAD 60 HD (Silica -
Epoxy resin)



* Swedlow S33478
(Nylon cloth - Acrylic resin)

* - Radiant Heat Flux 200 BTU/ft² sec.

Figure 129 TEST SAMPLE AFTER EXPOSURE TO RADIANT HEATING

b. Radiant heating. The peak radiant heat rate for the reference design ($M/C_{DA} = 0.9 \text{ slug/ft}^2$) is $2000 \text{ Btu/ft}^2 \text{ -sec}$ for Mars entry. No quantitative data are available at the present on the effect of radiant heating for radiative heat rates of this level. However, a series of test were run on several samples at a pure radiant heat flux of $450 \text{ Btu/ft}^2 \text{ -sec}$. By comparing Avco 5026 to other materials of known or assumed good radiant energy resistance, an estimate of this material's usefulness can be made.

An argon gas stabilized arc was used to determine qualitatively the effect of pure radiant heating, at a heat flux of $450 \text{ Btu/ft}^2 \text{ -sec}$, on several materials. These included the proposed Mars heat shield material, graphite and silica based materials, and one sublimator. The radiant arc is shown schematically in figure 128. The test sample is a flat disk with a 1-1/4-inch center hole through which the arc is struck. Tangentially injected argon stabilizes the arc column and prevents the column from contacting the sample. Radiation measurements, made with an Eppley thermopile, indicate that the sample "sees" essentially pure radiant heating. Test times (15 seconds at steady state operation) were constant.

Cross-section views of the tested samples are shown in figure 129. Note that sample 18 was tested at only $200 \text{ Btu/ft}^2 \text{ -sec}$. A previous test of this material, which is essentially a pure sublimator, at the regular heat flux of $450 \text{ Btu/ft}^2 \text{ -sec}$ completely vaporized the sample. Heats of ablation cannot be calculated because of insufficient data. Also, the sides of the samples received appreciable amounts of radiation, as seen by the char layer, so that the heating was not one dimensional. It is difficult to determine the char depth for the graphite-cloth-reinforced samples. It is known that degradation occurred because the weight losses for these samples were 10 to 15 percent. These materials did not ablate, however. In fact, sample 15 swelled slightly. These facts are in agreement with the known extremely high erosion resistance of the graphite-based materials. The silica-based materials all eroded considerably, and lost weight. Variations of the proposed Mars heat shield material (samples 5, 6, and 7) showed similar behavior. It should be noted that the char layer depth is similar to that of the silica based materials, and the char thickness is generally greater.

A major difference in the ablation under radiant and convective heating then, is the lack of shear forces under pure radiant heating. This fact would permit a relatively weak char layer to remain on the surface. Samples 5 and 6 (figure 129) possess this type of weak char layer. The char layer is composed of two zones; a weak outer layer, and a stronger inner layer. Convective shear forces might remove some of this outer layer. Sample 7, a variation of the proposed Mars heat shield material with equivalent thermal conductivity, possessed a harder, more uniform char layer.

3. Physical properties. Typical physical properties of the proposed Mars heat shield are shown in table 10. Since the material is contained in a fiberglass

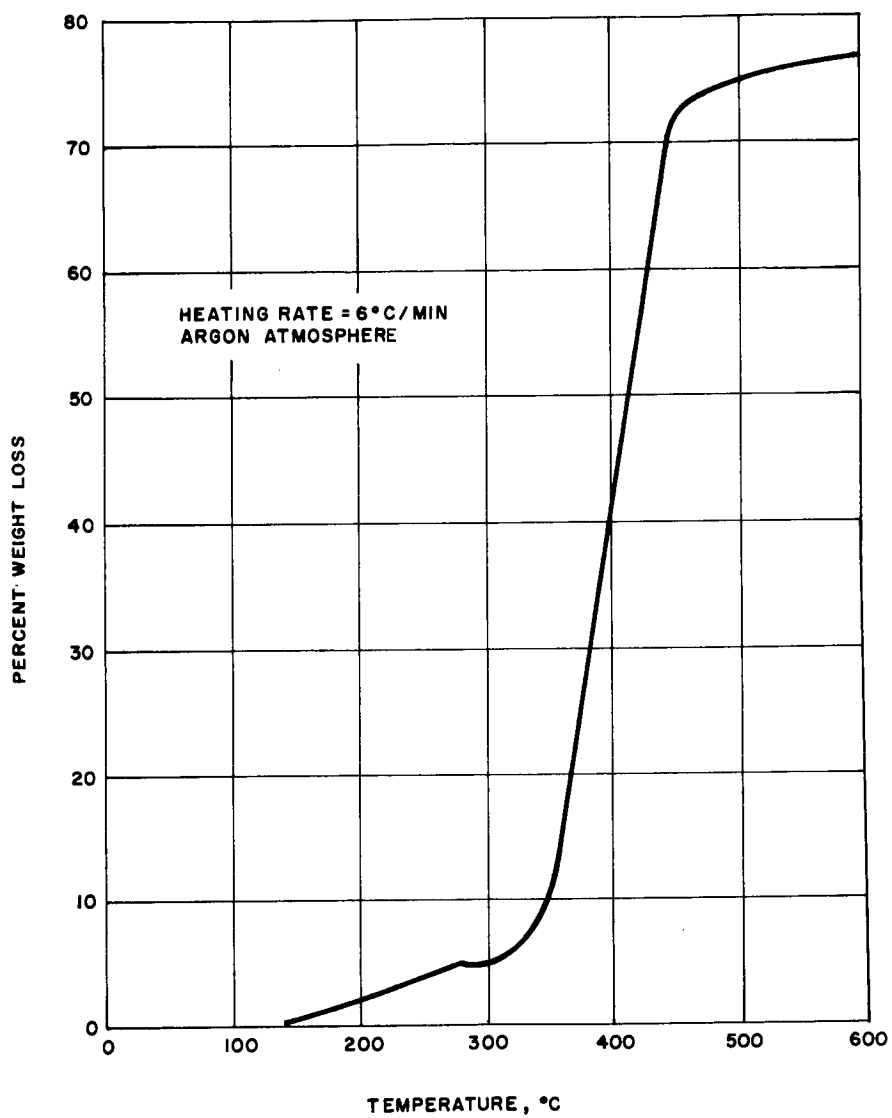
honeycomb, mechanical data are given both perpendicular and parallel to the honeycomb node direction. A variation of the honeycomb material possesses both higher ultimate strength and percent total strain to failure while retaining essentially the same thermal properties. At room temperature, ultimate strengths of 2000 psi and 5 percent total strain are obtained. High and low temperature properties are also significantly improved. The bond strength of the material can be made equal to the strength of the virgin material, providing the proper adhesives and cure cycles are used. Generally, epoxy adhesives are employed, with cure temperatures of 200 to 300 °F. Adhesives with cure temperature above 300°F are available, which can be used in the event heat sterilization of the capsule is required.

The thermal stability of the base resin in the ablator is given in figure 130. It is seen that at the reference sterilization temperature of 135 °C, no degradation occurs. The other components of the material are inorganic, and are not effected by these temperatures. In addition, the material undergoes temperatures in excess of 150 °C for several hours in air during the cure cycle. Tensile bars of the material were exposed to temperatures up to 300 °F for 4 days in argon. Tests indicated that no significant changes were produced in the mechanical properties. It can be reasonably concluded that the proposed Mars heat shield material will safely withstand the sterilization cycle, especially if the heating is conducted under an inert atmosphere. As the heat shield will be bonded to the substructure during the sterilization, the greatest danger is differential thermal expansion setting up sufficiently high stresses to cause failure. However, the coefficient of thermal expansion for the Avcoat 5026-39 material is similar to that of aluminum, so these thermal stresses will be minimized. Curved panels of the heat shield material bonded to aluminum honeycomb have been cycled over a temperature range of room temperature to -260 °F without failure.

4. Space effects. The effects of a simulated space environment on the proposed heat shield material have been evaluated. Since the material is a composite of inorganic fiber fillers and thermosetting resins, it would not be expected that significant physical changes would occur, which is the case.

The solar simulator vacuum chamber is shown in figure 131. The vacuum attainable is less than 10^{-5} mm Hg. Samples are mounted on a water-cooled copper plate with a temperature of about 15 °C. The samples are irradiated through a quartz window by a Westinghouse SAHX 2500-watt mercury-xenon short-arc lamp. At 2500 watts, this lamp produces a spectral distribution similar to that of a black body at approximately 6000 °K, which is similar to the solar spectrum. The quartz lamp cuts off wavelengths below 2000 Å.

Specimens of the proposed heat shield material were irradiated for 300 to 400 hours at an intensity of 0.14 watts/cm². During these exposure times, the samples reached temperatures of roughly 130 °C at the surface, and 60 to



63-8720

Figure 130 TGA CURVE FOR AVCOAT 5026 RESIN SYSTEM ONLY

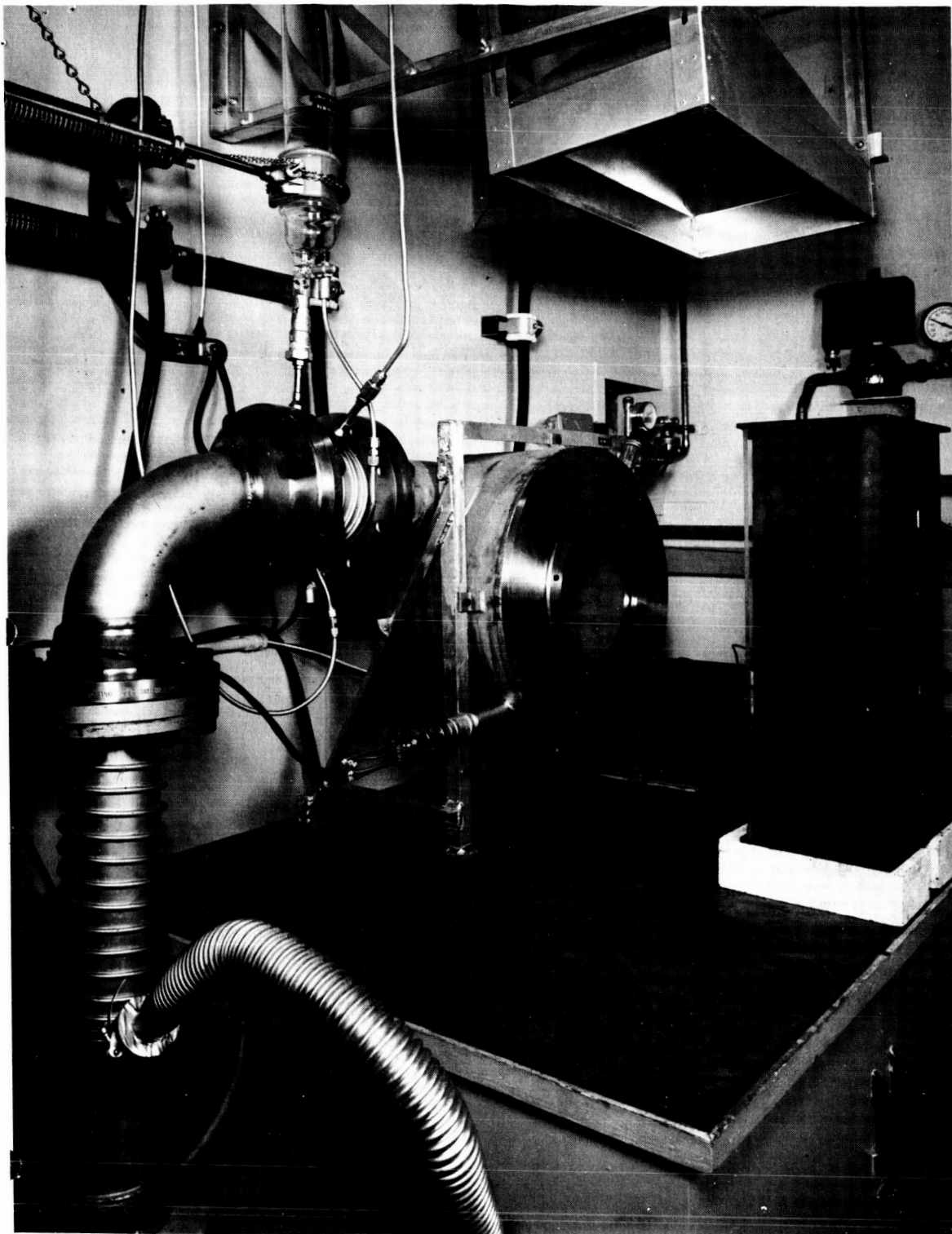


Figure 131 VACUUM SYSTEM FOR SOLAR SIMULATOR

70 °C near the center, while the backface remained near 15 °C. Test samples were held at the following conditions:

- a. Irradiation plus vacuum
- b. Vacuum only
- c. Room conditions -- no exposure.

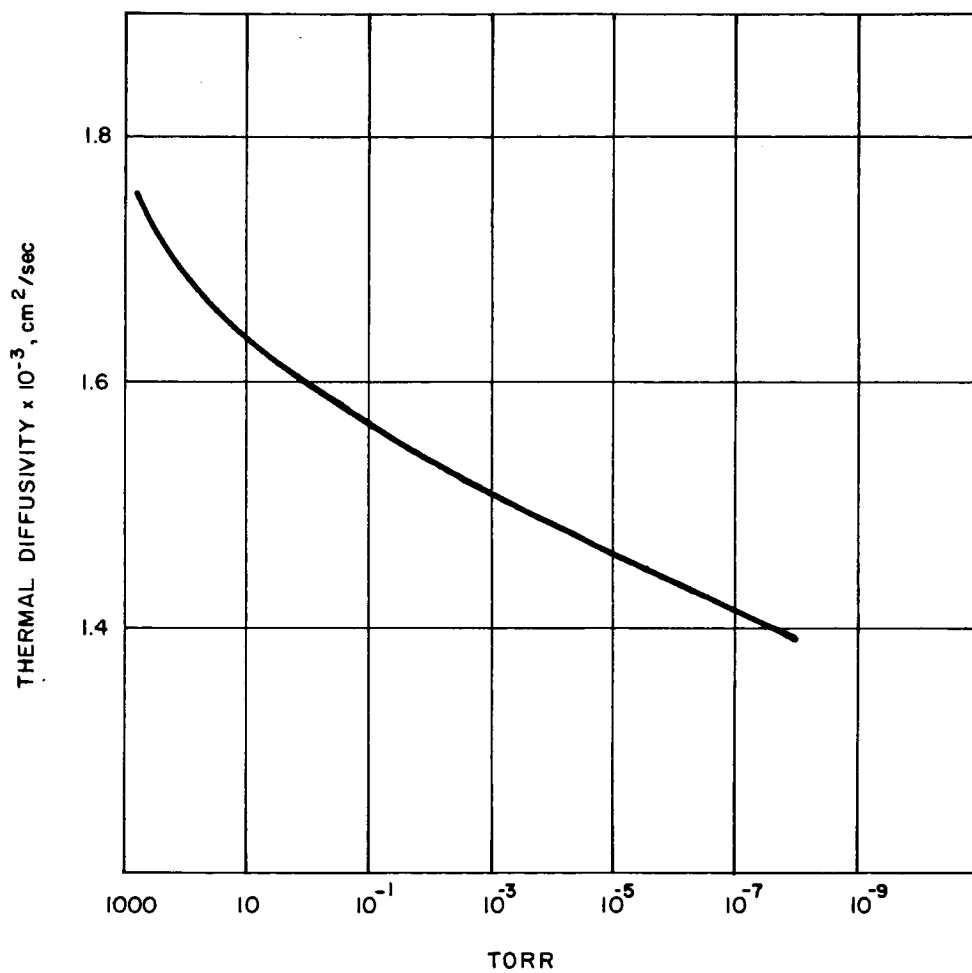
The test samples included specific heat (C_p), thermal conductivity (K), tensile, heat of ablation (Q^*), and optical (percent reflectance) specimens.

The specific heat and thermal conductivity values were not affected by either exposure conditions (a) and (b). Heats of ablation were raised roughly 30 percent for both exposure conditions (a) and (b). This may have been due to a furthering of the resin cure during the heat up to near 130 °C. The exposed specimens became slightly discolored during exposure, but percent reflectance changed less than 5 percent. Tensile tests indicate that these exposures do not significantly affect mechanical properties.

Another test was conducted by exposing tensile bars to temperatures of 250 to 350 °F in a vacuum chamber capable of 10^{-9} mm Hg. The time of exposure was 4 days. The maximum weight loss per specimen was 1.75 to 2.50 percent at 300 °F. No significant changes in room temperature tensile properties were noted.

An experiment was conducted to determine the change in thermal properties as a function of ambient pressure (ref. 32). The sample was suspended in a vacuum chamber held at 10^{-8} mm Hg, and heated by a mercury-xenon lamp through a quartz window. A brief thermal pulse was supplied by an Edgerton, Germeshausen, and Grier type FX-42 xenon flash tube, and the backface temperature rise recorded. A decrease of approximately 20 percent the thermal diffusivity of the sample was recorded during a 418 hours exposure at a pressure of 10^{-8} mm Hg at room temperature. The thermal diffusivity was a function of the pressure, as seen in figure 132. Heating the sample to 100 °C had no apparent effect other than increasing the outgassing rate. Since $a = k/\rho C_p$ (where a = thermal diffusivity, k = thermal conductivity, ρ = density, and C_p = specific heat), it is seen that a is a direct function of k . Moreover, the material is 20 to 30 percent porous. Therefore, the decrease in thermal diffusivity may be attributed to a decrease in thermal conductivity caused by the removal of air from the porous structure. Upon returning the material to room pressure, the original thermal diffusivity is obtained.

5. Fabrication. The proposed Mars heat shield material has undergone extensive fabrication development, and is now nearing the production stages (ref. 28). The reference heat shield material has been fabricated into large curved panels up to approximately 10 feet by 6 feet. It is fabricated by gunning



63-8722

Figure 132 THERMAL DIFFUSIVITY VERSUS PRESSURE FOR PROPOSED MARS HEAT SHIELD MATERIAL

the fiber-resin mixture into the individual honeycomb cells, after bonding the honeycomb to the substructure. The honeycomb can also be filled by tamping in the resin-fiber mixture.

Variations of the heat shield can be fabricated without the honeycomb. One technique involves compression-molding the resin-fiber mixture into tiles, and bonding the tiles onto the substructure. Since the size of the tiles is limited by the available press size, several tiles must be bonded together to make a continuous surface, resulting in exposed bond lines. Another technique involves the fabrication of a composite fiber felt, which is then impregnated with the liquid resin system and bag molded. With this method, it is possible to fabricate large shapes in one piece without exposed bond lines. This material also possesses equivalent thermal and superior mechanical properties over those of the honeycomb-based material.

TABLE 10

TYPICAL PHYSICAL PROPERTIES OF PROPOSED MARS HEAT

Density - (gm/cm ³)	0.55	
Thermal Conductivity at 250°F $\frac{\text{Btu}}{-\text{hr}+\text{ft}+^{\circ}\text{F}}$	0.065	
C _p - Btu/lb-°F	0.37	
Coefficient of thermal expansion - °F ⁻¹	17-30 x 10 ⁻⁶	
Ultimate Strength (psi) versus Temperature (°F)	<u>11 to HC</u>	<u>1 to HC</u>
-100	1410	950
78	1250	860
+350	200	130
Percent Total Strain versus Temperature (°F)		
-100	0.74	0.58
> 78	1.02	0.86
+350	0.7	0.65
Modulus (Ex 10 ⁻⁶ psi) versus Temperature (°F)		
-100	0.21	0.18
78	0.71	0.13
+350	0.04	0.025
11 to HC = parallel to honeycomb		
<u>1</u> to HC = perpendicular to honeycomb		

5. STRUCTURE DESIGN--MARS

5.1 General Approach

1. Major structural functions. The structural functions of the lander can be categorized in major areas which are: the external structure which is the aerodynamic load bearing structure of the thermal protection system during entry; the internal structure which serves as the load carrying member for the payload during launch, entry and landing; the structure which serves as protection if toppling occurs after impact and is also used for reerection; the impact attenuation structure which has the function of limiting the loads transmitted to the internal structure during impact.

a. External structure. The external shape chosen for the Mars reference design is the V-2 configuration. The aerodynamic load bearing structure of the entry vehicle is aluminum sandwich construction in order to minimize weight required for the general instability mode of failure to which the vehicle is subjected under planetary entry aerodynamic loads. There are a number of other reasons in favor of choosing this particular design. One of these deals with the effect of the vibration environment encountered during ascent although the detailed effects of vibration cannot be evaluated at this stage of the study. The inherent bending rigidity of the sandwich structure tends to alleviate the problem of failure caused by vibration. Another factor is the use of aluminum rather than steel for the substructure because of a weight advantage in heat shield design due to the greater specific heat of aluminum. Also thermo-structural considerations favor the use of aluminum because of the thermal compatibility between the heat shield material (5026) and aluminum.

b. Internal structure. The Mars lander internal structure is stiffened monocoque construction. The structure provides overall protection for the payload during the mission and is the load carrying member to which the payload components are mounted. The inertia loads of the payload must be transmitted through this structure and distributed into the external structure. The thermal environment of this structure is not severe for the Mars lander so that aluminum is used as the structural material.

c. Reerection structure. The petals of the reference design for Mars are constructed with an aluminum box beam central rib. This is the load carrying member for the main parachute load and also the load imposed on the lander during reerection. The top of the petal structure is made from fiberglass due to the necessity of communicating through the petal structure. The remainder of the lower portion of the petal is an aluminum sandwich construction that surrounds the central rib. This part of the petal provides protection for the payload if the landed package does not remain erect

after impact. It is difficult to assess the structural integrity of the petals because of the large number of design possibilities imposed by the unknown terrain.

d. Impact structure. The impact attenuation system used in the reference design for Mars consists of cylindrical pads of spiral-wound corrugated aluminum foil. It is a passive system, requiring no actuation or deployment. The impact energy is absorbed by progressive buckling of the cylinders.

A metal energy absorber was used rather than a plastic foam or balsa wood because it could withstand the environments of sterilization, launch acoustics, and space flight to a greater degree than the nonmetallics. Further, it can be crushed to 20 percent of its original height, as compared to 50 or 60 percent for plastics.

This particular design was chosen because it exhibits higher shear resistance than a honeycomb or laminated grid structure and is relatively easy to manufacture. It is made by bonding or brazing a strip of corrugated aluminum to a flat strip, then winding this composite into a cylinder. Perhaps the best advantage it possesses is that by varying the number of corrugations per unit length of strip, the crushing stress can be varied over wide ranges. This property is used in the present design, where the lower halves of the cylindrical pads have a low crushing stress and the upper halves have a higher crushing stress. This permits the capsule to accept impacts at an angle without requiring that excessive strokes be provided.

A base plate is provided beneath the pads to distribute uneven loadings caused by rough terrain and to help protect the payload from damage due to small rocks.

2. Design criteria. The structural weights for this study have been generated from design criteria formulated with regard to the following definitions:

a. Limit load. Operational limit load is that experienced under the specified environmental conditions.

b. Failure criteria.

1) Static loads. Modes of failure which are governed by yield are referenced to limit loads and modes of failure for ultimate strength are referenced to ultimate load conditions of 1.25 times limit load.

2) Dynamic loads. The environmental conditions are applied directly in order to establish accelerations. The resultant accelerations are treated as static loads with no factors for transmissibility unless specified.

3) Instability. This mode of failure was referenced to ultimate loading conditions (1.25 times limit load).

The margins of safety chosen for the study were zero except in the cases where the structural sizes were dictated by manufacturing limitations which necessitated margins greater than zero.

The manufacturing constraints imposed on the lander design primarily consist of limiting the minimum face sheet thickness of the sandwich structure for the lander to 0.008-inch for stainless steel and 0.012 inch for aluminum. These minimum thicknesses were assumed because of the necessity of manufacturing a large structure which could be held to close dimensional tolerances to ensure that the heat shield would be adequately bonded to the structure.

The design approach employed in the lander was to size the aerodynamic load-bearing structure for general instability under the worst postulated atmosphere for loads. The inertia loads encountered under these conditions were also used in the evaluation of the internal structure and petal structure. It is difficult to assess the design criteria that should be used in the analysis of the petal structure because of the many possibilities that can be conceived for the landing phase of the mission. The unknown terrain presents a most difficult evaluation of what conditions should be examined in the design of the structure.

Several design criteria were established for the impact attenuation system. It was decided that accelerations imposed during impact would not be allowed to exceed those felt during the worst possible atmospheric entry. Aerodynamic stability requirements set the limit for the maximum permissible height above the blunt nose of the center of gravity of the lander at entry. Knowing the payload dimensions and those of the spherical cap structure and heat shield leads to a determination of the maximum possible stroke of the impact system.

Finally, the impact loads into the internal structure follow the same load paths as were provided for the entry loads.

Meteoroid impact is a hazard which can seriously affect the lander. While the lander is attached to the orbiter, a penetration of the sterilization can enclosing the lander could compromise the sterility requirement. After the lander has separated from the orbiter and sterilization can, two modes of failure could be brought about by meteoroids. A single meteoroid impact may cause a pit in the heat shield deep enough to form a hot spot during entry, resulting in possible degradation of the payload or the function of the payload. Alternately, a large number of impacts of very small particles could change the radiation characteristics of the surface of the heat shield to such an extent that thermo-structural failure occurs during entry.

Although aspects of these problems have been investigated in connection with other Avco programs, predicting the probability of occurrence of any of these modes of failure is not possible at this time. This is due to a lack of knowledge of the meteoroid environment in the vicinity of Mars and an incomplete understanding of the physical processes which take place during impact. The best estimates possible at the present state of the art would include uncertainties of several orders-of-magnitude. This circumstance is discussed in greater detail in the discussion of structural considerations of the orbiter-bus module.

3. Environmental criteria. The lander is subjected to a number of environments which were considered under the general headings of: 1) ground handling, 2) ascent, 3) interplanetary transit, 4) planetary entry, and 5) planetary landing.

The environmental criteria for the structure during the ground handling, ascent, and interplanetary transit phases of the mission are presented in table 11.

The environment experienced during planetary entry cannot be presented as a general condition as it is a function of the specific vehicle and atmosphere. The load and thermal environment during the entry phase is governed by the vehicle trajectory and shape, the atmosphere, the ballistic parameter $M/C_D A$, and entry conditions. A description of the parametric study involved in the analysis of entry conditions is described elsewhere. The particular load environments chosen for the reference designs are presented below.

Mars Reference Design - Direct Entry

$V_E = 24,000 \text{ ft/sec}$
 $\gamma_E = -20 \text{ to } -90 \text{ degrees}$
 $M/C_D A = 0.9$

Decelerations

Axial - 125 g (Earth) =
 Lateral - 20 g (Earth) =
 $q = 3,600 \text{ lb/ft}^2$

In the instances where there were ranges of variables to be considered which would affect the design, the worst possible environment was chosen as the one to be considered in the design of the structure.

The impact attenuation system was based on the following considerations. The maximum descent velocity which could be permitted was determined by specifying a minimum required descent time while the capsule was suspended from the parachute. This velocity also sets an upper limit to the kinetic energy which the impact attenuation system must dissipate.

Another requirement imposed on the impact attenuation system is that, due to swaying under the parachute and to large scale roughnesses of the terrain, the system would have to accept impacts at large angles to the vertical. Further, small scale terrain irregularities, such as rocks, provide another hazard to the impacting payload. Protection against this danger must also be provided by the landing system.

TABLE 11

MARS LANDER ENVIRONMENTAL CRITERIA

	Ground Handling	Ascent	Interplanetary Transit
<u>Configuration</u>	All assemblies unpackaged	Orbiter and lander in ascent configuration	Orbiter and lander in flight configuration
<u>Acceleration</u>	Ascent conditions always govern; payload must be shock mounted for transportation	Max g Axial + 5.0 - 2.0 Lateral \pm 1.0 Max g; M = 1.0 Axial + 3.0 Lateral \pm 2.0	Axial + 1.0 Lateral \pm 0.5 g
<u>Vibration</u> Superimposed on steady state acceleration for max g and m = 1.0 conditions	and ground handling in order to maintain levels less than ascent loads	Sweep test-transient 16 to 42 cps 2.0 g (peak) 42 to 95 cps 0.022-inch DA 95 to 2000 cps 10 g (peak) Resonance test-steady state 16 to 42 cps 1.0 g (peak) 42 to 95 cps 0.011-inch DA 95 to 2000 cps 5 g (peak)	
<u>Shock</u>		Acceleration and vibration levels are critical; sufficient attenuation is available in structure designed by ascent loads	Orbiter-lander separation insignificant
<u>Thermal</u>	+ 80 to + 60 °F	+ 150 to + 60 °F	-10 to +300 °F

TABLE 11 (Concl'd)

	Ground Handling	Ascent	Interplanetary Transit
<u>Miscellaneous</u>	Sterilization - three -36-hr. soak periods at 295 °F Humidity - 99 per- cent	Booster malfunction rotational velocity and acceleration equal zero	
		Component levels (any one of the follow- ing in any direction) 1. Symmetric tri- angular pulse 35 g peak 10 msec 2. Half sine pulse 35 g peak 8 msec 3. Rectangular pulse 35 g 5 msec	

5.2 Analysis

1. External structure. The load-bearing structure of the entry vehicle was analyzed for two primary modes of failure which were general instability and yielding due to the loads imposed by the entry environment. The instability criteria were developed by the extension of test data and theory for an isotropic shell to the formulation of an instability expression for an orthotropic shell. This was accomplished by a transformation of equivalent parameters in an isotropic and orthotropic shell based on a comparison of the strain energy expressions. It should be noted that it is necessary for final detail design to perform structural testing to verify the validity of this transformation.

A parametric study was performed on the external structure of the lander involving such considerations as shape (V-1, V-2), entry angle, entry velocity and $M/C_D A$. The results of this analysis are presented in figures 133 to 135. The weight of the basic sandwich structure obtained from the failure criteria cited above was multiplied by a factor to account for local structural members needed for such detail considerations as load distribution, discontinuity stresses and unsymmetrical effects. Due to the fact that this study effort was

not a detailed structural design, influence of local detail design on structural weight was based on past experience at Avco.

Figures 136 to 138 demonstrate the comparison in the variation of structural weight of the aerodynamic load-bearing structure versus M/C_{DA} for the V-1 and V-2 shapes for Mars entry.

A comparison of the weight of aluminum for the substructure is presented in figures 139 and 140.

Figure 141 presents a typical variation in the unit area structural weight referenced to the design conditions for the Mars lander.

It is apparent from the curves of weight versus M/C_{DA} that the structural weight becomes extremely significant or even prohibitive for low values of M/C_{DA} ; therefore, it is desirable to design the vehicle to the largest permissible value of M/C_{DA} .

The study did not include a complete investigation of the temperature history of the substructure in relation to the aerodynamic loading for every trajectory used in the parametric investigation. However, the use of 5026 as the heat shield material exhibits a small backface temperature rise at maximum dynamic pressure. The heat shield must satisfy a soak requirement at which time the aerodynamic loads are small so that strength at temperature is not critical. At the present time, the allowable temperature of the bond between the heat shield and substructure does not allow the full potentialities of the stainless steel structure to be realized. Also, since the substructure does contribute to the thermal protection system in that it absorbs heat, the higher specific heat of the aluminum structure shows an advantage over the steel in the requirements for the heat shield.

A detailed investigation of the thermal stresses experienced during entry was not performed because of the wide range of entry conditions and vehicle designs. It is not expected that thermal stress conditions will constitute a mode of failure in the substructure because of the compatibility between the heat shield and structure.

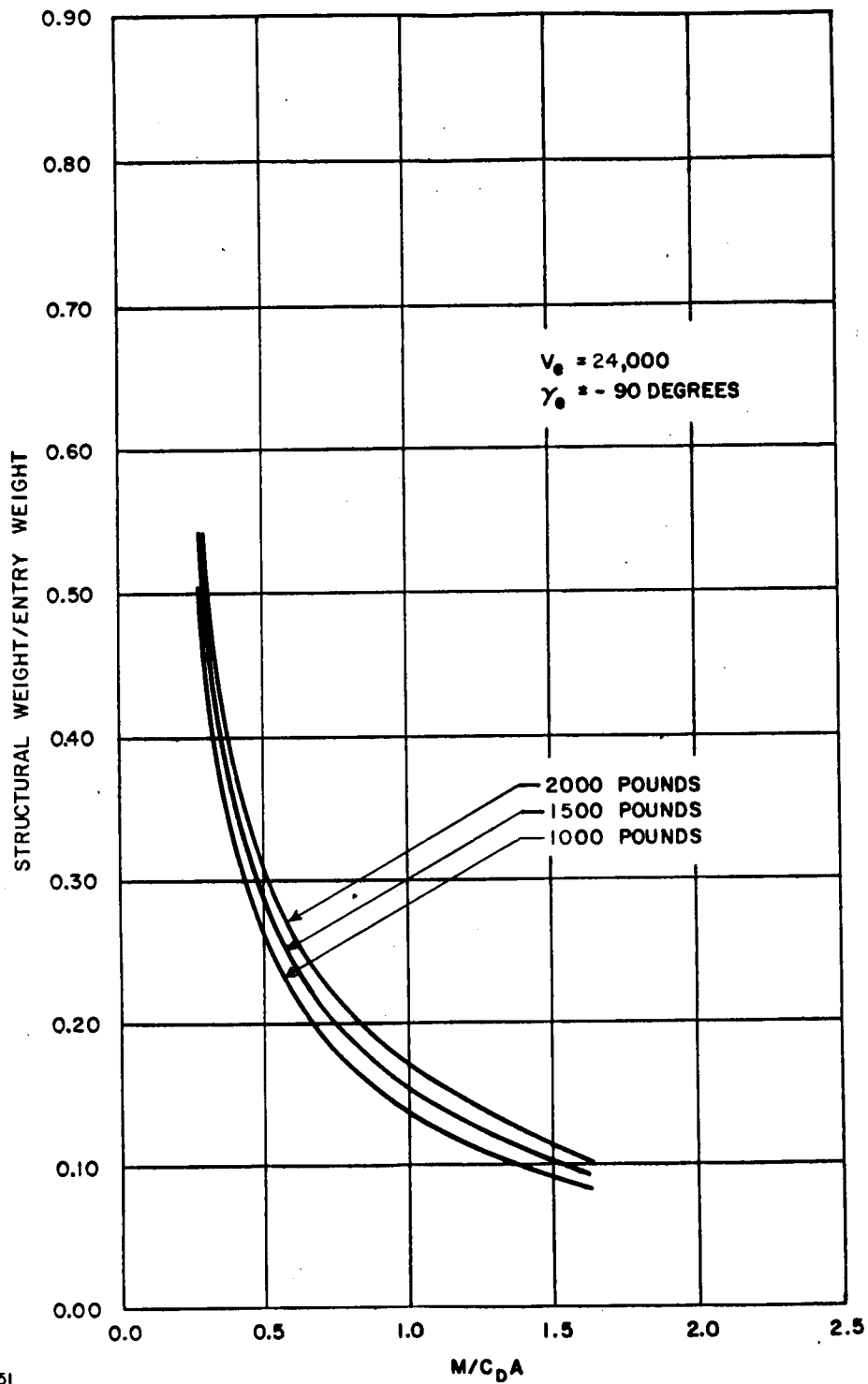
2. Internal structure. Preliminary methods of analysis were employed in the evaluation of the petal structure and the internal structure of the lander. The internal structure is stiffened sheet construction in which the primary modes of failure are yielding and buckling due to the axial and lateral inertia loads during entry and impact. The Mars reference design is an aluminum structure because of the thermal environment. The internal structure is provided with a direct load path to the spherical cap through pads which transmit the inertia loads. The lateral loads are carried from the internal structure to the external structure through webs which introduce the load into a ring built into the cylindrical section of the entry vehicle. Ascent inertia loads are

also transmitted through this load path. Webs are provided for the internal structure in order to distribute the inertia loads and impact loads through the structure. The weight of the internal structure is difficult to evaluate because of the unknown structure involved in the detail design of supporting the payload components; therefore, a factor was used on the overall weight sized by the general failure criteria to account for the structural details.

3. Reerection structure. The petal structure central rib reacts the main parachute inertia loads during entry and also serves as the load path for the main parachute when it is deployed. The mode of failure of the rib is yielding due to bending stresses. The rib also provides the bending and torsional rigidity required for reerection. The central rib of the petals is surrounded by an aluminum, and fiberglass sandwich structure which protects the payload during toppling. It is difficult to establish the structural requirements for the petals because of the unknown terrain. Figure 141 describes the variation of these structural weights for the Mars reference design.

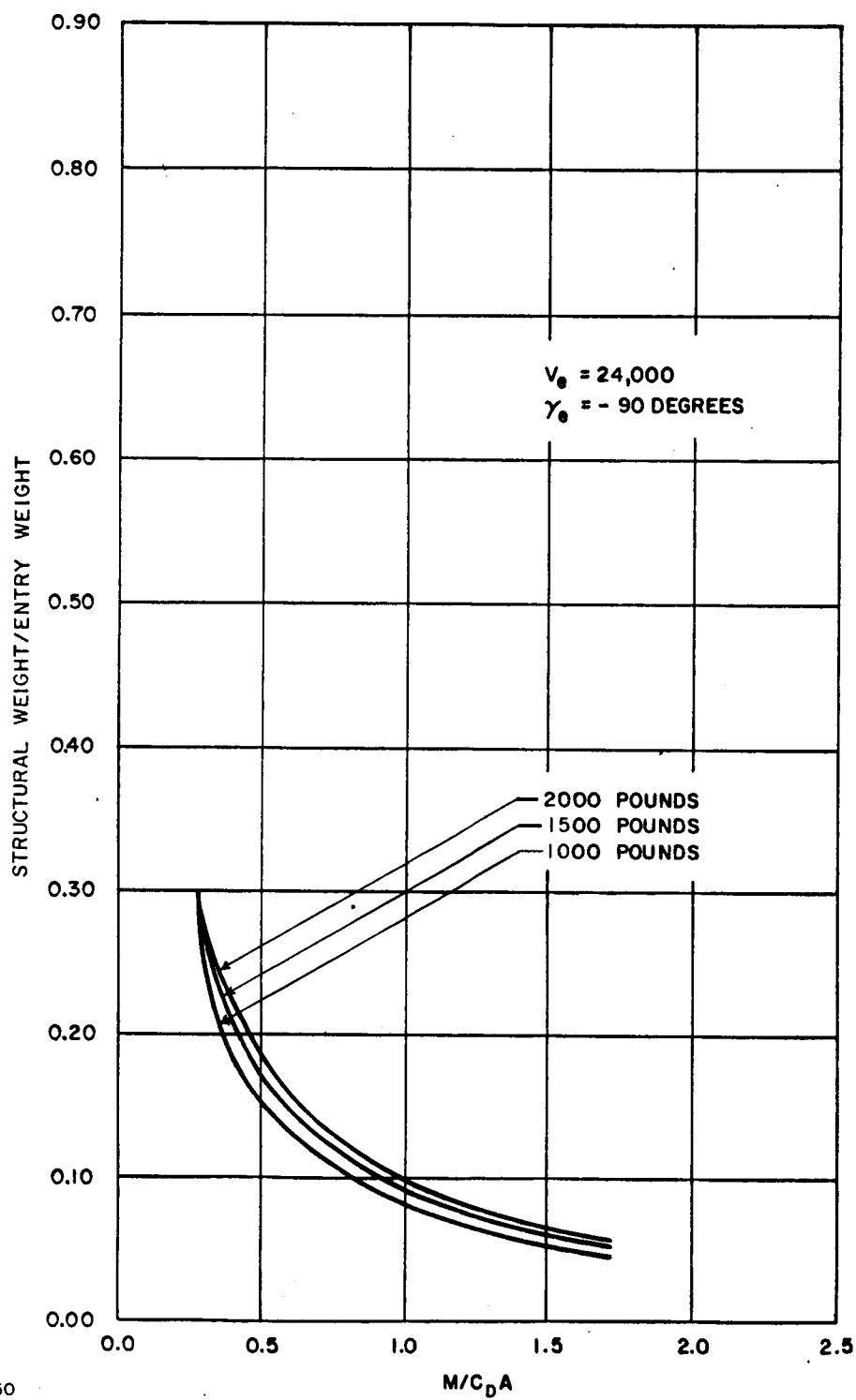
4. Impact structure. There are three interrelated dynamic parameters which influence the design of the impact attenuation system. These three stroke, velocity, and acceleration, all have limits imposed by other considerations (i.e., entry vehicle c.g. location, descent time, and entry accelerations, respectively). However, since the parameters are related through the equations of impact dynamics, it may happen that one of the constraints cannot be met. For example, consider the simplest case, in which the payload is brought to rest with constant deceleration by the energy absorption system (this is the case, in fact, in the reference design when the payload impacts flat). Then, the parameters are related by the equation $V^2 = 2as$. If it should happen that this equation cannot be satisfied without exceeding the acceleration or stroke limit, then one of three alternatives must be used. The maximum permissible velocity could be reduced, which would require a larger and heavier parachute. The stroke could be increased, but only at the expense of aerodynamic stability. The best alternative appears to be to increase the impact decelerations to values higher than those felt during atmospheric entry. This imposes more stringent requirements on the instruments in the payload; however, if the increase in acceleration is not too great, most of the instruments could be made to withstand these loads with only slight modifications. Should some components require extensive modification, they could, alternatively, be provided with their own isolation systems to allow them to move relative to the internal structure, thereby reducing the accelerations experienced by them.

A tradeoff exists between parachute system and impact attenuation system weights, the former decreasing with increasing velocity while the latter increases. There is an optimum velocity at which the combined weight is a minimum. If this optimum is less than the maximum permissible velocity, then the optimum velocity would be used in the design. However, for the present reference design for Mars, the optimum velocity was about twice the velocity permitted by the descent time requirements and so was not a factor in the design.



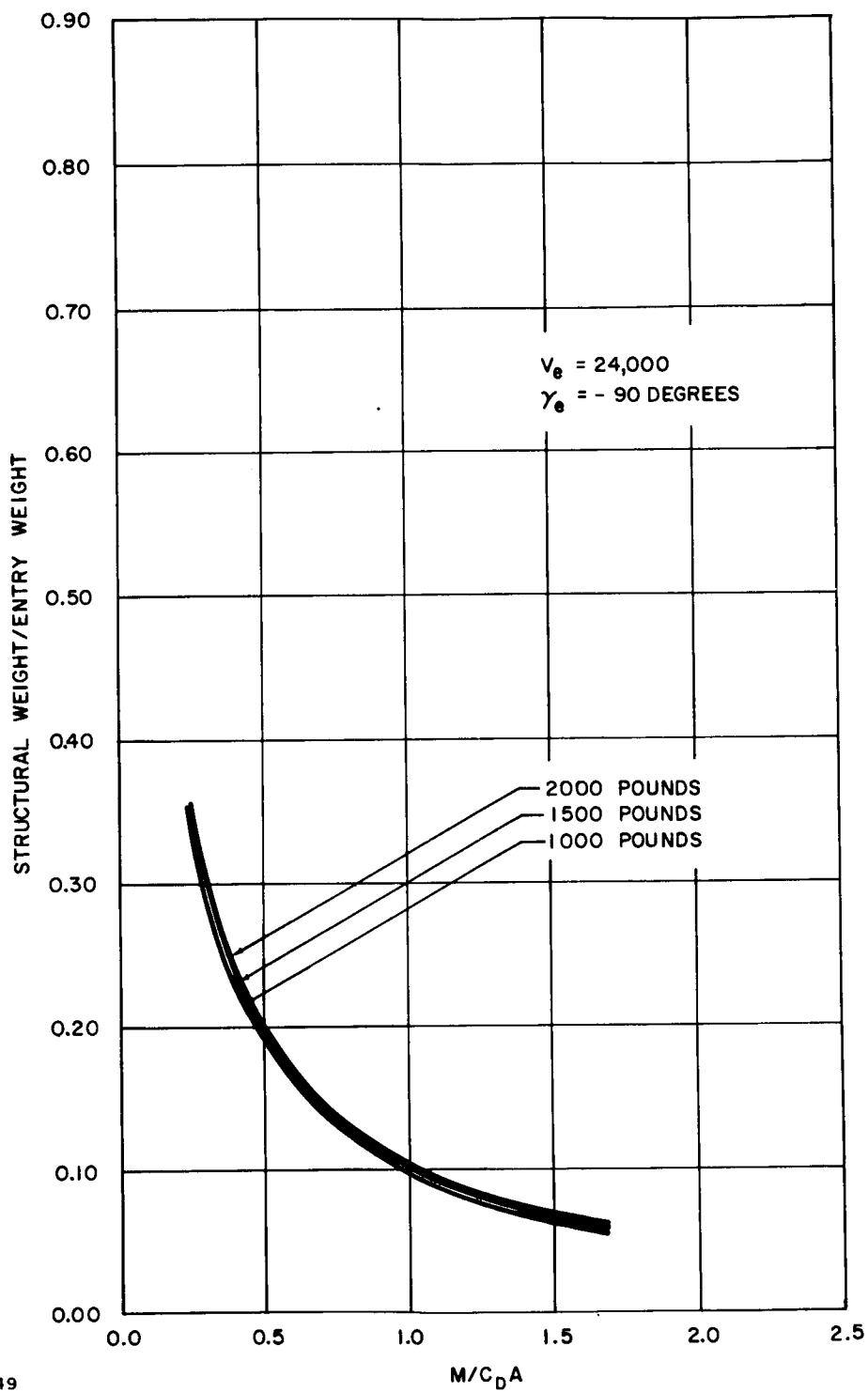
63-9851

Figure 133 STRUCTURAL WEIGHT/ENTRY WEIGHT RATIO VERSUS $M/C_D A$



63-9850

Figure 134 STRUCTURAL WEIGHT/ENTRY WEIGHT RATIO VERSUS $M/C_D A$



63-9849

Figure 135 STRUCTURAL WEIGHT/ENTRY WEIGHT RATIO VERSUS $M/C_D A$

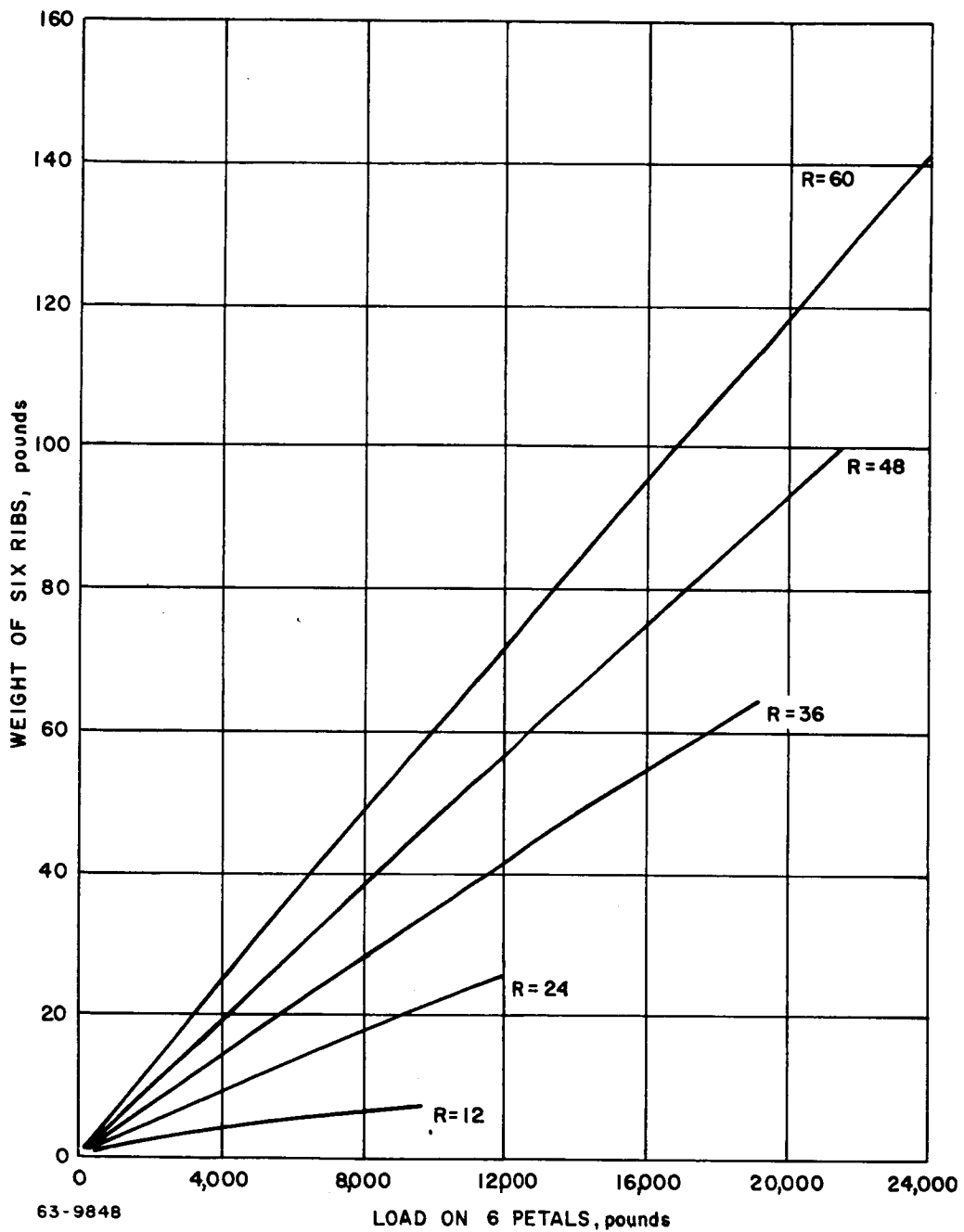


Figure 136 WEIGHT OF SIX PETAL RIBS VERSUS LOAD ON SIX PETALS

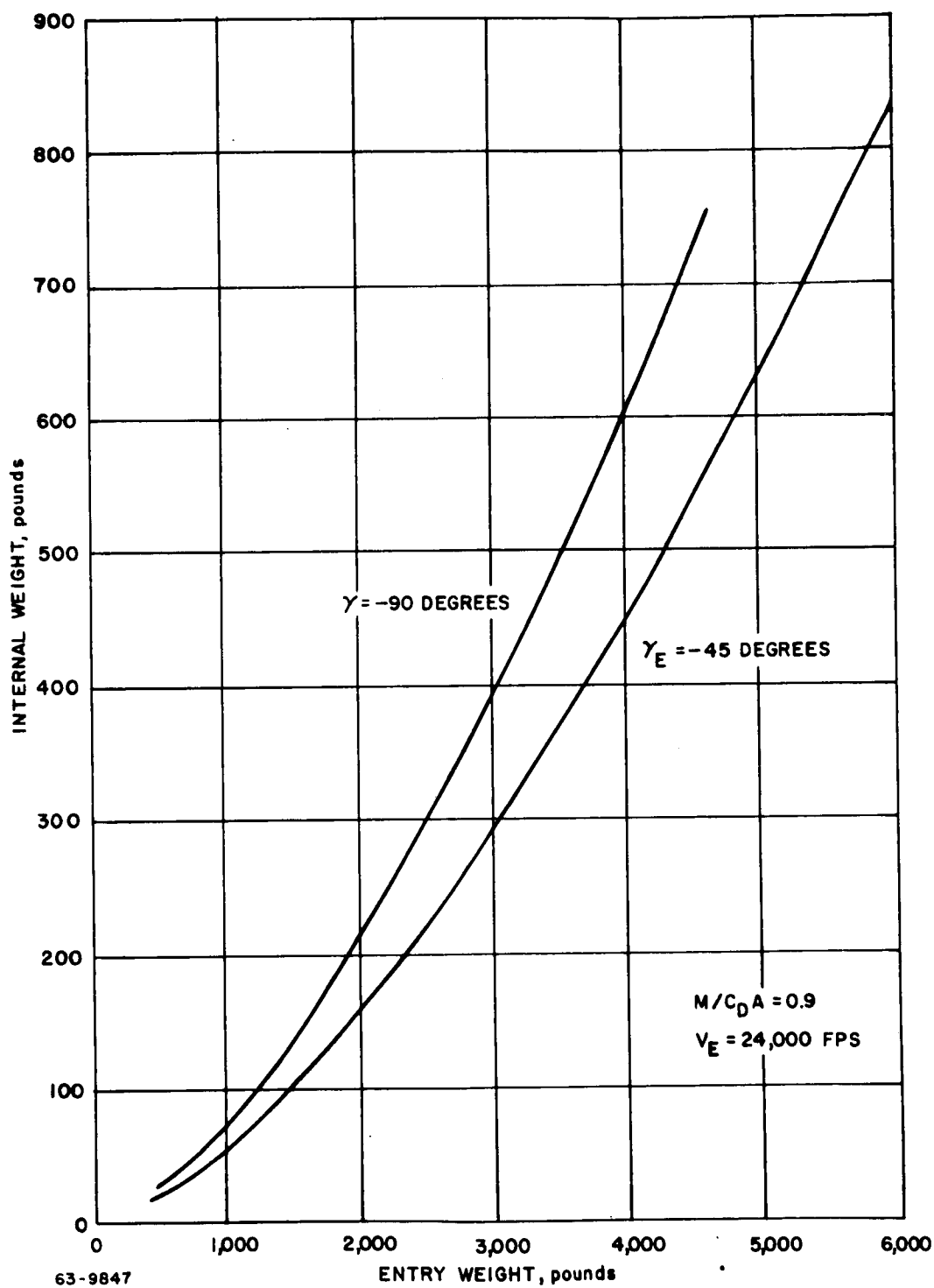


Figure 137 WEIGHT OF INTERNAL STRUCTURE VERSUS ENTRY WEIGHT

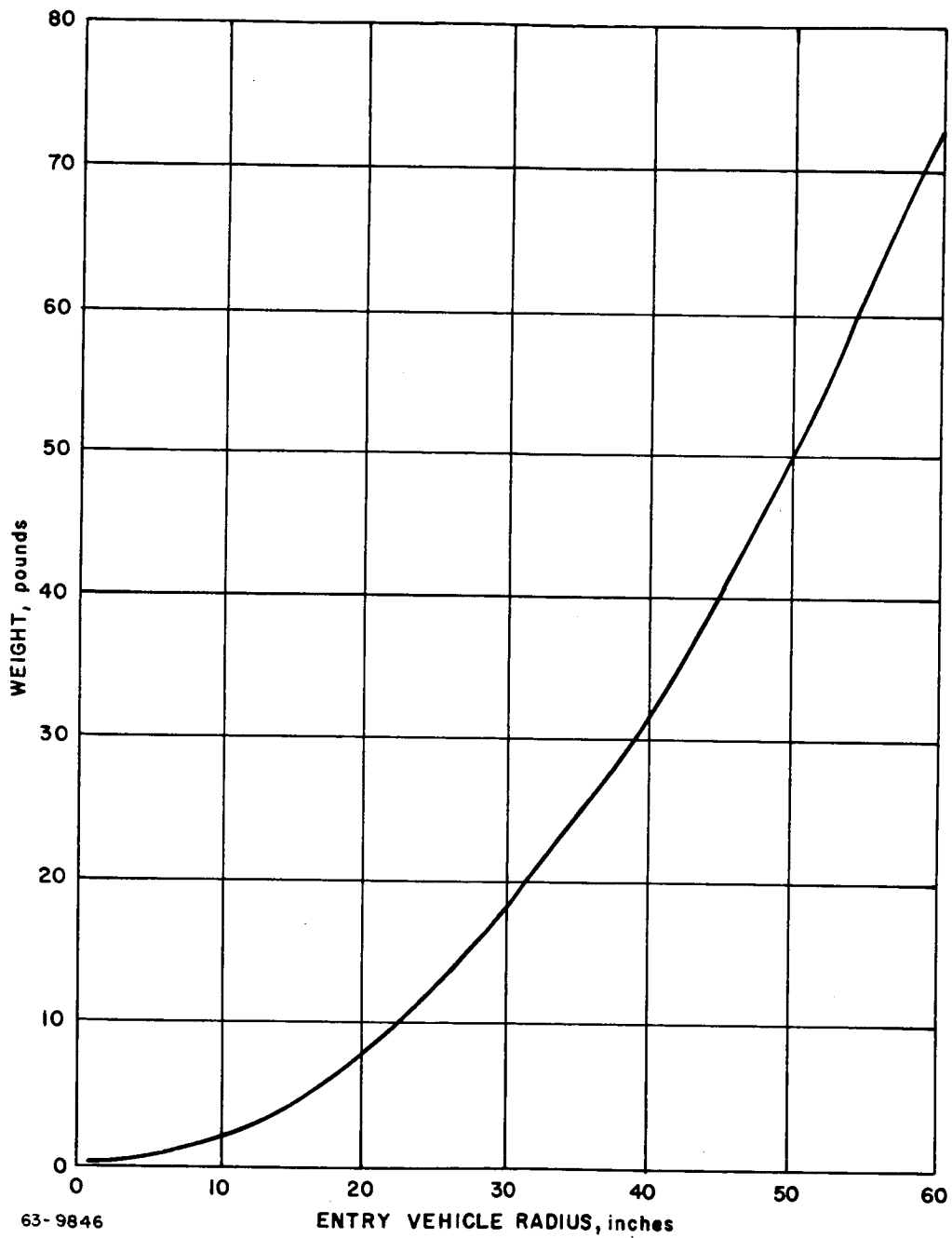
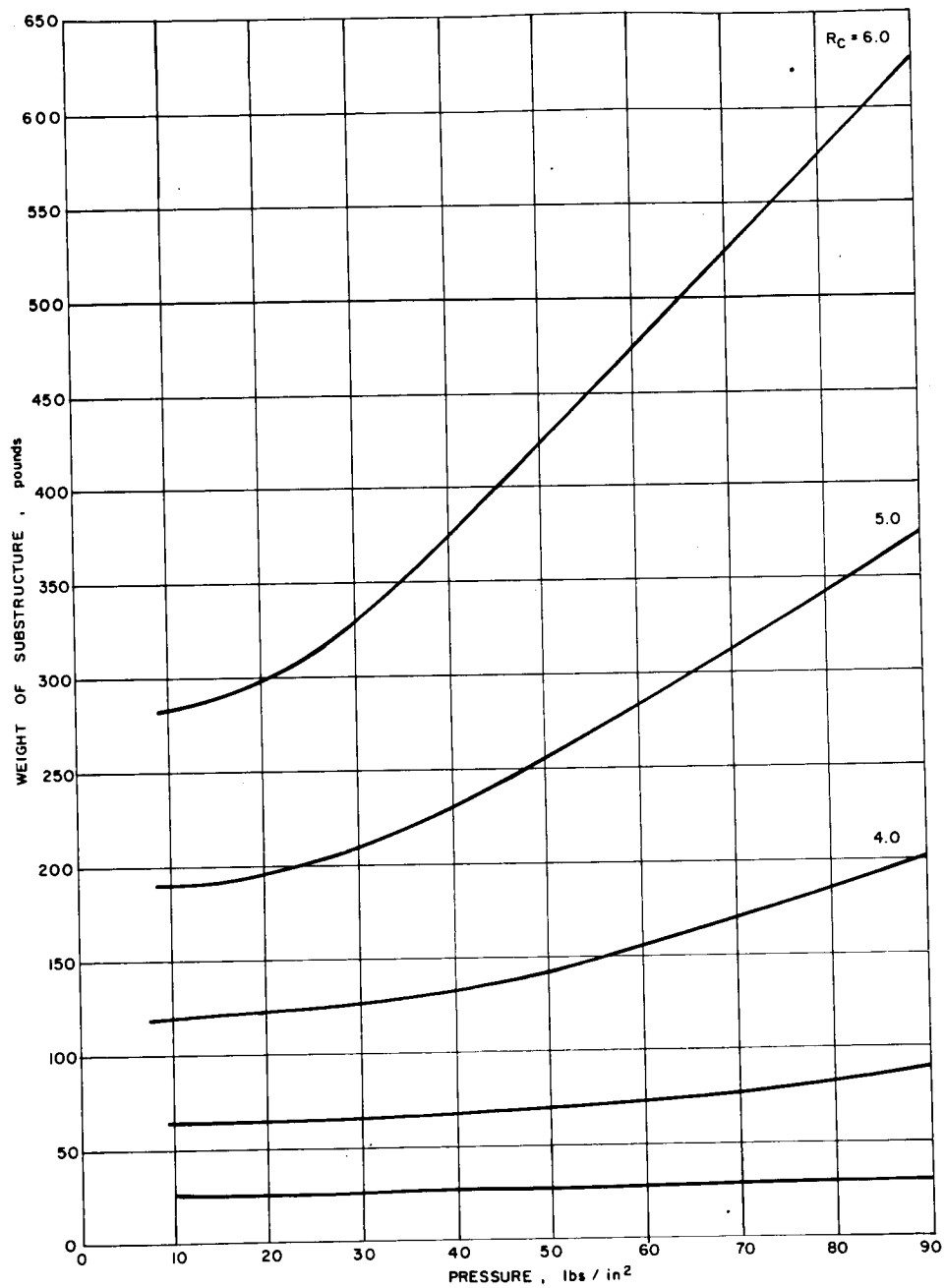


Figure 138 WEIGHT OF PETAL STRUCTURE VERSUS ENTRY VEHICLE RADIUS



63-9845

Figure 139 WEIGHT OF SUBSTRUCTURE VERSUS PRESSURE

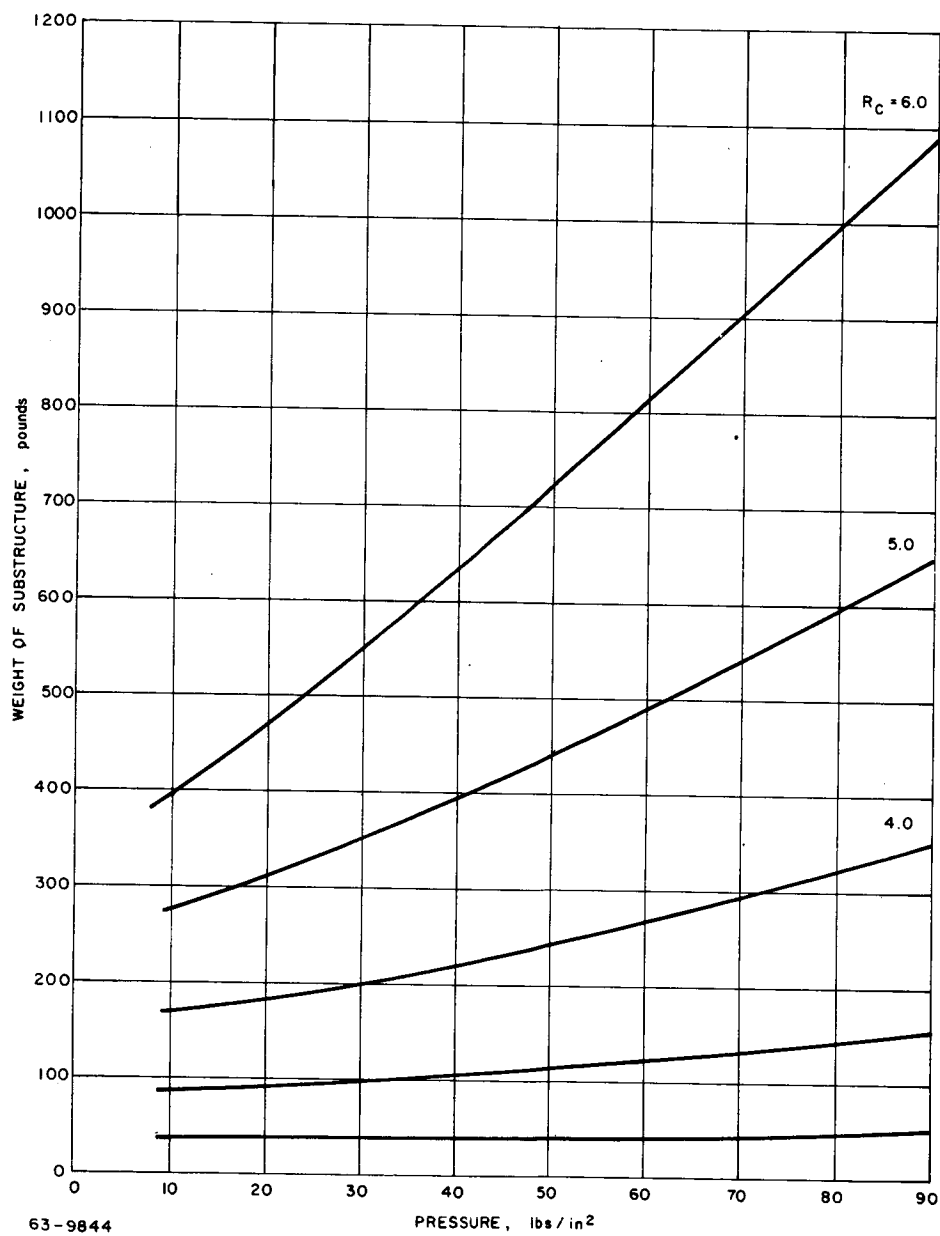
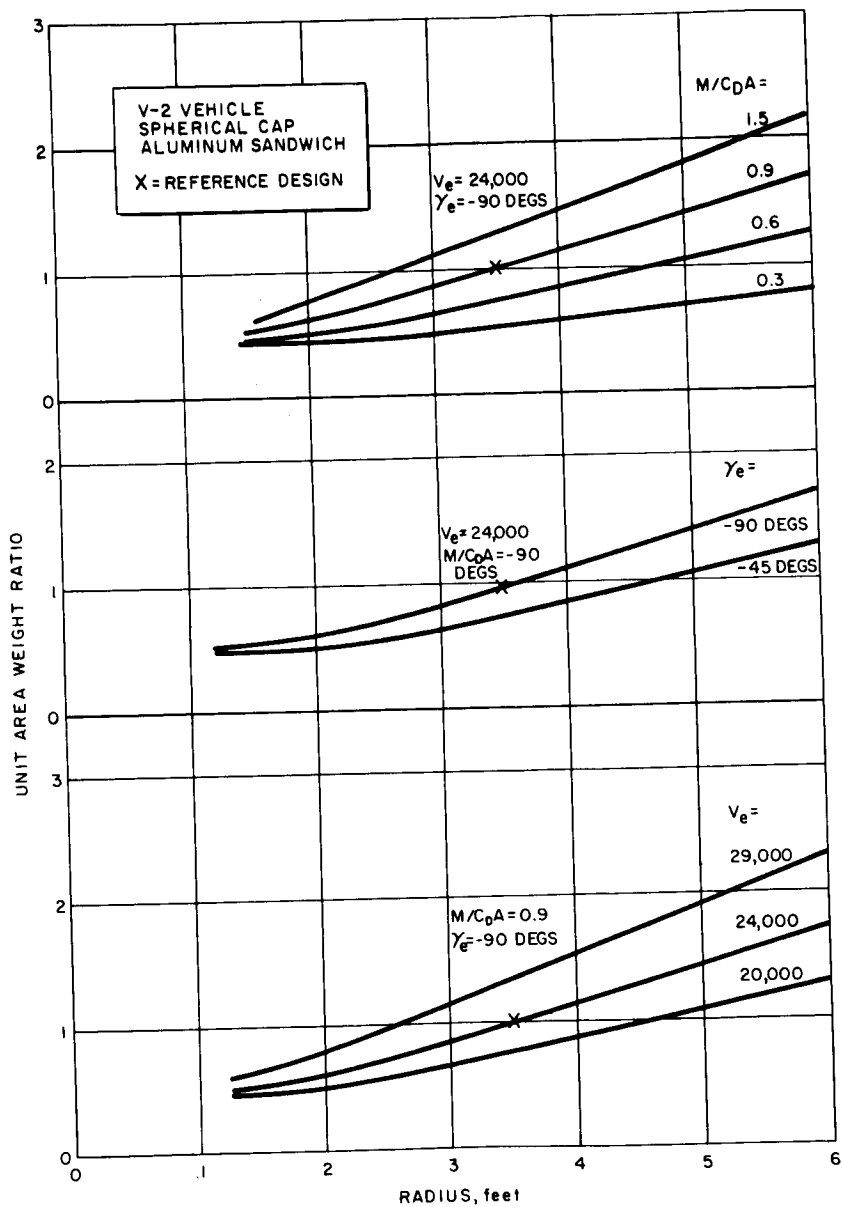


Figure 140 WEIGHT OF SUBSTRUCTURE VERSUS PRESSURE



63-9843

Figure 141 VARIATION OF TYPICAL UNIT AREA WEIGHT FOR MARS ENTRY

Once the basic parameters of velocity, acceleration, and stroke have been determined, the design can proceed to the details of material selection, geometry, etc. These details are secondary to the general conclusion that the impact attenuation system for the Mars lander accounts for less than 3 percent of the landed weight. This is based on using a material which can absorb on the order of 6,000 ft-lb of impact energy per pound of material used.

5.3 Structural Consequences of Kaplan's Low-Pressure Atmosphere

1. External structure. The proposed low density atmosphere has serious consequences on the design of the Mars lander. Due to the very low density of the postulated atmosphere and its implications on the parachute system weight, the M/C_{DA} suitable for design is less than 0.3 slug/ft^2 . In this range of M/C_{DA} , the weight of the external structure becomes very significant.

The criteria investigated in the design of the entry vehicle were general instability and yield considerations. The aerodynamic loading encountered by the vehicle in the JPL 11 mbar atmosphere is approximately the same as the Schilling minimum temperature atmosphere. It is apparent for the curves presented previously that the structural weight increases with decreasing M/C_{DA} . Although the weight per unit area necessitated by general instability requirements decreases as M/C_{DA} becomes smaller, the increase in the total surface area more than compensates for the decreased unit area weight and the total weight of the structure increases. Therefore, in order to minimize the large surface areas associated with a low M/C_{DA} vehicle, the afterbody of the Mars lander was modified to the Apollo shape. This could be accomplished because aerodynamic stability requirements, stroke of the impact attenuation system, and packaging constraints could be realized in a vehicle with such a low M/C_{DA} and the Apollo shape.

The type of construction used in the entry vehicle structure was aluminum sandwich type structure. A ring-stiffened beryllium afterbody was also considered for this design. The beryllium would serve as combination structure-heat sink for entry heating and loading. This concept was rejected because it was thought that any small weight saving realized by the use of beryllium would not justify the added complexity of designing a beryllium structure for the sizes contemplated for the Mars lander.

2. Internal structure. The packaging of the payload in the Apollo shape requires that additional structure be provided to transmit the inertia loads of the payload to the external structure. Another modification of this design is the requirement that the loads due to drogue chute deployment be transmitted into the petal structure rather than the external structure.

The deceleration loading occurring during entry are comparable to those for the original reference design; therefore, the internal structure of the landed package is essentially the same as the original.

3. Impact structure. The impact inertia loads imparted to the payload and internal structure can be limited to those experienced during entry if the possibility of 200 ft/sec winds is ignored. The overall structure can then be designed to entry inertia loads and provisions can be made locally for the structure of selected payload components to withstand the much higher inertia loads associated with the possibility of encountering 200 ft/sec winds.

If a surface wind of 200 ft/sec must be accounted for in the design of the impact attenuation system, then several alternatives exist:

- a. Nonsurvivable lander--This is, of course, the simplest solution.
- b. Deployable system--In order to obtain the necessary stroke and still maintain deceleration limits of 100 to 200 g, a deployable impact system could be employed, such as a large toroidal air-bag or even a segmented, spherical bag completely enclosing the payload.
- c. Retrorockets--This scheme is quite complex, since in order to cancel out horizontal velocity the speed of the payload relative to the ground must be determined during descent.
- d. Payload packaged upside-down or sideways--Although the necessary stroke cannot be obtained between the payload and the front cap of the entry vehicle, there may be sufficient room to package the impact system to the side or the back of the lander.
- e. Higher g level--In order to adapt the present design with as few changes as possible, the deceleration level must be raised to over 500 g. As a variation on this procedure, nominal and extreme acceleration limits could be specified. This means that the payload would be designed so that everything survived under nominal conditions of 30 ft/sec winds and that only a certain number of instruments would be required to survive under the extreme condition of a 200 ft/sec wind.
- f. Skidding--Instead of providing for eliminating the high horizontal velocity by means of an internal system, which has proven so difficult, we can hope that the terrain is smooth enough to allow the package to bounce and skid along without hitting an obstruction and thus lose its horizontal velocity by friction.

Assuming the payload can be landed, the question remains whether or not 200 ft/sec gusts of wind will topple the package or skid it along the surface. It has been found that this situation is dynamically equivalent to the payload sitting on the Earth's surface in a 35 mph wind. This does not appear to be a critical problem.

REFERENCES

1. Project Voyager Status Report, RAD TM-62-80, June-August 1962.
2. Stephenson, C. V., W. S. Wilcox, H. T. Crenshaw, H. L. Hancock, and E. B. Dismukes, Stanford Research Institute, ASD-TDR-63-57, February 1963.
3. McGrath, J. C., Aeronautical Systems Division, ASD-TDR-63-61, April 1963.
4. Neff, R. J., Phoenix Trimming Co., ASD-TDR-63-248, March 1963.
5. Schilling, G. F., Limiting Model Atmospheres of Mars, The Rand Corporation, R-402-JPL, August 1962.
6. Hill, F. J., Jr., and L. N. Morrisette, A Six-Degree-of-Freedom Re-entry Trajectory Program for Ballistic and Lifting Vehicles, Avco RAD-TM-62-70, September 1962.
7. McKinzie, D. J., Jr., Experimental Results of the LMSD E-5 Cornell 24-Inch Shock-Tunnel Tests, Avco RAD-TM-61-8, May 1961. Confidential
8. Schilling, G. F., Limiting Model Atmospheres of Mars, The Rand Corporation, R-402-JPL, August 1962.
9. Kaplan, L. D., A Preliminary Model of the Venus Atmosphere, JPL Technical Report 32-379, December 1962.
10. Detra, R. W., and H. Hidalgo, Generalized Heat Transfer Formulae and Graphs, AERL Research Report 72, March 1960.
11. Fay, J. A., and F. R. Riddell, Theory of Stagnation Point Heat Transfer in Dissociated Air, AERL Research Report 1, April 1957.
12. Rutowski, R. W., and K. K. Chan, Shock Tube Experiments Simulating Entry Into Planetary Atmospheres. Adv. in the Astronaut Sci. 5, Proceedings of the Second Western National Meeting, 1960.
13. Gilmore, F. R., Equilibrium Composition and Thermodynamic Properties of Air to 24,000°K, Rand Report RM-1543, 1955.
14. Hansen, F. C., Approximations for the Thermodynamic and Transport Properties of High Temperature Air, NASA TR R-50, 1959.

15. Raymond, J. L., Thermodynamic Properties of Carbon Dioxide to 24,000°K With Possible Application to the Atmosphere of Venus, Rand RM-2292, November 1958.
16. Treanor, C. E., and J. G. Logan, Jr., Thermodynamic Properties of Nitrogen from 2000°K to 8000°K, Cornell Aero Lab. Inc., Report BE-1008-A-5, January 1957.
17. Waldman, G., Blunt Body Velocity Gradients and Shock Detachment Distance, Avco RAD Memorandum, February 1961.
18. Chandrasekhar, S., Radiative Transfer, Dover Pub. Inc., New York, New York, 1960.
19. Flinn, D. J., A Solution of the Radiative Transfer Equation, Avco RAD TR-S230-DJF-209.
20. Patch, R. W., W. L. Shockleford, and S. S. Penner, Approximate Spectral Absorption Coefficient Calculations for Electronic Band Systems Belonging to Diatomic Molecules, J. Quant. Spectrosc, Radiant Transfer, vol. 2, 1962, pp. 263-271.
21. Unsold, A., Continuous Spectrum of High-Pressure Hg. Lamp and Similar Gas Discharges. Ann. der. Physic, vol. 33, 1938, pp. 607-616.
22. Biberman, L. M., and G. E. Norman, Calculation of Photo-Ionization Absorption. Opt. i. Spektr. vol. 8, 1960, pp. 433-438.
23. Biberman, L. M., G. E. Norman, and K. N. Ulyanov, On the Calculation of Photoionization Absorption in Atomic Gases. Opt. i. Spektr. vol. 10, pp. 565-569.
24. Bergess, A., and M. J. Seaton, A General Formula for the Calculations of Atomic Photoionization Cross-Sections. Monthly Notices of the Roy. Astron. Soc., vol. 120, 1960, pp. 121-151.
25. Kivel, B., and K. Bailey, Tables of Radiation from High Temperature Air. Avco Research Laboratory, RR 21.
26. Morris, J. C., Research On Radiation from Arc Heated Plasmas, Avco RAD, Quart. Progress Report 7, Contract AF 33 (616)-8390, 6 September 1963.

27. McAllister, L. E., J. C., Bolger, E. L. McCaffery, P. J. Roy, F. W. Ward, and A. C. Walker, Jr., Behavior of Pure and Reinforced Charring Polymer During Ablation Under Hypervelocity Reentry Conditions. From Applications of Plastic Materials in Aerospace, Chemical Engineering Progress, Symposium Series 40, vol. 59, 1963.
28. Apollo Heat Shield Monthly Progress Reports. Avco RAD, Avco Report Series 201. Confidential
29. Avco RAD Doc. 63-799. Internal Confidential
30. John, R. R., Internal Technical Release, Avco RAD, October 1959.
31. Avco RAD Doc. RAD-SR-63-136. Confidential
32. Ceccon, H., to R. Schlier, Avco RAD Internal Memo, Experimental and Theoretical Physics Section -62, 20 May 1963.
33. Rice, S. O., Selected Papers on Noise and Stochastic Processes, Edited by Wax, Nelson, p. 239.
34. Theory and Design of Chirp Radars. See B.S.T.J. July 1960, p. 745.
35. Springett, J. C., Command Techniques for the Remote Control of Interplanetary Spacecraft. National Telemetry Conference, vol. 2 proc. 1962.
36. Viterbi, On Coded Phase - Coherent Communications. IRE Trans. figure 8, for word error probability 5×10^{-3} , March 1961, p. 9.
37. Jaffee, Digilock Telemetry System, IRE Trans. Set, figure 6, March 1962, p. 48.
38. Hannan, P. W., Microwave Antennas Derived from Cassegrain Telescope, IRE Transactions on Antennas and Propagation, vol. AP-9, no. 2, March 1961, p. 147.
39. Frazer, A. H., J. J. Kane, and F. T. Wallenberger, E. I. duPont deNemours & Co., from Symposium on Fibrous Materials, Sponsored by Nonmetallic Materials Laboratory, ASD, October 1962.
40. Johnson, D. E., E. H. Newton, E. R. Benton, L. E. Ashman, and D. H. Knapton, Metal Filaments for High-Temperature Fabrics. Arthur D. Little, Inc., ASD-TR-62-180, February 1962.
41. Johnson, D. E., and E. H. Newton, Metal Filaments for High-Temperature Fabrics. Arthur D. Little, Inc., ASD-TR-62-180, Part II, February 1963.

42. Hritzay, D., and R. Wiant, Wire Cloth Structure for a Radiating Reentry Vehicle. Avco-Everett Research Laboratory, Research Report 123, March 1962.
43. Kaplan, L. D., A Preliminary Model of the Venus Atmosphere, JPL Technical Report 32-379, December 1962.
44. Avco RAD Doc. 63-288. Confidential
45. Avco RAD Doc. 63-1521. Confidential
46. Avco RAD Doc. 63-799. Confidential
47. Louis, J. F., R. Decker, R. A. Allen, and T. R. Brogan, Simulation of Reentry Radiation Heat Transfer. Avco-Everett Research Laboratory, August 1963.
48. Timmins, R. S., Private Communication, Avco RAD.
49. Carlson, W., Private Communication, Ames Research Center, NASA, 10 September 1963.